Antimicrobial PLA and Calcium Phosphate Coatings and Thin Film Composites for Implants Applications

by Ipek Karacan Soylu

Thesis submitted in fulfilment of the requirements for
the degree of

Doctor of Philosophy (Science)

Under the supervision of Prof. Besim Ben-Nissan
Prof. Stella Valenzuela
Dr. Jerran Santos

University of Technology Sydney
Faculty of Science

[December2020]

CERTIFICATE OF ORIGINAL AUTHORSHIP

I, [Ipek Karacan Soylu] declare that this thesis is submitted in fulfilment of the requirements for the award of [Doctor of Philosophy], in the [Faculty of Science / School of Life Science] at the University of Technology Sydney.

This thesis is wholly my own work unless otherwise reference or acknowledged. In addition, I certify that all information sources and literature used are indicated in the thesis.

This document has not been submitted for qualifications at any other academic institution.

This research is supported by the Australian Government Research Training Program.

Production Note:
Signature: Signature removed prior to publication.

Date: 24/08/2020

Acknowledgements

I've been a dreamer ever since I was a child and my biggest and most important dream was always to become a scientist. Being accepted as a Ph.D. student at the University of Technology Sydney allowed me to raise and progress this journey and moved it from Turkey to Australia

This Ph.D. thesis is the summary of my three-year long journey. It would not have been possible to write this doctoral thesis without the help and great support of the kind people around me, to only some of whom it is possible to give a particular mention here.

Firstly, I would like to express my sincere gratitude to my supervisors, Prof. Besim Ben-Nissan, Prof. Stella Valenzuela, and Dr. Jerran Santos, for the continuous support of my Ph.D. research and their insightful comments and encouragement. Besides being the reason I was able to come and create this piece of work and everything else that happened in my life due to my arrival here, Prof. Besim Ben-Nissan was more than a great supervisor and more than a mentor. He with his wife Ariela Ben-Nissan and her warm motherly love became family.

I would like to thank Prof Bruce Millthorpe for his great feedback and encouragement as a great advisor.

I express my warm thanks to the following people for helping with this research: Dr. Joshua Chou of the Faculty of Biomedical Engineering at UTS, Dr. Matt Padula of Proteomics, Metabolomics, Lipidomics Core Facility at UTS, and also our collaborators; Prof. Michael Swain of the University of Sydney, Prof. Wolfgang Muller of Technical University of Berlin, Germany, A/Prof. Sophie Cazalbou of the University of Toulouse, France, Prof Faik Nuzhet Oktar of Marmara University, Turkey. Their advices, feedback, and constructive comments were highly valuable for me to build my research ideas strongly.

I would like to acknowledge the staff in the Microstructural Analysis Unit and Microbial Imaging Facility at UTS for helping me out in various aspects of this project, especially the fluorescent imaging, SEM, XRD aspects. My sincere gratitude to Sarah Ambrose for editing my thesis, your help, and kindness was invaluable.

I also would like to thank my parents, brother and special friends Meltem Yilmaz and Cansu Isler, for their friendship, love, and support. The distance between us never stopped them from caring about me, and I always felt their love and support during my Ph. D. journey.

Finally, I would like to thank the most valuable and important person in my life, my team mate, my partner in life and husband Orkun Soylu for his unconditional love and support.

During the ups and downs typical to all Ph.D. journeys he was always there for me when I needed him. His encouragement and faith in me over the years of this journey were integral to this works quality and completion.

Abstract

Implant-related infections after the insertion of biomedical implants are still prevalent, and the current treatment methodology requires the use of large doses of antibiotics systemically. Large doses can lead to a number of side effects including antibiotic resistance and adverse effects on the other organs. These infections delay healing, worsen functional outcome and incur significant socio-economic costs. Bone implant related infections, surgery site infections (SSI), and osteomyelitis remain the most challenging clinical problems faced. This thesis aimed to develop a novel implant coating system based on a 'Local and Controlled Antibiotic Delivery System with Biodegradable Polymeric Thin Film Composite Coating' for metallic bone implants.

The specific aim of this study was to design a novel multi-functional and antibacterial coating for implants as the drug delivery systems to prevent post-operative complications and osteomyelitis. The main challenge was to obtain the perfect design and the selection of appropriate biomaterials; implantable device with antibacterial, biocompatible and bioactive properties. Therefore, gentamicin antibiotic (Gm) and Gm loaded coralline hydroxyapatite (HAp) particles were incorporated into a poly-lactic acid (PLA) matrix as the main biocomposite. A number of systems were produced, characterized and tested, which included PLA, PLA-Gm mixture, and a PLA-Gm-(HAp-Gm) biocomposite.

The coral skeleton ($CaCO_3$) was converted to HAp by using the hydrothermal conversion method. These microspheres were loaded with Gm and HAp-Gm particles and incorporated within the PLA thin film composites. Coralline-HAp possesses a unique nano- and meso-porous structure and can be used as a drug carrier for the sustained release of antibiotics on metallic bone implants. While the physiochemical characterizations of the PLA biocomposite coating were evaluated, their Gm release profile were analyzed by the continuous dissolution method. The bioactivity and biocompatibility of the design was tested on Adipose-derived stem cells using *in vitro* studies. The antibacterial activity and biofilm formation behaviour were also analyzed with *S. aureus* and *S. epidemidis*.

Different Gm concentrations (5%, 10%, 15%, 20% and 30% [w/w]) were incorporated into the PLA biocomposites and were found to be highly effective on the inhibition of *S. aureus* and *S. epidermidis* growth at the planktonic stage. At the biofilm formation stage of S. *aureus*, the significant reduction of bacterial attachment and the increasing of dead microcolonies were observed for even the lowest 5% (w/w) PLA-Gm-(HAp-Gm) coated samples. This research showed that the biodegradable and antibacterial PLA biocomposite coatings design has high potential as a viable alternative method for existing clinical applications on many metallic orthopedic and maxillofacial bone implants.

Table of Contents

Certificate of Original Authorship i

Acknowledgements ii

Abstract iv

List of Figures xi

List of Tables xix

Publication List xxii

Conference Posters xxiv

Chapter 1. Background & Literature Review 1

1.1 Bone Structure and Function 2

1.2 Bone Disorders 5

1.3 Implant insertions and implant-related infections 7

1.4 The design of medical bone implants and their applications 9

1.5 Biomaterials for Bone Implants 11

1.5.1 History of Biomaterials 11

1.5.2 Metallic Biomaterials 16

1.5.3 Ceramic Biomaterials 19

Calcium Phosphates 21

1.5.4 Polymeric Biomaterials 24

1.6 Surface Modifications: Thin Film Coating 29

1.6.1 Dip coating technique 32

1.6.2 Spin coating technique 33

1.7 Combination of Metallic Implants with Drug Delivery Systems 34

1.8 References 38

Statement of Research 43

Hypothesis 43

Aims and Objectives 43

Thesis Format 44

Graphical Abstract 45

Chapter 2. Synthesis of Hydroxyapatite from Porites Coral and Drug Loading Studies 46

2.1 Hydrothermal Conversion of Porites Coral and Physio-chemical characterization analyses of Coral vs. Coral-Based Hydroxyapatite 47

2.1.1 Introduction 47

2.1.2 Experimental Methods 49

2.1.2.1 Coral Sample Preparation 49

2.1.2.2 Hydrothermal Conversion Method 50

2.1.2.3 The Thermal, Chemical and Physical Analyses of Coral and Coral-Based Hydroxyapatite 52

2.1.3 Results and Discussions 53

2.1.3.1Thermal Analysis (DTA-TGA) 53

2.3.1.2 Physiochemical Analyses: X-Ray Diffraction Analysis (XRD) 54

2.3.1.3 Chemical Analyses: Fourier transform infrared spectroscopy (FT-IR) and Inductively coupled plasma-mass spectroscopy (ICP–MS) analysis 55

2.1.3.4 Scanning Electron Microscope Analysis (SEM-EDS) 58

2.1.3.5 Surface Area and Particle Size Analysis 60

2.1.4 Conclusions 62

2.2 Drug Loading Study and Physio-Chemical Characterizations of Drug Loaded Coralline Hydroxyapatite with Medical Grade Drugs 63

2.2.1 Introduction 63

2.2.2 Experimental Methods 65

2.2.2.1 Drug loading Method 65

2.2.2.2 Drug Encapsulation Efficiency (DEE) 67

2.2.2.3 Analysis of HAp-Gm particles 68

2.2.3 Results and Discussions 68

2.2.4 Conclusions 72

2.3 References 73

Chapter 3. Production and Characterization for PLA Biocomposite and The Coating Process for the metallic implants 77

3.1 Introduction 78

3.2 Experimental Methods 80

3.2.1 The Ti6Al4V substrate material preparation 81

3.2.2 The synthesis of PLA biocomposite thin films and the dip coating method 82

3.2.3 Surface characterization of PLA and PLA-Gm-(HAp-Gm) thin film coated Ti6Al4V discs 83

3.2.3.1 Scanning Microscope Analysis (SEM) 84

3.2.3.2 Atomic Force Microscope (AFM) 84

3.2.3.3 Profilometer 84

3.2.3.4 Fourier transform infrared spectroscopy (FT-IR) 84

3.3 Results and Discussions 85

3.3.1 The Surface Characterization of PLA thin film coated Ti6Al4V disc 85

3.3.2 The Surface Characterization of PLA-Gm, and PLA-HAp thin film coated Ti6Al4V polished discs 87

3.3.3 The Surface Characterization & Particle Distribution Analysis of PLA-Gm-(HAp-Gm) thin film coated Ti6Al4V discs at predetermined Gm concentrations (5% - 30% w/w) 89

3.3.4 Physicochemical analyses of PLA and PLA-Gm-(HAp-Gm) thin film coated Ti6Al4V disc surfaces 95

3.3.5 Application of PLA-Gm-(HAp-Gm) thin film coating system on different metallic bone implants 96

3.4 Conclusion 99

3.5 References 100

Chapter 4. Cumulative and Continuous Drug Release Studies on PLA Biocomposite Coated Implants 102

4.1 Introduction 104

4.2 Experimental Methods 107

4.2.1 Continuous Dissolution Method 108

4.2.2 Cumulative Dissolution Method 108

4.2.3 Surface Morphology and Chemical Characterization Analyses 109

4.2.3.1 Scanning Microscope Analysis (SEM) and Energy-Dispersive Spectroscopy (EDS) 109

4.2.3.2 Fourier-transform infrared spectroscopy (FT-IR)..... 110

4.3 Results and Discussions..... 110

4.3.1 Gm release pattern from PLA thin film biocomposite coated Ti6Al4V discs with the Continuous in vitro dissolution method 110

4.3.2 Surface morphology of PLA thin film biocomposite coated Ti6Al4V discs during the Gm release study (SEM and EDS) 115

4.3.3 Chemical characterization on the surface of PLA thin film biocomposite coated Ti6Al4V discs during the Gm release study (FT-IR) 124

4.3.4 In vitro Continuous vs. Cumulative Dissolution Methods for Gm release from PLA thin film biocomposite coated Ti6Al4V discs 126

4.3.5 Comparison of PBS solution and Ultra-pure water as a dissolution medium for the Continuous Dissolution Method for Gm release 128

4.4 Conclusion..... 129

4.5 References..... 131

Chapter5. Mechanical testing of antimicrobial biocomposite coating on metallic medical implants as a drug delivery system..... 133

5.1 Introduction 134

5.1.1 Nanoindentation testing 136

5.1.2 Scratch testing 137

5.2 Experimental Methods..... 138

5.2.1 The Substrate Material Preparation 138

5.2.2 Surface Characterization and Chemical Composition 139

5.2.2.1 Scanning Electron Microscope Analysis (SEM) 139

5.2.2.2 X-Ray mapping (XRM) and Energy Dispersive Spectroscopy (EDS)..... 139

5.2.2.3 Secondary ion mass spectroscopy (SIMS)..... 139

5.2.2.4 Atomic Force Microscope (AFM) 139

5.2.3 Mechanical and Adhesion Testing 140
5.2.3.1 Nanoindentation 140
5.2.3.2 Micro Scratch Test 140
5.3 Results and Discussions 140
5.3.1 Surface Characterization and Chemical Composition analyses of untreated and anodized Ti6Al4V discs 141
5.3.2 The Analyses of the Mechanical and Adhesion Properties 147
5.4 Conclusion 156
5.5 References 157
Chapter 6: Antibacterial Studies for PLA Biocomposite Thin Film Coated Ti6Al4V Bone Implants 160
6.1 Introduction 161
6.2 Experimental Methods 164
6.2.1 Determination of Clear Zone for *S. Aureus* and *S. Epidermidis* using the Modified Agar Disc Diffusion Method 164
6.2.2 *S. aureus* growth curve co-cultured with PLA-Gm-(HAp-Gm) coated Ti6Al4V discs 164
6.2.3 *S. aureus* biofilm formation and cytoxicity on PLA-Gm-(HAp-Gm) coated Ti6Al4V discs . 165
6.3 Results and Discussions 166
6.3.1 PLA-Gm-(HAp-Gm) coated Ti6Al4V implants inhibited *S. aureus* exponential growth 169
6.3.2 PLA-Gm-(HAp-Gm) coated Ti6Al4V implants inhibited S. aureus biofilm formation 172
6.4 Conclusion 175
6.5 References 176
Chapter 7. Human Adipose Derived Stem Cell Studies on PLA Biocomposite Thin Film Coated Implants 179
7.1 Introduction 180
7.2 Experimental Methods 183
7.2.1 Cell Culture Method for Human Adipose-Derived Stem Cells (ADSCs) 183
7.2.2 Scanning Electron Microscope (SEM) 184
7.2.3 Fluorescent Imaging with Fluorescence Deconvolution Microscope 185

7.2.4 Bio-plex Assay 185

7.2.5 Protein Extraction 187

7.2.6 LC/MS/MS Analysis 188

7.2.7 Data Processing and Analysis 189

7.3 Results and Discussions 189

7.3.1 In vitro bioactivity analyses with Human Adult Adipose-Derived Stem Cells 189

7.3.2 The effects of PLA, PLA-HAp, PLA-Gm, and PLA-Gm-(HAp-Gm) thin film coated Ti6Al4V metallic implants on ADSCs 190

7.3.3 The Gm dose effects of PLA-Gm-(HAp-Gm) thin film coated Ti6Al4V metallic implants at predetermined Gm concentration (5%, 10%, 15%, 20% and 30% w/w) on ADSCs 194

7.3.4 The effects of Ti6Al4V metallic implants before and after the anodization process on ADSCs 201

7.3.5 Proteomics Analysis 205

7.3.5.1 Mass Spectroscopy Protein Data from ADSCs on Ti6Al4V and PLA coated Ti6Al4V discs 206

7.3.5.2 Mass Spectroscopy Protein Data to determine effect of Gm release from PLA-Gm-(HAp-Gm) coated Ti6Al4V discs on ADCSs at different Gm concentrations 215

7.3.5.3 Mass Spectroscopy Protein Data from ADSCs on the untreated and thermally anodized Ti6Al4V discs 231

7.4 Summary and Conclusion 243

7.5 References 247

Major Findings 252

Chapter 8. Final Discussions and Conclusions 253

Appendix A 261

List of Figures

Figure 1. 1 The structure of long human bone (Karacan et al., 2019)

Figure 1. 2 Bone and bone cells (Kargozar et al., 2019)

Figure 1. 3 Supporting factors and fields for the improvement of medical device performance (Pruitt & Chakravartula, 2011)

Figure 1. 4 Three Generations of the Biomaterials (Ratner et al., 2012)

Figure 1. 5 The structural classification of biomaterials; a) bio-inert, b) bioresorbable, c) surface-active and d) bioactive (Choi et al., 2017)

Figure 1. 6 The effective nano-particle Properties for Biocompatibility (Naahidi et al., 2012)

Figure 1. 7 The categorization and application fields of bioceramics (Planell, 2009).

Figure 1. 8 The categorization scheme of some bioceramics according to their chemical reactivity (Dey and Mukhopadhyay, 2015)

Figure 1.9 The bond strength graph of HAp coated and bare implants (Dey and Mukhopadhyay, 2015).

Figure 1.10 The schema of the dip coating technique step by step (Ben-Nissan et al., 2011)

Figure 1.11 The general schema for spin coating method (Ben-Nissan et al., 2014)

Figure 2.1 The conversion process of the cleaned coral skeleton with Parr reactor.

Figure 2.2 Conventional Thermal (A) and Microwave heating (B) treatments (Li et al., 2017)

Figure 2.3 Thermal analysis of the coral powder

Figure 2.4 X-Ray diffractogram for Cleaned-calcined pure coral and coralline HAp

Figure 2.5 FT-IR spectra for cleaned-calcined hard coral (A) and coralline HAp (B), respectively

Figure 2.6 The ICP-MS chemical composition analysis results show the Porites coral skeleton before and after hydrothermal conversion with a graph (A), and a table (B)

Figure 2.7 The Porites coral microstructure before the grinding process, showing the micropores for bone growth.

Figure 2.8 SEM (A) and EDAX (B) results of Porites coral particles after the ball milling process

Figure 2.9 SEM (A) and EDAX (B) results of the crystalline structure of hydroxyapatite plates and related nano and meso pores of the coralline apatite after the hydrothermal conversion

Figure 2.10 Nitrogen adsorption and desorption for coral based HAp powder

Figure 2.11 BHJ pore size distribution curve for the coral based HAp powder

Figure 2.12 Diagram of drug loading procedure

Figure 2.13 Gm particles (A) before drug loading process, and 5% (B), 10% (C), 15% (D), 20% (E), 30% (F) Gm loaded HAp particles after drug loading process, respectively

Figure 2.14 EDAX spectrum for the HAp-Gm particles showing S peaks for Gm

Figure 2.15 Standard curve for the conversion of absorbance measurement values of HAp-Gm samples by UV-Vis spectroscopy to concentration values

Figure 3.1 The Dip coater device and the illustration schema for the dip coating process

Figure 3.2 SEM images for the surface of PLA thin film coated Ti6Al4V disc at low and high magnifications

Figure 3.3 3D AFM images and the surface roughness parameters for Ti6Al4V disc (A) and PLA coated Ti6Al4V disc (B) surfaces

Figure 3.4 The Profilometer spectra graphs for the three different locations (A, B, C) on the half PLA thin film coated Ti6Al4V disc. The height difference between M to R lines refers to the areas of the PLA thin film coating which is 400 nm thick

Figure 3.5 SEM images for the surface of PLA-Gm (A, B) and PLA-HAp (C, D) thin film coated Ti6Al4V

Figure 3.6 3D optical microscope imaging to observe the whole surface area of PLA-Gm-(HAp-Gm) thin film coated Ti6Al4V discs at 5% (A), 10% (B), 15% (C), 20% (D) and 30% Gm (E) showing small fine particles ad agglomerated larger deposits

Figure 3.7 The surface characterization of PLA-Gm-(HAp-Gm) thin film coated Ti6Al4V discs at 5% (A), 10% (B), 15% (C), 20% (D) and 30% (E) Gm concentrations at low (50x) magnifications with the particle number versus particle area graphs (F) according to SEM images of all samples at low (50x) magnifications

Figure 3.8 The surface characterization of PLA-Gm-(HAp-Gm) thin film coated Ti6Al4V discs at 5% (A), 10% (B), 15% (C), 20% (D) and 30% (E) Gm concentrations at high (500x) magnifications with 3D illustrations of the particles for the images at high magnification. The particle number versus particle area graphs (F) according to SEM images of all samples at high (500x) magnifications

Figure 3.9 The observation of Gm and HAp-Gm agglomerated particles in and on PLA thin film coating at low and high magnifications at two different locations (A and B) on Ti6Al4V disc

Figure 3.10 FT-IR results of all sets of PLA biocomposite coated Ti6Al4V discs. The characteristic peaks of Gm (1619 and 1523 cm^{-1}, which are amide group I-II) and HAp (600–502 cm^{-1} that are PO_4 group) were labeled on the spectrum separately

Figure 3.11 The Ti6Al4V metallic screw-shaped dental implant, Alabama, Birmingham (*A*), Huckstep intramedullary implant (*B*), and hip – amputee implant, BresMed Australia (*C*) with and without PLA-Gm-(HAp-Gm) thin film coating

Figure 4. 1 The diagram for the dissolution study to obtain Gm amount release from the PLA thin film biocomposite

Figure 4.2 Schematic diagram of the proposed cross-sectional view of the biocomposite, showing possible particle size distribution and dissolution paths.

Figure 4. 3 Gm release results of (A) PLA-Gm and (B) PLA-Gm-(HAp-Gm) coated Ti6Al4V discs at 5%, 10%, 15%, 20% and 30% Gm concentrations for 30 days dissolution experiment in 10ml PBS solution (Error bars refer to the mean values (SEM) of the data)

Figure 4. 4 The surface observations of PLA coated Ti6Al4V discs for the drug release study at Day-0 (A), Day-7 (B), Day-30 (C) with EDS-surface mapping results with the EDS spectra (D)

Figure 4. 5 The surface observations for PLA-Gm coated Ti6Al4V discs at 5%-30% Gm concentrations before and after (Day-0 and Day-30) the drug release study.

Figure 4. 6 The surface observation and EDS-surface mapping results for PLA-Gm coated Ti6Al4V discs after the drug release study (Day-30)

Figure 4. 7 SEM surface observations of PLA-Gm-(HAp-Gm) coated Ti6Al4V discs at 5%-30% Gm concentrations before and after (Day-0 and Day-30) the drug release study

Figure 4. 8 The surface observation and EDS-surface mapping results for PLA-Gm-(HAp-Gm) coated Ti6Al4V discs after the drug release study. It is showing Ti6Al4V substrate, Ca, P, Na, and Cl

Figure 4. 9 FT-IR spectra for PLA, PLA-Gm and PLA-Gm-(HAp-Gm) coated Ti6Al4V discs before and after the drug release study

Figure 4. 10 *Full* FT-IR spectra for PLA-Gm-(HAp-Gm) coated Ti6Al4V discs at 5%, 10%, 15%, 20% and 30% Gm concentrations after the drug release study (Day-30)

Figure 4. 11 The dissolution experiment for PLA-Gm and PLA-Gm-(HAp-Gm) thin film coated Ti6Al4V discs with the cumulative method for 7 days

Figure 4. 12 The comparison between the cumulative method and continuous method on 15% PLA-Gm-(HAp-Gm) thin film coated Ti6Al4V disc for 30 days dissolution experiment

Figure 4. 13 The comparison between the phosphate buffer PBS solution and ultra-pure water as a dissolution mediums on the 30% PLA-Gm-(HAp-Gm) coated Ti6Al4V disc for 6weeks by using the continuous dissolution method

Figure 5. 1 Schema of nanoindentation device (a) (Roest et al., 2011), various indenter tip shapes Vickers indenter (b), diamond-shaped indenter (c), spherical indenter (d), Berkovich indenter (e) (Choi et al., 2016)

Figure 5. 2 The schema for scratch testing devices (Ben-Nissan et al., 2013)

Figure 5. 3 The anodized and untreated Ti6Al4V discs before (A) and after (B) PLA biocomposite coating

Figure 5. 4 SEM results of both uncoated [A] untreated and [B] anodized Ti6Al4V disc showing the surface structure differences before and after the anodization process and the resultant grain structure on the treated Ti6Al4V disc

Figure 5. 5 X-Ray mapping results of the three different locations (A, B, C) on Ti6Al4V discs with the their Ti, Al, and V ratios, and the 2D scatter diagrams for location A of Ti6Al4V surface

Figure 5. 6 EDS (A, B) and pseudo coloring (C, D) map analyses of both untreated and anodized Ti6Al4V discs

Figure 5. 7 SIMS depth profile shows for the anodized Ti6Al4V sample

Figure 5. 8 3D images from AFM analysis for untreated (A) and anodized (B) surfaces of Ti6Al4V discs with roughness parameters (Ra, Rz and Rq)

Figure 5. 9 Nanoindentation results for H and E plotted versus radius of contact at maximum load. (A) H and (B) E of treated uncoated Ti6Al4V disc, respectively. (C) H and (D) E of untreated, uncoated Ti6Al4V disc respectively. The influence of the anodized layers is labeled in both A and B graphs

Figure 5. 10 Comparison of Berkovich force-displacement indentation observations of both uncoated [A] untreated and [B] anodized Ti6Al4V discs at 5mN load. Note the steeper initial slope and inflection of the curve for the anodized sample

Figure 5. 11 The Nano-Indentation Results for Uncoated (A), PLA coated (B) and PLA-biocomposite coated (C) untreated Ti6Al4V discs, and their hardness and Young's modulus values (D)

Figure 5. 12 Nanoindentation results of anodized PLA-Gm-(HAp-Gm) coated Ti6Al4V disc: (A) H values against radius of contact, and (B) E values as a function of radius respectively; and nanoindentation results of untreated PLA-Gm-(HAp-Gm) coated Ti6Al4V disc: (C) H values versus contact radius, and (D) E values versus contact radius

Figure 5. 13 Nanoindentation force-displacement observations of PLA-HAp-Gm coated anodized and untreated samples according to various loading conditions

Figure 5. 14 Nanoindentation test results of E and H values of PLA-Gm-(HAp-Gm) coated anodized and untreated Ti6AL4V discs as a function of load

Figure 5. 15 Micro-scratch test results for anodized and untreated PLA biocomposite coated Ti6Al4V samples. These observations were generated by the SPM scan facility of the triboindenter system

Figure 5. 16 Friction coefficient vs. Lateral displacement graph for [A] PLA coated untreated, [B] PLA coated anodized, [C] PLA-Gm-(HAp-Gm) coated untreated, [D] PLA-Gm-(HAp-Gm) coated anodized Ti6Al4V discs

Figure 6. 1 The Antibacterial test results for Ti6Al4V disc without PLA biocomposite coating (A) and 5% (B), 10% (C), or 20% (D) PLA biocomposite coating on the Ti6Al4V discs, using *S. aureus* S34 bacterial strain, following 16h incubation at 37˚C. (E) Bar graph with standard deviations, of the clear zone areas for each condition

Figure 6. 2 The Antibacterial test results for Ti6Al4V disc without PLA biocomposite coating (A) and 5% (B), 10% (C) and 20% (D) PLA biocomposite coating on the Ti6Al4V discs are given to use S. *epidermidis* (S29) bacterial strain after sixteen hours incubation at 37C˚. Additionally, the clear zones of the all samples are plotted as a bar diagram (E)

Figure 6. 3 Graph represents the twenty-four hour growth curve of S. *aureus* biofilm formation. Optical density was measured at 600 nm (OD_{600})

Figure 6. 4 Graph depicts the *S. aureus* growth curves, and the addition of the PLA-Gm-(HAp-Gm) coated Ti6Al4V discs during the early exponential phase (two hours after bacterial growth was

initiated). Absorbance was measured at 600 nm for twenty-four hours. Statistical analysis performed using two-way ANOVA with Tukey's post-test. n=3. Error bars denote SD. **p<0.01, ****p<0.0001

Figure 6. 5 Representative fluorescent images S. aureus following twenty-four hours of co-culture with Ti6Al4V discs (as indicated). Samples were co-stained with DMOA (live; green) and EtD-III (dead; red), merged images are also shown. Scale bar represents 20 µm

Figure 6. 6 Graph represents the percentage of DMOA-positive (live) *S. aureus* following twenty-four hours of co-culture with the controls (A) (as indicated), and (B) PLA and PLA-Gm-(HAp-Gm) thin film coated Ti6Al4V discs (5% to 30% w/w Gm concentrations). The analysis was performed using ImageJ software. Statistical analysis performed using one-way ANOVA with Tukey's post-test. n=3 (15 images per sample). Error bars denote SEM. *p<0.05, **p<0.01

Figure 7. 1 The live image of ADSCs in T75 flask (A) and the graph for the cell number and live/dead ratio for ADSCs with Trypan blue staining (B)

Figure 7. 2 SEM images of ADSCs on the Ti6Al4V disc (A), PLA thin film (B), PLA-HAp thin film (C), PLA-Gm (30% w/w) thin film (D), and PLA-Gm-(HAp-Gm) (30% w/w) thin film coated Ti6Al4V discs after 14 days experiment

Figure 7. 3 Bio-plex assay heat map data for ctrl, Ti6Al4V disc, PLA, PLA-HAp, PLA-Gm, and PLA-Gm-(HAp-Gm) thin film coated Ti6Al4V discs for Day7 and Day 14. (The heat map scale is 2 fold increases in above red and 2 fold decreases in below green)

Figure 7. 4 SEM images of ADSCs on PLA-Gm-(HAp-Gm) (30% w/w) thin film coated Ti6Al4V discs at the 5% (A), 10% (B), 15% (C), 20% (D), and 30% (E) (w/w) Gm concentrations after 14 days experiment

Figure 7. 5 Fluorescence staining for Ti6Al4V, PLA coated Ti6Al4V and PLA-Gm-(HAp-Gm) coated Ti6Al4V at 5%, 10%, 15%, 20% and 30% Gm with Phalloidin (red, F-actin) and DAPI (blue, cell nuclei)

Figure 7. 6 Graph represents the comparison of (A) the cell numbers, (B) total cell area %, (C) single cell area mm^2, and (D) circularity for PLA-Gm-(HAp-Gm) thin film coated Ti6Al4V discs (5% to 30% w/w Gm concentrations). The analysis was performed using ImageJ software. Statistical analysis performed using one-way ANOVA with Tukey's post-test. n=3. Error bars denote SEM. P values: *p<0.04, **p<0.008, **** p<0.0001

Figure 7. 7 Fluorescence staining with Phalloidin (red, F-actin) and DAPI (blue, cell nuclei) for ADSCs on PLA thin film coated Ti6Al4V (x40)

Figure 7. 8 The heat map for the Bioplex assay that includes 27 cytokines (y-axis) and 32 samples (x-axis), Ti6Al4V disc, PLA thin film coated Ti6Al4V disc, PLA-Gm-(HAp-Gm) thin film coated Ti6Al4V discs at predetermined Gm concentrations (5%, 10%, 15%, 20%, and 30%) for D3, 7, 10 and 14

Figure 7. 9 Graph represents the comparison of (A) the cell numbers, (B) total cell area %, (C) single cell area mm^2, and (D) circularity for Ti6Al4V and A-Ti6Al4V discs. The analysis was performed using ImageJ software. Statistical analysis performed using Student t-test, unpaired , two-tails, n=3, P values: * p=0.04, ** p= 0.002 (D) Fluorescence staining with Phalloidin (red, F-actin) and DAPI (blue, cell nuclei) for ADSCs on Ti6Al4V and A-Ti6Al4V discs

Figure 7. 10 The heat map for the Bioplex assay that includes 27 cytokines (y-axis) and 8 samples (x-axis), untreated Ti6Al4V disc, and anodized Ti6Al4V discs for Day3, 7, 10 and 14

Figure 7.11 The graphs show the number of total identified gene ontologies biological processes for ADSCs which were seeded on Ti6Al4V discs, PLA coated Ti6Al4V discs and PLA-Gm-(HAp-Gm) coated Ti6Al4V discs at predetermined Gm concentrations (5%, 10%, 15%, 20% and 30% w/w)

Figure 7.12 two-way Venn diagram illustrates the identified gene ontology biological processes for unique Ti6Al4V, unique PLA coated Ti6Al4V and shared proteins for Ti6Al4V and PLA coated Ti6Al4V

Figure 7.13 three-way Venn diagram illustrates the identified GO biological processes numbers for the comparison of Ti6Al4V, PLA coated Ti6Al4V with 5% (A), 10% (B), 15% (C), 20% (D), and 30% (E) PLA-Gm-(HAp-Gm) coated Ti6Al4V samples, separately

Figure 7.14 five-way Venn diagram illustrates the only unique identified protein numbers for 5% (A), 10% (B), 15% (C), 20% (D), and 30% (E) PLA-Gm-(HAp-Gm) coated Ti6Al4V samples, separately

Figure 7.15 Cytoscape protein interaction network graph of proteins identified by mass spectrometry. Blue – unique 5%, Red – unique 10%, Green – unique 15%, Purple – unique 20% , Orange – unique 30% PLA-Gm-(HAp-Gm) coated Ti6Al4V samples, Yellow – shared Ti6Al4V and PLA coated Ti6Al4V, Grey – shared proteins for all

Figure 7.16 two-way Venn diagram illustrates the protein numbers for unique Anodized Ti6Al4V (A-Ti6Al4V), unique untreated Ti6AlV and shared proteins for A-Ti6Al4V and Ti6Al4V

Figure 7.17 The graphs show the refined number ontologies of proteins identified with direct roles in a osteogenic biological process for unique A-Ti6Al4V sample and (B) the shared of Anodized and untreated Ti6Al4V samples

Figure 7.18 Cytoscape protein interaction network graph of the unique A-Ti6Al4V proteins relevant to osteogenesis development and antimicrobial activities were identified by mass spectrometry

Figure 7.19 Cytoscape protein interaction network graph of proteins identified by mass spectrometry. Blue - unique proteins for A-Ti6Al4V, Orange – unique Ti6Al4V (orange), and Green - shared proteins for both A-Ti6Al4V and Ti6Al4V

List of Tables

Table 1. 1 The mechanical properties of metallic implant materials (Pruitt and Chakravartula, 2011)

Table 1. 2 The basic properties of Calcium Phosphates (modified from ;(BEN-NISSAN and PEZZOTTI, 2003)

Table 1. 3 The various medical applications and devices according to the type of polymers and their performance (Ratner et al., 2012)

Table 1.4 Mechanical properties and degradation rates of PDLLA, PLLA, PGA, PLGA, PCL and P3HB (Thavornyutikarn et al., 2014)

Table 1.5 The thermal properties of polyesters (modified from (Armentano et al., 2018))

Table 1.6 The descriptions and properties of various types of coating methods (modified from (Ben-Nissan et al., 2015)).

Table 1.7 Clinical applications of different antimicrobial coated implants (modified from (Pan et al., 2018)

Table 2.1 The particle size parameters for HAp particles

Table 2.2 Calculated Gm amounts for 1 g HAp powder to produce 5%, 10%, 15%, 20% and 30% HAp-Gm powders with the drug loading technique

Table 2.3 The particle surface area parameters for Porites coral, HAp and 5% HAp-Gm particles

Table 2.4 It illustrates calculated vs UV-Vis measured Gm concentrations for 5 different HAp-Gm samples which have 5% to 30% Gm contents

Table 3.1 2003D PLA properties (from NatureWorks, Ingeo Pty Ltd.)

Table 3.2 The total Gm concentrations in the 5%, 10%, 15%, 20%, and 30% PLA-Gm-(HAp-Gm) solutions for the dip coating technique.

Table 4.1 The average Gm release concentrations after Day-1 and Day-7 for PLA-Gm and PLA-Gm-(HAp-Gm) thin film coated Ti6Al4V discs

Table 5.1 The Hardness (H) and Young`s modulus (E) values of the samples are given according to low (0.1-5mN) and high (50-70 mN) applied nanoindentation loads

Table 7. 1 All Cytokine names and their types in Bio-plex assay

Table 7.2 Unique GO Biological Process in table from two-way Venn diagram for the Ti6Al4V and PLA coated Ti6Al4V samples with most pertinent roles in cellular changes, osteo-related development, adhesion and immune system regulation

Table 7.3 The GO of proteins identified in biological processes with osteogenic associations with the identified protein groups across the unique PLA coated Ti6Al4V dataset

Table 7.4 The GO of proteins identified in biological processes with osteogenic associations with the identified protein groups across the unique Ti6Al4V dataset

Table 7.5 The GO of proteins identified in biological processes with osteogenic associations with the identified protein groups across the shared Ti6Al4V and PLA coated Ti6Al4V datasets

Table 7.6 Unique GO Biological Process in table from three-way Venn diagram for the unique PLA-Gm-(HAp-Gm) coated Ti6Al4V samples at predetermined Gm concentrations (5%-30% w\w) compared the Ti6Al4V and PLA coated Ti6Al4V samples with most pertinent roles in cellular changes, osteo-related development, adhesion and immune system regulation

Table 7.7 The GO of proteins identified in biological processes with osteogenic associations with the identified protein groups across the unique 5% PLA-Gm-(HAp-Gm) coated Ti6Al4V dataset

Table 7.8 The GO of proteins identified in biological processes with osteogenic associations with the identified protein groups across the unique 10% PLA-Gm-(HAp-Gm) coated Ti6Al4V dataset

Table 7.9 The GO of proteins identified in biological processes with osteogenic associations with the identified protein groups across the unique 15% PLA-Gm-(HAp-Gm) coated Ti6Al4V dataset

Table 7.10 The GO of proteins identified in biological processes with osteogenic associations with the identified protein groups across the unique 20% PLA-Gm-(HAp-Gm) coated Ti6Al4V dataset

Table 7.11 The GO of proteins identified in biological processes with osteogenic associations with the identified protein groups across the unique 30% PLA-Gm-(HAp-Gm) coated Ti6Al4V dataset

Table 7.12 The highest number of associated biological process and strongest relevance to osteogenic differentiation and development for unique 5% PLA-Gm-(HAp-Gm) coated Ti6Al4V samples

Table 7.13 The highest number of associated biological process and strongest relevance to osteogenic differentiation and development for unique 10% PLA-Gm-(HAp-Gm) coated Ti6Al4V samples

Table 7.14 The highest number of associated biological process and strongest relevance to osteogenic differentiation and development for unique 15% PLA-Gm-(HAp-Gm) coated Ti6Al4V samples

Table 7.15 The highest number of associated biological process and strongest relevance to osteogenic differentiation and development for unique 20% PLA-Gm-(HAp-Gm) coated Ti6Al4V samples

Table 7.16 The highest number of associated biological process and strongest relevance to osteogenic differentiation and development for unique 30% PLA-Gm-(HAp-Gm) coated Ti6Al4V samples

Table 7.17 The GO of proteins identified in biological processes with osteogenic associations with the identified protein groups across the unique A-Ti6Al4V

Table 7.18 The highest number of associated biological process and strongest relevance to osteogenic differentiation and development for the unique A-Ti6Al4V proteins (individual identified proteins)

Table 7.19 The highest number of associated biological process and strongest relevance to osteogenic differentiation and development for shared A-Ti6Al4V and Ti6Al4V proteins (individual identified proteins)

Publication List

1. Karacan, I., Senturk, D., Oktar, F. N., Ficai, A., Ficai, D., Trusca, R., Vasile, B. S., Gokce, H., Ozuyar, H. D., Gunduz, O., (2016). Structural and characterisation analysis of zinc-substituted hydroxyapatite with wet chemical precipitation method. Int. J. Nano and Biomaterials, 6(3/4) pp.188-204.

2. Karacan, I., Gunduz, O., Gokce, H., Ben-Nissan, B., Akyol, S., Oktar, F. N., (2017). The Natural Nano-Bioceramic Powders Production from Organ Pipe Red Coral (Tubipora musica) by a Simple Chemical Conversion Method, J Aust Ceram Soc., 54, 317–329. https://doi.org/10.1007/s41779-017-0156-1

3. Karacan, I., Macha, I., Choi, G., Cazalbou, S., Ben-Nissan, B., (2017). Antibiotic containing poly lactic acid/hydroxyapatite biocomposites for dental implant applications. Key Engineering Materials, 758, 120-125. https://doi.org/10.4028/www.scientific.net/KEM.758.120

4. Choi, G., Karacan, I., Cazalbou, S., Evans L., Sinutok, S., Ben-Nissan, B., (2017). Conversion of calcified algae (*Halimeda sp)* and hard coral (*Porites sp)* to hydroxyapatite. Key Engineering Materials, 758, 157-161 https://doi.org/10.4028/www.scientific.net/KEM.758.157

5. Sariyer Akbulut, B., Avci, G. F., Altinisik, F. E., Karacan, I., Senturk, D., Ersahin, S., Eren, A., Sayar, N. A., Vardar Ulu, D. Ozkirimli, Olmez E., (2018). Targeting a hidden site on class A beta-lactamases, Journal of Molecular Graphics and Modelling, 84, 125-133. https://doi.org/10.1016/j.jmgm.2018.06.007

6. Choi, A.H., Karacan, I., Ben-Nissan, B., Surface modifications of titanium alloy using nanobioceramic-based coatings to improve osseointegration: a review. Materials Technology, 1-10. https://doi.org/10.1080/10667857.2018.1490848.

7. Karacan, I., Chou, J., Ben-Nissan, B., Cazalbou, S., Mithorpe, B., (2018). Multifunctional-Dual Drug Delivery PLA Coating for Bone Implants. Key Engineering Materials, 782, 212-217. https://doi.org/10.4028/www.scientific.net/KEM.782.212.

8. Karacan, I., Chou, J., Ben-Nissan, B., Macha, I., Juritza, A., Wang, A. H., Muller, W., Grossin, D. and Swain, M., (2018). Adhesion and scratch testing of antibiotic loaded HAp/PLA biocomposite thin films on metallic implants. Key Engineering Materials, 782, 195-200. https://doi.org/10.4028/www.scientific.net/KEM.782.195

9. Macha, J.I., Karacan, I., Ben-Nissan, B., Cazalbou, S., Muller, W. H., (2019). Development of antimicrobial composite coatings for drug release in dental, orthopaedic and neural prostheses applications. SN Appl. Sci., 1, 68. DOI: 10.1007/s42452-018-0064-1

10. Akyol, S., Ben-Nissan, B., Karacan, I., Yetmez, M., Gokce, H., Suggett, D. J., Oktar, F. N., (2019). Morphology, characterization, and conversion of the corals Goniopora spp. and Porites cylindrica to hydroxyapatite. Journal of the Australian Ceramics Society, 55, 893–901. https://doi.org/10.1007/s41779-018-00304-4

11. Karacan, I., Ben-Nissan, B., Sinutok, S. (2019) Marine-Based Calcium Phosphates from Hard Coral and Calcified Algae for Biomedical Applications. In: Choi A., Ben-Nissan B. (eds) Marine-Derived Biomaterials for Tissue Engineering Applications. Springer Series in Biomaterials Science and Engineering, vol 14. Springer, Singapore

12. Ben-Nissan, B., Choi, A.H., Green, D.W., Karacan, I., Akyol, S., Cazalbou, S. (2019) Thoughts and Tribulations on Bioceramics and Marine Structures. In: Choi A., Ben-Nissan B. (eds) Marine-Derived Biomaterials for Tissue Engineering Applications. Springer Series in Biomaterials Science and Engineering, vol 14. Springer, Singapore

13. Karacan, I., Ben-Nissan, B., Wang, H. A., Juritza, A., Swain, M. V., Müller, W. H., Chou, J., Stamboulis, A., Macha, I. J., Taraschi, V., (2019). Mechanical testing of antimicrobial biocomposite coating on metallic medical implants as drug delivery system. Materials Science and Engineering: C, 104, 109757. https://doi.org/10.1016/j.msec.2019.109757

14. Sayahi, M., Santos, J., El-Feki, H., Charvillat, C., Bosc, F., Karacan, I., Milthorpe, B., Drouet, C., (2020). Brushite (Ca,M)HPO4, 2H2O doping with bioactive ions (M = Mg2+, Sr2+, Zn2+, Cu2+, and Ag+): a new path to functional biomaterials?. Materials Today Chemistry, 16, 100230, https://doi.org/10.1016/j.mtchem.2019.100230.

Conference Posters

1. Structural and Characterization Analysis of Zinc-Substituted Hydroxyapatite (Zn-HAp) with Wet Chemical Precipitation Method, (2015), 10th Anniversary Conference of the Hellenic Society for Biomaterials, Greece – Poster Presentation
2. Mutations of a conserved tryptophan residue of the TEM 1 ß lactamase, (2015), The 29th Annual Meeting of the Protein Society, Barcelona, Spain – Poster Presentation
3. Antibiotic containing poly lactic acid/hydroxyapatite biocomposite coatings for dental implant applications, (2017), Bioceramics 29 - Toulouse, France – Oral and Poster Presentation
4. Development of PLA Biocomposite Coatings as Drug Delivery System for Dental Implants, (2018) The Australasian Society for Biomaterials and Tissue Engineering community (ASBTE) Meeting - Oral Presentation
5. Development and Testing of a New Antibiotic Loaded Biodegradable Biocomposite Coating on Ti6Al4V Metallic Implants, (2018), Australian Society for Medical Research Annual Meeting – Poster Presentation
6. Multifunctional-Dual Drug Delivery PLA Coating with HAp for Bone Implants, (2018), Bioceramics30, Nagoya, Japan- Oral and Poster Presentations

Chapter 1

Background & Literature Review

Chapter 1: Background & Literature Review

1.1 Bone Structure and Function

The bones of the human skeleton serve many different functions for the human body. These cover mobility, physical support, protect vital organs, provide a reservoir of growth factors, cytokines, and various essential minerals especially calcium and phosphorus for the other organs. Additionally, they are a source of stem cells and hematopoietic cells. The bones are categorized structurally into four general parts. They are long bones (the clavicles, humeri, radii, ulnae, metacarpals, femurs, tibiae, fibulae, metatarsals, and phalanges), short bones (the carpal and tarsal bones, patellae, and sesamoid bones), flat bones (the skull, mandible, scapulae, sternum, and ribs), and irregular bones (vertebrae, sacrum, coccyx, and hyoid bone) (Office of the Surgeon, 2004, Clarke, 2008).

Principally, human bones consist of two highly organized solid and liquid phases that have both inorganic and organic components, and the architecture of the phases is unique and complex. The major components of bone are the mineralized matrix composed of carbonated apatite skeleton, collagen, and non-collagenous organic proteins. They are the reasons behind its excellent mechanical properties. Bone tissue is comprised of 35% w/w collagen and 65% w/w carbonated apatite. In addition, the ratio and compositions of organic and mineral phases can vary with different factors including the skeletal site, age, sex, mechanical loading and physical function (Kruzic and Ritchie, 2008, Pal, 2014, Macha and Ben-Nissan, 2018). The organic component (the collagen) provides bone with flexibility and at the same time prevents brittleness. The inorganic components, particularly carbonated hydroxyapatite, provide the overall unique porous structure and the necessary mechanical properties. Bone tissue contains two different parts which are commonly referred to as trabecular or cancellous and cortical. The structure of the human bone is shown in *Figure 1.1*. Cortical bone is dense and hard and is composed of cylindrical shells, whereas trabecular bone is porous and is four times softer than cortical bone. The porosity of trabecular bone is between 50 and 90% depending on the location within the human body (site-specific) (Pal, 2014).

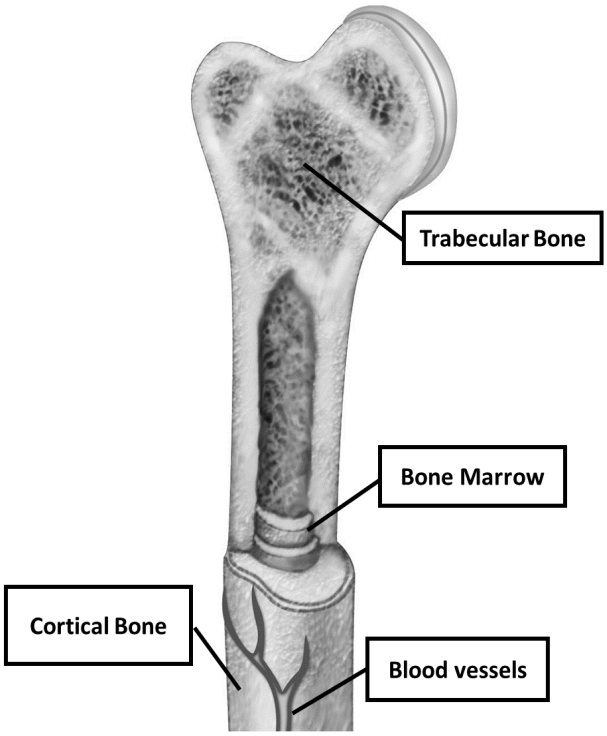

Figure 1.1 The structure of long human bone (Karacan et al., 2019)

While the bone structure is observed biologically, it is a mineralized connective tissue which contains four types of cells. These are osteoblast, osteoclast, osteocytes, and bone lining cells which are given in *Figure 1.2*. Although bone has an inert appearance, it is not a static organ, its metabolism changes actively via continuous bone resorption by osteoclast and new bone regeneration by osteoblast in order to carry on its functions. The balance between the bone reformation function of osteoblasts which secrete the extracellular matrix to mineralize and strengthen the bone and the resorption function of osteoclasts which secrete acid to destroy bone is controlled by osteocytes. The bone remodeling process is the result of the balance between functions of osteoblasts and osteoclasts cells in the bone structure according to the stress concentrations under functional loading. Osteocytes have mechanosensors and orchestrators to control this bone remodeling process. Although the function of bone lining cells is not completely clear, it seems like they have an important role in the bone remodeling process (Nam and Kampa, 2013).

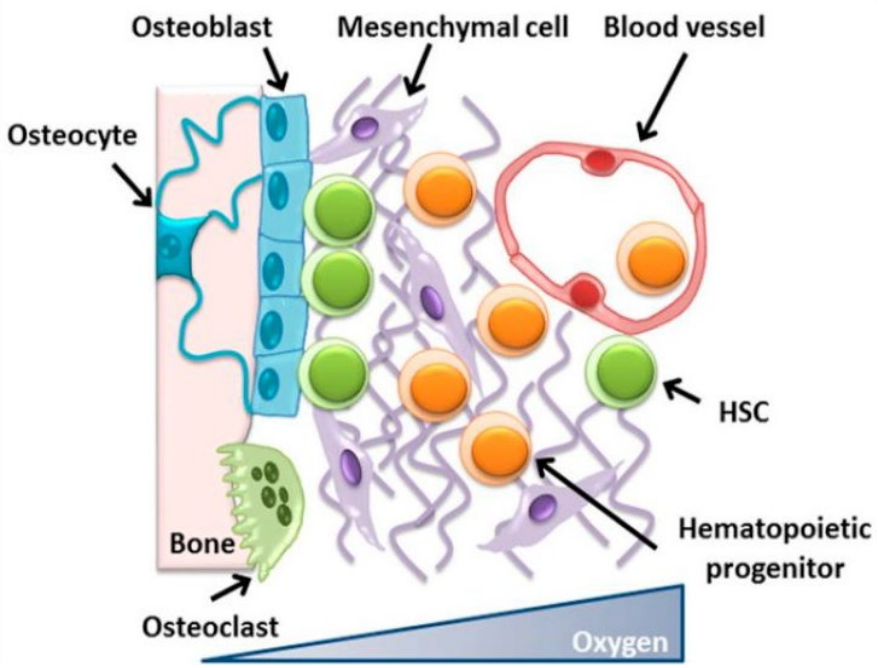

Figure 1.2 Bone and bone cells (Kargozar et al., 2019)

Osteoblasts (cuboidal cells) are found on the bone surface as a continuous cell layer, and mostly adjacent to endothelial cells. Mesenchymal stem cells of the bone marrow are the precursors for osteoblasts which are specialized fibroblast-like cells. Their most important function is the regeneration role in the bone remodeling process. Bone formation through osteoblasts occurs in two steps. The first step is to generate an extracellular matrix of the bone. It includes the secretion of collagen proteins, mostly type 1 collagen which is nearly 90% of the organic matrix, and also the secretion of numerous proteoglycans such as decorin, biglycan, non-collagenous such as OCN, osteonectin, BSP II, osteopontin and cell attachment proteins. The second step is the mineralization of bone matrix, by osteoblasts which promotes the mineralization of the bone matrix (Mohamed, 2008, Florencio-Silva et al., 2015, Kargozar et al., 2019).

Osteoclasts are differentiated multinucleated cells that originate from mononuclear cells of the hematopoietic stem cell lineage. Their main function is the ability to resorb and degrade mineralized bone tissue. Additionally, osteoclasts are a source of cytokines that influence the other cells and their activities such as controlling osteoblasts during the bone remodeling process and regulating hematopoietic stem cells (Florencio-Silva et al., 2015, Kargozar et al., 2019).

The other two cell types in the bone structure are bone lining cells and osteocytes. The bone lining cells are observed when the bone remodeling system is in balance which means neither resorption

nor formation. The bone surface is covered by elongated and flattened bone lining cells. On the other hand, osteocytes are placed in the bone and they detect mechanical stress, so they act as mechanoreceptors to control the bone remodeling process. In addition, osteocytes are an important regulator of bone mass and a key endocrine regulator of phosphate metabolism (Mohamed, 2008). All types of cells provide the balance for the bone remodeling process and their interactions promote bone healing. However, bone disorders occur because of the unbalanced interactions between the bone cells due to aging or environmental factors like accident-related traumas.

1.2 Bone Disorders

Bone tissue can easily repair itself and has a high regenerative capacity compared to other tissues within the human body. Consequently, bone fractures and injuries will heal or recover naturally without the formation of scars in many cases. In spite of this, bone healing and repair is a long process that usually takes at least 6–8 weeks. At the same time, certain bone disorders and pathological infections can negatively impact the bone healing process (Green et al., 2017, Oryan et al., 2014).

Osteoporosis, osteoarthritis, and bone cancer like osteosarcoma are the most common bone disorders. The consequences of bone disorders, especially osteoporosis and osteoarthritis, are mostly fracture, bone defects or bone loss (Zanget al., 2017). Millions of people worldwide have been suffering from bone and/or joint-related problems such as post-operative inflammation, massive bone defects, osteoporosis, and joint diseases such as osteoarthritis. Worldwide, one in three women and one in five men, over the age of 50, will suffer a fragility fracture due to osteoporosis, and with an aging population these numbers will rise (Tu et al., 2018). While, according to the report of The Department of Health, Commonwealth of Australia (CommonwealthofAustralia, 2019), over 1.2 million Australians suffer from osteoporosis, in the U.S., that number reaches approximately 10 million. Despite this, we are currently seeing a large gap in the management and treatment of osteoporosis, especially in the post-fracture setting, with an estimated four out of five patients remaining undiagnosed and untreated (Tu et al., 2018).

The surgical site infections (SSI) like bacterial infections and biofilm formation, especially for the fixation of open fractured bones and/or joint surgeries are another very important problem because the surgery field often gets contaminated due to bacterial penetration through open wounds to

broken bones. It increases the infection risk from 10% to 50% for open fracture cases. Surgery related infections have a high risk of causing osteomyelitis, an inflammatory bone disease that occurs as a result of infecting pathogenic microorganisms. It causes a big challenge for the bone healing capacity in fractures. Without proper care or access to effective intervention options, they remain at risk of painful and disabling fractures in the future (Ribeiro et al., 2012, Seebach and Kubatzky, 2019).

Osteomyelitis can lead to osteolysis also known as bone destruction. In this case, both healthy and necrotic bone tissues are converted to a good environment for foreign organisms to grow and attach to the bone surface. Either single or multiple organisms can cause osteomyelitis due to direct contamination from open fractures, spreading via the bloodstream or implants. However, Staphylococcus sp. are the most common species for bone infections, especially S. aureus (Fernandez-Yague et al., 2015, Inzana et al., 2016, Kavanagh et al., 2018, Lee et al., 2016).

SSI is one of the most common complications associated with surgery. According to the guideline of the Australian Commission on Safety and Quality in HealthCare, (HealthCare, 2017) in Australia, SSI occurs in approximately 3% of surgical procedures. Therefore, the period of hospital stay for patients increases by approximately 20 more days. As the national average cost per admitted acute overnight stay is $2.0745, each hospitalization involving a surgical site infection may be associated with $42.102 in extra costs.

For most of the cases, bone implants are pertinent in solving the above-mentioned issues such as injuries, fractures, postoperative inflammation, or osteoporosis. Therefore, after a blood transfusion, bone replacement with implantable medical devices is the second most common application in the medical area. Currently, a number of materials are used as bone grafts, but none of them have been fully satisfactory. An alternative approach is the development of a new generation of bone grafts that are capable of stopping infections in the first place. On occasion, surgical interventions are necessary to address certain musculoskeletal problems such as osteoporosis, joint diseases, bone fractures, infections, skeletal abnormalities, and tumor resections. Hence, biodegradable, temporary, or permanent devices and prostheses have been created by scientists using natural, synthetic or human-derived products (Oryan et al., 2014, Mahyudin et al., 2016, Green et al., 2017).

Implantable bone graft material can support bone healing and substitution. Additionally, the combination of bone graft with other biomaterials such as bone morphogenic proteins, or bone-like structures such as bioceramics can provide osteogenesis, osteoconduction and/or osteoinduction. Allotransplantation, and in particular allograft, utilizes the tissues from the patient. The procedure is

the most common and has been successfully applied to treat bone-related problems. However, there are issues concerning the number of tissues available for transplantation within our body, and the necessity for numerous operations to extract these tissues results in unnecessary pain and suffering to the patients and often restricts their utilization. As a result, synthetic or natural-based biomimetic materials have been investigated and developed to improve the regeneration of bone tissue. It is an option that is safer and more attractive than bone tissue derived from humans (Oryan et al., 2014, Green et al., 2017).

In order to successfully design applicable implantable devices, choosing appropriate biomaterials, methodologies and production processes are the key points. For this reason, researchers have been focusing on new natural sources, and biomaterials. At the same time, the new generation of design approaches aim to develop biocompatible implantable devices for the human body.

1.3 Implant insertions and implant-related infections

The major challenge for implantable devices is the high risk of implant-related bacterial infections. The implant insertion surgery always carries the risk of bacterial infections, especially the fixation of open fractured bones and/or joint surgeries because the surgery field often gets contaminated due to bacterial penetrations. It has been reported that the infection risk increases from 10% to 50% for open fracture types of cases (Ribeiro et al., 2012, Seebach and Kubatzky, 2019).

Therefore, implant-related infections are a major problem for millions of people worldwide. Besides various adverse effects on the quality of human life it often causes the inability of open fracture to heal, and then implant failure (Darouiche, 2003).

There are various reasons for the infection such as the quality of operation facilities, surgical technique or can be related to after implantation hygiene and care. Various types of materials and also their combinations are used and new approaches have been investigated in order to improve the nature of implant biocompatibility (Ovaska et al., 2011). Despite advances in minimally invasive surgery and aseptic techniques, infection remains a very common complication after implant insertion (O'Cearbhaill, 2019).

The surgical room environment and implant surface might be very suitable for bacterial contamination and the bacterial attachment. Therefore, the treatment for implant-related infections is very difficult because of the biofilm formation on the implant surface. Although the immune system can normally control the infection at the planktonic stage (where bacteria are freely floating in the environment) there is still an adverse immunological effect on the implant insertion (Seebach and Kubatzky, 2019).

The implant is recognized as foreign material in the body and the immune system attacks that reason by activating neutrophils, phagocytic cells. It creates an inflammatory and cytotoxic local environment, causing cell death and tissue damage. The host has priority to repair the environment instead of protecting itself from the bacteria. This is another challenge to solve in implant-related infections (Singh, 2018, Seebach and Kubatzky, 2019).

Staphylococci are very common pathogen organisms that cause infection in the human body. They are gram-positive bacteria. While their morphology is round, the diameter range for Staphylococci is between 0.5 to 1.8 μm. While more than 20 different staphylococcal species exist, Staphylococcus *aureus* and S. *epidermidis* are mostly observed as a case of human soft tissue or implant infections (Kavanagh et al., 2018, Singh, 2018).

In most of the cases, S. aureus causes a chronic and complex bone infection called osteomyelitis. Additionally, they have the capability of biofilm formation called the sessile type of bacteria population. In order to form a biofilm, bacteria attach to the surface and start to proliferate and develop multilayer cell communities with secreting extracellular polysaccharide matrix. Bacteria create biofilm to protect themselves from antibacterial agents, antibiotics and also the dynamic environment they are in. Therefore, the biofilms are typically up to 1000 times more resistant to antimicrobial treatments (Chen et al., 1998, Peng et al., 2002, Goldberg, 2002, Garrett et al., 2008, Fernandez-Yague et al., 2015). The current treatments are surgically removing the implant and the infected tissue around it, and long-term (up to 6 weeks) antibiotic therapy, systemically. Systemic antibiotic administration is not usually effective enough for combating bacterial infection in the soft tissue and in the bone because of the bacterial drug resistance. A high dosage of antibiotics causes systemic toxic effects on the body. While local antibiotic administration directly to the infected area is more effective than systemic administration, the systems such as system local injections and implantable pumps are not efficient enough to use for clinical application. The biggest challenge is to develop successful strategies to combat implant-related bacterial infections after surgery without increasing the risk of bacterial drug resistance and the toxic effect of antibiotics or antimicrobial agents. (Khan, 2012, Chou et al., 2014, O'Cearbhaill, 2019).

The solution currently under investigation is surface modifications on the implants and improvement of design using a combination of different biomaterials like ceramics or polymer-like composites.

1.4 The design of medical bone implants and their applications

The medical implants (devices inserted into the human body) are manufactured with one or more combinations of biomaterials in order to provide the achievable integration of the implant within the surrounding hard or soft tissue (Barfeie et al., 2015, Dhaliwal et al., 2017). Medical implants have been used since the ancient Egyptians, and the first implantable device was a gold dental implant. Although the early medical implants were designed in order to use very basic materials like bone, wood, and ivory, metals such as gold began to be used for teeth stabilization during the historical evolution of the implants. In the last 60 years, the design and improvement of modern implants has occurred using the new generation of biomaterials (Pruitt and Chakravartula, 2011, Abraham, 2014). The different designs of implants are mostly used as dental, orthopedic, cardiovascular, brain/neural, sensory, and cosmetic implants, however, the most commonly used are hip prosthesis, and knee replacement implants. Additionally, they have applications in immunology, histopathology, experimental surgery, and veterinary medicine, and also ophthalmology areas (Manivasagam et al., 2010, Prakasam et al., 2017).

The design of successful implantable devices depends on various factors, and especially the collaboration of different fields such as engineering, manufacturing, medicine, and biology which requires producing good quality implants. In *Figure 1.3*, a collaboration of various areas for the implant design is shown as a circular schema (Pruitt and Chakravartula, 2011).

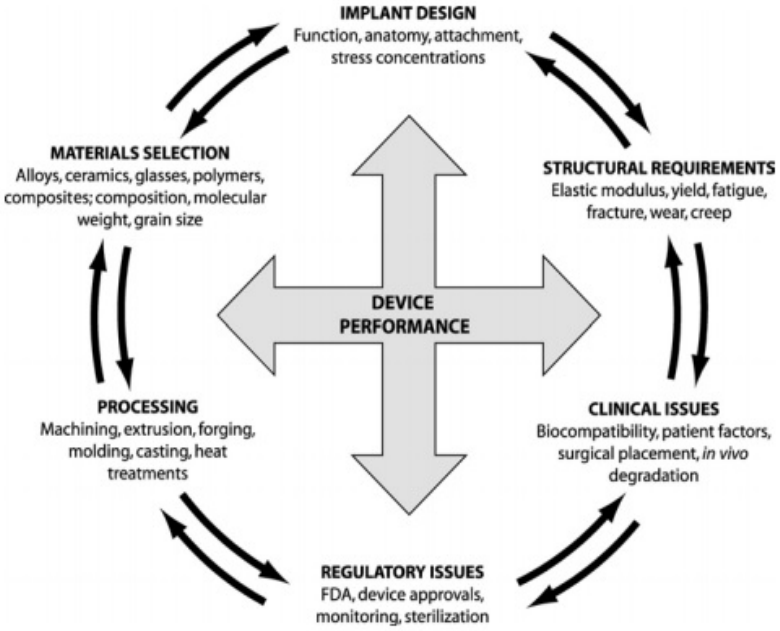

Figure 1.3 Supporting factors and fields for the improvement of medical device performance (Pruitt and Chakravartula, 2011)

The requirements of implants are: for replacing failed components, improving function, and assisting the natural organs. So, the implantable devices are designed in order to provide stability, biocompatibility, and successful integration within the tissue extracellular matrix (ECM). Additionally, their design and performance has to be highly effective in the healing period of tissue after the implant insertion surgery (Agarwal and Garcia, 2015, Prakasam et al., 2017).

The first and most crucial requirement for the implants is to choose appropriate biomaterial which should be acceptable and biocompatible to the human body. It should also not cause any adverse effects like inflammation or toxicity. Although metallic materials have been commonly used for various types of implants, in order to improve longevity, physical, mechanical and biological properties, different alloy compositions, or combinations with ceramics, polymers or composite materials have been applied widely in the experimental work and in clinics (Manivasagam et al., 2010, Mantripragada et al., 2013).

The detailed explanations about the biomaterials used for the various implant designs are given in the next section.

1.5 Biomaterials for Bone Implants

1.5.1 History of biomaterials

Biomaterial science covers the applications of materials in medical areas in order to repair and/or treat injured and wounded hard and soft tissues in the human body. Various applications of biomaterials in the biomedical area have been proposed since the early 1960s by a large number of investigators. Additionally, biomaterials for medical applications are always chosen according to their biocompatibility and their surface and bulk physical properties. Researchers have been increasingly attracted to investigating novel biomaterials and their medical applications due to improved quality of life and increased longevity in the global population. Therefore, new and advanced healthcare technologies have been developed in order to save the lives of millions of people and to improve the quality of human life (Hench and Polak, 2002, Ratner et al., 2012, Chou et al., 2013).

During the historical evolution of biomaterials, three different biomaterial generations have been proposed. They can be categorized as the first generation (bioinert materials), second-generation (bioactive and biodegradable materials) and the third generation (new concept materials that have cellular interactions in addition to supportive roles). Additionally, the three types of biomaterials and their structural specifications are given in *Figure 1.4* with their historical periods (Hench, 2005). According to archaeological researchers, some natural and simple biomaterials were processed as implants and prostheses in order to repair some unhealthy and wounded parts of the human body by various ancient civilizations such as Egyptian, Roman, and Greek (Hench and Polak, 2002, Merolli and Joyce, 2009).

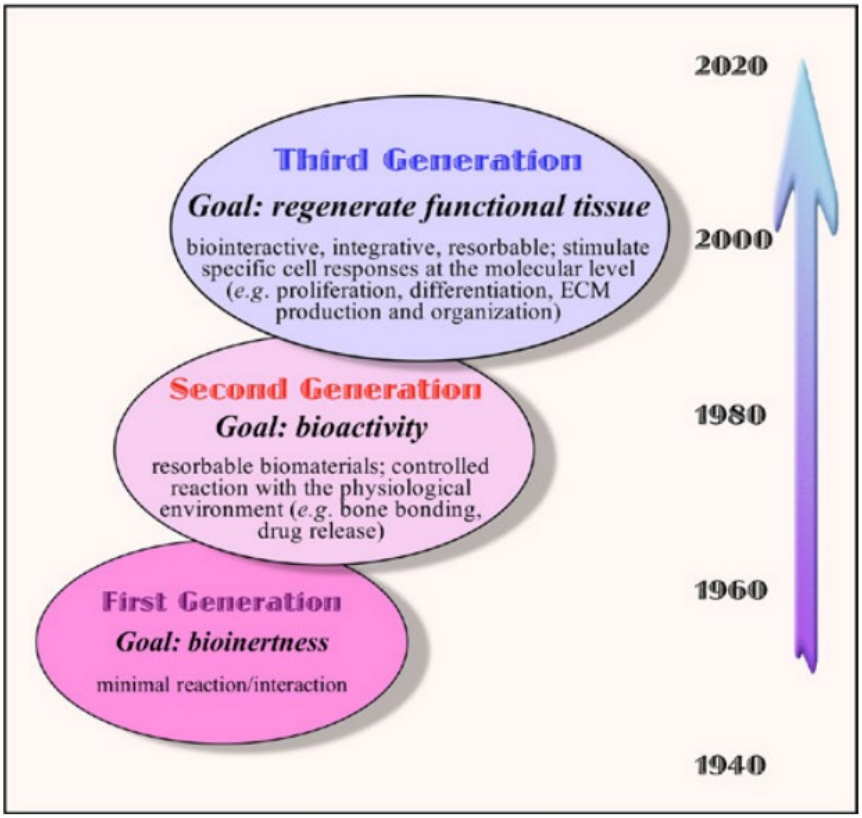

Figure 1.4 Three Generations of the Biomaterials (Ratner et al., 2012)

Most of the early biomaterials contained marketable industrial materials instead of the medical and healthcare-related materials. However, during the 1960s, the first generation biomaterials were being improved directly proportional to the progress of human knowledge about the immune system. In this period, the biomaterials were chosen according to their physical properties in order to obtain an appropriate and successful match with the material and replaced tissue of the host with minimum toxic effect. According to the Hench's definition, the most important property of the first generation biomaterials is the bio-inertness (Hench and Polak, 2002, Ratner et al., 2012, Mahyudin et al., 2016). The term of inertness refers to the minimum interaction between implanted materials and host tissue. When material such as titanium, stainless steel, alumina, and partially stabilized zirconia is placed into the human body as an implant, it affects its surrounding soft or hard tissues (Mahyudin et al., 2016, Choi and Ben-Nissan, 2017).

The second generation biomaterials had complex properties and functions because of the improvement of knowledge in biology, in synthesis methods and biomechanics despite the simplicity and bio-inert properties of the first generation biomaterials. From 1980 to 2000, these biomaterials

were designed according to two new points which are bioactivity and biodegradability. Bioactivity refers to the interaction of the implantable materials with the biological environment such as soft or hard tissues. The improvements of bonding between tissue and material and the enhancement of biological responses were provided by the bioactive biomaterials such as hydroxyapatite bioceramics. Additionally, other calcium phosphates such as bioresorbable tricalcium phosphate and bioglass also were used. When the second generation of biomaterial is inserted within the human body, they degrade and dissolve progressively and are replaced slowly to generate new bone (Mahyudin et al., 2016, Choi and Ben-Nissan, 2017, Choi et al., 2017; Mahyudin et al., 2016).

Third generation biomaterials are called the new advanced biomaterials as they have been enhanced for the various specific medical applications. The third generation biomaterial contains the combination of bioactive and bioresorbable properties, and different kinds of biogenic materials and surface modifications to stimulate the regeneration of tissues in the body. Additionally, they provide support and improve the attachment, proliferation, and functionalization of specific cells and tissues (Hench and Polak, 2002). The third generation biomaterials have a very crucial role as a complementary factor for the development of tissue engineering and regenerative therapeutic medicine.

Tissue engineering has been a progressively developed healthcare area. It provides regeneration, treatment, and formation of new tissues and organs with the appropriate combination of living cells and scaffolds which are constructed by the synthetic or natural third-generation biomaterials (Ratner et al., 2012, Mahyudin et al., 2016). The structural classification of implantable biomaterials which are bio-inert, bioresorbable, surface-active and bioactive is given as a schema in *Figure 1.5*. Although the bio-inertness, bioactivity, biodegradability and positive host response of biomaterials are very effective on the success of the implantation process, biocompatibility is the main and crucial point in choosing the correct and appropriate biomaterials which have good quality and combination with the host tissue for the specific medical implant application (Ratner et al., 2012).

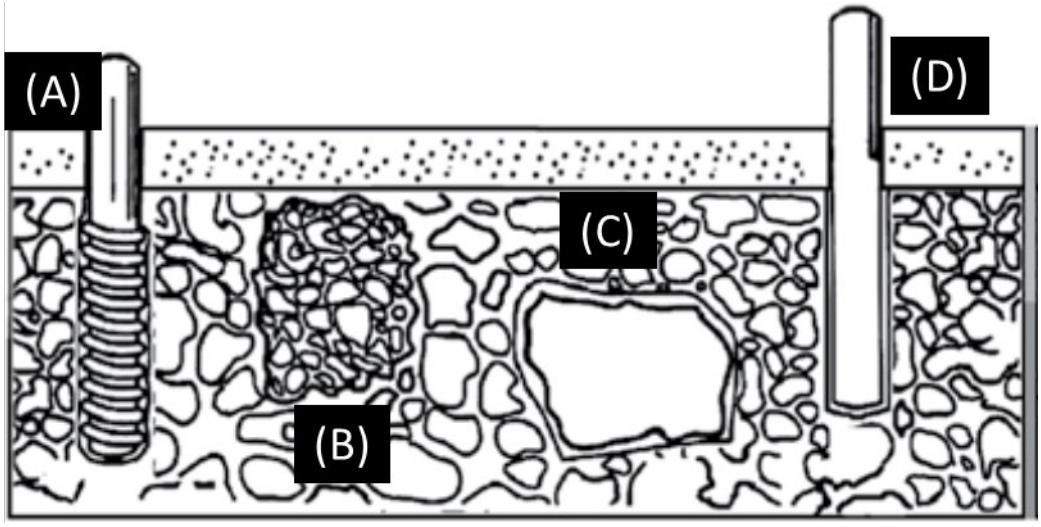

Figure 1.5 The structural classification of biomaterials; a) bio-inert, b) bioresorbable, c) surface-active and d) bioactive (Choi et al., 2017)

Bio-functionality and biocompatibility are very effective factors in order to improve the success of medical and clinical applications because both of them are highly related to the interaction between tissues and implant materials. Investigations for the improvement of the implants'biocompatibility in enhancing the interactions between implant and host were started around the 1940s, and the importance of biocompatibility for biomedical implant designs is increasing. The general definition of biocompatibility is the ability of the material to interact with the cellular and tissue response successfully without any undesirable toxic effects in a specific application. However, the biocompatibility property of the materials changes case by case. Therefore, biocompatibility is a very specific and unstable property for the materials, because the types of tissue, specific applications and biological environments are effective matters to influence it. For that reason, there is no any accurate measurement of biocompatibility for the materials, and it depends on the structure, formulation, surface properties and any other factors and properties of the materials shown in *Figure 1.6* (Naahidi et al., 2013).

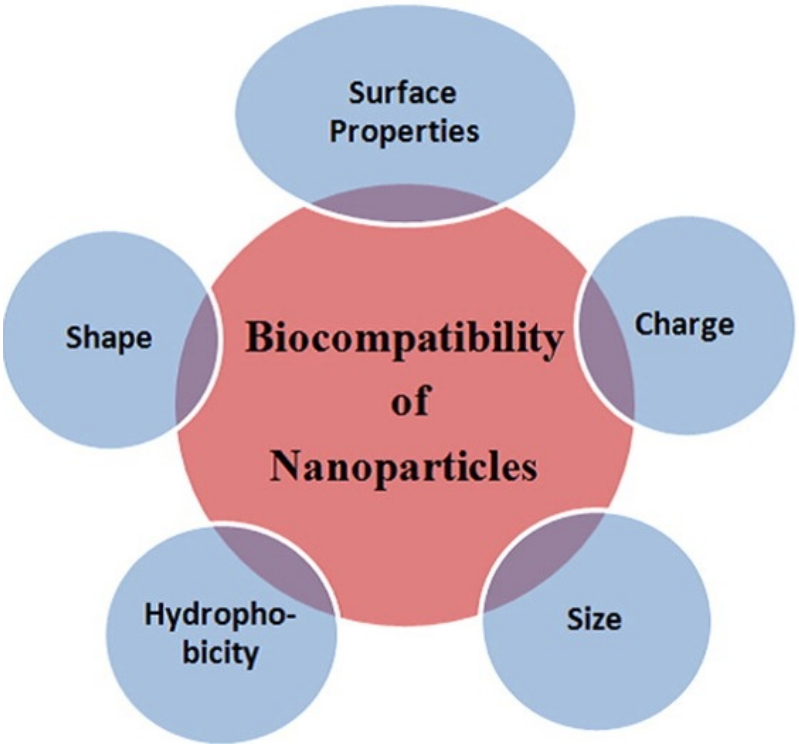

Figure 1.6 The effective nano-particle Properties for Biocompatibility (Naahidi et al., 2013)

The classification of the biomaterials includes three main categories which are polymers, ceramics, and metals. According to medical and clinical research, these categories are defined as soft and hard materials. Soft materials refer to polymers, and their clinical applications contain generally soft tissues in the human body such as skin, cartilage, and vascular tissues. Furthermore, the application areas of hard materials such as ceramics and metals which are very wide can be used in the replacement or support of bone and hard tissues. While these biomaterials have been used as surgical, orthopedic, cardiovascular and dental applications, they are also useful in many different clinical areas such as implantable sensors, drug delivery systems and so on. Although each biomaterial categorized has different applications, the researchers have developed innovative and novel composite materials in order to improve the quality of the clinical applications such as implant devices as multifunctional devices (Merolli and Joyce, 2009, Pruitt and Chakravartula, 2011).

In the next sections, ceramics, polymers, and metals have been described with their applications at biomedical areas to design implantable devices.

1.5.2 Metallic Biomaterials

Metals, especially noble metals such as gold have been used as implantable materials in the medical field for many thousand years. Gold was highly applicable for dentistry around 500 BC. Common novel implantable metals are stainless steel, cobalt chrome, and titanium and its alloys which have been designed in order to improve the biocompatibility of the materials. In order to design successful metallic implant devices, the researchers must correctly determine appropriate mechanical and chemical properties such as the fatigue strength and the corrosion resistance. At the same time, the implantable device must have biocompatibility for its surrounding tissue and bone to obtain the successful surgical outcome. Although the metals and metal alloys have wide application areas, especially load-bearing applications, because of the high constraints of the medical areas, only a few metal systems have been used (Merolli and Joyce, 2009, Pruitt and Chakravartula, 2011, Luo et al., 2013).

The undesired biological responses such as chronic inflammatory response or adverse reaction between the bone-metal interfaces after implant insertion are very important problems for metallic implants. For instance; certain stainless steel alloys support the formation of multilayer fibroblasts between bone and implant which causes loosening of the implants. Many investigators strongly stated biocompatibility, fatigue strength, and corrosion resistance as the required properties for the metallic implants in order to prevent the implant loosening after surgery and to improve implant integration. Stainless steel, cobalt-chromium (CoCr) alloys, titanium and zirconium alloys are the most common alloys and are utilized in orthopedics, dentistry and maxillofacial devices. Some of the mechanical properties and application areas of stainless steel, CoCr alloys, and titanium alloys are shown in *Table 1.1* (Pruitt and Chakravartula, 2011).

Table 1.1 The mechanical properties of metallic implant materials (Pruitt and Chakravartula, 2011)

Material	ASTM	Thermal treatment	Elastic modulus (GPa)	Yield strength (MPa)	Tensile strength (MPa)	Applications
Stainless Steels	F745	Annealed	190	220	480	Surgical implants
	F55–56,	Annealed	190	331	586	Bone screws
	F138–139	Cold-worked (30%)	190	792	930	Fracture fixation
		Cold-forged	190	1200	1351	
CoCr Alloys	F75	As-cast/Annealed	210	450–517	655–890	Knee bearing
	F799	Hot isostatic press	250	840	1300	Hip Implants
	F90	Hot-forged	210	900–1200	1400–1600	Hip implants
	F562	Annealed	210	450–650	950–1200	Orthopedic implants
		Cold-worked (40%)	210			
		Hot-forged	232	1600	1900	Fixation
		Cold-worked, aged	232	965–1000	1200	Intervertebral disc
				1500	1795	Orthopedics
Titanium Alloys	F136	Forged annealed	116	896	965	Dental implants
	F67	Forged, heat-treated	116	1034	1103	Hip stem
		Cold-worked (30%)	110	485	760	Dental implants

The Young modulus (elasticity), yield and tensile strength are determinative properties for the functionalities of these metallic materials in biomedical applications. Therefore, the young modulus property of metals is highly related to stress shielding (and hence bone resorption) which causes some catastrophic failure after implantation surgery such as bone loss and implant loosening. For example, titanium and titanium alloys have lower density and elasticity than stainless steel and CoCr alloys. As a result, the stress shielding and its negative effects are reduced when Ti or Ti alloy is used for medical applications (Pruitt and Chakravartula, 2011, Luo et al., 2013, Sonntag et al., 2013). Therefore, titanium and titanium alloys have been used most widely as a component of the implants especially for hard tissue applications in dental and orthopedic use. Especially, commercially pure titanium (CP Ti) and Ti6Al4V alloy have been accounts for 50% of the total market for the biomedical industry such as implantable devices (Singh and Dahotre, 2007).

Titanium and titanium alloys might contain one or more mixtures of the two main crystallographic forms (allotropy), which are alpha (α), and beta (β). While α form which exists at room temperature refers to the hexagonal close-packed crystal structure (HCP), the β form is called the body-centered cubic structure (BCC). A β form of the titanium element is obtained when it is heated above 883 °C or when it is transformed from liquid to solid phases. This temperature is critical and phase change can cause dimensional variations and should be avoided (Guillemot, 2005).

The titanium element can be alloyed with another element according to the stabilization of selective α and/or β phases at room temperature. For this reason, titanium alloys contain three different categories which are α-stabilizers (Al, O, N, C), β-stabilizers (Mo, V, Fe, Cr) and neutrals (Zr). α phase titanium alloys have high corrosion resistance, however, their low-temperature strengths are limited. Therefore, a titanium alloy with mixed α+ β phases reflect the properties of both, so they have superior corrosion resistance, thermal-treatment, and low Young modulus. For this reason, the most commonly used titanium alloy is Ti6Al4V because it has α + β crystallographic phases (Liu et al., 2004, Singh and Dahotre, 2007, Roest, 2008).

As stated earlier titanium alloys have been used commonly in various implant applications because of their considerably superior biocompatibility, better mechanical and physical properties like high corrosion resistance compared to other types of metals and alloys. The good corrosion resistance feature is essential for the metallic implants to avoid adverse effects of metallic ion release because body fluid is recognized as highly corrosive for the metallic materials that causes the metal ion release to other parts of the body. Especially Ti–6Al–4V alloys have been used at implant applications for various areas such as dental, total hip, knee, wrist, spine, shoulder, elbow and orthodontics. However, there is a long-term risk associated with the release of Al and V elements that it might possibly initiate Alzheimer's disease, osteomalacia and other neurological conditions (Treves et al., 2010, Prakasam et al., 2017, Prasad et al., 2017).

The good mechanical strength, corrosion resistance and high biocompatibility of titanium and titanium alloys, especially for Ti6Al4V alloy have been justified by many researchers (Bruni et al., 2005, de Viteri and Fuentes, 2013, Shah et al., 2016). However, there is a possible risk with the undesired metal ion release, especially vanadium from the implant surface. In order to reduce the risk, recently, the surface modifications on the metallic implants have been investigated to improve the properties. The modifications on the metallic implant surfaces with mechanical, chemical and biological means has been reported. Micro and nano coating of the metallic implants with ceramics, polymers or their composites, and combining with biological or pharmaceutical agents is the current research areas of a number of the groups and is very promising (Paital and Dahotre, 2009, Rath et al., 2012).

Titanium oxide (TiO_2) is formed naturally because of the high affinity between titanium and oxygen ions as a few nanometers of passive film layers on the titanium and titanium alloy surfaces. The high corrosion resistance feature of CP Ti and Ti6Al4V alloy is due to the thermodynamically stable TiO_2 layer (Singh and Dahotre, 2007). In order to obtain the stable TiO_2 layer, anodizing or oxidation of titanium alloy surfaces is one of the most commonly used surface modification methods for the

improvement of the surface interactions and biological responses of the metallic implants and the increasing resistance of corrosion. Additionally, the thin oxygen layer on the metal surface is used to increase the wettability and the bioactivity of the substrate. The general definition of anodizing is the formation of an oxygen layer on the surface of the metals and its thickness range is between 50-700nm. Thin film thickness, thermal or electrolytic methods are applied in order to increase oxygen. In this method, the film formation with anodic oxidation occurs with the electrode reaction combinations which provide metal-oxygen ions diffusion. The thickness of the oxygen layer on the metal substrate depends on different variables which are electrode composition, temperature, anode potential. Additionally, the thickness of the film affects the color of the metal substrate. Different types of acidic solutions with different concentrations have been used during the anodizing process of titanium and titanium alloy substrates (Aladjem, 1973, Roest, 2008, Roest et al., 2011). The relationship between surface roughness and osseointegration has been reported to increase surface roughness by means of anodizing improves osseointegration of the titanium alloy based metallic implants (Roest et al., 2011).

There are different types of surface modifications on the metallic implants in addition to the anodization process to obtain a successful connection between implant and its surrounding host tissue, and to prevent any adverse effects from the implant itself. One of the most applicable and attractive methodologies is to combine the metallic implants with the other biomaterials, mostly bioceramics (calcium phosphates, bioglass), biodegradable natural or synthetic polymers or the biocomposite materials that can be designed as a coating material on the implant surface. Moreover, the bioceramics and polymeric materials along with their applications on the metallic implants are going to be explained at the next sections (Choi et al., 2015, Choi et al., 2017).

1.5.3 Ceramic Biomaterials

Ceramic based biomaterials are one of the main sources for many different medical applications, especially, the bioceramics have been utilized for repairing, treatment and regeneration of damaged tissue into the human body. Therefore, the bioceramics are used as powders, solid pieces and granules and range of macro and nano coatings whose application examples are the coating of metallic implants, bone filling and injectable products (Baino et al., 2015, Planell, 2009). Therefore, the components of orthopedic, dental implant devices; bone screws and plates; space-filling materials for damaged bone; coating materials on the metallic surfaces in order to support implant-tissue interactions; drug delivery systems are some of the most important clinical applications of bioceramics (Heness and Ben-Nissan, 2004).

When bioceramics are categorized according to their reactivity, they have three groups which are nearly bioinert, bioactive and bioresorbable. From bio-inert biomaterials to bioresorbable biomaterials, the historical perspective of bioceramics can be observed. While the nearly inert bioceramics such as zirconia and alumina (generally used instead of metallic hip, knee and dental implants), the second generation biomaterials consist of bioactive properties that react with the surrounding tissues (Hench and Polak, 2002, Heness and Ben-Nissan, 2004, Hench, 2005).

Other second generation materials are bioglasses and calcium phosphates. Additionally, some calcium phosphates such as β and α tri calcium phosphate and coral sources which are CaCO3 can be given as examples of bioresorbable bioceramics (Hench, 1980, Hench & Polak, 2002, Guillemot, 2005, Mahyudin et al., 2016). In *Figure 1.7*, the categorization of bioceramics according to their reactivity and application are shown schematically.

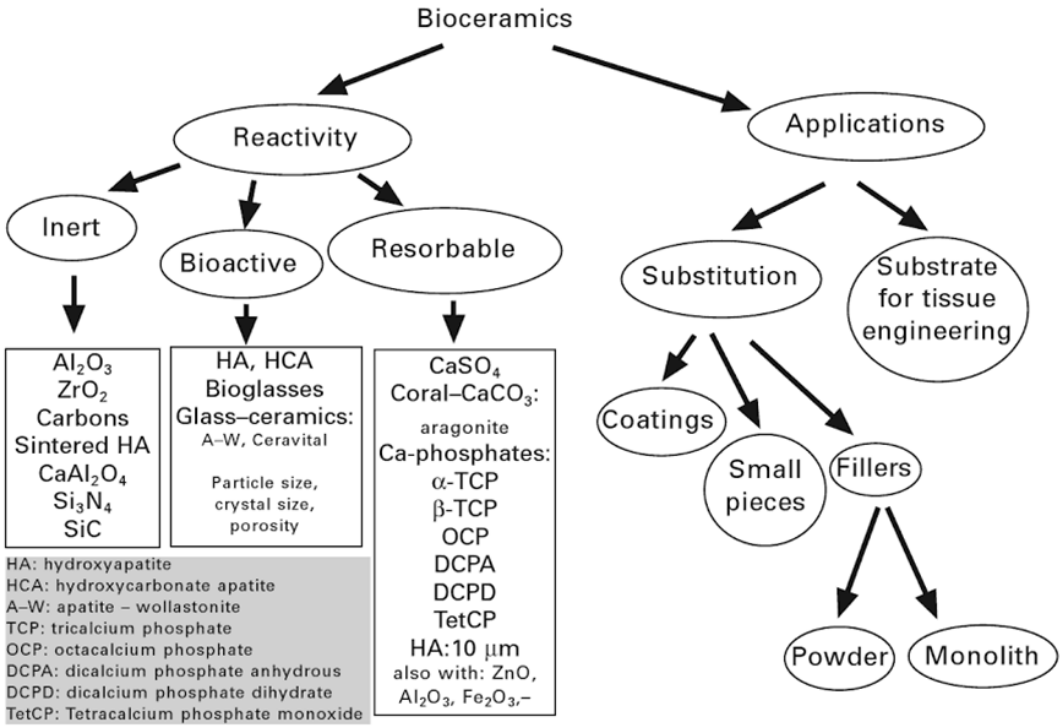

Figure 1.7 The categorization and application fields of bioceramics (Planell, 2009)

Not commonly accepted or used bioceramics can also be categorized according to their "structures," and these are crystalline ceramics (calcium phosphates), bio-glasses, and glass-ceramics (Baino et al., 2015). Although bioglass and crystalline ceramics have been mostly utilized in clinical and medical

applications, crystalline ceramics have generally been used as coating materials for metallic implants and drug delivery systems (Paital and Dahotre, 2009).

Calcium phosphates

Calcium phosphate ceramics (crystalline bioactive or bioresorbable ceramics) have been researched since 1920s and progressed well because of their wide clinical application areas. Calcium phosphate bioceramics are used in orthopedic and dentistry areas such as bone augmentation, repair, and substitution. They are also applied to tissue regeneration, maxillofacial and cosmetic surgery (Gunduz et al., 2014, Macha et al., 2016a).

Hydroxyapatite (HAp), Brushite (DCPD), Monetite (DCPA) and Whitlockite (β-TCP), and combination of Hap and (β-TCP), which is called Biphasic calcium phosphate (BCP) are some members of the calcium phosphate bioceramic materials (BEN-NISSAN and PEZZOTTI, 2003). Additionally, the grain sizes of bioceramics have been reported to be around 1-1000 µm, although new generation nanoceramics are between 10 to 100 nm range and are used in many different clinical applications (Hench and Jones, 2005).

All calcium phosphate bioceramics involve three elements: calcium, phosphorus, and oxygen, and, some of them might also contain carbon and (OH). Therefore, they are defined according to the structure and type of phosphate anions. Each type of calcium phosphate has a unique formula and Ca/P ratio. While the formulas of HAp and Whitlockite refer to $Ca_{10}(PO_4)_6(OH)_2$ and β-$Ca_3(PO_4)_2$, there Ca/P ratios are 1.67 and 1.50, respectively. Besides this, all properties which are Ca/P ratios, chemical formulas and solubility values of calcium phosphates are shown in *Table 2*. When both types of TCP and HAp are compared, HAp is more stable physically than others, and it has lower solubility. Additionally, calcium phosphates are separated into two main groups according to production temperatures. While the first group needs low temperature during the synthesis process and consists of DCPD, DCPA, OCP and so on, a second group whose synthesis temperatures are higher than the first group and contains HAp, TCP, OA (Barinov et al., 2008, BEN-NISSAN *and* PEZZOTTI, 2003, Cegla et al., 2014, Dorozhkin, 2013).

HAp bioceramic has very similar structure to the inorganic mineral part of natural human bone apatite which includes 70% cancellous bone approximately. It has a hexagonal crystal structure, and its formula is $Ca_{10}(PO_4)_6OH_2$. Therefore, it is commonly used for bone and tissue engineering applications in dentistry and orthopedic areas, because of its high biocompatibility and osteoconductivity (Franklin-Ford et al., 2013).

Table 1.2 The basic properties of Calcium Phosphates (modified from ;(BEN-NISSAN and PEZZOTTI, 2003)

Chemical Name	Abbreviation	Chemical Formula	Phase	Ca/P	Solubility Product
Monocalcium Phosphate Hydrate	MCP	$Ca(H_2PO_4).H_2O$	-	0.5	$1.0x10^{-3}$
Dicalcium Phosphate Hydrate	DCPD	$CaHPO_4.2H_2O$	Brushite	1.00	$1.87x10^{-7}$
Dicalcium Phosphate Anhdrous	DCPA	$CaHPO_4$	Monetite	1.00	$1.26x10^{-7}$
Octacalcium Phosphate Pentahydrate	OCP	$Ca_8H_2(PO4).5H_2O$	-	1.33	$5.01x10^{-15}$
B-Tricalcium Phosphate	TCP	$Ca_3(PO_4)_2$	B-Whitlockite	1.50	$2.83x10^{-30}$
Penta-calcium Hydroxyl Phosphate	HAp	$Ca_5(PO_4)_3OH$	Hydroxyapatite	1.67	$2.35x10^{-59}$
Tetra-calcium Phosphate Monoxide	TCPM	$Ca_4O(PO_4)_2$	Hilgenstockite	2.00	-

Moreover, the calcium phosphates are categorized with one more different system which is illustrated in *Figure 1.8* except for their phosphate anions. They are defined by their bioactivity and resorption properties (Dey and Mukhopadhyay, 2015, Macha et al., 2015a).

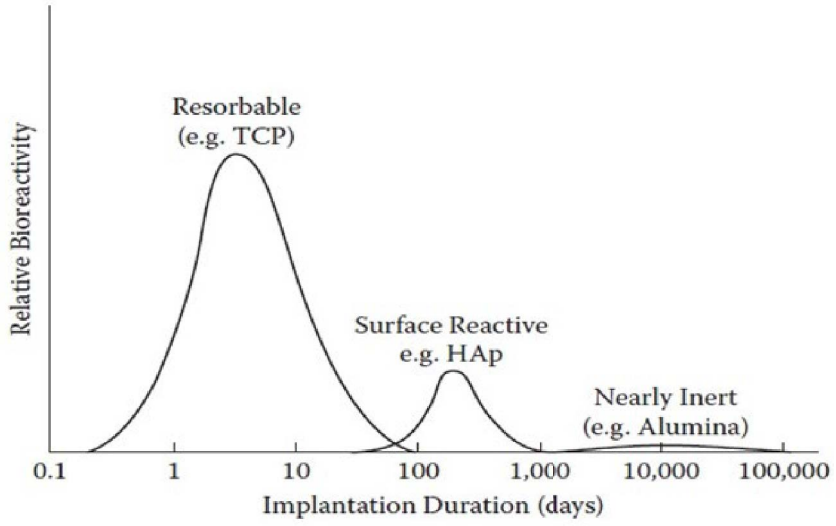

Figure 1.8 The categorization scheme of some bioceramics according to their chemical reactivity (Dey and Mukhopadhyay, 2015)

During the last 100 years many different types of synthesis methods for calcium phosphates have been reported. These include chemical synthesis, sol gel, hydrothermal and chemical conversion

from natural material and solid state reactions (Andrés-Vergés et al., 1998). However, non-stoichiometric products, long reaction time, uncontrolled particle size and agglomeration are the most important restrictions in some of these methods. Sol Gel method has been an easy method to produce nano powders and coatings. Chemical synthesis methods through precipitation method are the most commonly used. In addition, the hydrothermal conversion method has been preferred in clinical applications because this method controls morphology and chemical stoichiometry of the product with elevated temperature and pressure. Although not important in clinical applications due to the additional proper sterilization required, with Gamma radiation, preliminary sterilization of the product is reported with the hydrothermal conversion method (Xu et al., 2001, Bingöl and Durucan, 2012).

One of the most important applications for the calcium phosphate bioceramics is using them as a coating material on the metallic implants. Calcium phosphates especially HAp were used as coating materials for metallic implants in order to provide successful bonding with implant-tissue surfaces and improve the osseointegration surrounding tissue surface. Roest *et al.*, (2011) reported that CP Ti and Ti6Al4V substrates after anodizing were coated with HAp by an alkoxide based a sol-gel coating method. According to their results, while HAp coated metallic substrates is an effective method in order to improve implant-bone interfacial surface interactions and biological responses, the adhesive bonding of the HAp coated Ti6Al4V substrate is better than the CP Ti substrate (Roest et al., 2011).

According to Rath *et al.*, (2013) the anodizing TiAlV alloy substrate was coated with HAp which is a combination of two systems. When only HAp coated substrate was compared with TiO_2 and HAp coated a substrate, they reported that TiO_2/HAp coated substrate had more corrosion resistance, adhesive strength, and cellular biocompatibility and bioactivity than only HAp coated substrate (Rath et al., 2012). Finally, Zreiqat *et al.* (2005) reported that the HAp coating on the Ti6Al4V samples improved the surface bioactivity, so the bioactive bone-like HAp sol-gel coating modulated the extracellular pathway signals of the human bone derived osteoblast cells, and the system was contributing the successful osteoblast growth, function and differentiation on the HAp coating surface (Zreiqat et al., 2005).

Natural sources have been used to synthesize calcium phosphate bioceramics, such as animal sources (cow, sheep bone) and marine sources (sea urchin, coral). Marine skeletons have been used to support various functions of human tissues as medical materials due to their unique architecture and interconnected porous structures, mechanical properties and microstructural composition. Most marine structures such as coral, seashells, cuttlefish, nacre, sea urchins, and marine algae have

calcium carbonate ($CaCO_3$) composition which is a precursor material of the calcium phosphates such as HAp. During the production of calcium phosphate bioceramics, the marine sources have been converted to CaPs with various methodologies to use in pharmaceutical and biomedical areas. Another important point is the chemical compositions of marine skeletons, especially coral skeleton which contains Sr, Mg elements and increases the bioactivity, mechanical properties and capability to influence bone growth in osteoporotic patients with additional Ca and s which can influence bone growth. In addition, their pore sizes fall between 20 and 500 µm and values within this range are extremely appropriate for bone cells and vascularization (Andrés-Vergés et al., 1998, Macha et al., 2015b, Karacan et al., 2019).

Marine-based exoskeletons have been of significance for applications such as tissue regeneration, drug delivery systems, and drug therapy because of these properties and their natural unique structures (Mann, 1988, Chou et al., 2013, Macha et al., 2015a). When the medical applications of calcium phosphates are searched, the most important medical applications of the natural source derived calcium phosphate particles are obtained in drug delivery system areas with the combination of polymeric biomaterials as a coating system on the metallic implant devices. As an example of the combined system of CaP particles and polymeric biomaterials, Macha *et al.* reported that drug-loaded calcium phosphate which is HAp microspheres were mixed with a biodegradable polymer which was utilized as biodegradable PLA film composites. Dissolution studies were carried out to observe the drug-release rate which was inside of the calcium phosphate microspheres. Therefore the drug release was successfully controlled with calcium phosphate particles (Macha et al., 2015a). The polymeric biomaterials with their applications on the metallic implants and biocomposite systems will be explained in detail at the next section.

1.5.4 Polymeric Biomaterials

Polymers have been used in medical areas especially for implants for approximately 80 years, and the first polymer which was applied as a biomaterial is polymethacrylate (PMMA), because of its stiffness, biocompatibility and optical properties (Pruitt and Chakravartula, 2011). The evaluation of polymers was carried out from stable to biodegradable which was in both enzymatically and hydrolytically. The advantages of polymer usage in various implant applications are to be easily manufactured to complex shapes such as fiber, latex, film sheet, reasonable cost, and easy applicable. However, sterilization difficulties and easy water absorption are some of the disadvantages of the polymers (Paital and Dahotre, 2009, Wong et al., 2012).

Table 1.3 The various medical applications and devices according to the type of polymers and their performance (Ratner et al., 2012)

Synthetic Degradable Polyesters	**Current Major Research Applications**
Poly(glycolic acid) (PGA), poly(lactic acid) (PLA) and copolymers	Barrier membranes, drug delivery, hormone delivery, guided tissue regeneration (in dental applications), orthopedic applications, vascular/urological stents, staples, sutures, injectable fillers, dura mater substitutes, skin replacement materials, tissue engineering
Poly(hydroxybutyrate) (PHB), poly(hydroxyvalerate) (PHV), and copolymers thereof	Long-term drug delivery, orthopedic applications, stents, artificial skin, surgical patching materials for congenital heart defects, sutures
Polycaprolactone (PCL)	Long-term drug delivery, implantable contraceptive drug devices, orthopedic applications, staples, stents
Polydioxanone (PDS)	Fracture fixation in non-load-bearing bones, sutures, wound clips
Other Synthetic Degradable Polymers	
Polyanhydrides	Drug delivery
Polycyanoacrylates	Adhesives, drug delivery
Poly(amino acid)s and "pseudo"-poly(amino acid)s	Drug delivery, tissue engineering, orthopedic applications, stents, anti-adhesion barriers
Poly(ortho ester) (POE)	Drug delivery, and stents
Polyphosphazenes	Blood contacting devices, drug delivery, skeletal reconstruction, vaccine adjuvants
Poly(propylene fumarate) (PPF)	Orthopedic applications
Poly(trimethylene carbonate) (PTMC)	Sutures, orthopedic applications
Some Natural Resorbable Polymers	
Collagen	Drug delivery, gene delivery, artificial skin, coatings to improve cellular adhesion, guided tissue regeneration in dental applications, spinal dural repair, orthopedic applications, soft tissue augmentation, tissue engineering, scaffold for reconstruction of blood vessels, wound closure, hemostatic agents
Fibrinogen and fibrin	Tissue sealant, cell delivery
Elastin-like peptides (ELP)	Drug delivery, coating of vascular grafts
Gelatin	Capsule coating for oral drug delivery, hemorrhage arrester
Hyaluronic acid	Wound dressing applications, drug delivery, tissue engineering, synthetic bone grafts, synovial fluid substitutes
Cellulose	Adhesion barrier, hemostat
Various polysaccharides such as chitosan, alginate	Drug/vaccine delivery, encapsulation of cells, sutures, wound dressings/healing
Starch and amylose	Oral drug delivery

The polymers have two main groups which are natural polymers and synthetic polymers, and both groups have very wide application areas in the biomedical fields. Some of these applications are given based on the type of polymers in *Table 1.3*. Additionally, the application areas and systems are determined depending on their type and properties (Nair and Laurencin, 2007).

Natural polymers are usually derived from natural sources like collagen and are generally used in medical and implant applications because of their high flexibility and biocompatibility. The main reason for the biocompatibility of natural polymers such as collagen is that bone consists of type 1 collagen. In addition to the type 1 collagen, the bone contains ground substances which are proteoglycans and glycoproteins. The natural polymers support hard or soft human tissues such as muscles, cartilage, and bones; and are biocompatible with the biological environment and cause less inflammatory response. However, they have very poor mechanical properties and a high degradation rate (Paital and Dahotre, 2009, Thavornyutikarn et al., 2014).

Synthetic polymers have been utilized in polymeric drug delivery systems, tissue engineering, in orthopedics as medical implants, and as dental and prosthetic devices. In biomedical applications in order to improve mechanical properties, and control the degradation rate and to promote osseointegration, a wide range of synthetic polymers have been investigated and developed. The advantages are many dependents on the chemistry and their structure. The advantages of biodegradable synthetic polymers include: extending shelf life, decreasing inflammatory and toxic effects in implantable devices, improving mechanical properties and processability, reducing cost, matching the degradation and healing time and also to avoid second surgical operation for retrieved non-biodegradable implants (Nair and Laurencin, 2007, Paital and Dahotre, 2009, Planell, 2009, Thavornyutikarn et al., 2014). The production temperature and strain rate during functional applications are highly important to the mechanical properties of the polymers. On the other hand, the deformation of polymers depends on a number of various parameters such as crystallinity, molecular weight, backbone chemistry and cross-linking (Pruitt and Chakravartula, 2011). The mechanical properties of some of the bio-polymers and their degradation times are given in *Table 1.4*.

Table 1.4 Mechanical properties and degradation rates of PDLLA, PLLA, PGA, PLGA, PCL and P3HB (Thavornyutikarn et al., 2014)

Polymers	Tensile or compressive[a] strength (MPa)	Modulus (Potijanyakul et al. 2010)	Degradation time (months)
PDLLA	Pellet: 35–150[a] Film or disk: 29–35	Film or disk: 1.9–2.4	12–16
PLLA	Pellet: 40–120[a] Film or disk: 28–50 Fibre: 870–2,300	Film or disk: 1.2–3.0 Fibre: 10–16	>24
PGA	Fibre: 340–920	Fibre: 7–14	6–12
PLGA	41.4–55.2	1.4–2.8	Adjustable
PCL	10–15	0.15–0.33	Bulk >24
P3HB	25–45	1.5–1.8	Very slow

PGLA > PGA > PDLLA > PLLA

Degradation Time

Polyesters are thermoplastic polymers, and they are degradable because there are short aliphatic chains between ester bonds of their backbone. Polylactic acid (PLA), Polyglycolic acid (PGA),

Poly(εcaprolactone) (PCL) and their copolymers have been investigated and also improved by researchers for medical applications (Nair and Laurencin, 2007, Thavornyutikarn et al., 2014). The thermal transition temparatures (glass transition Tg, and melting Tm temperatures) for some of the well known polyesters are shown in *Table 1.5* (Armentano et al., 2018).

Table 1.5 The thermal properties of polyesters (modified from (Armentano et al., 2018))

Polymer	T_g (°C)	T_m (°C)
PLLA	55–65	170–200
PDLLA	50–60	Amorphous
PGA	35–45	220–233
PCL	(−65)–(−60)	56–65
PHB	9	175–180
PBS	(−37)–(−30)	111–115
PBCE	12	167

The biodegradable polymers were introduced in the 1960s. The new application areas for synthetic biodegradable polymers which are currently being investigated in the biomedical areas include the drug delivery systems and the design of new generation implant devices. The determination of appropriate biodegradable polymers for the desired biomedical applications depends on various factors including the degree of biodegradability, biocompatibility, surface properties and functionality of the final product. Additionally, the properties of the drug and the drug-releasing profile of the system are important (Naahidi et al., 2013).

Polyglycolide (PGA) is the first biodegradable polymer used in the biomedical area. While its glass transition temperature range is between 35-40 °C, the melting temperature of PGA is 225-230 °C. PGA has very acceptable and applicable mechanical properties for biomedical applications due to its high crystallinity (approximately 45-55%). However, its degradation rate is very high, and the solubility in various solvents is very low. PGA loses its strength in 1-2 months while the major mass loss occurs in 6-12 months. In order to counter these disadvantages of PGA, copolymers such as PGLA (PLA-PGA copolymer) have been proposed and investigated (Nair and Laurencin, 2007, Wong et al., 2012, Mahyudin et al., 2016).

In comparison to other copolymers the degradation rate of Poly(εcaprolactone) (PCL) is improved by adjusting the monomer to final copolymer ratio. It has been reported that its application areas include the drug delivery systems, tissue engineering, and in the design of new generation implants (Wong et al., 2012). Some of PGLA's important properties include: solvent solubility, great

permeability for drugs and non-toxicity. Additionally, it has a low melting point which is between 55-60 °C and a glass transition temperature of -54 °C. Because of these properties of PCL, the miscible blends with various types of polymers which have been produced easily. Although PCL has poor wettability, cell adhesion properties and also low tensile strength about 23MPa, the combination of PCL and human tissues promotes good cell adhesion and mechanical properties (Nair and Laurencin, 2007, Wong et al., 2012).

In addition, Polylactides (PLA) is the first polyester applied in tissue engineering; the most important reason is that it is biodegradable, economical and easily produced. The degradation rate of PLA is less than the PGA degradation which is also given in *Table 4* (Rezwan et al., 2006, Nair and Laurencin, 2007, Wong et al., 2012). This allows PLA to be easily mixed with drugs for slow delivery and long-term implant and coating applications for dental and orthopaedic use.

The glass transition temperature range of PLA is about 60-65 °C while its melting temperature is between 173-178 °C. Additionally, this biodegradable polymer has three stereoisomers that are poly (L-lactic acid) (PLLA), poly (D-lactic acid) (PDLA), and poly (D, L-lactic acid) (PDLLA). While PLLA has a 37% crystalline structure, its advantageous properties have good tensile strength, and high modulus of elasticity which is approximately 4.8 GPa, low extension, and slow degradation rates. Because of these properties, various new products such as sutures, blood vessels, and implantable devices for dental and orthopedic application have been developed (Rezwan et al., 2006, Nair and Laurencin, 2007, Wong et al., 2012, Naahidi et al., 2013).

Both PLLA and PDLA are semi-crystalline polymers and their tensile strength values which are 4-8GPa and elongation at break (1-8%) are comparable. On the other hand, PDLLA amorphous polymer is produced by the random distribution of PLLA and PDLA polymers. PLLA has highly crystalline structure when compared with PDLLA, so it causes low strength and a relatively high degradation rate. Therefore, the ratio of D and L isomers in PDLLA allows to manipulate degradation rate of the polymer. The adjustable degradation rate is the key point for the biodegradable polymeric based biomedical applications, such as drug delivery implant coating systems and degradable surgery sutures (Narayanan et al., 2016).

PLA synthetic biodegradable polymer has been approved by FDA due to good tensile strength, the biodegradable feature, biocompatibility and suitable degradation rate. It has also already been used by many biomedical companies as wound dressing and surgical sutures (Ferrandez-Montero et al., 2019). Additionally, PLA usage for different applications on tissue engineering and local drug delivery

systems has been significantly increased with the combination of many types or pharmaceuticals or minerals (Narayanan et al., 2016, Armentano et al., 2018, Ferrandez-Montero et al., 2019).

1.6 Surface Modifications: Thin Film Coating

Metallic or non-metallic coatings can be categorized as macro, micro, and nano-coatings according to their thickness. The thin film coatings and nanocoatings do not have the exact same definition, because the thin film coatings refer to micro coatings (500nm to 1 mm). The nano-coatings are thin film coatings with a nano-size thickness (2-300 nm). Some of the most important advantages of the nano-coatings are their wide application areas and their application methods, purity, homogeneity, low cost, ease of mixing with various other compounds or nano-particles and wide raw material choices (Choi et al., 2017).

The coating methods are usually determined according to the type of implant biomaterials used and their application areas. The basic requirements of the metallic, ceramic, polymeric or composite implants are mainly to improve biological fixation, bioactivity and to promote osseointegration; and to avoid osteolysis and the post-operative complications after surgery. In order to provide these crucial requirements, the surface modification of implants is one of the most important strategies and can be easily applied (Choi et al., 2015, Choi and Ben-Nissan, 2017).

During the insertion of the metallic implants, the biological tissue or bone-implant interaction is supported by the prior surface modifications carried out and macro- or micro-texturing. In order to obtain a successful chemical bonding between tissue and implant, and to prevent metallic ion release, calcium phosphate biomaterials, biodegradable polymers and/or composites have been used as coating materials in both dental and orthopedic applications (Choi et al., 2015, Choi et al., 2017).

Calcium phosphates as a bioactive coating on the surface of bio-inert metallic implants have been attracting scientists since the 1980s. In particular, HAp has been utilized as a coating material because of its biocompatible and bioactive properties. The unique and supportive properties of HAp coating on metallic implants are;

- It improves the bioactivity on the metallic surface, so biological fixation and biological attachments between implant and tissue increases.

- It accelerates the healing process and supports new tissue regeneration with the release of Calcium and Phosphate ions after the insertion of the implant.
- It inhibits the release of metal ions from the surface of metallic implants.

Interfacial bond strength differences between HAp coated, and uncoated implants are observed clearly in *Figure 1.9*. Bond strength of HAp coated implants is always higher than uncoated implants (Rath et al., 2012, Ben-Nissan et al., 2015a, Dey and Mukhopadhyay, 2015).

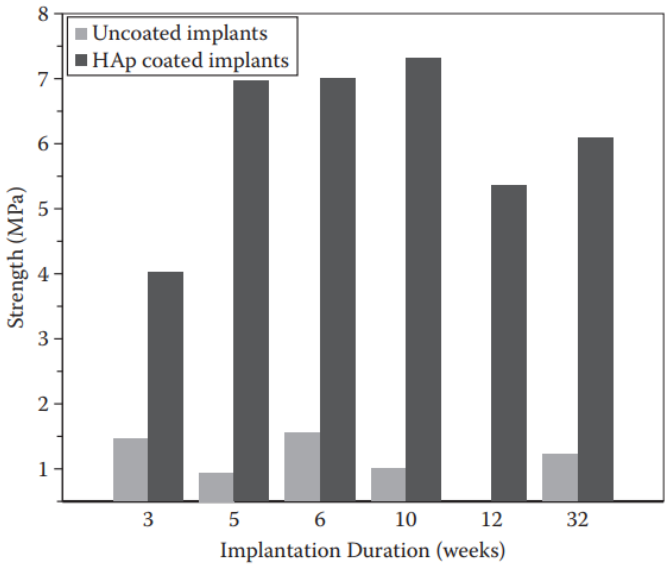

Figure 1.9 The bond strength graph of HAp coated and bare implants (Dey and Mukhopadhyay, 2015).

Despite these advantages of HAp for the development of implantable devices, porous HAp bioceramic has some constraints due to its mechanical properties. Although there are chemical similarities between the HAp structure and human bone, the mechanical properties of the porous HAp bioceramic is unfavorable. Because of the incompatible mechanical properties, it is not useable at load-bearing applications without any modifications, so new generation monolithic biocomposites have been developed. In addition, these biocomposites can be applied to metallic implants to utilize their stiffness and strength and used as biocompatible and high-quality coating materials (Choi et al., 2017).

Novel biocomposite thin films have recently been developed and investigated in order to improve drug-gene delivery systems, surface modifications of implantable devices, tissue engineering applications, cancer treatments and to inhibit bacterial or viral infections, and the toxic effects of

implantable implants. One of the most attractive types of research is the production of novel bioceramic and biodegradable synthetic polymer micro or nano biocomposites, especially; collagen, chitosan and biodegradable polymers such as PLA and PLGA mixed with HAp which is used as coating materials (Choi et al., 2014, Choi and Ben-Nissan, 2017, Choi et al., 2017).

Coating and surface modifications on the metallic implants such as titanium and titanium alloy implants have been introduced in order to improve surface activity such as bioactivity, osseointegration, mechanical properties and adhesion properties of the implants. Osseointegration, also called secondary stability is defined as the characterization of the implant surface – newly formed living bone connection functionally and structurally. Osseointegration includes wound healing, fracture healing and the formation of new bone or tissue on the implant surface after surgery. Biocompatible implantable materials do not cause any inflammation or foreign material response to the body or for the host. For instance, calcium phosphate bioceramics, especially hydroxyapatite, have biocompatible properties because of their chemical structure similarity with bone (Das et al., 2019, Jeong et al., 2019). Therefore, various modification studies for the implant surfaces have been progressed in order to regulate osteoblastic adhesion, migration, differentiation, and proliferation (Milošev, 2010, Smeets et al., 2016).

For clinical applications various coating techniques have been investigated including: in sol gel method spin coating, dip coating, in thermal processes; plasma spraying technique, physical vapor deposition, and chemical vapor deposition techniques etc. (Choi et al., 2017).

The coating techniques and their short definitions, advantages and film thickness are given in *Table 1.6*.

Table 1.6 The descriptions and properties of various types of coating methods (modified from (Ben-Nissan et al., 2015a)).

Coating Technique	Advantages	Drawbacks	Coating Thickness
Electrochemical deposition	Low cost, coat complex shapes, rapid, uniform coating thickness	The bonding strength between coating and substrate is not strong enough	0.05-0.5 mm
Electrophoretic deposition	Coat complex shapes, rapid, uniform coating thickness	Difficult to produce a crack free coating	0.1-2 mm
Plasma coating	Low cost, high deposition rate	High temperature induce thermal decomposition, line of sight technique, amorphous coating due to rapid cooling	0.05-0.5µm
Pulse laser deposition	Coating by crystalline and amorphous phases, both porous and dense coating	Line of sight technique, low deposition rate, expensive	30-200 µm
Sol-Gel nanocoating	High purity, homogenous, no residual stresses, coat complex shapes	Edge cracking might occur, cannot induce mechanical interlock, post treatment needed (curing)	50-400 nm
Sputter coating	Dense and uniform coating thickness	Amorphous coating, line of sight technique, time-consuming, low deposition rate, expensive	0.5-3 µm

1.6.1 Dip coating technique

The dip coating technique is utilized in order to manufacture coating on substrates with intricate complex shapes such as implants, and other engineering surfaces. It is also applied to various complex shape substrates such as screws, rods, fibers, and pipes, so it is easily applicable to the dental implants. Another important advantage of this technique is to produce a multilayered coating film on the surface of the substrates. Because of this property, the thickness of the coating film is adjustable in the system. While the coating thickness of the single-layer film is controlled with pulling speed, it can be modified and regulated with physical properties such as viscosity and chemical properties of the film solution. Although the thickness of single-layer film coating on the substrate is obtained around 70-100nm, the thickness of multilayered film coating can be up to 1µm ((Ben-Nissan et al., 2011, Ben-Nissan et al., 2015a, Choi and Ben-Nissan, 2017, Choi et al., 2017). However, coating thickness determines the mechanical properties and it is an important factor to consider and control.

It is regarded that, the thickness of the coating can be easily uniformly applied when the dip coating method is utilized as a continuous process. The dip coating technique contains five main steps: immersion, start-up, deposition, evaporation, and drainage, respectively. All steps are illustrated in *Figure 1.10* (Ben-Nissan et al., 2011, Choi et al., 2017).

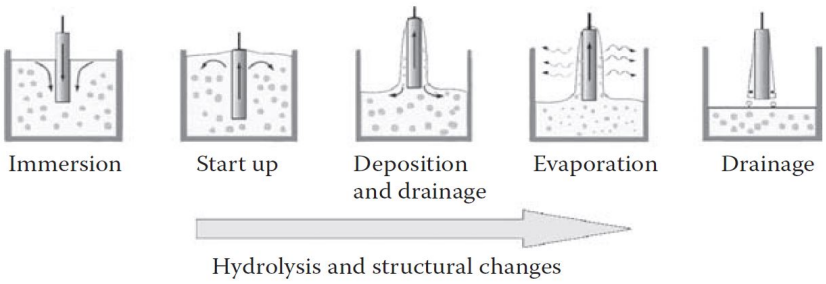

Figure 1.10 The schema of the dip coating technique step by step (Ben-Nissan et al., 2011*)*

In order to calculate the film thickness, we utilize the following formula

$$h = c(\frac{\eta U}{\rho g})^{1/2}$$

where c is constant, and it is approximately 0.8 for Newtonian fluids, U is withdrawal speed, Ƞ is the viscosity of sol, g is the acceleration due to gravity and ρ is density (Ben-Nissan et al., 2011).

1.6.2 Spin coating technique

The spin coating technique is applicable for flat surfaces such as discs, lenses, plates, and bowls. It is easily applied as a research tool to check the coatings. This technique contains four steps, and the general illustration for its application is given in *Figure 1.11*.

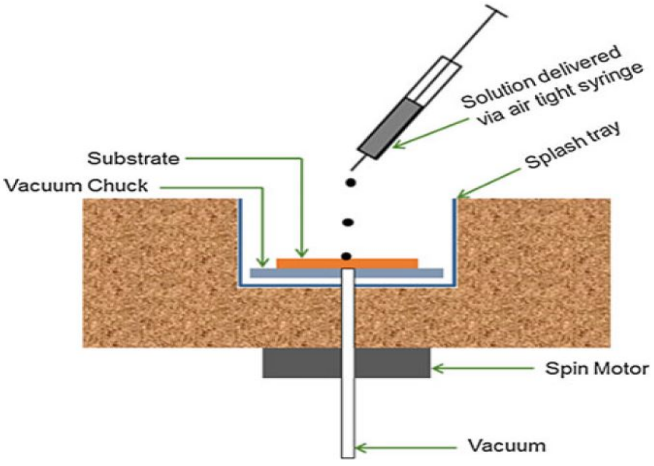

Figure 1.11 The general schema for spin coating method (Ben-Nissan et al., 2015b)

In the first step (deposition), a coating thin film solution is dropped on the surface of the substrate. Therefore, during the spinning, the first step delivers the excess coating material solution to the substrate. While the solution moves on the surface because of the centrifugal force which is created by the rotation of the disc (spin-up step), the excess liquid is detached from the substrate (spin-off). The final step is evaporation which is more effective in thinner films. After the application of the spin coating method, a uniform thin film on the surface of the substrate is obtained except for the edges because of the surface tension which creates the edge effect (edge cracks). According to the general definition, the uniformity of coating film occurs by the balance between viscosity and centrifugal force (Ben-Nissan et al., 2011, Choi and Ben-Nissan, 2017, Choi et al., 2017).

Scriven *et al.* (2011) reported the formula of the final thickness of the thin film (Scriven, 2011);

$$h = (\frac{\rho}{\rho_0})(\frac{3\eta e}{2\rho_0 w})^{\frac{1}{3}}$$

While ρ0 is the initial solvent volume, ρ refers to the solvent volume in the film. Ƞ, e, and w are viscosity, evaporation rate, and angular velocity, respectively. According to the equation, the thickness can be adjusted according to viscosity and spin speed (Scriven, 2011, Ben-Nissan et al., 2011).

The various properties of the nanocoatings such as mechanical properties, designs, and functions differ according to the application areas and the type of the implant devices. Due to complexities, more accurate and reliable testing methods are required to measure their nano mechanical and adhesion properties (Choi et al., 2016).

Aside from using coating materials in order to improve surface properties of the metallic implants, they can be utilized as drug delivery systems on the implants to design a range of novel multifunctional implantable systems to improve their clinical outcomes.

1.7 Combination of Metallic Implants with Drug Delivery Systems

During the last two decades, drug delivery systems have become very important in clinical medicine and related areas. Modifiable drug release patterns can help to improve the management of different diseases by controlling the dosage and release rates of the pharmaceutical agents. At the

same time, adjustable pharmaceutical doses can minimize the side effects of drugs on the body (Bruschi, 2015).

While there is a large impact of implant failures due to surgery-related infections, the combination of implants with a novel slow drug delivery system such as surface coating is a very attractive approach for solving or at least minimizing the problem. For the combination of the drug-metallic implantable device, the most standout application is for the orthopedic and dental implants to prevent surgery-related infections. In most cases, the drug delivery systems are designed with the metallic implants in the form of polymeric or ceramic coatings or their combinations that contain drugs (Campoccia et al., 2010, Inzana et al., 2016).

When the local-controlled drug delivery systems are compared with systemic drug delivery systems, local drug delivery systems have various advantages. They require (Simchi et al., 2011, Goodman et al., 2013):

1. reduced pharmaceutical dosage for treatment
2. control over toxicity and bioavailability of dose which is better than the systemic drug delivery systems
3. in antibiotic delivery the new local system to reduce the likelihood of increasing antibiotic resistance, and risk of systemic ototoxicity
4. control of the release from surfaces and the duration of release,
5. avoiding systemic drug exposure
6. providing direct mitigation of device centered infection
7. combining systemic drugs with different drug release kinetics
8. improved healing time and osseointegration

In most cases, the initial release rate (called burst release) has a higher rate because of the significant infection risk immediately after the surgery. While the rate of drug release is decreased, the duration of the release is extended to obtain enough therapeutic dosage to prevent late-stage infection (Wu and Grainger, 2006, Lyndon et al., 2014).

Biodegradable polymeric materials have recently been introduced for use as coating material for the local drug delivery systems on the surfaces of the metallic implants. Different examples from the literature are shown in *Table 1.7*. In order to design an ideal drug delivery system, it is important to use appropriate materials, good mechanical strength, an appropriate degradation rate for a polymeric matrix, and suitable drug-release profiles. As a matrix, although PMMA is one of the

matrices that was initiated previously, PLA, PGA or a combination of PLA-PGA which is called PLGA, has been used commonly in various forms to obtain desired drug release rates because of their biodegradability. They are mostly combined with antimicrobial agents like silver and antibiotics. In literature, for implant-related infections, aminoglycosides including gentamicin and tobramycin; oxazolidinone including linezolid; glycopeptides including vancomycin; and chloramphenicol have been preferred instead of penicillin because of their stability sensitivity (Lyndon et al., 2014, Pan et al., 2018).

Table 1.7 Clinical applications of different antimicrobial coated implants (modified from (Pan et al., 2018)

Authors	Implant	Coating technology	Study Type	Evidence level
Moghaddam *et al.*, 2016	Tibia nail (ETN PROtect™)	Gentamicin PLA with dip coating process	Case series	IV
Conway *et al.*, 2014	Rods (antibiotic cement coated)	Tobramycin and vancomycin cement (Biomet Cobalt) with metal molds or silicone tubing	Case series	IV
Wilding *et al.*, 2016	Knee arthrodesis nail (Mutars)	Silver with galvanic deposition	Case series	IV
Wafa *et al.*, 2015	Silver-enhanced custom-made endoprostheses	Silver with anodization of the titanium alloy	Case control studies	III
Tsuchiya *et al.*, 2012	Spinal instrumentation, plates, external fixator pins, prostheses, nails, cannulated screw	Povidone-iodine electrolyte-based process	Case series	IV

Chou *et al.*, (2014) reported that marine-derived a bioceramic based drug delivery system was constructed in order to control antibiotics such as gentamicin. In this system, β-TCP particles were used as drug carriers for gentamicin which is a very effective antibiotic on *S. aureus* bacteria caused surgery-related infections. They suggested that the system is highly applicable to bone-related procedures like implant surgeries (Chou et al., 2014). Macha *et al.*, (2015) reported that the antibiotic delivery system was produced with gentamicin including PLA-HAp thin film composites which have two control points for drug releasing; HAp particles and PLA degradation. According to their results, it was reported to be a very effective system as a coating material for the inhibition of surgery-related infections (Macha et al., 2015b, Macha et al., 2016b).

Next-generation implantable device applications for scaffolds and tissue engineering need to be designed as a personalized medicine approach (patient matching) that is specific for each person. Additionally, they must integrate the biological and physical properties for optimal bone

regeneration. In a proper composite system, the amount of drug released, and type of antibiotic are adjustable, and it makes the system more personalized than traditional systems. The unique point of this design is that it has two control points which are PLA matrix and HAp drug carrier particles, and it is applicable for various sizes and shapes of metallic implants. While “burst” or the initial drug release is controlled by the PLA matrix which contains Gm antibiotic particles both on and in it, long-term slow release is controlled by HAp particles which are loaded with the Gm antibiotic as well. These two steps allow us to adjust antibiotic concentration according to patients’ conditions.

The main gap in the research above is that the biodegradable biocomposite coating system has not been tested on the metallic implants by chemical, biological, in vitro and surface analyses. Therefore, this research focused on the applications of the gentamicin antibiotic (Gm) contained coral based hydroxyapatite particles (HAp) embedded biodegradable poly lactic acid thin film coating (PLA-Gm-(HAp-Gm)) on the Ti6Al4V metallic bone implants to prove the applicability of the coating system on the metallic implants. Additionally, the Gm dosage has been tested on human adipose derived stem cells and human pathogenic bacteria in order to optimize the range of antibiotic dosage for the patients. PLA biocomposites thin film which contains Gm particles and HAp-Gm particles, (PLA-Gm-(HAp-Gm)), coated Ti6Al4V disc is the focused design for this research. PLA biocomposites thin film coated Ti6Al4V discs were analyzed to determine the chemical, morphological and mechanical properties of the coating, and to examine Gm release pattern from the coating, finally, to investigate its effects on Human adipose derived stem cells and its bacterial infection and biofilm inhibition ability step by step in each chapter. The design of PLA-Gm-(HAp-Gm) thin film coated Ti6Al4V implants were illustrated with its production methods and its analyses steps in the graphical abstract at the end of this chapter.

1.8 References

ABRAHAM, C. M. 2014. A brief historical perspective on dental implants, their surface coatings and treatments. *Open Dent J,* 8**,** 50-5.

AGARWAL, R. & GARCIA, A. J. 2015. Biomaterial strategies for engineering implants for enhanced osseointegration and bone repair. *Adv Drug Deliv Rev,* 94**,** 53-62.

ALADJEM, A. 1973. Anodic oxidation of titanium and its alloys. *Journal of Materials Science,* 8**,** 688-704.

ANDRÉS-VERGÉS, M., FERNÁNDEZ-GONZÁLEZ, C. & MARTÍNEZ-GALLEGO, M. 1998. Hydrothermal synthesis of calcium deficient hydroxyapatites with controlled size and homogeneous morphology. *Journal of the European Ceramic Society,* 18**,** 1245-1250.

ARMENTANO, I., GIGLI, M., MORENA, F., ARGENTATI, C., TORRE, L. & MARTINO, S. 2018. Recent Advances in Nanocomposites Based on Aliphatic Polyesters: Design, Synthesis, and Applications in Regenerative Medicine. 8**,** 1452.

BARFEIE, A., WILSON, J. & REES, J. 2015. Implant surface characteristics and their effect on osseointegration. *Br Dent J,* 218**,** E9.

BEN-NISSAN, B., CHOI, A., ROEST, R., LATELLA, B. A. & BENDAVID, A. 2015a. Adhesion of hydroxyapatite on titanium medical implants. *In:* MUCALO, M. (ed.) *Hydroxyapatite (HAp) for Biomedical Applications.* Woodhead Publishing.

BEN-NISSAN, B., CHOI, A. H., GREEN, D. W., LATELLA, B. A., CHOU, J. & BENDAVID, A. 2011. Synthesis and Characterization of Hydroxyapatite Nanocoatings by Sol-Gel Method for Clinical Applications. United States: CRC Press.

BEN-NISSAN, B., CHOI, A. H., MACHA, I. J. & CAZALBOU, S. 2015b. Sol-gel Nanocoatings of Bioceramics. *In:* ANTONIAC, I. V. (ed.) *Handbook of Bioceramics and Biocomposites.* Cham: Springer International Publishing.

BEN-NISSAN, B. & PEZZOTTI, G. 2003. Bioceramics Processing Routes and Mechanical Evaluation. *Journal of the Ceramic Society of Japan,* 110**,** 601-608.

BINGÖL, O. R. & DURUCAN, C. 2012. Hydrothermal Synthesis of Hydroxyapatite from Calcium Sulfate Hemihydrate. *American Journal of Biomedical Sciences,* 4**,** 50-59.

BRUNI, S., MARTINESI, M., STIO, M., TREVES, C., BACCI, T. & BORGIOLI, F. 2005. Effects of surface treatment of Ti-6Al-4V titanium alloy on biocompatibility in cultured human umbilical vein endothelial cells. *Acta Biomater,* 1**,** 223-34.

BRUSCHI, M. L. 2015. Drug delivery systems. *In:* BRUSCHI, M. L. (ed.) *Strategies to Modify the Drug Release from Pharmaceutical Systems.* Woodhead Publishing.

CAMPOCCIA, D., MONTANARO, L., SPEZIALE, P. & ARCIOLA, C. R. 2010. Antibiotic-loaded biomaterials and the risks for the spread of antibiotic resistance following their prophylactic and therapeutic clinical use. *Biomaterials,* 31**,** 6363-77.

CHEN, M. J., ZHANG, Z. & BOTT, T. R. 1998. Direct measurement of the adhesive strength of biofilms in pipes by micromanipulation. *Biotechnology Techniques,* 12**,** 875-880.

CHOI, A. H. & BEN-NISSAN, B. 2017. Calcium Phosphate Nanocomposites for Biomedical and Dental Applications: Recent Developments. *In:* THAKUR, V. K., THAKUR, M. K. & KESSLER, M. R. (eds.) *Handbook of Composites from Renewable Materials.* Scrivener Publishing LLC.

CHOI, A. H., BEN-NISSAN, B. & BENDAVID, A. 2017. *Thin Films and Nanocoatings of Hydroxyapatite on Titanium Implants: Production Methods and Adhesion Testing*, LAP LAMBERT Academic Publishing.

CHOI, A. H., BEN-NISSAN, B., BENDAVID, A. & LATELLA, B. 2016. Mechanical behavior and properties of thin films for biomedical applications. *In:* GRIESSER, H. J. (ed.) *Thin Film Coatings for Biomaterials and Biomedical Applications.* Woodhead Publishing.

CHOI, A. H., BEN-NISSAN, B., CONWAY, R. C. & MACHA, I. J. 2014. Advances in Calcium Phosphate Nanocoatings and Nanocomposites. *In:* BEN-NISSAN, B. (ed.) *Advances in Calcium Phosphate Biomaterials.* Berlin, Heidelberg: Springer Berlin Heidelberg.

CHOI, A. H., CAZALBOU, S. & BEN-NISSAN, B. 2015. Nanobiomaterial Coatings in Dentistry.', Frontiers of oral biology. *In:* DEB, S. (ed.) *Biomaterials for Oral and Craniomaxillofacial Applications.* London: Front Oral Biol. Basel, Karger.

CHOU, J., HAO, J., BEN-NISSAN, B., MILTHORPE, B. & OTSUKA, M. 2013. Coral exoskeletons as a precursor material for the development of a calcium phosphate drug delivery system for bone tissue engineering. *Biol Pharm Bull,* 36**,** 1662-5.

CHOU, J., VALENZUELA, S., GREEN, D. W., KOHAN, L., MILTHORPE, B., OTSUKA, M. & BEN-NISSAN, B. 2014. Antibiotic delivery potential of nano- and micro-porous marine structure-derived beta-tricalcium phosphate spheres for medical applications. *Nanomedicine (Lond),* 9**,** 1131-9.

CLARKE, B. 2008. Normal bone anatomy and physiology. *Clin J Am Soc Nephrol,* 3 Suppl 3**,** S131-9.

COMMONWEALTHOFAUSTRALIA 2019. Development of the National Strategic Action Plan. *In:* HEALTH, T. D. O. (ed.). Creative Commons Attribution.

DAROUICHE, R. O. 2003. Antimicrobial approaches for preventing infections associated with surgical implants. *Clin Infect Dis,* 36**,** 1284-9.

DAS, S., DHOLAM, K., GURAV, S., BENDALE, K., INGLE, A., MOHANTY, B., CHAUDHARI, P. & BELLARE, J. R. 2019. Accentuated osseointegration in osteogenic nanofibrous coated titanium implants. *Sci Rep,* 9**,** 17638.

DE VITERI, V. S. & FUENTES, E. 2013. Titanium and Titanium Alloys as Biomaterials. *In:* GEGNER, J. (ed.) *Tribology - Fundamentals and Advancements.* IntechOpen.

DEY, A. & MUKHOPADHYAY, A. K. 2015. *Microplasma Sprayed Hydroxyapatite Coatings,* Boca Raton, CRC Press.

DHALIWAL, J. S., MARULANDA, J., LI, J., ALEBRAHIM, S., FEINE, J. S. & MURSHED, M. 2017. In vitro comparison of two titanium dental implant surface treatments: 3MESPE MDIs versus Ankylos(R). *Int J Implant Dent,* 3**,** 27.

FERNANDEZ-YAGUE, M. A., ABBAH, S. A., MCNAMARA, L., ZEUGOLIS, D. I., PANDIT, A. & BIGGS, M. J. 2015. Biomimetic approaches in bone tissue engineering: Integrating biological and physicomechanical strategies. *Adv Drug Deliv Rev,* 84**,** 1-29.

FERRANDEZ-MONTERO, A., LIEBLICH, M., GONZALEZ-CARRASCO, J. L., BENAVENTE, R., LORENZO, V., DETSCH, R., BOCCACCINI, A. R. & FERRARI, B. 2019. Development of biocompatible and fully bioabsorbable PLA/Mg films for tissue regeneration applications. *Acta Biomater,* 98**,** 114-124.

FLORENCIO-SILVA, R., SASSO, G. R., SASSO-CERRI, E., SIMOES, M. J. & CERRI, P. S. 2015. Biology of Bone Tissue: Structure, Function, and Factors That Influence Bone Cells. *Biomed Res Int,* 2015**,** 421746.

GARRETT, T. R., BHAKOO, M. & ZHANG, Z. 2008. Bacterial adhesion and biofilms on surfaces. *Progress in Natural Science,* 18**,** 1049-1056.

GOLDBERG, J. 2002. Biofilms and antibiotic resistance: a genetic linkage. *Trends in Microbiology,* 10**,** 264.

GOODMAN, S. B., YAO, Z., KEENEY, M. & YANG, F. 2013. The future of biologic coatings for orthopaedic implants. *Biomaterials,* 34**,** 3174-83.

GREEN, D. W., BEN-NISSAN, B., YOON, K. S., MILTHORPE, B. & JUNG, H. S. 2017. Natural and Synthetic Coral Biomineralization for Human Bone Revitalization. *Trends Biotechnol,* 35**,** 43-54.

GUILLEMOT, F. 2005. Recent advances in the design of titanium alloys for orthopedic applications. *Expert Rev Med Devices,* 2**,** 741-8.

GUNDUZ, O., SAHIN, Y. M., AGATHOPOULOS, S., BEN-NISSAN, B. & OKTAR, F. N. 2014. A new method for fabrication of nanohydroxyapatite and TCP from the sea snail cerithium vulgatum. 2014**,** Article 1.

HEALTHCARE, A. C. O. S. A. Q. I. 2017. Approaches to Surgical Site Infection Surveillance. *In:* ACSQHC (ed.). Australia: Creative Commons Attribution.

HENCH, L. L. 2005. Bioceramics. *Journal of the American Ceramic Society,* 81**,** 1705-1728.

HENCH, L. L. & JONES, J. R. 2005. *Biomaterials, artificial organs and tissue engineering*, Boca Raton : CRC Press ; Cambridge : Woodhead.

HENCH, L. L. & POLAK, J. M. 2002. Third-generation biomedical materials. *Science,* 295**,** 1014-7.

HENESS, G. L. & BEN-NISSAN, B. 2004. Innovative Bioceramics. *Materials Forum,* 27**,** 104-114.

INZANA, J. A., SCHWARZ, E. M., KATES, S. L. & AWAD, H. A. 2016. Biomaterials approaches to treating implant-associated osteomyelitis. *Biomaterials,* 81**,** 58-71.

JEONG, J., KIM, J. H., SHIM, J. H., HWANG, N. S. & HEO, C. Y. 2019. Bioactive calcium phosphate materials and applications in bone regeneration. *Biomater Res,* 23**,** 4.

KARACAN, I., BEN-NISSAN, B. & SINUTOK, S. 2019. Marine-Based Calcium Phosphates from Hard Coral and Calcified Algae for Biomedical Applications. *In:* CHOI, A. H. & BEN-NISSAN, B. (eds.) *Marine-Derived Biomaterials for Tissue Engineering Applications.* Singapore: Springer.

KARGOZAR, S., MOZAFARI, M., HAMZEHLOU, S., BROUKI MILAN, P., KIM, H.-W. & BAINO, F. 2019. Bone Tissue Engineering Using Human Cells: A Comprehensive Review on Recent Trends, Current Prospects, and Recommendations. 9**,** 174.

KAVANAGH, N., RYAN, E. J., WIDAA, A., SEXTON, G., FENNELL, J., O'ROURKE, S., CAHILL, K. C., KEARNEY, C. J., O'BRIEN, F. J. & KERRIGAN, S. W. 2018. Staphylococcal Osteomyelitis: Disease Progression, Treatment Challenges, and Future Directions. *Clin Microbiol Rev,* 31**,** e00084-17.

KHAN, S. A. 2012. Oral Treatment Options for Chronic Osteomyelitis. *US Pharm. ,* 37**,** HS-2-HS-8.

KRUZIC, J. J. & RITCHIE, R. O. 2008. Fatigue of mineralized tissues: cortical bone and dentin. *J Mech Behav Biomed Mater,* 1**,** 3-17.

LIU, X., CHU, P. & DING, C. 2004. Surface modification of titanium, titanium alloys, and related materials for biomedical applications. *Materials Science and Engineering: R: Reports,* 47**,** 49-121.

LUO, Y., YANG, L. & TIAN, M. 2013. 3 - Application of biomedical-grade titanium alloys in trabecular bone and artificial joints. *In:* DAVIM, J. P. (ed.) *Biomaterials and Medical Tribology.* Woodhead Publishing.

LYNDON, J. A., BOYD, B. J. & BIRBILIS, N. 2014. Metallic implant drug/device combinations for controlled drug release in orthopaedic applications. *J Control Release,* 179**,** 63-75.

MACHA, I., CHARVILLAT, C., CAZALBOU, S., GROSSIN, D., BOONYANG, U. & BEN-NISSAN, B. 2016a. Comparative study of coral conversion, Part 3: Intermediate products in the first half an hour. *Journal of The Australian Ceramic Society,* 52**,** 177-182.

MACHA, I., OZYEGIN, L., OKTAR, F. & BEN-NISSAN, B. 2015a. Conversion of Ostrich Eggshells (Struthio camelus) to Calcium Phosphates. *Journal of The Australian Ceramic Society,* 51**,** 9.

MACHA, I. J. & BEN-NISSAN, B. 2018. Marine Skeletons: Towards Hard Tissue Repair and Regeneration. *Mar Drugs,* 16**,** 225.

MACHA, I. J., BEN-NISSAN, B., SANTOS, J., CAZALBOU, S. & MILTHORPE, B. 2016b. Hydroxyapatite/PLA Biocomposite Thin Films for Slow Drug Delivery of Antibiotics for the Treatment of Bone and Implant-Related Infections. *Key Engineering Materials,* 696**,** 271-276.

MACHA, I. J., CAZALBOU, S., BEN-NISSAN, B., HARVEY, K. L. & MILTHORPE, B. 2015. Marine structure derived calcium phosphate-polymer biocomposites for local antibiotic delivery. *Mar Drugs,* 13**,** 666-80.

MAHYUDIN, F., WIDHIYANTO, L. & HERMAWAN, H. 2016. Biomaterials in Orthopaedics. *In:* MAHYUDIN, F. & HERMAWAN, H. (eds.) *Biomaterials and Medical Devices, A Perspective from an Emerging Country.* Springer.

MANIVASAGAM, G., DHINASEKARAN, D. & RAJAMANICKAM, A. 2010. Biomedical Implants: Corrosion and its Prevention - A Review, *Recent Patents on Corrosion Science,* 2**,** 40-54.

MANN, S. 1988. Molecular recognition in biomineralization. *Nature,* 332**,** 119-124.

MANTRIPRAGADA, V. P., LECKA-CZERNIK, B., EBRAHEIM, N. A. & JAYASURIYA, A. C. 2013. An overview of recent advances in designing orthopedic and craniofacial implants. *J Biomed Mater Res A,* 101**,** 3349-64.

MEROLLI, A. & JOYCE, T. J. 2009. *Biomaterials in Hand Surgery,* Milan, Springer Science & Business Media.

MILOŠEV, I. 2010. Metallic materials for biomedical applications: Laboratory and clinical studies. *Pure and Applied Chemistry,* 83**,** 309-324.

MOHAMED, A. M. 2008. An overview of bone cells and their regulating factors of differentiation. *Malays J Med Sci,* 15**,** 4-12.

NAAHIDI, S., JAFARI, M., EDALAT, F., RAYMOND, K., KHADEMHOSSEINI, A. & CHEN, P. 2013. Biocompatibility of engineered nanoparticles for drug delivery. *J Control Release,* 166**,** 182-94.

NAIR, L. S. & LAURENCIN, C. T. 2007. Biodegradable polymers as biomaterials. *Progress in Polymer Science,* 32**,** 762-798.

NAM, N. H. & KAMPA, N. 2013. Bone Cell Function: A Review. *The Thai Journal of Veterinary Medicine,* 43**,** 329-336.

NARAYANAN, G., VERNEKAR, V. N., KUYINU, E. L. & LAURENCIN, C. T. 2016. Poly (lactic acid)-based biomaterials for orthopaedic regenerative engineering. *Adv Drug Deliv Rev,* 107**,** 247-276.

O'CEARBHAILL, E. 2019. Shedding light on implant-associated infection. 11**,** eaaz3709.

OFFICE OF THE SURGEON, G. 2004. Reports of the Surgeon General. *Bone Health and Osteoporosis: A Report of the Surgeon General.* Rockville (MD): Office of the Surgeon General (US).

ORYAN, A., ALIDADI, S., MOSHIRI, A. & MAFFULLI, N. 2014. Bone regenerative medicine: classic options, novel strategies, and future directions. *J Orthop Surg Res,* 9**,** 18.

OVASKA, M., LINDAHL, J., MÄKINEN, T., MADANAT, R., PULLIAINEN, L., KILJUNEN, V., HIRVENSALO, E. & TUKIAINEN, E. 2011. Postoperative infection – removal of screws and plates? *Suomen Ortopedia ja Traumatologia,* 34.

PAITAL, S. R. & DAHOTRE, N. B. 2009. Calcium phosphate coatings for bio-implant applications: Materials, performance factors, and methodologies. *Materials Science and Engineering: R: Reports,* 66**,** 1-70.

PAL, S. 2014. *Design of Artificial Human Joints & Organs,* New York, Springer

PAN, C., ZHOU, Z. & YU, X. 2018. Coatings as the useful drug delivery system for the prevention of implant-related infections. *J Orthop Surg Res,* 13**,** 220.

PENG, J. S., TSAI, W. C. & CHOU, C. C. 2002. Inactivation and removal of Bacillus cereus by sanitizer and detergent. *Int J Food Microbiol,* 77**,** 11-8.

PLANELL, J. A. 2009. *Bone Repair Biomaterials*, Elsevier Science.

PRAKASAM, M., LOCS, J., SALMA-ANCANE, K., LOCA, D., LARGETEAU, A. & BERZINA-CIMDINA, L. 2017. Biodegradable Materials and Metallic Implants—A Review. 8**,** 44.

PRASAD, K., BAZAKA, O., CHUA, M., ROCHFORD, M., FEDRICK, L., SPOOR, J., SYMES, R., TIEPPO, M., COLLINS, C., CAO, A., MARKWELL, D., OSTRIKOV, K. K. & BAZAKA, K. 2017. Metallic Biomaterials: Current Challenges and Opportunities. *Materials (Basel),* 10**,** 884.

PRUITT, L. A. & CHAKRAVARTULA, A. M. 2011. *Mechanics of Biomaterials: Fundamental Principles for Implant Design*, Cambridge University Press.

RATH, P. C., BESRA, L., SINGH, B. P. & BHATTACHARJEE, S. 2012. Titania/hydroxyapatite bi-layer coating on Ti metal by electrophoretic deposition: Characterization and corrosion studies. *Ceramics International,* 38**,** 3209-3216.

RATNER, B. D., HOFFMAN, A. S., SCHOEN, F. J. & LEMONS, J. E. 2012. *Biomaterials Science: An Introduction to Materials in Medicine,* San Diego, UNITED STATES, Elsevier Science.

REZWAN, K., CHEN, Q. Z., BLAKER, J. J. & BOCCACCINI, A. R. 2006. Biodegradable and bioactive porous polymer/inorganic composite scaffolds for bone tissue engineering. *Biomaterials,* 27**,** 3413-31.

RIBEIRO, M., MONTEIRO, F. J. & FERRAZ, M. P. 2012. Infection of orthopedic implants with emphasis on bacterial adhesion process and techniques used in studying bacterial-material interactions. *Biomatter,* 2**,** 176-94.

ROEST, R. 2008. *INTERFACIAL CHARACTERISATION OF SOL- GEL DERIVED COATINGS OF HYDROXYAPATITE AND ZIRCONIA THIN FILMS WITH ANODISED TITANIUM SUBSTRATES. .* PhD, UNIVERSITY OF TECHNOLOGY SYDNEY.

ROEST, R., LATELLA, B. A., HENESS, G. & BEN-NISSAN, B. 2011. Adhesion of sol–gel derived hydroxyapatite nanocoatings on anodised pure titanium and titanium (Ti6Al4V) alloy substrates. *Surface and Coatings Technology,* 205**,** 3520-3529.

SCRIVEN, L. E. 2011. Physics and Applications of DIP Coating and Spin Coating. *MRS Proceedings,* 121**,** 717.

SEEBACH, E. & KUBATZKY, K. F. 2019. Chronic Implant-Related Bone Infections-Can Immune Modulation be a Therapeutic Strategy? *Front Immunol,* 10**,** 1724.

SHAH, F. A., TROBOS, M., THOMSEN, P. & PALMQUIST, A. 2016. Commercially pure titanium (cp-Ti) versus titanium alloy (Ti6Al4V) materials as bone anchored implants - Is one truly better than the other? *Mater Sci Eng C Mater Biol Appl,* 62**,** 960-6.

SIMCHI, A., TAMJID, E., PISHBIN, F. & BOCCACCINI, A. R. 2011. Recent progress in inorganic and composite coatings with bactericidal capability for orthopaedic applications. *Nanomedicine,* 7**,** 22-39.

SINGH, A. 2018. Bactericide hydrogel prevents orthopedic implant infections. 10**,** eaau0463.

SINGH, R. & DAHOTRE, N. B. 2007. Corrosion degradation and prevention by surface modification of biometallic materials. *J Mater Sci Mater Med,* 18**,** 725-51.

SMEETS, R., STADLINGER, B., SCHWARZ, F., BECK-BROICHSITTER, B., JUNG, O., PRECHT, C., KLOSS, F., GROBE, A., HEILAND, M. & EBKER, T. 2016. Impact of Dental Implant Surface Modifications on Osseointegration. *Biomed Res Int,* 2016**,** 6285620.

SONNTAG, R., REINDERS, J., GIBMEIER, J. & KRETZER, J. P. 2013. 4 - Fatigue strengthening of an orthopedic Ti6Al4V alloy: what is the potential of a final shot peening process? *In:* DAVIM, J. P. (ed.) *Biomaterials and Medical Tribology.* Woodhead Publishing.

THAVORNYUTIKARN, B., CHANTARAPANICH, N., SITTHISERIPRATIP, K., THOUAS, G. A. & CHEN, Q. 2014. Bone tissue engineering scaffolding: computer-aided scaffolding techniques. *Prog Biomater,* 3**,** 61-102.

TREVES, C., MARTINESI, M., STIO, M., GUTIERREZ, A., JIMENEZ, J. A. & LOPEZ, M. F. 2010. In vitro biocompatibility evaluation of surface-modified titanium alloys. *J Biomed Mater Res A,* 92**,** 1623-34.

TU, K. N., LIE, J. D., WAN, C. K. V., CAMERON, M., AUSTEL, A. G., NGUYEN, J. K., VAN, K. & HYUN, D. 2018. Osteoporosis: A Review of Treatment Options. *P T,* 43**,** 92-104.

WONG, J. Y., BRONZINO, J. D. & PETERSON, D. R. 2012. *Biomaterials: Principles and Practices*, Taylor & Francis.

WU, P. & GRAINGER, D. W. 2006. Drug/device combinations for local drug therapies and infection prophylaxis. *Biomaterials,* 27**,** 2450-67.

XU, Y., WANG, D., YANG, L. & TANG, H. 2001. Hydrothermal conversion of coral into hydroxyapatite. *Materials Characterization,* 47**,** 83-87.

ZREIQAT, H., VALENZUELA, S. M., NISSAN, B. B., ROEST, R., KNABE, C., RADLANSKI, R. J., RENZ, H. & EVANS, P. J. 2005. The effect of surface chemistry modification of titanium alloy on signalling pathways in human osteoblasts. *Biomaterials,* 26**,** 7579-86.

Statement of Research

Hypothesis

PLA biodegradable polymer biocomposite in combination with a controlled, slow release drug delivery system can be easily applied as a functional coating material for metallic bone implants to enhance their biocompatibility and longevity and reducing surgery related bacterial infections.

Aims and Objectives

The main objective of this study is to design, synthesize and assess the efficiency of a new biocompatible and bioactive antimicrobial implant coating which contains a local and controlled drug delivery system for commercially available metallic based implants. In order to achieve this objective, the following aims will be addressed and the following approaches adopted:

1. Production, morphological and physical characterization of the gentamicin antibiotic containing PLA biocomposite thin film coatings with the dip coating method

2. Determination of its nano- mechanical properties with nanoindentation and scratch test techniques

3. Examination of local drug release profiles, dissolution studies by using continuous drug release technique and theoretical considerations

4. Investigation of Human adipose derived stem cells actions and behaviors on the antimicrobial PLA biocomposites in thin film coated implants by using fluorescent imaging technique, the secretory cytokine assays, proteomic analysis with bioinformatics interrogation by systems biology

5. Determination of the antibacterial efficiency on Staphylococcus aureus and Staphylococcus epidermidis bacteria, bio-film formation on the antimicrobial PLA biocomposites thin film coating.
6. Determination of a safe antibiotic dosage range for the patient according to the results from in vitro cell study and antibacterial study

Thesis Format

This thesis contains 8 chapters as follows;

Chapter 1 Literature Review

Chapter 2 Synthesis of Hydroxyapatite from Porites Coral as a drug carrier particles and Drug Loading Study to obtain Gentamicin loaded Hydroxyapatite (HAp-Gm)

Chapter 3 Production and Characterization for PLA Biocomposites thin film and The dip coating process for the metallic implants

Chapter 4 Mechanical testing on PLA biocomposite coated metallic implants

Chapter 5 Drug Release Studies on the PLA biocomposites coated implants

Chapter 6 Antibacterial Studies for PLA biocomposites coated implants to obtain effects of PLA biocomposites thin film coating to inhibit surgery related infections and biofilm formation

Chapter 7 Human Adipose derived Stem Cells Studies on the PLA Biocomposites Coated Implants

Chapter 8 Discussion and Conclusions

Graphical Abstract

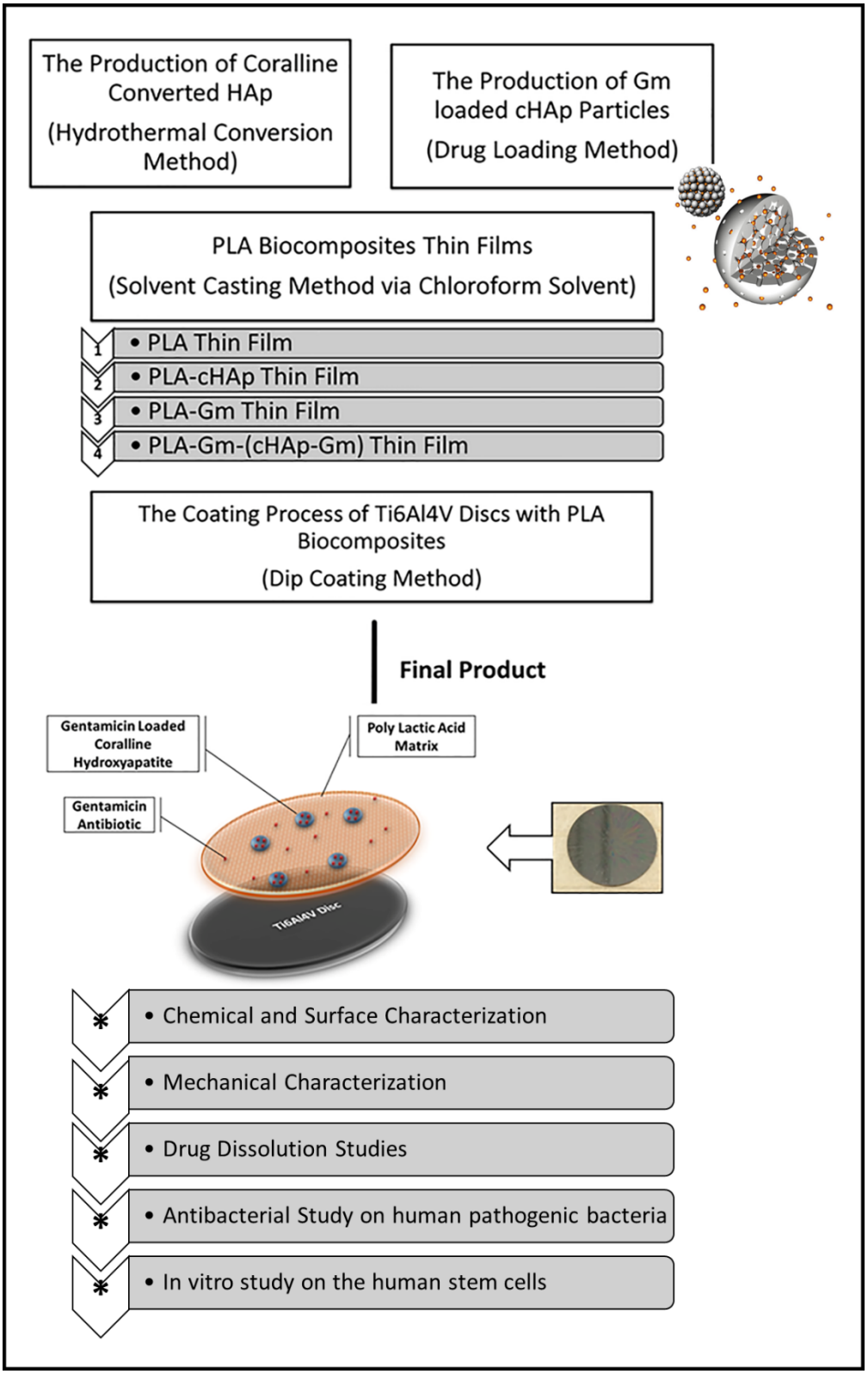

Chapter 2

Synthesis of Hydroxyapatite from Porites Coral and Drug Loading Studies

Chapter 2: Synthesis of Hydroxyapatite from Porites Coral and Drug Loading Studies

This chapter covers two sections to obtain coral skeleton derived Hydroxyapatite (HAp) particles in the first section and Gentamicin loaded Hydroxyapatite (HAp-Gm) particles in second sections. The first section provides the conversion of porous Porites coral skeleton to HAp particles and their characterization analyses. On the other hand, the second section contains the drug loading studies to use porous HAp particles as a drug carrier for Gm antibiotics. HAp-Gm particles are going to be used in biodegradable PLA biocomposite thin film coated bone implants as a slow, and controlled drug delivery system.

2.1 Hydrothermal Conversion of Porites Coral and Physio-chemical characterization analyses of Coral vs. Coral-Based Hydroxyapatite

2.1.1 Introduction

Hydroxyapatite (HAp) belongs to the calcium phosphate (CaPs) bioceramics group, and chemically, it is described as $Ca_{10}(PO_4)_6(OH)_2$ (Choi et al., 2017, Ghiasi et al., 2019). The synthesis of HAp from different synthetic and natural sources has been widely reported. This is due to its importance in the main constituent of the mammalian inorganic hard tissue structure, especially in human mammalian bone and teeth, which consists of 65-70% by weight of natural HAp. When HAp is compared with other calcium phosphates (CaPs), it has the highest structural and functional similarity with human bone and teeth (Xu et al., 2001, Loo et al., 2008, Ghiasi et al., 2019). It is osteoconductive, biocompatible and bioactive (Liu et al., 1997, Macha et al., 2015a, Pokhrel, 2018). While the bioactivity improves the tissue growth on the surface, the osteoconductive property of HAp promotes the new bone growth through its porous structure without any adverse reaction, toxicity or inflammation. Its affinity to biopolymers and high osteogenic potential are other reasons for its

high interest and demand for biomedical research and different clinical usages (Liu et al., 1997, Sadat-Shojai et al., 2013).

The synthetic HAp can be produced from natural sources like human or bovine bone or the marine vertebrate organisms such as the coral skeleton or shells. HAp has been clinically used in biomedical applications as coatings or as solid powder or monolithic forms in implantable devices, tissue engineering, bone graft, bone filler applications, implant surface coating and drug delivery systems (Damien and Revell, 2004, Loo et al., 2008, Szcześ et al., 2017).

Corals belong to the class of *Anthozoa of phylum Cnidaria*, and they have a hard calcium carbonate outer layer that protects the organism. The coral skeletons have unique architectures and structures, especially their tubular or slit-like shapes and various pore sizes and distributions. Additionally, their natural bioactivity with the bone cells motivates researchers to apply those biomaterials in bone regeneration to repair or replace orthopedic and dental bone defects. Porites, Goniopora, Acropora, and Lobophyllia coral species have the most similar physical structure to human bone. Their structure can be similar to cancellous or cortical bone dependent on the porosity size range and density. While Porites sp. have regular pore distribution and the smallest consistent interconnected pore size, which is between 100 to 500 µm, Acropora sp. have an irregular pore size and the largest permeability. The porous structure of Goniopora sp. is strongly disordered (Ben-Nissan et al., 2004, Pountos and Giannoudis, 2016, Green et al., 2017). The interconnected macro and microporous structure cause osseoconductivity which promotes cell adhesion, proliferation and in-growth. Porites coral skeleton is $CaCO_3$, aragonite form, and it has Mg, Sr, Na, F and Cl ions with a small amount of proteins and other organic materials. These ions can replace Ca ions in the HAp structure (Ige et al., 2012, Pountos and Giannoudis, 2016), which improve cell-material interactions. For example, both Mg and Sr minerals play an important role in living cells like osteoblasts and osteoclasts. Therefore, it has been suggested that in addition to Ca, the lack of Mg in the bone structure promotes osteoporosis (LeGeros et al., 1995).

Additionally, Mg is a cofactor for various enzyme and protein synthesis, so Mg homeostasis in the body impacts the bone cell functions and muscle tensions (Castiglioni et al., 2013, Havalda et al., 2013). On the other hand, the Sr element plays an important role in normal bone metabolism like the stimulation of bone formation and the reduction of bone resorption. Additionally, it improves bioactivity and it can be used for bone disorders. For example, in clinical applications, the “strontium ranelate” form can be used to treat osteoporosis (Pemmer et al., 2013, Roczniak et al., 2017).

However, a calcium carbonate coral skeleton is not suitable for long term load-bearing implant applications because of its high dissolution rate and poor stability. Therefore, the skeletons of coral

have been used mainly as natural raw materials for the synthesis of HAp to improve longevity and bioactivity while retaining interconnected porous structure and pore sizes (Ben-Nissan, 2003, Chou et al., 2012, Karacan et al., 2019). Another advantage of the conversion to HAp from the coral skeleton is an improvement in mechanical properties which include hardness; for example, the monolithic HAp (hardness=5 (Mohr)) is harder than aragonite (hardness=3.5-4 (Mohr)) or calcite (hardness=3 (Mohr)) form of $CaCO_3$ (Roy and Linnehan, 1974).

The composition, particle size, crystal morphology, particle shape, and physio-chemical properties of HAp, which can be produced from different natural sources, differ according to their production method (Damien and Revell, 2004). Chemical precipitation (Monmaturapoj, 2008, Karacan et al., 2016), hydrothermal conversion (Zhang et al., 2005, Chou et al., 2007, Rodríguez-Lugo et al., 2017), mechanochemical conversion (Cegla et al., 2014, Macha et al., 2015b), and sol-gel (Liu et al., 2001, Fathi and Hanifi, 2007) methods are some of the most widely used methods for the synthesis of HAp (Ben-Nissan et al., 2004, Ginebra et al., 2012, Macha et al., 2015a).

The hydrothermal conversion method is the conversion of HAp from $CaCO_3$ under elevated temperatures and pressures via an exchange reaction between CO_3^{-2} and PO_4^{3-}.

In 1974, Roy *et al.*, (1974) reported that the hydrothermal method could be applied for the synthesis of HAp from corals (Roy and Linnehan, 1974). While the aragonite structure of coral is replaced with phosphoric material via the hydrothermal reaction, the porous structure of coral is preserved (Ben-Nissan, 2003, Karacan et al., 2019). It has been suggested that high temperatures and pressures applied during the hydrothermal treatment can help to solve sterilization problems as well (Roy and Linnehan, 1974, Heness and Ben-Nissan, 2004, Karacan et al., 2019).

This chapter contains the production of hydroxyapatite powder from the skeleton of Porites coral via the hydrothermal method and its physicochemical characterization with several different methods.

2.1.2 Experimental Methods

2.1.2.1 Coral Sample Preparation

Fossilized or sun-bleached skeletons of Porites coral were collected from Australia`s Great Barrier Reef in Queensland. They were cleaned and cut into small pieces with a diamond blade and a diluted high purity bleach solution was applied to remove contaminants and organic matter.

No live coral was extracted due to environmental concerns. As our coral is unfortunately bleaching out some species are abundant as fossilized and high purity forms in specific areas of the Great Barrier Reef.

For this method, the coral samples were cleaned thoroughly in a 2% NaClO solution diluted with ultrapure (18 milliQ) water. This solution was poured over coral in a beaker until it was completely submerged, then sonicated in an ultrasonic cleaner (Ultrasonic pty. Ltd., UD80 SH-2L, Australia) for 5 min, at room temperature. The coral was further filtered with a Buchner funnel with a 9 cm filter paper under vacuum, and the sample was rinsed with ultrapure water. This rinsing process was repeated until the bleach solution was completely removed from the coral samples.

The cleaned coral samples were further calcined for the hydrothermal conversion with specific heat treatment at 350 ˚C overnight. Finally, they were ground in an alumina ball mill (Royal Doulton, R80.298, England) to obtain the required granular powder size. The ball mill was rotated at 46 rotations per minute (rpm) for 48hours for our specific coral pieces and sieved with a 150 µm mesh size sieve before the conversion process.

2.1.2.2 Hydrothermal Conversion Method

The key point of the HAp synthesis is to find the correct Ca/P ratio before starting the hydrothermal conversion process. The commonly accepted value for HAp, Ca/P ratio is 1.67 (Legeros et al., 1967, Ben-Nissan, 2003, Szcześ et al., 2017). In order to calculate the right amount of Ca within the coral a Differential Thermal Analysis/Thermogravimetry (DTA/TG) method was used. The amount of Ca was measured according to the weight loss during this method which is based on the dissociation of $CaCO_3$. Finally, according to the DTA/TGA analysis and the weight loss, the amount of CaO can be calculated. Based on the weight of the coral powder prepared for the hydrothermal treatment, the required amount of $(NH_4)_2HPO_4$ (98%, Sigma Aldrich, Australia) can be calculated.

The conversion process involves a hydrothermal reactor (Parr Instrument Company, USA) at pH 10, for 4 to 24 hours, which depends on the amount converted. The reactor is adjusted to temperatures between 160 and 220 °C, and at 1-3 MPa pressure, which is shown in *Figure 2.1*. As explained above the amount of the $(NH_4)_2HPO_4$ for the phosphate conversion is adjusted according to the amount of coral used. After the conversion the samples are further washed with ultrapure water under vacuum with 9 cm filter paper. Finally, the samples are dried in an oven at 60 °C overnight (Ben-Nissan, 2003, Chou et al., 2007).

The reaction of the HAp conversion can be given as (Roy and Linnehan, 1974):

$$10CaCO_3 + 6(NH_4)_2\,HPO_4 + 2H_2O \rightarrow Ca_{10}\,(PO_4)_6\,(OH)_2 + 6(NH_4)_2\,CO_3 + 4H_2CO_3$$

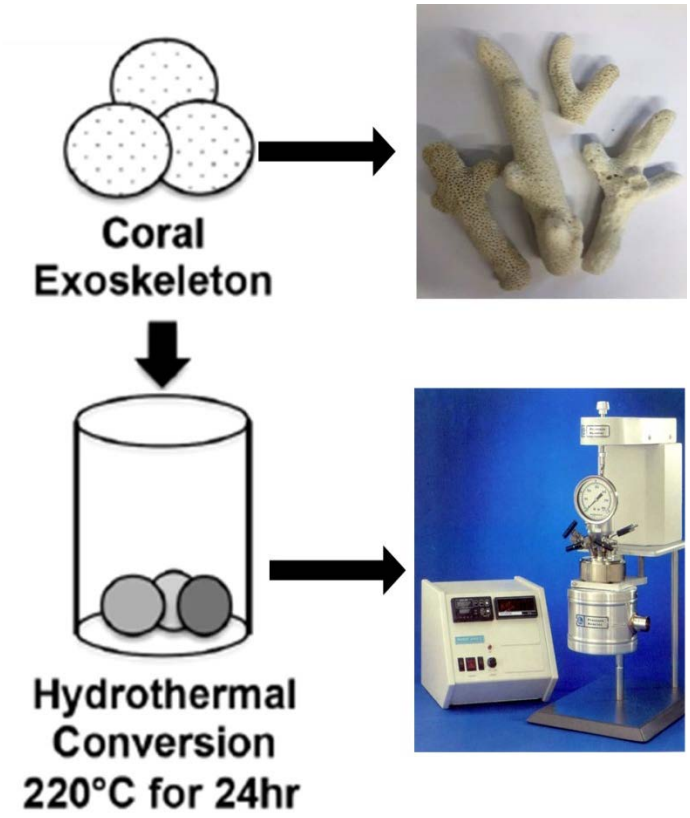

Figure 2.1 The conversion process of the cleaned coral skeleton with Parr reactor.

Since the early 1970s, the hydrothermal conversion technique – which is one of the most important and useful techniques – has been developed for the processing of ceramics and advanced materials. The reasons for the high interest on this technique are numerous; it is easily applicable, has a low-cost and low reaction temperatures.

The definition of the hydrothermal technique is to synthesize materials by chemical reactions at ambient pressures and temperatures in a closed reactor. It contains the production of various new materials such as microporous crystals, ionic conductors, inorganic-organic hybrid materials and various types of bio ceramics to use in different areas like medical, biological or environmental sciences (Feng and Xu, 2001, Li et al., 2017). The conversion of hydroxyapatite bio ceramics is one of the most important examples for the applications of the hydrothermal method (Liu et al., 1997, Ben-Nissan, 2003).

Conventional Thermal Treatment (CTT) and Microwave heating treatment (MHT) are two hydrothermal techniques given in *Figure 2.2*.

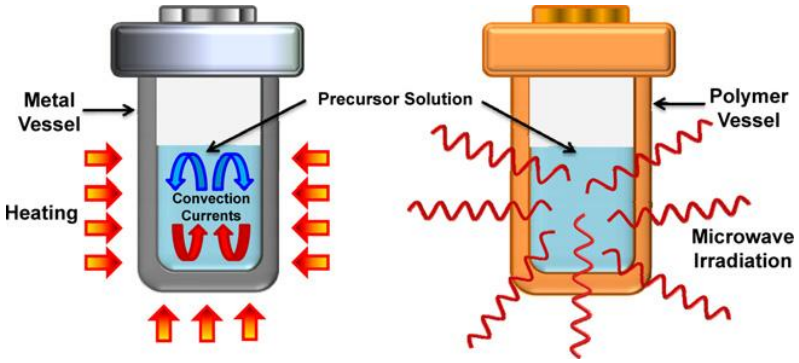

Figure 2.2 Conventional Thermal (A) and Microwave heating (B) treatments (Li et al., 2017)

While MHT provides energy to the reactants with high-frequency electromagnetic radiation, CTT provides energy by the convectional thermal treatment. The advantages of CTT include wide temperature and reaction time ranges. The batch reactor system is used under pressure for CTT (Li et al., 2017).

In this research, CTT has been used for the marine based raw material conversion.

2.1.2.3 The Thermal, Chemical and Physical Analyses of Coral and Coral-Based Hydroxyapatite

The differential thermal and thermo-gravimetric analysis (TG-DTA) was carried out to characterize both coral and converted coral samples. This includes the determination of weight loss on drying, phase transition temperatures, thermal stability, and whether water is bound or unbound within its structure. TG/DTA combines the measurement of a change in mass of a sample as a function of temperature (TG) with the temperature difference of a sample compared with inert reference material as a function of temperature (DTA).

Thermal Analysis was utilized in a TG-DTA supplied by, SDT 2960, TA Instruments, New Castle, DE, USA.

Coral powder of 15 mg was analyzed under circulating air environment with a heating rate of 10 °C/min, and its temperature rate was set as 25 °C to 1100 °C.

Fourier transform infrared spectroscopy (FT-IR) (Thermo Fisher Scientific, Madison USA) analysis was carried out for the cleaned and calcined coral and coralline HAp powders in the range of 4000-400 cm^{-1}.

The chemical composition of coral and coralline HAp powder samples were analyzed with ICP–MS Inductively coupled plasma-mass spectroscopy (ICP-MS 7700, Agilent technologies, , USA) with 7500ce lenses to analyze the elements, 24Mg, 87Sr, 31P and 43Ca. Eight high purity standards were used from 1000ppb to 1ppb. Sample preparation included digestion of 0.5 mg samples into the 6% HNO_3 and held overnight before analysis.

X-Ray diffraction analysis (XRD) (Siemens D5000, Germany) was carried out on both cleaned and calcined coral and coralline HAp. The diffractometer operated at 45 kV and 40 mA at a 2-theta range of 20-80° at a step size of 0.01° and at 4 second exposures. Monochromators with CuKα radiation was used (λ=1.5418A). Matching XRD patterns of the crystalline phases of the powders were identified with the Joint Committee on Powder Diffraction Standards (JCPDS).

Scanning Microscope Analysis (SEM) (ZEISS Supra SSVP, Zeiss, Germany) was used in order to obtain the morphological structure of both cleaned and calcined coral powder and coralline HAp powders. All samples were fixed by a conductive adhesive tape on stubs, they were kept under vacuum overnight to remove any moisture. They were coated with 7 nm thin layer of Au-Pd using a sputter coater (Leica EM ACE600 Sputtering and Carbon Thread Coater, Germany). Images were taken at various magnifications at an acceleration voltage of 10 kV.

The surface area and particle size analysis were carried out by the Brunauer-Emmett-Teller (BET) analysis in order to calculate the surface area and the pore size.

The specific surface area of coralline HAp was measured with a Tristar II apparatus from Micromeritics (AutoPore III, Micromeritics Instrument Inc., Norcross, GA, USA). Samples were initially degassed under vacuum at 77.3 K before analysis.

2.1.3 Results and Discussions

2.1.3.1 Thermal Analysis (DTA-TGA)

Thermal analysis was carried out in order to calculate the CaO amount and to calculate the amount of ammonium hydro phosphate required for the hydrothermal conversion of coral to hydroxyapatite.

According to *Figure 2.3*, maximum peak ($CaCO_3$ decomposition to coral) was observed at 743.61 °C while the thermal decomposition range was between 549.15 °C to 794.06 °C. The thermal decomposition occurs with the equation shown below:

$$CaCO_3 \rightarrow CaO + CO_2$$

Additionally, at that temperature range the weight loss of the coral is 42.99% which corresponds to the dissociation of calcium carbonate to calcium oxide and carbon dioxide and a small amount of organic matter.

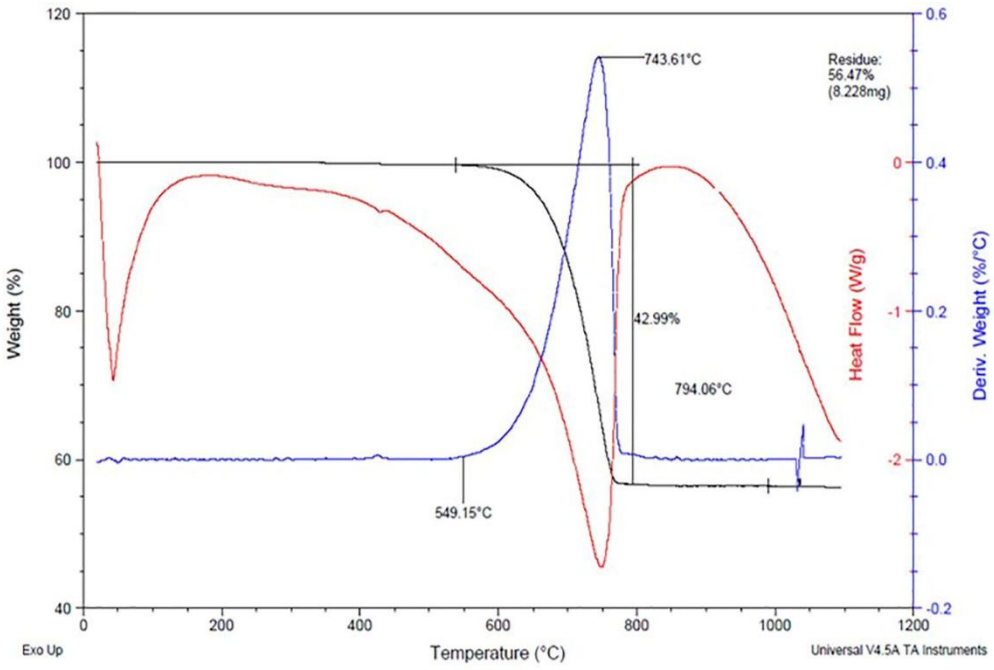

Figure 2.3 Thermal analysis of the coral powder

2.1.3.2 Physiochemical Analyses: X-Ray Diffraction Analysis (XRD)

Physical characterization of cleaned and calcined Porites coral skeleton before and after the hydrothermal treatment was carried out by XRD. *Figure 2.4* illustrates the comparison of the original cleaned coral skeleton prior to and after hydrothermal treatment. For the original Porites sp. coral, all major and minor peaks obtained were matched with aragonite (JCPDS Card 76–0606). On the other hand, as expected *Figure 2.4* shows that after the hydrothermal treatment all major and minor peaks clearly match HAp (JCPDS card no: 82-1943) calcium phosphate showing full conversion.

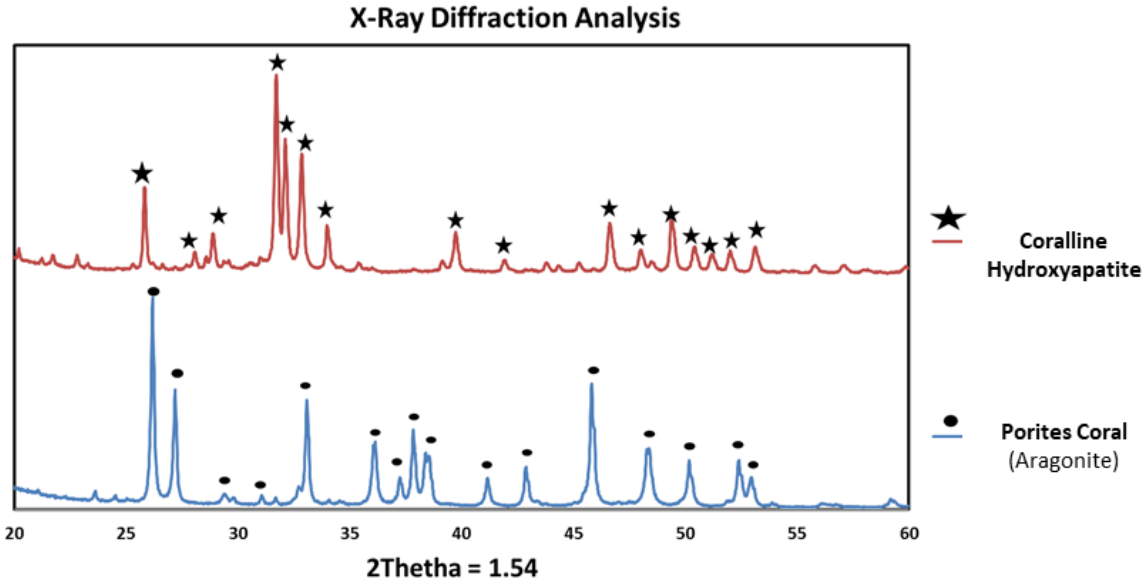

Figure 2.4 X-Ray diffractogram for cleaned-calcined pure coral and coralline HAp

According to XRD pattern, after the cleaning process, the coral sample is a fully aragonite form of $CaCO_3$. The XRD pattern of the hydrothermally converted coralline apatite contain only HAp peaks (the aragonite form of $CaCO_3$ is fully converted). However, in the past it was observed that some minor amounts of retained calcium carbonate might also exist within the structure.

2.1.3.3 Chemical Analyses: Fourier transform infrared spectroscopy (FT-IR) and Inductively coupled plasma-mass spectroscopy (ICP–MS) analysis

The FT-IR analysis presents mineral spectra of both the original cleaned Porites coral before and after the hydrothermal conversion to hydroxyapatite. FT-IR is used to detect the frequency of the vibrational motions in the functional groups of molecules at different wavelengths.

The spectrum of the coral sample before the conversion refers to calcium carbonate peaks (in *Figure 2.5 A*). According to *Figure 2.5 A*, aragonite is a major phase. The v4 in plane bending mode of the carbonate ion shows the characteristic doublet of aragonite at 699.9 cm^{-1} and 712.6 cm^{-1}. The v2 out of plane bending mode is seen at 854.6 cm^{-1} which is typical of aragonite, while the calcite v2 mode at 880 cm^{-1} is absent. The band at 1082.8 cm^{-1} is assigned to the v1(A'1) symmetric stretch of the carbonate ion. The v1 mode is infrared active in aragonite due to the site symmetry, but it is inactive in calcite. The broad asymmetric band at 1444.3 cm^{-1} is assigned to the v3 antisymmetric stretch

mode of carbonate in aragonite, and there is no peak evident at 1430 cm^{-1} due to the v3 mode in calcite.

The FT-IR spectra of the hydrothermally converted Porites coral powder are given in *Figure 2.5 B*. In *Figure 2.5 B*, the bands at 599.4 cm^{-1} and 561.5 cm^{-1} (medium intensity vibration bands of HAp) are attributed to v4 bend for phosphate bands (PO_4^{-3}), while the characteristic of broad and intensity band at 1023.3 cm^{-1} corresponds to v3 PO_4^{3-} antisymmetric stretching modes. Additionally, the band at 599.4 cm^{-1} refers to an asymmetric bending mode. The band of low intensity at 961.7 cm^{-1} is v1 PO_4^{-3} mode, proving that the substitution of PO_4 and OH groups in the structure of HAp occurred to HPO_4^{-2}. The bands which are located at 867.8 - 808.6 cm^{-1} (v3 modes) and 1448.3 cm^{-1} (v2 modes) correspond to v2 and v3 modes of the carbonate ion substituted for the phosphate in HAp (Berzina-Cimdina and Borodajenko, 2012). It is plausible that this substitution creates patches of minute amounts of carbonate apatite within the bulk hydroxyapatite. Carbonate apatite has been observed in previous hydrothermal conversions.

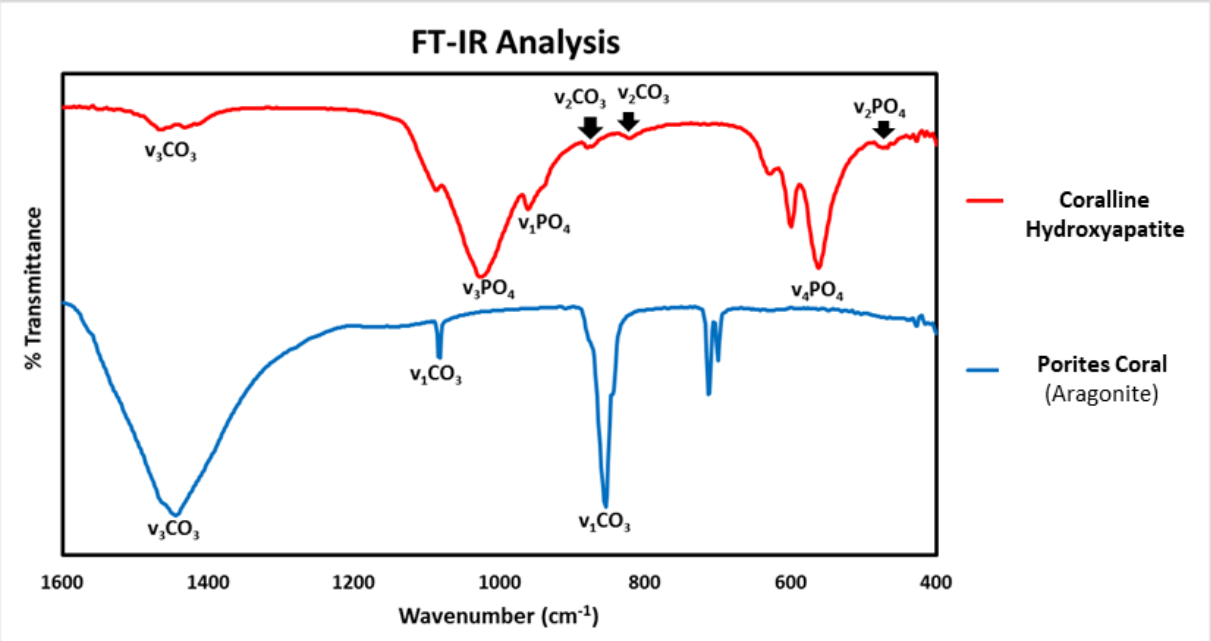

Figure 2.5 FT-IR spectra for cleaned-calcined hard coral (A) and coralline HAp (B), respectively

Although, XRD results show that HAp calcium phosphate was obtained after the hydrothermal process, after the conversion the FT-IR spectrum contains some minor CO_3^{-2}.

The CO_3^{-2} functional group can replace both PO_4^{-3} and OH^- in HAp structure. According to literature (Roy and Linnehan, 1974), there are type A and B substitutions of CO_3^{-2} in apatite. While Type-A is

the substitution at the OH^- site, Type-B is the substitution at the PO_4^{-3} site (Roy et al., 1974, Xu et al., 2001, Ivankovic et al., 2010). Small CO_3^{-2} peaks (see *Figure 2.5 B*) are also observed.

The CO_3^{-2} peaks at 867.8 cm^{-1}, 1448.3 cm^{-1} confirm that CO_3^{-2} group substitutes in the B-site of HAp structure. Therefore, B-type carbonated HAp is obtained after hydrothermal conversion of Porites coral confirming the previously published work (Roy and Linnehan, 1974, Xu et al., 2001, Ben-Nissan, 2003, Ivankovic et al., 2010).

The chemical composition of both coral and coralline hydroxyapatite particles was determined by ICP-MS analysis. The standards range was 1, 10, 100, 250, 500 and 1000 ppb. The results for Sr and Mg elements in the coralline HAp powder and cleaned calcined coral were given in *Figure 2.6 A*. The calibration curves (*Appendix A*) were obtained accurately. In order to apply ICP-MS, 0.5 mg cleaned calcined coral, and 0.5 mg coralline HAp samples and all standards were digested within 6% w/w nitric acid (HNO_3).

According to the ICP-MS results in *Figure 2.6 B*, the concentration of the Sr element was obtained as 579.7 ppb for coral powder and 507.3 ppb for coralline HAp, while the Mg element was obtained as 150.7 ppb for coral powder and 141.1 ppb for coralline HAp.

Additionally, concentration changes for Ca and PO_4 ions are observed in the structure of the coral skeleton before and after the hydrothermal conversion technique. Increase of PO_4 for the hydrothermally converted coral skeleton shows the conversion from $CaCO_3$ to CaP, which is HAp for this study. DeGroot *et al.* (1984) and Le Geros *et al.* (1995) reported that the Mg and Sr elements in the HAp structure are highly effective on the biological and mechanical properties of HAp for biomedical applications (de Groot, 1984, LeGeros et al., 1995). They also reported that both elements improved the osseointegration. The concentrations of the Mg and Sr elements are given in *Figure 2.6 A and B*.

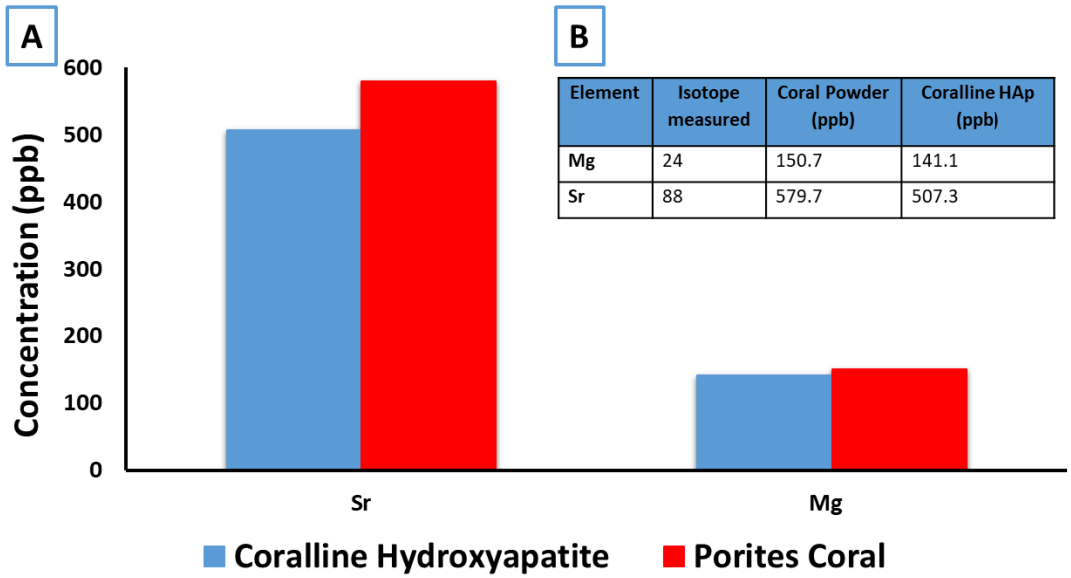

B

Element	Isotope measured	Coral Powder (ppb)	Coralline HAp (ppb)
Mg	24	150.7	141.1
Sr	88	579.7	507.3

Figure 2.6 The ICP-MS chemical composition analysis results show the Porites coral skeleton before and after hydrothermal conversion with a graph (A), and a table (B)

2.1.3.4 Scanning Electron Microscope Analysis (SEM-EDS)

The Porites coral morphology prior to and after the conversion process were investigated by a scanning electron microscope (SEM). The microstructure of cleaned coral investigated micro-, meso- and nano- pores, shown in *Figure 2.7* and *2.8*.

The interconnected macro and meso pores are highly applicable for bone growth and tissue engineering applications because the connection between the pores allows tissue growth and vascularization (Xu et al., 2001). These interconnected micropores are between the ranges of 160 to 400 µm which is appropriate for bone growth. Meso and nanopores assist better bonding, tissue-graft interaction and can be utilized for drug delivery purposes due to easy drug loading and encapsulation abilities.

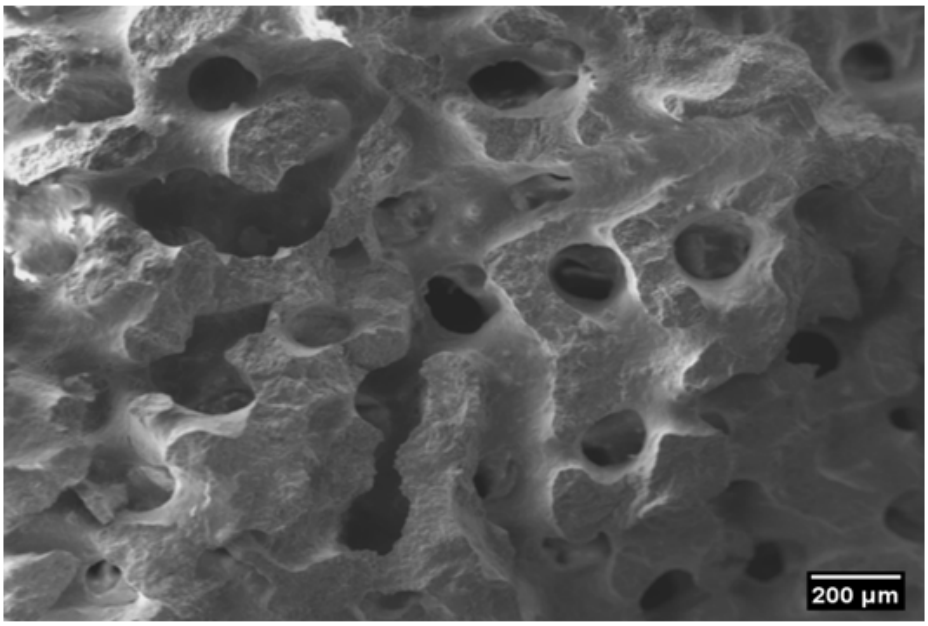

Figure 2.7 The Porites coral microstructure before the grinding process, showing the micropores for bone growth.

Energy dispersive X-Ray analysis (EDAX) of natural coral showed in addition to expected Ca and P peaks additional minor Mg, Sr and Na peaks.

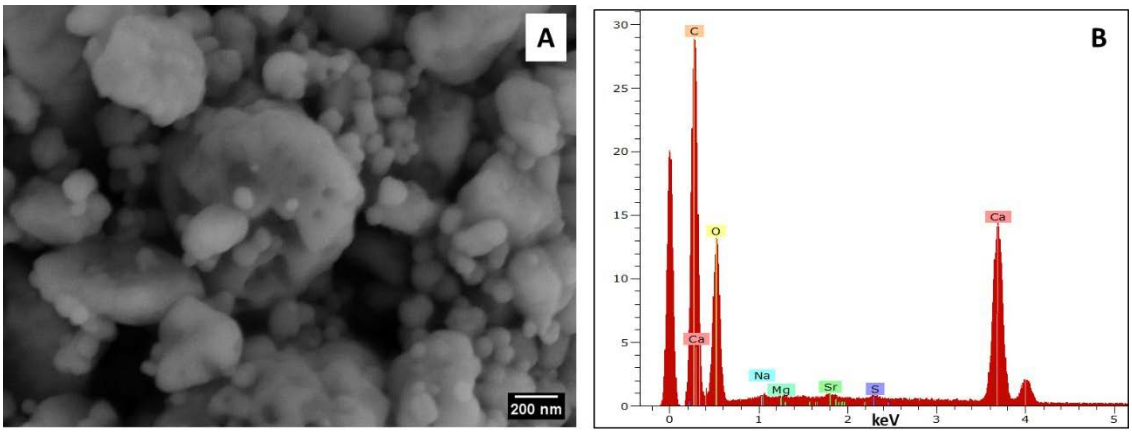

Figure 2.8 SEM (A) and EDAX (B) results of Porites coral particles after the ball milling process

Figure 2.8 clearly shows the ground coral structure, particle shape and sizes ranging from 10 to 30 nm spherical particles and some agglomerated large particles of 100 to 200 nm. Under SEM they showed only a small part of their distribution. It is dependent on the many factors including matrix mixture, the solution used, and the effect of further additional agitation and mixing.

Figure 2.9 shows that the hydrothermal conversion treatment changed the morphology of the coral. It was observed that the irregular size of spherical clusters of the original coral was converted by a dissolution and precipitation process into plate-like HAp particles, which are much finer than before conversion. The morphological changes of the coral after the conversion process aligns with the previous work by Macha *et al.* (2017) Their sizes were further determined with BET analysis (Macha et al., 2017).

It can be observed in *Figure 2.11* that there are some 10 nm and mainly a range of 20 to 50 nm size pores (*Table 2.1*) between the plate-like crystalline particles in converted coral which were confirmed by both SEM and the BET analyses which will be covered in the next section (Hu et al., 2001, Ben-Nissan et al., 2004, Green et al., 2017).

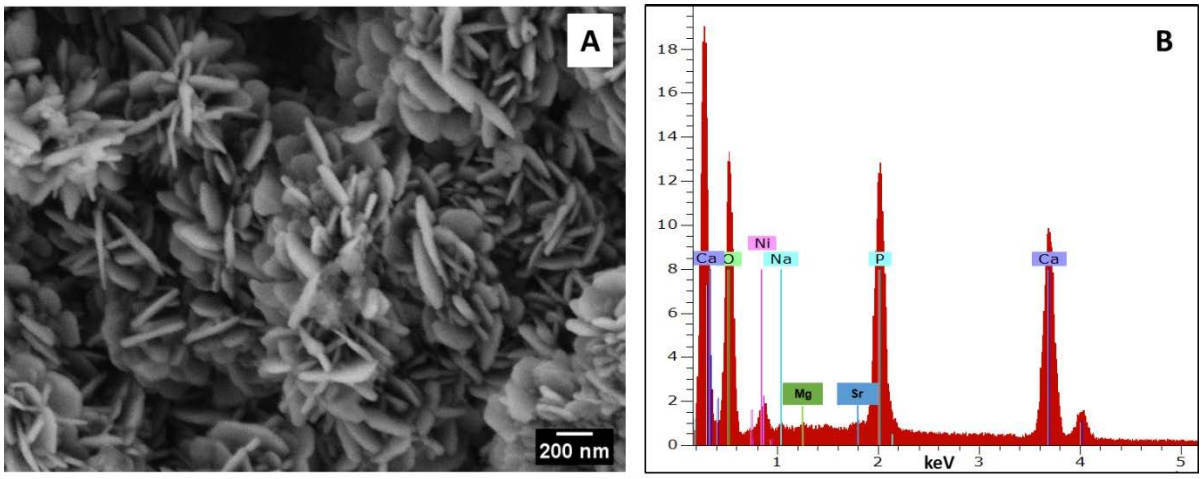

Figure 2.9 SEM (A) and EDAX (B) results of the crystalline structure of hydroxyapatite plates and related nano and meso pores of the coralline apatite after the hydrothermal conversion

2.1.3.5 Surface Area and Particle Size Analysis

The surface area and pore size distributions of HAp particles were carried out by a Brunauer-Emmett-Teller (BET) analyzer under nitrogen gas absorption at 77.3K. *Figure 2.10* gives nitrogen adsorption and desorption isotherms which can be classified as a type-IV isotherm loop. The type-IV class represents the material which has a mesoporous structure (Sing et al., 1985, Chen et al., 2011, Tan et al., 2012). This confirms our microstructural observations.

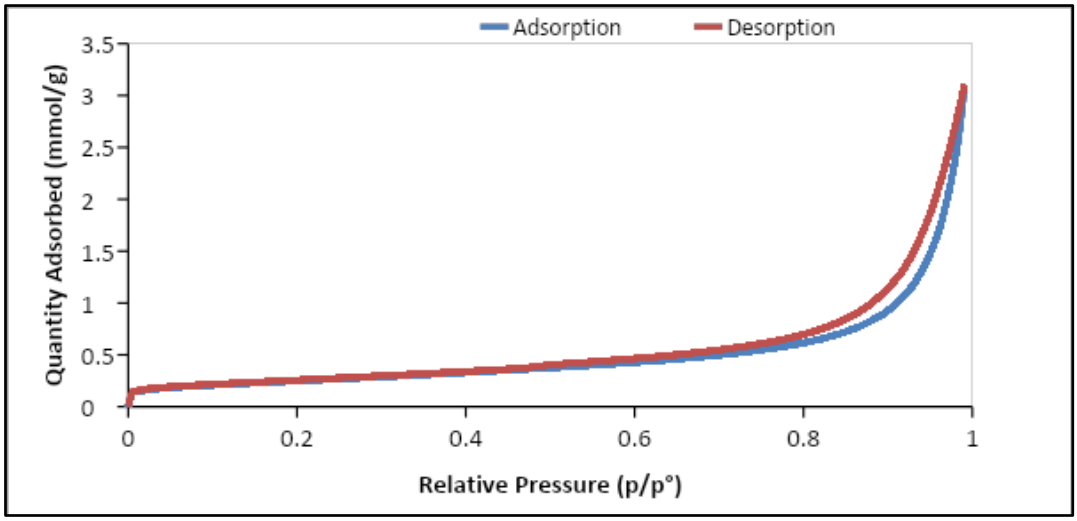

Figure 2.10 Nitrogen adsorption and desorption for coral based HAp powder

Figure 2.11 represents the corresponding Barrett-Joyner-Halenda (BJH) pore size distribution curves of the meso porous structure of HAp powder. The porosity analysis shows the range of pore sizes which is between 20 and 50 nm.

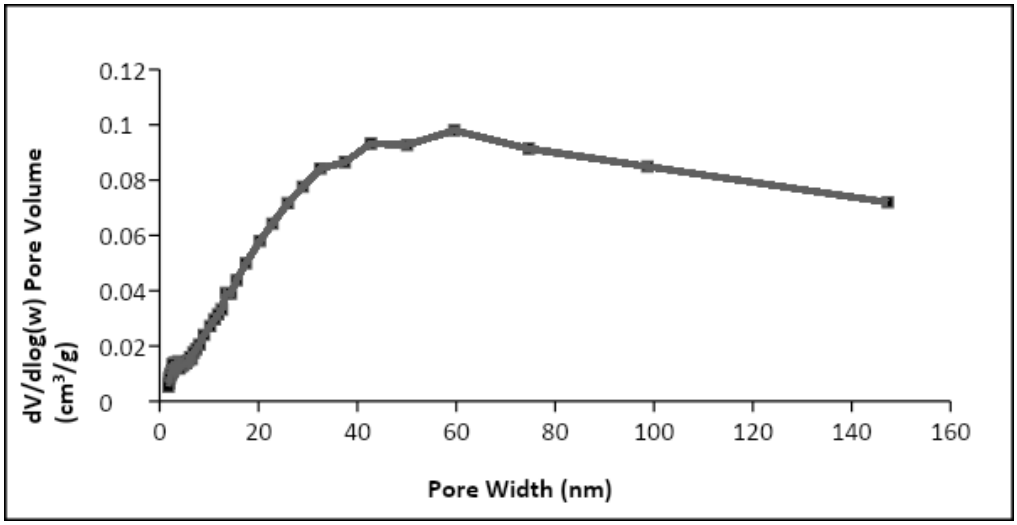

Figure 2.11 BHJ pore size distribution curve for the coral based HAp powder

According to *Table 2.1*, the BET surface area is ~20 m^2/g while average pore diameter (adsorption) is ~21 nm. The SEM results show particles 10 to 20 nm thick and platelets 100 to 300 nm long. In addition, some agglomeration in large sizes was observed which gave erroneous values for the average sizes in BET analysis (*Table 2.1*). In addition to BET, the particle sizes were observed under SEM and compared. There is a good agreement in the results between BET and SEM measurements

based on the particle size and some agglomeration. However, during further mixing and production processes these agglomerates dissociated.

Table 2.1 The particle size parameters for HAp particles

BET Surface Area	20.27 m^2/g
Adsorption average pore diameter (4V/A by BET)	21.26 nm
Average Particle Size	295.98 nm
Pore Size Distribution Range	20-50 nm

Pore size and interconnectivity play an important role in the structural integrity of bone scaffolds (Cunningham et al., 2010, Ben-Nissan and Green, 2013, González Ocampo et al., 2016). Cunningham et al. (2010) indicates that a pore size between 40-100 µm is ideal for osteoid growth (Cunningham et al., 2010). However, the well-established clinical work shows that for full vascularization pore sizes ranging from 100 to 500 µm is required (Cunningham et al., 2010, Ben-Nissan and Green, 2013, González Ocampo et al., 2016). In this current system, the meso and nano pores on the hydrothermally converted HAp particles are major advantages during drug loading and their dissolution for the slow and controlled drug delivery.

2.1.4 Conclusion

In structural characterization by XRD, FT-IR and SEM of the natural and cleaned coral showed an aragonite form of $CaCO_3$. ICP-MS analysis showed strontium and magnesium as trace elements. However, it does not contain any heavy metals or other impurities. Although the compositions are different, the amounts of Sr and Mg have not changed. On the other hand, particle size analysis showed differing results before and after conversion. After the grinding and conversion process, the coral had a unique meso and macro porous structure and pores were both on the surfaces and within the bulk of the particles. Their sizes and surface areas were also different after the conversion.

After the grinding process, the powder obtained contained approximately 10 nm size particles. On the other hand, coralline HAp particles showed some agglomeration and the particle size range was around 200 to 400 nm. However, 100 nm range particles were also detected in both SEM and BET analysis. Pores were interconnected and 20 to 50 nm range.

The coral was successfully converted hydrothermally to HAp particles in the presence of an ammonium phosphate solution at 220 ˚C and 4 MPa pressure. Major Hydroxyapatite peaks and some very minor $CaCO_3$ peaks were observed with XRD, and FT-IR analysis. The CO_3^{-2} peaks at 867.8 cm^{-1}, 1448.3 cm^{-1} confirm that CO_3^{-2} group substitutes in the B-site of HAp structure.

It was concluded that the HAp – which was synthesized from a natural biogenic material – has a high potential in drug delivery systems because of the unique chemistry, porous structure and biocompatibility.

In the next part of this chapter, specific drug loading techniques and related characterizations are covered.

2.2 Drug Loading Study and Physio-Chemical Characterizations of Drug Loaded Coralline Hydroxyapatite with Medical Grade Drugs

2.2.1 Introduction

Drug delivery systems (DDS) are designed to target different pharmaceuticals to specific local areas within the human body. The systems are directed to control the drug release rates and the pattern. The advantages of using local controlled drug delivery systems instead of current systemic delivery systems such as injection or by oral consumable tablets are many. The most important advantage is the control of drug release rates in a specific targeted area that reduces possible drug-related systemic adverse effects to other organs and minimizing sudden undue drug concentration for the treatment (Ben-Nissan and Green, 2013, Santos et al., 2014).

Additionally, local and controlled DDS can be used to prolong the therapeutic effect of the compounds such as bone morphogenic proteins, growth factors, anti-cancer and immunodepression drugs and antibiotics. Therefore, local controlled DDS improve drug efficacy and efficiency and provide significant cost savings for the health care system (Ben-Nissan and Green, 2013, Choi et al., 2014, Choi and Ben-Nissan, 2017).

DDS covers multiple disciplinary areas, which include pharmaceutical, biomaterial, medical and chemical engineering. This interdisciplinary approach and understanding of the function of each component of the system are the key points to obtaining successful and medically applicable DDS designs. Therefore, the performance of the system depends on many chemical, biological and material-based factors which are related to properties of the compounds used. This includes factors such as the solubility and degradation rates of the constituent pharmaceutical substances in a specific biologic environment (Ginebra et al., 2012, Naahidi et al., 2012, Macha et al., 2015c).

Although the design and development of new and novel drug delivery systems for various treatments, especially for osteomyelitis have been in very high demand, there are several challenges for most efficient designs of DDS which are controlled by the release rates and a steady-state long term delivery of drugs and control of the concentration (Macha et al., 2018).

In order to improve the steady drug release, calcium phosphate (CaP) based porous bioceramics have been proposed as drug carriers and have shown advantages because of their critical pore size and interconnectivity, providing the required controlled delivery rates and dispersion (Chou et al., 2013, Choi et al., 2014, Macha et al., 2015c).

Marine materials such as coral skeleton derived porous hydroxyapatites present better promises for the DDS applications because of their nano to micro porous structure which improves the capacity of drug incorporation and provides easily controllable drug dissolution rates (Ben-Nissan and Green, 2013). HAp particles provide several advantages due to its chemistry and ability to interact with the bone tissues as a bioactive material. Therefore, they provide the controlled release local drug delivery with increased drug efficacy (Loca et al., 2015).

During the last decade the design of different types of drug delivery systems have been proposed for the treatment of many diseases. For instance, using coral derived HAp particles for antibiotic delivery systems provides dual effects: stimulating bone growth and osseointegration, and preventing surgery related infections or bone (Chou et al., 2013, Macha et al., 2015c).

Another advantage of using HAp as a drug carrier instead of other synthetic materials is the non-toxic feature of its biodegradation products and its biocompatibility (Ben-Nissan et al., 2016).

The drug loading method is very critical in determining dissolution rates and interactions with the biologic environment. There are different techniques such as adsorption, chemical linking or physical and mechanical methods for the incorporation of drugs to HAp materials (Bose and Tarafder, 2012, Kolmas et al., 2016).

The drug loading techniques for hydrothermally converted materials can be classified according to the loading sequence prior to and after the conversion method. For example, in bone cement applications homogenous distribution of the drug is obtained by dissolving it into a liquid phase, then incorporating it with the second solid phase of the bone cement (Ginebra et al., 2012).

In another technique, drugs can be loaded as droplets into the solid material or pieces, or powders can be immersed into the appropriate drug solution. The advantage of this technique is maintaining the microstructure of the original materials (Ginebra et al., 2012).

In this project, one of the aims was to load an antibiotic commonly used in orthopedic surgery namely gentamicin (Gm). The drug carrier was hydrothermally converted coralline hydroxyapatite (HAp) powder and their nano and meso pores of these were loaded with Gm to avoid surgery related infections and possible treatment for osteomyelitis.

As stated above, Gm is one of the most popular antibiotics for the treatment of bone infections and surgery related bacterial infections in both maxillofacial and orthopedic surgery. It belongs to the aminoglycoside group. Although it is one of the broad-spectrum antibiotics and is mostly used for the treatment of gram-negative bacteria related infections, it has been found that a high concentration of gentamicin has a toxic effect on the human body (Ben-Nissan et al., 2016, Varghese et al., 2017). It also causes toxicity and specifically nephrotoxicity when applied at a high dosage. For these reasons, the gentamicin antibiotic contained drug delivery system designed must be a local release system and possibly directed at a targeted area. Its release rate must also be controlled to avoid these long term side effects (Kolmas et al., 2016, Choi and Ben-Nissan, 2017, Varghese et al., 2017).

Gm loaded HAp micro or nano-spheres and a biodegradable matrix drug delivery system can be coated on implantable medical devices in order to prevent surgery related infections. The following section covers this new production method.

2.2.2. Experimental Methods

In this section, previously explained converted HAp particles were loaded with Gm using Rotavapor than incorporated into a biodegradable polymer PLA matrix to be coated on to several metallic materials using the dip coating method.

2.2.2.1 Drug loading Method

Rotary evaporator with a vacuum controller (laborota 4000, with v-700 vocuum pump, John Morris Scientific, USA) was the device for the drug loading process. Gentamicin Sulphate (Sigma Aldrich)

was dissolved in ultrapure 18 MΩ (MilliQ, Millipore, Victoria, Australia) water. This gentamicin solution was mixed with HAp powder (which is not soluble in water), and this mixture was ultrasonicated for 5 min before the mixture was placed in a glass flask at Rotary evaporator. The water bath temperature was set at 60 °C, and a vacuum was applied at 72Mbar. The glass flask which contained the Gm solution-HAp powder mixture was placed into the water bath and rotated at 100rpm until all the water in the flask evaporated. The Gm loaded HAp powder (HAp-Gm) produced with this method was kept in a vacuum desiccator overnight to remove all of the retained moisture. The steps of this procedure are illustrated in *Figure 2.12*.

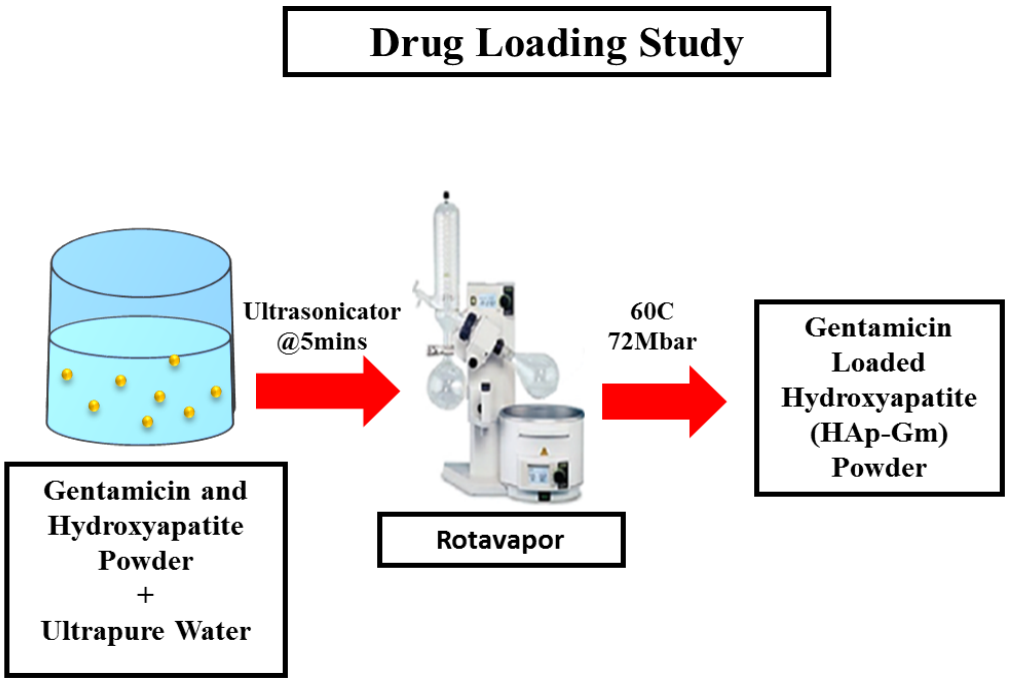

Figure 2.12 Diagram of drug loading procedure

In order to determine the effect of different amounts of Gm, a protocol was prepared that included different amounts of solutions containing Gm. Several Gm amounts prepared were: 5%, 10%, 15%, 20% and 30% Gm. The Gm amounts were calculated according to the weight of total HAp powders after the drug loaded process. The calculated Gm amounts were given in *Table 2.2* for 1g HAp powders.

Table 2.2 Calculated Gm amounts for 1 g HAp powder to produce 5%, 10%, 15%, 20% and 30% HAp-Gm powders with the drug loading technique

HAp-Gm (w_{HAp}/w_{Gm})	**5%**	**10%**	**15%**	**20%**	**30%**
Gm (g) for 1g HAp	0.05	0.1	0.15	0.2	0.3

2.2.2.2 Drug Encapsulation Efficiency (DEE)

Drug encapsulation efficiency (DEE, %) was calculated for Gm loaded HAp particles by soaking 1mg HAp-Gm powders into a 1ml 0.1M phosphate buffered saline (PBS) solution. The PBS solution was prepared by dissolving PBS tablets (Astral Scientific; [0.14 M NaCl, 0.0027M KCl, 0.01M Phosphate buffer, pH 7.4]) in ultrapure MilliQ water at room temperature, the PBS solution was then sterilized by the autoclave.

The HAp-Gm particles and PBS solution mixture was placed into an ultrasonic water bath for 5min to dissolve the Gm into HAp-Gm particles completely. Excess HAp particles were centrifuged for 5min. 1ml volume from the supernatant was used to measure the Gm content with UV-Vis Spectroscopy (Agilent Technologies, Victoria, Australia, Cary Series UV-Vis Spectrophotometer). The Gm concentrations in the PBS solution were measured by the absorbance of gentamicin-o-phthaldialdehyde complex at λ_{max} =332 nm by using procedures described by (Aviv et al., 2007), and (Chou et al., 2014).

2.5g of the O- phthaldialdehyde reagent was prepared by dissolving in 62.5ml methanol and by further adding 3ml of 2-hydroxyethylmercaptan to 560ml, of 0.04M sodium borate in ultrapure MilliQ water. Further, 1ml of previously prepared supernatant Gm-PBS solution, 1ml O-phthaldialdehyde reagent and 1ml Isopropanol were mixed and incubated for 30 minutes at room temperature. O-phthaldialdehde and gentamicin reacted with each other and a complex molecule was formed which then could be easily detectable at a 332 nm wavelength.

In order to convert the absorbance values of Gm in PBS solution to the concentration values, the standard curve was prepared with six different Gm-PBS solutions which have known Gm concentrations (0.250, 0.125, 0.062, 0.031, 0.016 mg/ml) in a PBS solution. The absorbance values of six different Gm-PBS solutions were measured as described above, then an absorbance versus concentration graph was plotted to obtain the unknown Gm concentrations.

2.2.2.3 Analysis of HAp-Gm particles

The microstructure of the particles was determined by SEM (ZEISS Supra SSVP, Zeiss, Germany) in order to obtain the morphology of Gm loaded HAp powders with different concentrations of Gm (%, 10%, 15%, 20%, 30%Gm).

All samples were fixed on carbon stubs by a conductive adhesive tape. They were kept under vacuum overnight to extract all retained moisture. They were then coated with a 7nm thin layer of Au-Pd using a sputter coater (Leica EM ACE600 Sputtering and Carbon Thread Coater, Germany). Images were taken at various magnifications at an acceleration voltage of 15kV. Energy Dispersive X-Ray Analysis (EDAX) was also used to determine the semi-quantitative chemical composition of HAp-Gm powder.

The specific surface area of Porites coral, coralline HAp, and 5% HAp-Gm particles were measured with a Tristar II apparatus from Micromeritics (AutoPore III, Micromeritics Instrument Inc., Norcross, GA, USA) to identify the effects of the hydrothermal and the drug loading processes on the surface area of the Porites coral. Samples were initially degassed under vacuum at 77.3 K before analysis.

2.2.3 Results and Discussions

A scanning electron microscope was used to confirm the distribution of Gm particles and the coating on HAp particles. Additionally, SEM analysis also supplied their distribution and the nature of Gm loading as a function of Gm percentages.

Figure 2.13 shows the Gm particles before the loading process and after immersion into the dissolved Gm at 5%, 10%, 15%, 20% and 30% Gm. As received the original Gm particles are perfectly spherical and relatively large sized particles ranging between 10-50 µm. However, during the mixing, after ultra-pure water addition and strong agitation, the Gm particles broke down to smaller sizes and dissolved. Preceding studies in SEM showed that they coated the HAp particles efficiently and homogenously (*Figure 2.13*).

The coating efficiency of Gm is seen more clearly when the Gm ratio is increased. For example, while some plate-like HAp particles were observed on the surface of 5% HAp-Gm, in larger percentages such as 30% Gm the HAp particles have relatively smoother and thicker Gm coating. However, some large agglomerated clusters were also observed.

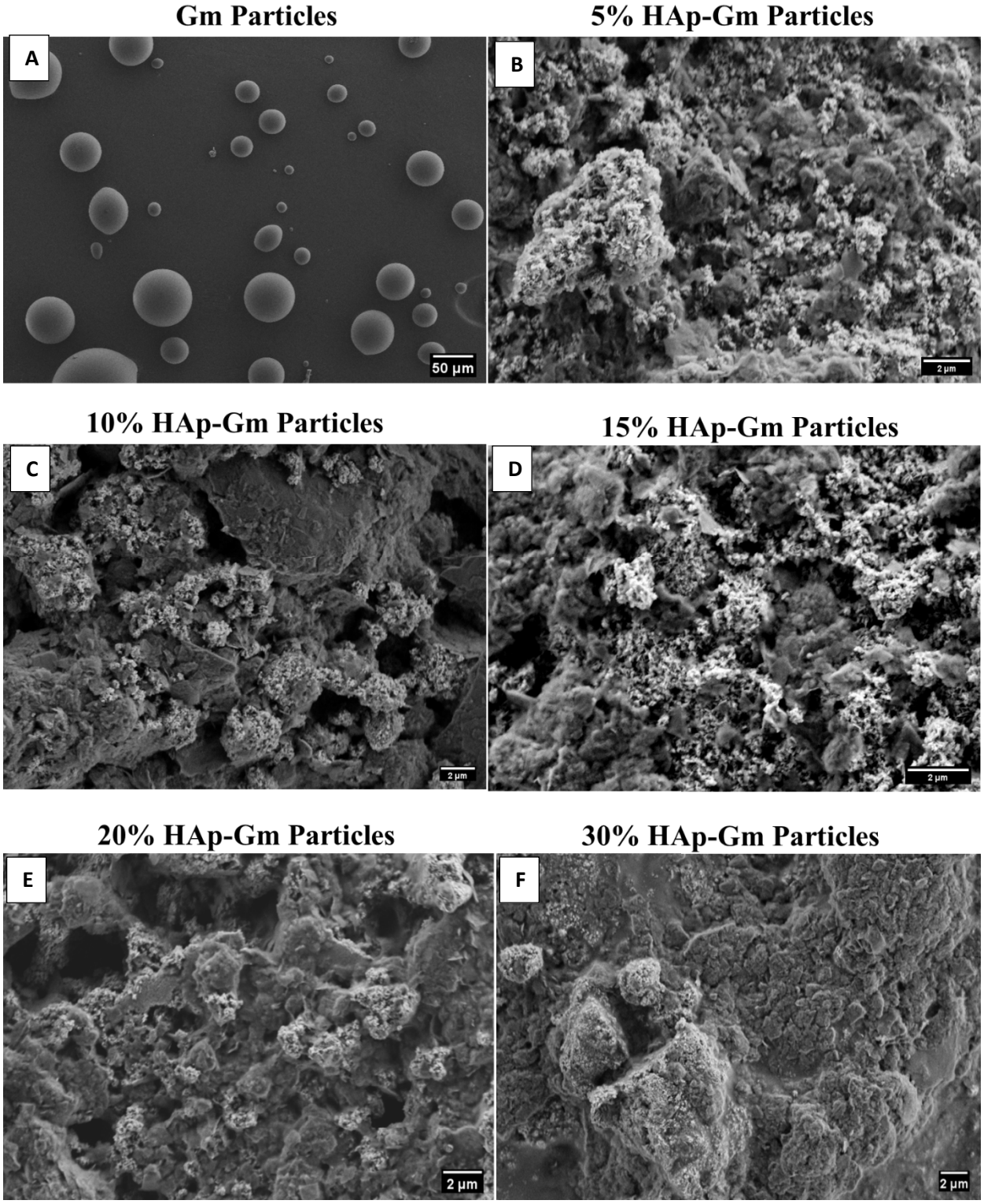

Figure 2.13 Gm particles (A) before drug loading process, and 5% (B), 10% (C), 15% (D), 20% (E), 30% (F) Gm loaded HAp particles after drug loading process, respectively

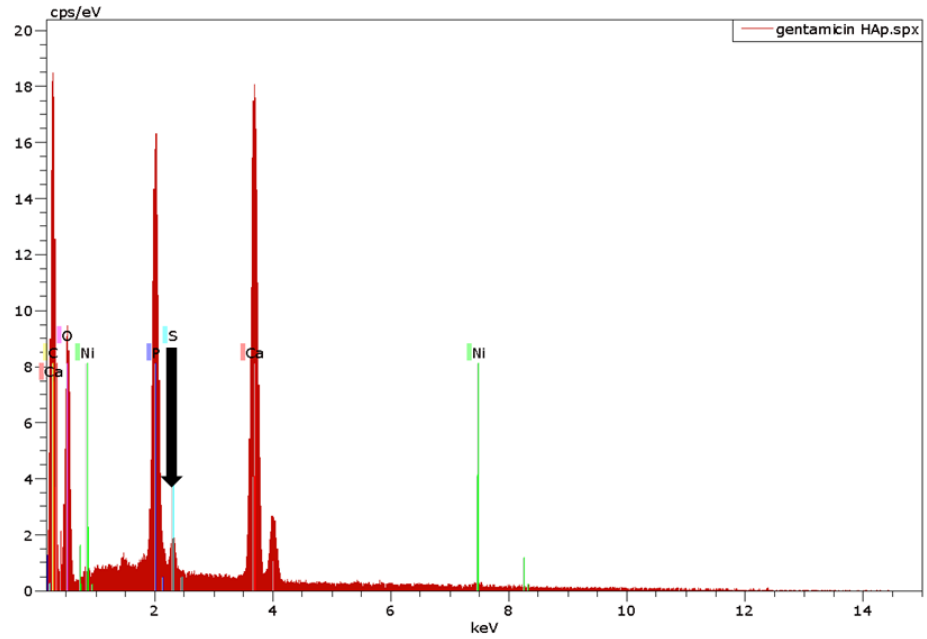

Figure 2.14 EDAX spectrum for the HAp-Gm particles showing S peaks for Gm

Figure 2.14 represents the EDAX spectrum for HAp-Gm powder. It has sulphate peaks due to the Gentamicin Sulphate, different from the HAp spectrum which was given in *Figure 2.9*.

The surface area parameters which were measured by the Tristar II apparatus from Micromeritics for Porites coral, HAp and 5% HAp-Gm particles were given in *Table 2.3*. While the surface area of the Porites coral particle was measured at 0.78 m^2/g, the surface area of HAp was found to be 18.93 m^2/g. The surface area of the coral depends on coral age and morphology such as the meso and nano porous structure of the coral particle.

There are several factors for observing the surface area increase after the hydrothermal conversion. These are: the cleaning efficiency of the coral before the conversion, and the hydrothermal conversion process. Therefore, the pores of the Porites coral were not open; hence it has less surface area than HAp. Due to the treatments, the meso and nano pores of HAp were opened; hence its surface area increased.

On the other hand, after the 5% Gm drug loading process, the surface area of 5% HAp-Gm particles, which is 8.79 m^2/g, was less than the surface area of the HAp particles, but it was higher than the Porites coral's surface area. Therefore, the meso and nano pores of HAp particles were partially filled with Gm due to the drug loading process. The surface area might be affected according to the Gm concentration.

Table 2.3 The particle surface area parameters for Porites coral, HAp and 5% HAp-Gm particles

	Porites coral	**HAp**	**5% HAp-Gm**
BET surface area	0.78 m^2/g	18.93 m^2/g	8.79 m^2/g

Drug Encapsulation Efficiency (DEE) was calculated by the percentages of the Gm concentrations in the PBS solution, and the measured Gm concentrations in the PBS solution with UV-Vis spectroscopy. The results are given in *Table 2.4*.

While the absorbance values of Gm from HAp-Gm samples in the PBS solution were obtained from UV-Vis spectroscopy at 332nm, the absorbance values were further converted to the concentration values (mg/ml) by using a standard curve, given in *Figure 2.15*. When theoretically calculated results and measured values are compared, the rate of DEE was nearly 100% for all HAp-Gm samples.

Table 2.4 It illustrates calculated vs UV-Vis measured Gm concentrations for 5 different HAp-Gm samples which have 5% to 30% Gm contents

SAMPLES	**5% HAp-Gm**	**10% HAp-Gm**	**15% HAp-Gm**	**20% HAp-Gm**	**30% HAp-Gm**
In 1mg/ml (calculated)	0.05mg	0.1mg	0.15mg	0.2mg	0.3mg
UV-Vis Results	0.067mg	0.097mg	0.163mg	0.206mg	0.293mg

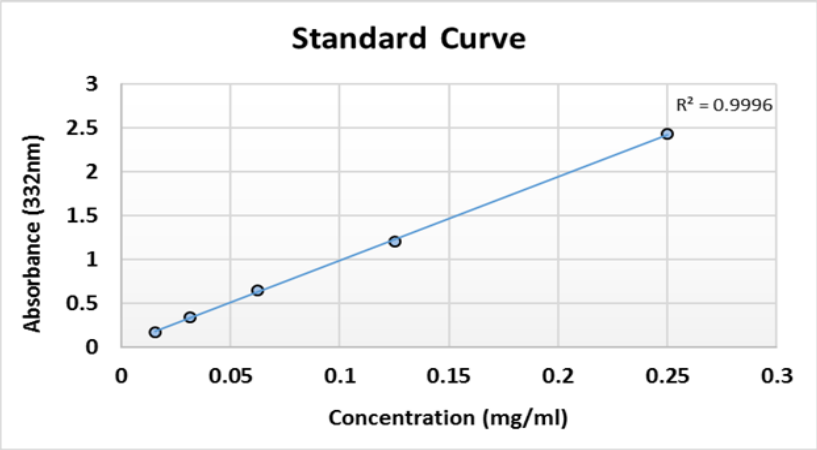

Figure 2.15 Standard curve for the conversion of absorbance measurement values of HAp-Gm samples by UV-Vis spectroscopy to concentration values

2.2.4 Conclusion

In the second part of this chapter, hydrothermally converted coral particles were loaded with Gm antibiotics at different ratios ranging from 5%, 10%, 15%, 20% and 30% (w/w). The drug encapsulation efficiency percentage of 5% to 30% Gm contained HAp-Gm particles was 100%. It was confirmed that hydrothermally converted coral based HAp particles have surface topography that includes a nano and meso interconnected porous structure and provides adequate space to obtain the highest capacity for drug incorporation.

During SEM studies, it was observed that the Gm solution coats the coralline HAp particles homogeneously and it fills the nano and meso pores efficiently. On the other hand, the drug loading process during the mixing causes some agglomeration of the HAp particles which was observed on the surfaces during SEM studies. Thus, agglomeration and the size of the particles increased at higher Gm concentrations.

In summary, Gm drug loading into HAp particles was carried out successfully for slow drug delivery multifunctional antimicrobial coating design.

The HAp-Gm particles prepared are possibly one of the most important components in a multifunctional coating to control local and slow drug release to the targeted area of the human body to prevent or treat implant related infections. In order to achieve this combination of HAp-Gm particles with Poly Lactic Acid (PLA), a biodegradable polymeric matrix composite and a functional coating technique was developed, applied to Ti-Al-V alloy metallic bone implants and tested. This will be covered in the next few chapters.

2.3 References

AVIV, M., BERDICEVSKY, I. & ZILBERMAN, M. 2007. Gentamicin-loaded bioresorbable films for prevention of bacterial infections associated with orthopedic implants. *J Biomed Mater Res A,* 83**,** 10-9.

BEN-NISSAN, B. 2003. Natural bioceramics: from coral to bone and beyond. *Current Opinion in Solid State and Materials Science,* 7**,** 283-288.

BEN-NISSAN, B. & GREEN, D. W. 2013. Marine materials in drug delivery and tissue engineering: from natural role models to bone regeneration and repair and slow delivery of therapeutic drugs, proteins, and genes. *In:* KIM, S. K. (ed.) *Marine biomaterials: Characterization, isolation and applications.* CRC Press.

BEN-NISSAN, B., MACHA, I., CAZALBOU, S. & CHOI, A. H. 2016. Calcium phosphate nanocoatings and nanocomposites, part 2: thin films for slow drug delivery and osteomyelitis. *Nanomedicine (Lond),* 11**,** 531-44.

BEN-NISSAN, B., MILEV, A. & VAGO, R. 2004. Morphology of sol-gel derived nano-coated coralline hydroxyapatite. *Biomaterials,* 25**,** 4971-5.

BERZINA-CIMDINA, L. & BORODAJENKO, N. 2012. Research of Calcium Phosphates Using Fourier Transform Infrared Spectroscopy. *In:* THEOPHANIDES, T. (ed.) *Infrared Spectroscopy - Materials Science, Engineering and Technology.* IntechOpen.

BOSE, S. & TARAFDER, S. 2012. Calcium phosphate ceramic systems in growth factor and drug delivery for bone tissue engineering: a review. *Acta Biomater,* 8**,** 1401-21.

CASTIGLIONI, S., CAZZANIGA, A., ALBISETTI, W. & MAIER, J. A. M. 2013. Magnesium and osteoporosis: current state of knowledge and future research directions. *Nutrients,* 5**,** 3022-3033.

CEGLA, R. N. R., MACHA, I. J., BEN-NISSAN, B., GROSSIN, D., HENESS, G. & CHUNG, R. J. 2014. Comparative study of conversion of coral with ammonium dihydrogen phosphate and orthophosphoric acid to produce calcium phosphates. *Journal of the Australian Ceramic Society,* 50**,** 154-161.

CHEN, F., ZHU, Y.-J., ZHANG, K.-H., WU, J., WANG, K.-W., TANG, Q.-L. & MO, X.-M. 2011. Europium-doped amorphous calcium phosphate porous nanospheres: preparation and application as luminescent drug carriers. *Nanoscale Research Letters,* 6**,** 67.

CHOI, A. H. & BEN-NISSAN, B. 2017. Calcium Phosphate Nanocomposites for Biomedical and Dental Applications: Recent Developments. *In:* THAKUR, V. K., THAKUR, M. K. & KESSLER, M. R. (eds.) *Handbook of Composites from Renewable Materials.* Scrivener Publishing LLC.

CHOI, A. H., BEN-NISSAN, B., CONWAY, R. C. & MACHA, I. J. 2014. Advances in Calcium Phosphate Nanocoatings and Nanocomposites. *In:* BEN-NISSAN, B. (ed.) *Advances in Calcium Phosphate Biomaterials.* Berlin, Heidelberg: Springer Berlin Heidelberg.

CHOI, G., KARACAN, I., CAZALBOU, S., EVANS, L., SINUTOK, S. & BEN-NISSAN, B. 2017. Conversion of calcified algae (Halimeda sp) and hard coral (Porites sp) to Hydroxyapatite. *Key Engineering Materials,* 758**,** 157-161.

CHOU, J., AUSTIN, C., DOBLE, P., BEN-NISSAN, B. & MILTHORPE, B. 2014. Trace elemental imaging of coralline hydroxyapatite by laser-ablation inductively coupled plasma-mass spectroscopy. J Tissue Eng Regen Med, 8, 515-20.

CHOU, J., BEN-NISSAN, B., CHOI, A., WUHRER, R. & GREEN, D. 2007. Conversion of coral sand to calcium phosphate for biomedical application. *Journal of the Australian Ceramic Society,* 43, 44-48.

CHOU, J., ITO, T., BISHOP, D., OTSUKA, M., BEN-NISSAN, B. & MILTHORPE, B. 2013. Controlled Release of Simvastatin from Biomimetic β-TCP Drug Delivery System. *PLOS ONE,* 8**,** e54676.

CHOU, J., VALENZUELA, S., GREEN, D. W., KOHAN, L., MILTHORPE, B., OTSUKA, M. & BEN-NISSAN, B. 2014. Antibiotic delivery potential of nano- and micro-porous marine structure-derived beta-tricalcium phosphate spheres for medical applications. *Nanomedicine (Lond),* 9**,** 1131-9.

CUNNINGHAM, E., DUNNE, N., WALKER, G., MAGGS, C., WILCOX, R. & BUCHANAN, F. 2010. Hydroxyapatite bone substitutes developed via replication of natural marine sponges. *Journal of Materials Science: Materials in Medicine,* 21**,** 2255-2261.

DAMIEN, E. & REVELL, P. A. 2004. Coralline hydroxyapatite bone graft substitute: A review of experimental studies and biomedical applications. *J Appl Biomater Biomech,* 2**,** 65-73.

DE GROOT, K. 1984. Calcium Phosphate Bioceramics. *In:* PAUL, J. P., GAYLOR, J. D. S., COURTNEY, J. M. & GILCHRIST, T. (eds.) *Biomaterials in Artificial Organs: Proceedings of a seminar on biomaterials held at the University of Strathclyde, Glasgow in September 1983.* London: Palgrave Macmillan UK.

FATHI, M. H. & HANIFI, A. 2007. Evaluation and characterization of nanostructure hydroxyapatite powder prepared by simple sol–gel method. *Materials Letters,* 61**,** 3978-3983.

FENG, S. & XU, R. 2001. New Materials in Hydrothermal Synthesis. *Accounts of Chemical Research,* 34**,** 239-247.

GHIASI, B., SEFIDBAKHT, Y. & REZAEI, M. 2019. Hydroxyapatite for Biomedicine and Drug Delivery. *In:* RAHMANDOUST, M. & AYATOLLAHI, M. R. (eds.) *Nanomaterials for Advanced Biological Applications.* Cham: Springer International Publishing.

GINEBRA, M. P., CANAL, C., ESPANOL, M., PASTORINO, D. & MONTUFAR, E. B. 2012. Calcium phosphate cements as drug delivery materials. *Adv Drug Deliv Rev,* 64**,** 1090-110.

GONZÁLEZ OCAMPO, J. I., ESCOBAR SIERRA, D. M. & OSSA OROZCO, C. P. 2016. Porous bodies of hydroxyapatite produced by a combination of the gel-casting and polymer sponge methods. *Journal of Advanced Research,* 7**,** 297-304.

GREEN, D. W., BEN-NISSAN, B., YOON, K. S., MILTHORPE, B. & JUNG, H.-S. 2017. Natural and Synthetic Coral Biomineralization for Human Bone Revitalization. *Trends in Biotechnology,* 35**,** 43-54.

HAVALDA, R., PILLI, S. C. & PUTTI, B. B. 2013. Effects of Magnesium on Mechanical Properties of Human Bone. *IOSR Journal of Pharmacy and Biological Sciences,* 7**,** 08-14.

HENESS, G. L. & BEN-NISSAN, B. 2004. Innovative Bioceramics. *Materials Forum,* 27**,** 104-114.

HU, J., RUSSELL, J., BEN-NISSAN, B. & VAGO, R. 2001. Production and Analysis of Hydroxyapatite From Australian Corals via Hydrothermal Process. *Journal of Materials Science Letters,* 20**,** 85-87.

IGE, O. O., UMORU, L. E. & ARIBO, S. 2012. Natural Products: A Minefield of Biomaterials. *ISRN Materials Science,* 2012**,** 983062.

IVANKOVIC, H., TKALCEC, E., ORLIC, S., GALLEGO FERRER, G. & SCHAUPERL, Z. 2010. Hydroxyapatite formation from cuttlefish bones: kinetics. *Journal of Materials Science: Materials in Medicine,* 21**,** 2711-2722.

KARACAN, I., BEN-NISSAN, B. & SINUTOK, S. 2019. Marine-Based Calcium Phosphates from Hard Coral and Calcified Algae for Biomedical Applications. In: CHOI, A. H. & BEN-NISSAN, B. (eds.) *Marine-Derived Biomaterials for Tissue Engineering Applications. Singapore: Springer.*

KARACAN, I., SENTURK, D., OKTAR, F. N., FICAI, A., FICAI, D., TRUSCA, R., VASILE, B. S., GOKCE, H., OZUYAR, H. D. & GUNDUZ, O. 2016. Structural and characterisation analysis of zinc-substituted hydroxyapatite with wet chemical precipitation method. 6**,** 188-204.

KOLMAS, J., KRUKOWSKI, S., LASKUS, A. & JURKITEWICZ, M. J. C. I. 2016. Synthetic hydroxyapatite in pharmaceutical applications. 42**,** 2472-2487.

LEGEROS, R. Z., KIJKOWSKA, R., BAUTISTA, C. & LEGEROS, J. P. 1995. Synergistic effects of magnesium and carbonate on properties of biological and synthetic apatites. *Connect Tissue Res,* 33**,** 203-9.

LEGEROS, R. Z., TRAUTZ, O. R., LEGEROS, J. P., KLEIN, E. & SHIRRA, W. P. 1967. Apatite crystallites: effects of carbonate on morphology. *Science,* 155**,** 1409-11.

LI, S., ZHANG, G., ZHENG, H., ZHENG, Y. & WANG, P. 2017. Stability of BiFeO3 nanoparticles via microwave-assisted hydrothermal synthesis in Fenton-like process. *Environ Sci Pollut Res Int,* 24**,** 24400-24408.

LIU, D. M., TROCZYNSKI, T. & TSENG, W. J. 2001. Water-based sol-gel synthesis of hydroxyapatite: process development. *Biomaterials,* 22**,** 1721-30.

LIU, H. S., CHIN, T. S., LAI, L. S., CHIU, S. Y., CHUNG, K. H., CHANG, C. S. & LUI, M. T. 1997. Hydroxyapatite synthesized by a simplified hydrothermal method. *Ceramics International,* 23**,** 19-25.

LOCA, D., LOCS, J., DUBNIKA, A., ZALITE, V. & BERZINA-CIMDINA, L. 2015. 9 - Porous hydroxyapatite for drug delivery. *In:* MUCALO, M. (ed.) *Hydroxyapatite (Hap) for Biomedical Applications.* Woodhead Publishing.

LOO, S. C. J., SIEW, Y. E., HO, S., BOEY, F. Y. C. & MA, J. 2008. Synthesis and hydrothermal treatment of nanostructured hydroxyapatite of controllable sizes. *Journal of Materials Science: Materials in Medicine,* 19**,** 1389-1397.

MACHA, I., BOONYANG, U., CAZALBOU, S., BEN-NISSAN, B., CHARVILLAT, C., OKTAR, F. & GROSSIN, D. 2015a. Comparative study of Coral Conversion, Part 2: Microstructural evolution of calcium phosphate. *JOUrnal of the Australian Ceramic Society,* 51**,** 149-159.

MACHA, I., OZYEGIN, L., OKTAR, F. & BEN-NISSAN, B. 2015b. Conversion of Ostrich Eggshells (Struthio camelus) to Calcium Phosphates. *Journal of The Australian Ceramic Society,* 51**,** 9.

MACHA, I. J., CAZALBOU, S., BEN-NISSAN, B., HARVEY, K. L. & MILTHORPE, B. 2015c. Marine structure derived calcium phosphate-polymer biocomposites for local antibiotic delivery. *Mar Drugs,* 13**,** 666-80.

MACHA, I. J., CAZALBOU, S., SHIMMON, R., BEN-NISSAN, B. & MILTHORPE, B. 2017. Development and dissolution studies of bisphosphonate (clodronate)-containing hydroxyapatite-polylactic acid biocomposites for slow drug delivery. *J Tissue Eng Regen Med,* 11**,** 1723-1731.

MACHA, I. J., KARACAN, I., BEN-NISSAN, B., CAZALBOU, S. & MÜLLER, W. H. 2018. Development of antimicrobial composite coatings for drug release in dental, orthopaedic and neural prostheses applications. *SN Applied Sciences,* 1**,** 68.

MONMATURAPOJ, N. 2008. Nano-size Hydroxyapatite Powders Preparation by Wet-Chemical Precipitation Route. *Journal of Metals, Materials and Minerals,* 18**,** 15-20.

NAAHIDI, S., JAFARI, M., EDALAT, F., RAYMOND, K., KHADEMHOSSEINI, A. & CHEN, P. 2013. Biocompatibility of Engineered Nanoparticles for Drug Delivery. *Journal of controlled release : official journal of the Controlled Release Society,* 166, 182-94.

PEMMER, B., ROSCHGER, A., WASTL, A., HOFSTAETTER, J. G., WOBRAUSCHEK, P., SIMON, R., THALER, H. W., ROSCHGER, P., KLAUSHOFER, K. & STRELI, C. 2013. Spatial distribution of the trace elements zinc, strontium and lead in human bone tissue. *Bone,* 57**,** 184-193.

POKHREL, S. 2018. Hydroxyapatite: Preparation, Properties and Its Biomedical Applications. *Advances in Chemical Engineering and Science,* 08**,** 225-240.

POUNTOS, I. & GIANNOUDIS, P. V. 2016. Is there a role of coral bone substitutes in bone repair? *Injury,* 47**,** 2606-2613.

ROCZNIAK, W., BRODZIAK-DOPIERAŁA, B., CIPORA, E., MITKO, K., JAKÓBIK-KOLON, A., KONIECZNY, M. & BABUŚKA-ROCZNIAK, M. 2017. The Content of Structural and Trace Elements in the Knee Joint Tissues. *Int J Environ Res Public Health,* 14, 1441.

RODRÍGUEZ-LUGO, V., SALINAS-RODRÍGUEZ, E., VÁZQUEZ, R. A., ALEMÁN, K. & RIVERA, A. L. 2017. Hydroxyapatite synthesis from a starfish and β-tricalcium phosphate using a hydrothermal method. *RSC Advances,* 7**,** 7631-7639.

ROY, D. M., EYSEL, W. & DINGER, D. 1974. Hydrothermal synthesis of various carbonate containing calcium hydroxyapatites. *Materials Research Bulletin,* 9**,** 35-39.

ROY, D. M. & LINNEHAN, S. K. 1974. Hydroxyapatite formed from coral skeletal carbonate by hydrothermal exchange. *Nature,* 247**,** 220-2.

SADAT-SHOJAI, M., KHORASANI, M.-T., DINPANAH-KHOSHDARGI, E. & JAMSHIDI, A. 2013. Synthesis methods for nanosized hydroxyapatite with diverse structures. *Acta Biomaterialia,* 9**,** 7591-7621.

SANTOS, A., SINN AW, M., BARIANA, M., KUMERIA, T., WANG, Y. & LOSIC, D. 2014. Drug-releasing implants: current progress, challenges and perspectives. *Journal of Materials Chemistry B,* 2**,** 6157-6182.

SING, K. S. W., EVERETT, D. H., HAUL, R. A. W., MOSCOU, L., PIEROTTI, R. A., ROUQUÉROL, J. & SIEMIENIEWSKA, T. 1985. Reporting Physisorption Data for Gas/Solid Systems With Special Reference to the Determination of Surface Area and Porosity. *Pure and Applied Chemistry,* 57**,** 603-619.

SZCZEŚ, A., HOŁYSZ, L. & CHIBOWSKI, E. 2017. Synthesis of hydroxyapatite for biomedical applications. *Adv Colloid Interface Sci,* 249**,** 321-330.

TAN, Y. H., DAVIS, J. A., FUJIKAWA, K., GANESH, N. V., DEMCHENKO, A. V. & STINE, K. J. 2012. Surface area and pore size characteristics of nanoporous gold subjected to thermal, mechanical, or surface modification studied using gas adsorption isotherms, cyclic voltammetry, thermogravimetric analysis, and scanning electron microscopy. *Journal of Materials Chemistry,* 22**,** 6733-6745.

VARGHESE, D. S., PARWEEN, S., ARDAH, M. T., EMERALD, B. S. & ANSARI, S. A. 2017. Effects of Aminoglycoside Antibiotics on Human Embryonic Stem Cell Viability during Differentiation In Vitro. *Stem Cells Int,* 2017**,** 2451927.

XU, Y., WANG, D., YANG, L. & TANG, H. 2001. Hydrothermal conversion of coral into hydroxyapatite. *Materials Characterization,* 47**,** 83-87.

ZHANG, F., ZHOU, Z.-H., YANG, S.-P., MAO, L.-H., CHEN, H.-M. & YU, X.-B. 2005. Hydrothermal synthesis of hydroxyapatite nanorods in the presence of anionic starburst dendrimer. *Materials Letters,* 59**,** 1422-1425.

Chapter 3

Production and Characterization for PLA Biocomposite and the coating process for the metallic implants

Chapter 3: Production and Characterization for PLA Biocomposite and the coating process for the metallic implants

This chapter provides a background of production and characterization of the PLA biodegradable polymeric drug delivery coating system and its applications to the specific metallic bone implants. The aims for this chapter are to cover the production of the Gm and HAp-Gm particles containing PLA biocomposite thin film coatings on Ti6Al4V metallic bone implants and to analyze their morphological and physical properties. The results are represented by a detailed discussion comparing PLA, PLA-Gm, PLA-HAp, and PLA-Gm-(HAp-Gm) thin film coated implants and their particle distribution and influence over the different amount of Gm addition.

3.1 Introduction

Combinational drug delivery coating systems and metallic medical implants, including dental and orthopedic, have been often used to solve many well-known clinical problems such as implant-related bacterial infections and lack of integration within the implant surrounding tissue, and incompatibility, or total rejection. The innovative drug-device combination concept is based on the permanent biomedical implants with the additional benefit of delivering the drug to the specific targeted area (Wu and Grainger, 2006, Trajkovski et al., 2012, Santos et al., 2014). Many types of research and trials were conducted for the combination of implants and local controlled drug delivery coating systems; however, there is not any currently available system to fulfill all the primary key criteria. Some of the key criteria for designing long-lasting and successful implants are: biocompatibility, sufficient mechanical integrity, minimal adverse effects, minimal cytotoxicity, high pharmaceutical stability, controllable drug release kinetics, ability to apply to clinical trials, long shelf life, easy sterilization before surgery, effectiveness against bacterial colonization, and easy manufacture. Therefore, designing the drug delivery coating-implant combined system to cover all the key criteria above is the main challenge (Goodman et al., 2013, Tobin, 2017, Choi et al., 2018).

The polymer-based materials have been used in the design of a range of drug delivery coating systems, and on biomedical implants to obtain the easy applicable drug-device combination concept with controllable drug release performance (Santos et al., 2014, Nandi et al., 2016).

The polymers for medical applications are generally categorized into two groups: non-biodegradable and biodegradable polymers (Gavasane and Pawar, 2014). The non-biodegradable polymers are used for the drug delivery system as beads or coating material that might contain the different types of pharmaceuticals like antibiotics (Inzana et al., 2016). Moreover, Chaloun *et al.* (1993) reported that the gentamicin impregnated non-biodegradable polymethylmethacrylate (PMMA) beads had been used in clinical trials on 52 patients to treat bacterial infection by inserting gentamicin (Gm) contained PMMA beads into the open wound area. The outcome showed a 94% success rate (Calhoun et al., 1993). However, the non-biodegradable polymer containing drug delivery systems has limitations. These limitations are: the requirement of second surgery due to removing the drug carrier and the choice of antibiotic because of the heat sensitivity of the antibiotics during the exothermic polymerization process (Lucke et al., 2003, Inzana et al., 2016). Therefore, synthetic biodegradable polymers have been used as coating materials on biomedical implants for designing the combined drug delivery system with implants using different types of techniques. These techniques are: the spray coating, spin coating, dip coating, or solvent casting techniques (Choi and Ben-Nissan, 2014, Nandi et al., 2016).

The dip coating method is applicable to complex implant shapes, such as rods, pipes, tubes, and discs. Additionally, multifunctional, multilayered coatings, and adjustable coating thickness up to 1000nm are the other advantages of the dip coating method (Choi et al., 2017).

Poly-alpha-hydroxy acids, such as polylactide (PLA) and related copolymers Polylactide-co-glycolide (PLGA), have been studied mainly for biomedical applications due to their biocompatibility and biodegradability. The degradation rate of biodegradable polymers is related to hydrophobic/hydrophilic properties. It is essential to design a controlled drug delivery system because the release of pharmaceuticals or agents is controlled by diffusion and erosion or dissolution mechanisms, respectively (Lyndon et al., 2014). For instance, PLA is hydrophobic and provides a slow degradation rate; however, PLGA is hydrophilic (Dorati et al., 2017).

PLA has good biodegradability, biocompatibility, absence of adverse immunological reactions with the human body, a high mechanical strength, and excellent shaping and molding properties. Therefore, a PLA biodegradable polymer has been used to develop different types of biomedical tools for treating vascular disease, drug delivery systems, scaffolds in tissue engineering, and clinical applications (Gavasane and Pawar, 2014, Ahmed et al., 2014). It has also been reported that PLA is a preferable thermoplastic polymer for designing a medical coating system that has long-term local

and slow drug release (Kimura et al., 1992, Prior et al., 2000, Macha et al., 2015). PLA biodegradable polymeric thin films loaded with gentamicin have been synthesized to behave as 'composite coatings' for metallic bone implants to prevent implant-associated infections (Strobel et al., 2011, Macha et al., 2014, Macha et al., 2015).

In this research, the PLA biocomposite thin film coating system is designed on the combination of the long-term controlled drug delivery system with metallic bone implants. The PLA biocomposite thin film coating system contains Gm antibiotic particles, and the Porites coral skeleton derived HAp drug carrier particles that were loaded with Gm antibiotic. The production of HAp and drug loading techniques were explained in **Chapter 2** in detail. The production of PLA biocomposite thin films and their application on the Ti6Al4V bone implants with the dip coating technique was the main focus.

PLA thin film biocomposite used in this work include:

1. PLA thin film (PLA),

2. Gm contained PLA thin film (PLA-Gm),

3. HAp contained PLA thin film (PLA-HAp), and

4. Gm and HAp-Gm contained PLA thin film (PLA-Gm-(HAp-Gm)) coating materials

3.2 Experimental Methods

In this study, we used the 2003D poly lactic acid (PLA) (NatureWorks, Ingeo Pty Ltd. Australia) (density; 1.24 g/cm^3, MW; 2x10^4 g/mol, melting temperature; 210 °C, and all other properties are given in *Table 3.1*), and chloroform as the solvent (with ≥ 99%, Sigma Aldrich, Castle Hill, Australia), were used. The metallic materials included high purity Ti6Al4V rods and discs (Good Fellows, UK) and 3D print medical hip implants (Bresmed, Australia).

Table 3.1 2003D PLA properties (from NatureWorks, *Ingeo Pty Ltd.*)

Typical Material & Application Properties [1]		
Physical Properties	**Ingeo 2003D**	**ASTM Method**
Specific Gravity	1.24	D792
MFR, g/10 min (210°C, 2.16kg)	6	D1238
Clarity	Transparent	
Mechanical Properties		
Tensile Strength @ Break, psi (MPa)	7,700 (53)	D882
Tensile Yield Strength, psi (MPa)	8,700 (60)	D882
Tensile Modulus, kpsi (GPa)	500 (3.5)	D882
Tensile Elongation, %	6.0	D882
Notched Izod Impact, ft-lb/in (J/m)	0.3 (16)	D256
Shrinkage is similar to PET [2]		
Heat Distortion Temperature (°C)	55	E2092

3.2.1 The Ti6Al4V substrate material preparation

Ti6Al4V disc implants were used as experimental substrates in this study. Ti6Al4V discs of 1.3 cm diameter and 3 mm thick were cut from the 50 mm long rod by a diamond blade (vc-50 diamond wafering saw, leco pty. Ltd., Australia). The specimens were further polished in four steps to obtain a highly polished surface. The first step of the polishing was utilizing 320 grit, then 1200PSA SiC emery papers. The final polishing was done in two steps using 0.3 and 0.05 µm alumina particles to get a mirror surface. The specimens were degreased with 100% acetone, followed by ultrasonic cleaning with deionized water. They were dried under vacuum overnight within a sealed desiccator.

On the other hand, the thermal anodization treatment was applied on a highly polished Ti6AL4V disc. One set of the substrate samples was a highly polished untreated Ti6Al4V as is, and the other set was anodized by thermal treatment in this project. The thermal anodization process was carried out at 500 °C for 16 hours in the air. Although the Ti6Al4V surface naturally reacts with oxygen in the air and the surface contains a thin oxide layer, the thermal anodization process was applied to increase the naturally existing oxide layer thickness, improving the surface properties mechanically and biologically.

In this chapter, only the highly polished untreated Ti6Al4V set was used as a substrate for the production and characterization of the PLA biocomposite thin film coating system. The thermally anodized Ti6Al4V discs will be explained in detail and analyzed in **Chapter 5.**

3.2.2 The synthesis of PLA biocomposite thin films and the dip coating method

PLA biodegradable thin films were prepared by the solvent film casting technique using chloroform solvent. The methodology of the PLA biocomposite solution preparation is modified from our team's previous study (Macha et al., 2014). PLA thin films were prepared by dissolving 0.5 g PLA particles into 30 mL chloroform solvent (1.12 %w/v polymer concentration) and mixed with a magnetic stirrer at room temperature. PLA-chloroform ratio affects the viscosity of the solution and hence the coating thickness. PLA biocomposite thin films designated as PLA, PLA-HAp, PLA-Gm, and PLA-Gm-(HAp-Gm) were prepared to use as a coating material for the metallic bone implants.

Initial Gm concentrations for 5%, 10%, 15%, 20% and 30% PLA biocomposite thin film coating were calculated based on the percentage of the total weight of PLA biocomposite thin film which includes all weight of PLA, Gm and HAp-Gm particles for each sample in PLA-Gm-(HAp-Gm) solutions. The calculation of the Gm amount in HAp-Gm particles with their production process was given in **Chapter 2** for each percentage (5% to 30% w_{HAp} /w_{Gm}). The Gm amounts for each percentage are given in Table 3.2 for 10 ml PLA chloroform solution, and the initial Gm concentration was calculated accordingly. For instance, 5% of the total amount of PLA polymer, Gm particles and 5% HAp-Gm particles in per 1 ml of PLA chloroform solution were referred to the initial concentration of Gm into the PLA biocomposite coating solution before the dip coating process.

Table 3.2 The total Gm concentrations in the 5%, 10%, 15%, 20%, and 30% PLA-Gm-(HAp-Gm) solutions for the dip coating technique.

W_{total}/w_{Gm}	Total Gm amount in 10 ml PLA chloroform solution	Gm concentrations
5%	(HAp-Gm) particles; 0.167g +Gm particles; 0.0087g	1.7mg/ml
10%	(HAp-Gm) particles; 0.167g +Gm particles; 0.02g	3.7mg/ml
15%	(HAp-Gm) particles; 0.167g +Gm particles; 0.029g	5.4mg/ml
20%	(HAp-Gm) particles; 0.167g +Gm particles; 0.042g	7.5 mg/ml
30%	(HAp-Gm) particles; 0.167g +Gm particles; 0.06g	11 mg/ml

The dip coater (*Figure 3.1*) with dipping rate and speed controller was built by our team to work at constant down and up speeds to apply the coating. The dip coating method was applied. During

which the sterilized Ti6Al4V discs were held by their edge and, firstly, dipped into PLA biocomposite solutions at a constant speed of 8.5 mm/seconds, then pulled up at a constant 7 mm/sec speed. Finally, the sample was allowed to drain for 10 seconds.

The steps shown below were repeated five times to form the PLA, PLA-Gm, PLA-HAp, and PLA-Gm-(HAp-Gm) thin film coatings on the Ti6Al4V discs. In order to obtain consistency and uniform Gm and HAp-Gm particle distribution into the mixture, the particles into the PLA solution were stirred continuously during the coating process. The dipping process is shown step by step in *Figure 3.1*. After finalizing the coating process, all samples were placed in a vacuum furnace at 60 °C for 16 hours. The chloroform solvent evaporated entirely with this vacuum process.

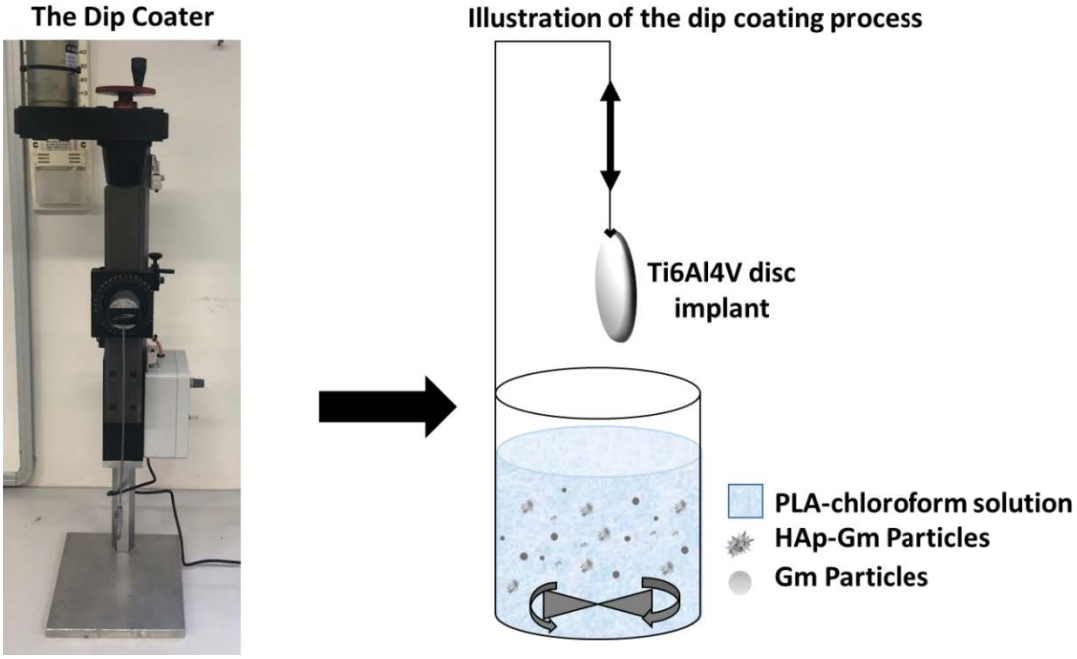

Figure 3.1 The Dip coater device and the illustration schema for the dip coating process

3.2.3 Surface characterization of PLA and PLA-Gm-(HAp-Gm) thin film coated Ti6Al4V discs

The surface characterization and morphology of PLA, PLA-Gm and PLA-HAp thin film coated Ti6Al4V discs were analyzed in the first part of this chapter. Then, PLA-Gm-(HAp-Gm) biocomposite mixtures as a coating material at 5%, 10%, 15%, 20%, and 30% (w/w) Gm concentrations were investigated and analyzed to determine the surface and chemical characterization of the PLA biocomposite coating for different Gm concentrations.

3.2.3.1 Scanning Microscope Analysis (SEM)

Surface structure, morphology, and chemical composition of the PLA and PLA biocomposite thin film coated Ti6Al4V discs were established by a Scanning Electron Microscope (SEM) (ZEISS Supra SSVP, Zeiss, Germany) equipped with an EDS analyzer. The samples were sputter-coated with a 7 nm thin layer of Au/Pd (Leica EM ACE600 Sputtering and Carbon Thread Coater, Germany) in order to reduce charging. The samples were kept under vacuum overnight to remove any moisture before the imaging process. Images were taken at various magnifications at an acceleration voltage of 5-15 kV.

The particle size of Gm and HAp-Gm particles and their distribution on the PLA-Gm-(HAp-Gm) coated Ti6Al4V discs were analyzed by FIJI-image J software (Java-based Image Processing and Analysis Software by NIH Image) at 50x low magnifications and 500x high magnifications.

3.2.3.2 Atomic Force Microscope (AFM)

The surface topography of the untreated and anodized samples was characterized using a Multimode 5 atomic force microscope (AFM, Park Systems, South Korea) operating in tapping mode. All investigations were performed under ambient conditions. For each sample, the area of 5 × 5 µm was scanned. Commercial silicon cantilevers type NSC16AlBS (a nominal tip radius of approximately 8 nm, nominal cantilever force constant of 26 N/m, and the nominal resonance frequency of 190 Hz were used.

3.2.3.3 Profilometer

A profilometer (Dektak XT-stylus Profilometer, Bruker, USA) was used to measure the thickness of the PLA thin films on Ti6Al4V discs. The Ti6Al4V discs were coated with the PLA solution using the dip coating method. Then half of the PLA thin films on the disc were removed by the reactive ion etcher via chemically reactive plasma. Therefore, half of the PLA thin film coated Ti6Al4V discs were used to obtain the PLA thin film thickness of the Ti6Al4V disc.

3.2.3.4 Fourier transform infrared spectroscopy (FT-IR)

FT-IR spectra of the PLA biocomposite thin film coated samples were collected at Nicolet FT-IR (Nicolet, Magna-IR 6700 Spectrometer FT-IR, Thermo-Scientific, Madison, USA), using the ATR mode, from wavenumber 2000 to 200 cm^{-1} at a resolution of 4 cm^{-1}.

3.3 Results and Discussions

PLA biocomposite film solutions were prepared using the modified solution casting technique. With the modified technique, the PLA composite transparent films were deposited on Ti6Al4V discs. The films included PLA thin film and PLA with Gm, HAp, and HAp-Gm particles at predetermined Gm concentrations (5%-30% w/w). After coating, the discs were dried at 60 ˚C in a vacuum oven, which reduced the solvent retention.

3.3.1 The Surface Characterization of PLA thin film coated Ti6Al4V disc

The SEM images showing the surface morphology of the PLA thin film coating on Ti6Al4V discs are given in *Figure 3.2* at both low (A) and high (B) magnifications. The PLA thin film coated Ti6Al4V discs showed a homogeneously coated surface without any surface or edge cracks.

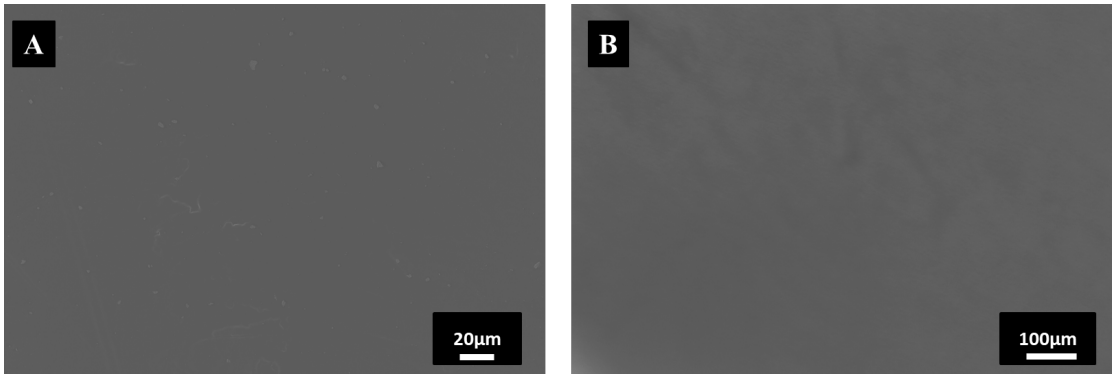

Figure 3.2 SEM images for the surface of PLA thin film coated Ti6Al4V disc at low and high magnifications

An Atomic Force Microscope (AFM) allows observation of the surface topography and surface roughness of the material. In this case, the 3D view of uncoated Ti6Al4V and PLA thin film coated Ti6Al4V disc surfaces are given in *Figure 3.3* with their surface roughness parameters (Ra, Rz, and Rq). AFM results show that the PLA thin film coating on the Ti6Al4V surface is smoother than the Ti6Al4V surface without coating. Cracks or holes aren't observed on the PLA film surface, so the smooth PLA film coating on the Ti6Al4V surface is seen in the SEM image results as well. The average roughness values of the PLA thin film coated surface (Ra= 1.5 ± 0.5 nm, Rz= 16.6 ± 2.8 nm, Rq= 1.2 ± 0.3 nm) is slightly lower than the uncoated surface (Ra= 2.6 ± 0.2 nm, Rz= 19.6 ± 1.4 nm, Rq= 3.2 ± 0.3 nm) due to nature of PLA polymer. However, the roughness values are very close for Ti6Al4V

surface with and without PLA thin film coating. It can be explained by the effect of Ti6Al4V surface on the PLA thin film coating as a substrate effect.

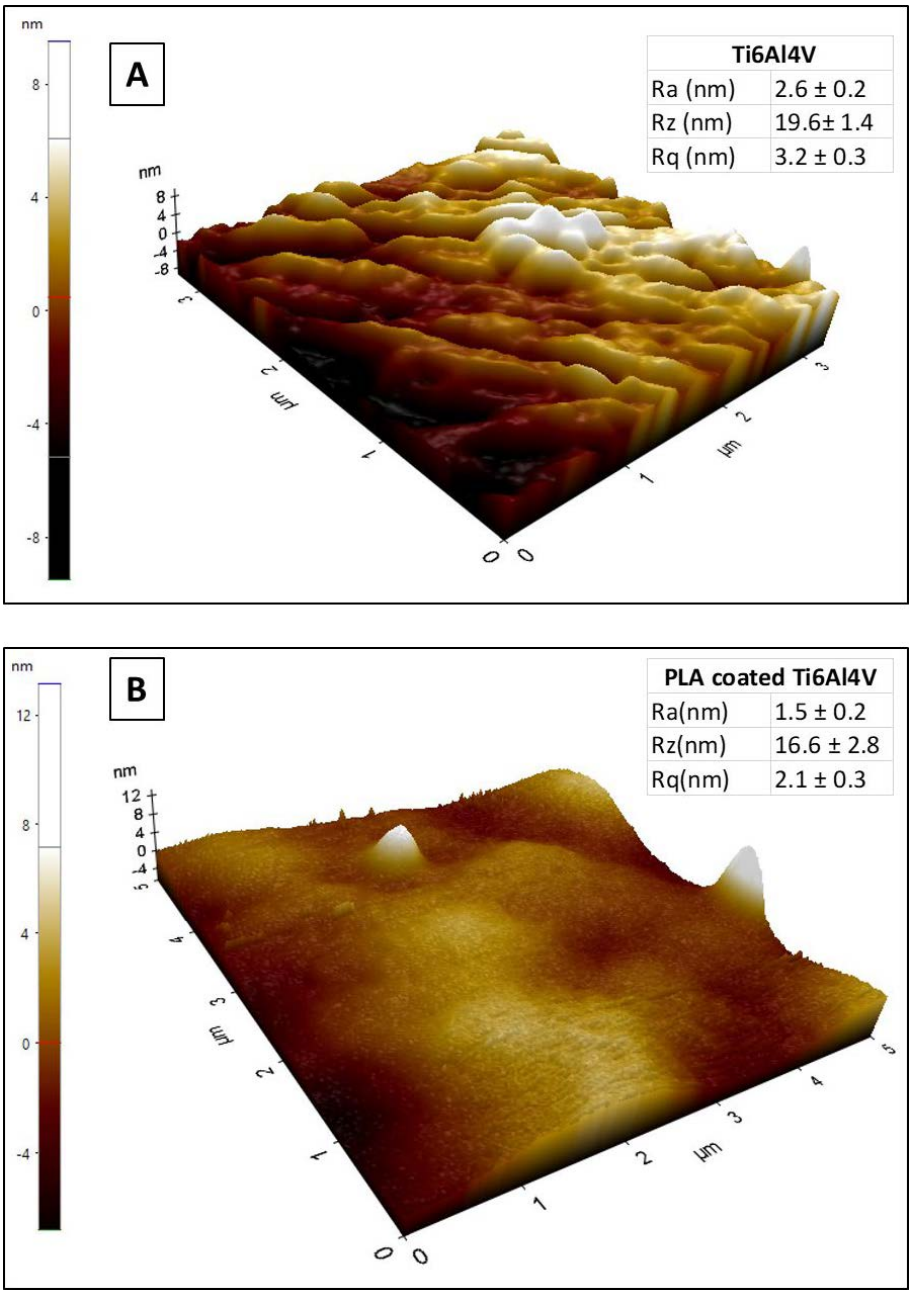

Figure 3.3 3D AFM images and the surface roughness parameters for Ti6Al4V disc (A) and PLA coated Ti6Al4V disc (B) surfaces

The thickness of the PLA thin film coating on the surface was measured with a profilometer. *Figure 3.4* shows the height differences of the half PLA thin film coated Ti6Al4V disc between the PLA thin film coated area and the substrate, which is Ti6Al4V at three different locations. Profilometry measurements show that the PLA thin film dip-coated samples have ~ 400 nm film thicknesses. The

minor peaks observed at the profilometer spectra are background noise because of the substrate, which is the Ti6Al4V disc surface.

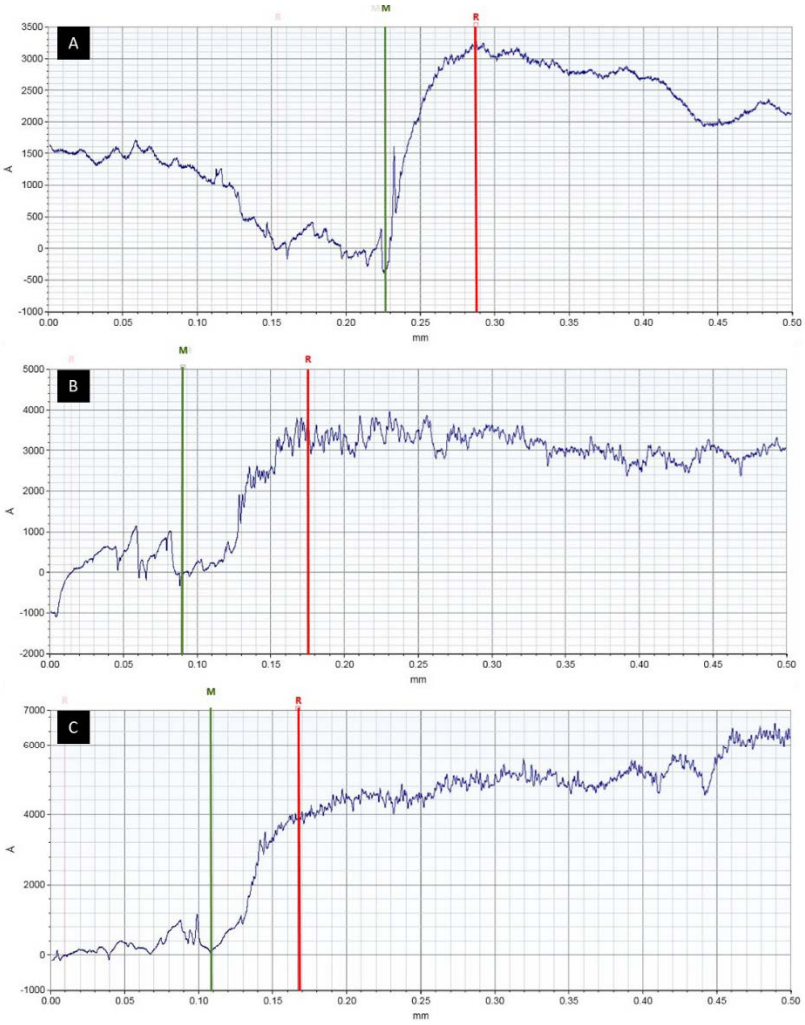

Figure 3.4 The Profilometer spectra graphs for the three different locations (A, B, C) on the half PLA thin film coated Ti6Al4V disc. The height difference between M to R lines refers to the areas of the PLA thin film coating which is 400 nm thick

3.3.2 The Surface Characterization of PLA-Gm, and PLA-HAp thin film coated Ti6Al4V polished discs

The surface morphology of PLA-Gm (*Figure 3.5 A and B*) and PLA-HAp (*Figure 3.5 C and D*) thin film coated Ti6Al4V discs were investigated under SEM at low and high magnifications. *Figure 3.5* (*A, B*) shows undissolved single and agglomerated Gm particles on the Ti6Al4V surface. The average particle size of Gm particles in the PLA thin film is 1-10 µm, and Gm particles on the PLA thin film is

around 10-50 µm. The different size of Gm particles was spread on PLA-Gm thin film coated surface at *Figure 3.5 A, B.*

In *Figure 3.5 C, D*, some agglomerated HAp particles were observed on the surfaces of the samples to obtain the PLA-HAp coated Ti6Al4V discs. Although the average particle size of HAp was 100-300 nm, and agglomerated particles up to 300–600 nm were measured by the Brunauer-Emmett-Teller (BET) method. A few of the HAp particles were agglomerated, and they became large size clusters during the production process of PLA biocomposite thin film coating. These agglomerated HAp particles (up to 10 µm) were also spread on the surface with PLA thin film coating on Ti6Al4V discs in *Figure 3.5 C, D*. The analysis of these particles was covered in **Chapter 2**.

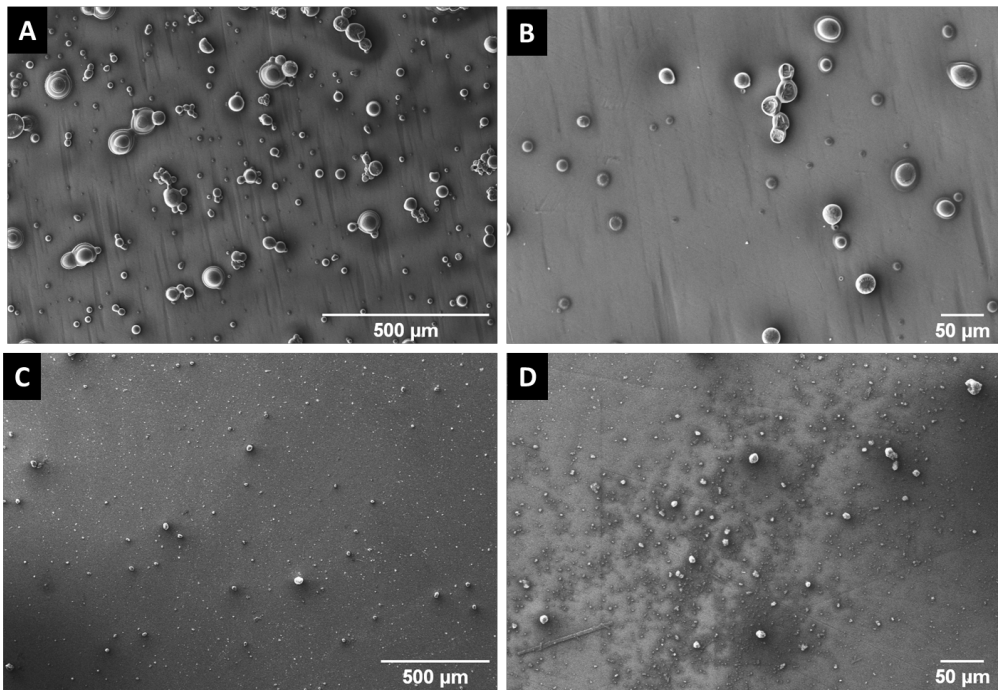

Figure 3.5 SEM images for the surface of PLA-Gm (A, B) and PLA-HAp (C, D) thin film coated Ti6Al4V

PLA-Gm and PLA-HAp thin film coated Ti6Al4V discs were the first step in observing the behavior of the PLA coating with an antibiotic (Gm) and bioceramics (HAp) separately before the investigation of the actual design that is the PLA-Gm-(HAp-Gm) coated Ti6Al4V disc. This will be explained in next section.

3.3.3 The Surface Characterization & Particle Distribution Analysis of PLA-Gm-(HAp-Gm) thin film coated Ti6Al4V discs at predetermined Gm concentrations (5% - 30% w/w)

In order to obtain sufficient Gm release dosage in the PLA-Gm-(HAp-Gm) coating to avoid the adverse effect of Gm antibiotic on the human body and at the same time to inhibit implant-related bacterial infections, different Gm percentages were prepared with the PLA matrix which was 5%, 10%, 15%, 20% and 30% w/w Gm.

The overall surface area and the general microstructure of the PLA-Gm-(HAp-Gm) coated Ti6Al4V discs for all Gm concentrations investigated ranging from 5% to 30% were analyzed by a 3D optical microscope shown in *Figure 3.6.*

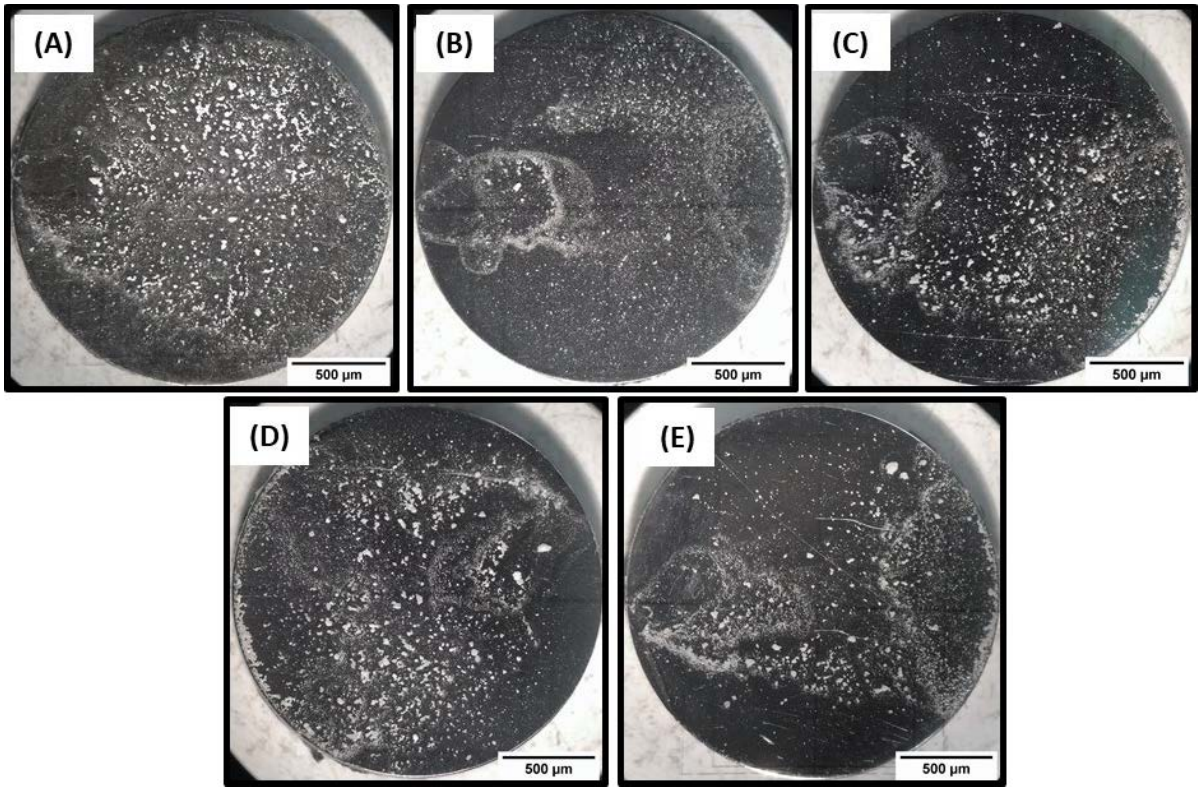

Figure 3.6 3D optical microscope imaging to observe the whole surface area of PLA-Gm-(HAp-Gm) thin film coated Ti6Al4V discs at 5% (A), 10% (B), 15% (C), 20% (D) and 30% Gm (E) showing small fine particles ad agglomerated larger deposits

The surface structure of 5% (A), 10% (B), 15% (C), 20% (D) and 30% (E) PLA-Gm-(HAp-Gm) thin film coated Ti6Al4V discs is illustrated at a low magnification (50x) in *Figure 3.7* and a high magnification (500x) in *Figure 3.8*. These figures also show the smaller and agglomerated large particles at high

magnification. The Gm and HAp-Gm agglomerated particles are distributed on the surface with a wide range of particle sizes. Although the size of HAp particles before Gm loading is around 100nm, the drug loading process causes the agglomeration of the HAp-Gm particles. The particle size of HAp-Gm particles in the PLA thin film is approximately between 0.1 to 5 µm. Additionally, the system contains agglomerated HAp-Gm particles which have around 10-30 µm particle size onto the PLA thin film, which are all fully embedded within and on the surface of the PLA thin film.

On the other hand, during the mixing of Gm and HAp-Gm particles with the PLA solution for the dip coating process, the agglomeration of the particles might occur at different particle sizes. Therefore, to minimize the agglomeration for Gm and HAp-Gm particles into the PLA solution, the ultrasound was applied before the dip coating process. However, still a few larger (around 50 µm) agglomerated HAp-Gm clusters were observed on the PLA thin film coated TiAl4V disc.

Image J software was used to determine the estimated range of Gm and HAp-Gm particle areas on the substrate surface according to the SEM images at low and high magnifications. Only the top surface of the PLA biocomposite thin film coated Ti6Al4V samples were analyzed to obtain the particle size and the area because of the limitation of obtaining cross sectional area without damaging the coating.

In this new system, the main advantage of having a wide particle size range is to allow control of Gm release rates at different levels and time periods. This is because the large size agglomerated particles are not fully embedded within the PLA matrix but fully covered with the PLA thin film; they have an important role during the initial Gm burst release. The Gm release pattern for PLA-Gm-(HAp-Gm) thin film coated Ti6Al4V will be explained in **Chapter 4** in detail.

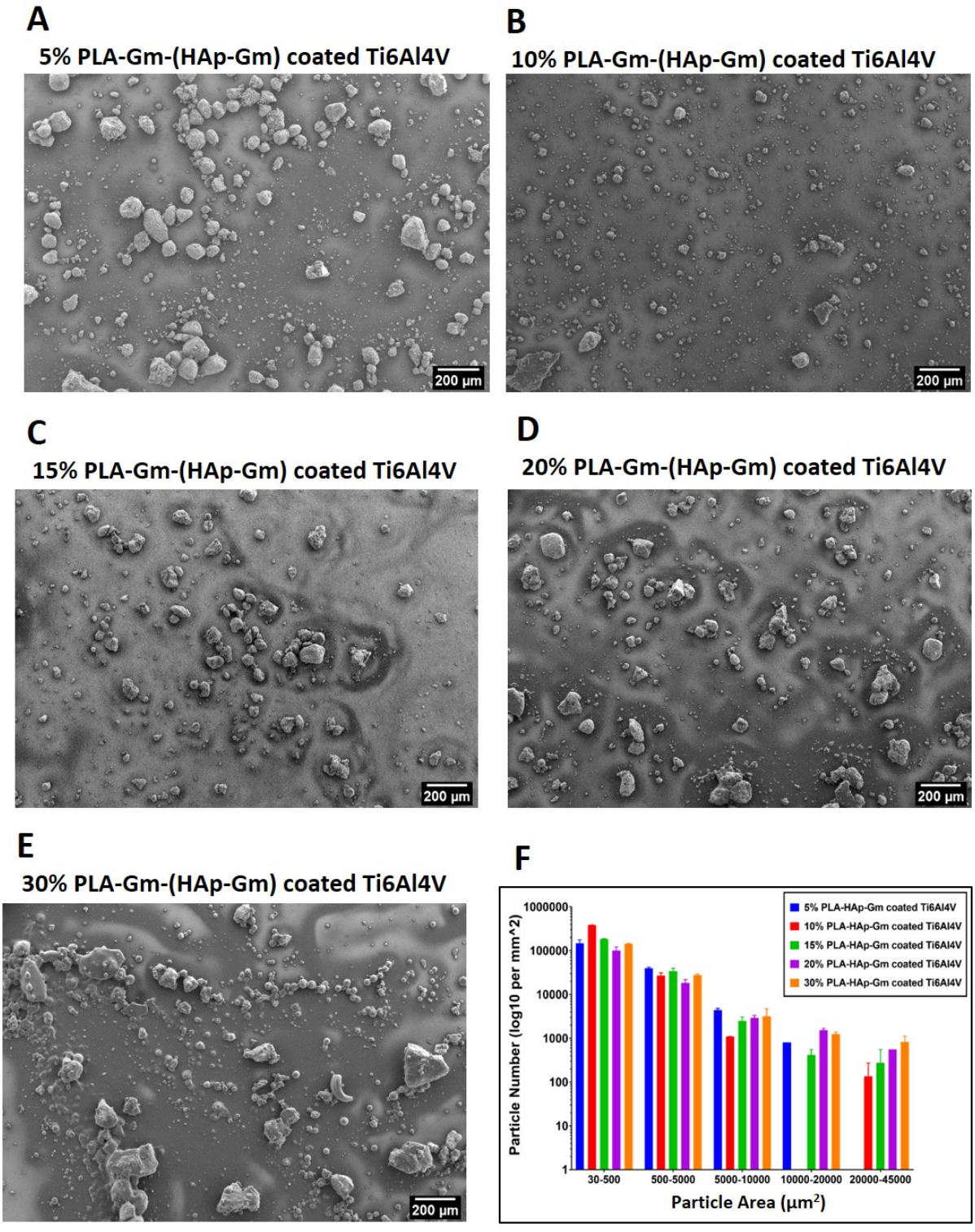

Figure 3.7 The surface characterization of PLA-Gm-(HAp-Gm) thin film coated Ti6Al4V discs at 5% (A), 10% (B), 15% (C), 20% (D) and 30% (E) Gm concentrations at low (50x) magnifications with the particle number versus particle area graphs (F) according to SEM images of all samples at low (50x) magnifications

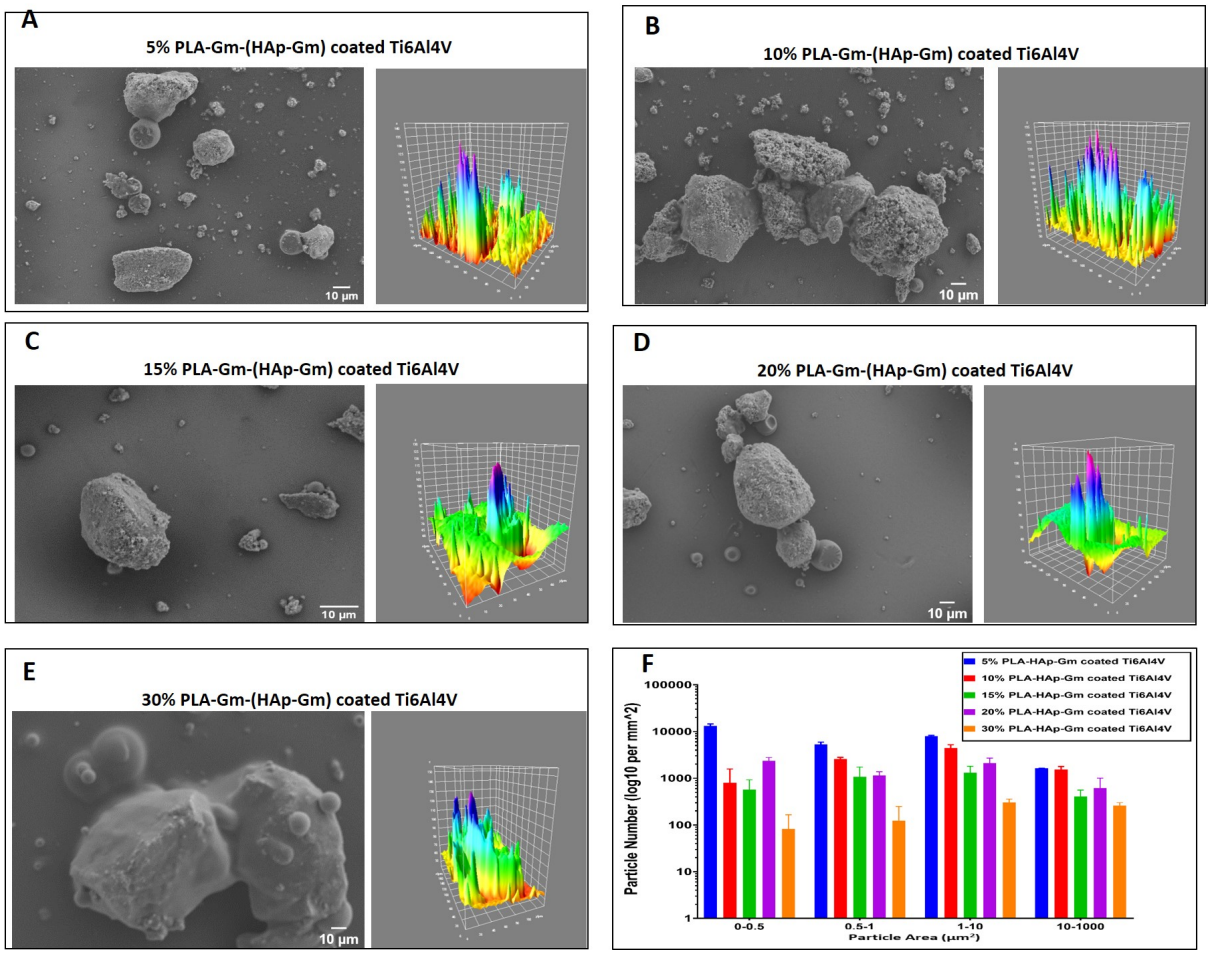

Figure 3.8 The surface characterization of PLA-Gm-(HAp-Gm) thin film coated Ti6Al4V discs at 5% (A), 10% (B), 15% (C), 20% (D) and 30% (E) Gm concentrations at high (500x) magnifications with 3D illustrations of the particles for the images at high magnification. The particle number versus particle area graphs (F) according to SEM images of all samples at high (500x) magnifications

Figure 3.9 represents the observation of the Gm, and HAP-Gm particles on the surface of PLA-Gm-(HAp-Gm) thin film coated Ti6Al4V in detail. The two separate Gm particles and the large agglomerated HAp-Gm particles on the surface are clearly shown in *Figure 3.9 A*. The large agglomerated HAp-Gm particles, which are approximately 30 µm size, were observed in SEM analysis. It can be seen that they were only partially embedded into the PLA thin film matrix. Besides, 0.5 to 1 µm size plate-like HAp particles, which were partially coated with Gm particles, were also noticed.

On the other side of *Figure 3.9 A*, the small agglomerated HAp-Gm particles (1 to 2 µm size) were also embedded within the PLA thin film. *Figure 3.8 B* also includes approximately 40 µm size large

agglomerated clusters. These clusters are made of smaller size 1-5 μm and smaller particles. Therefore, the PLA-Gm-(HAp-Gm) thin film coated Ti6Al4V surface has relatively small HAp-Gm agglomerated particles that were embedded into the PLA thin film, and larger agglomerated clusters that contain much smaller particles of HAp-Gm and Gm particles.

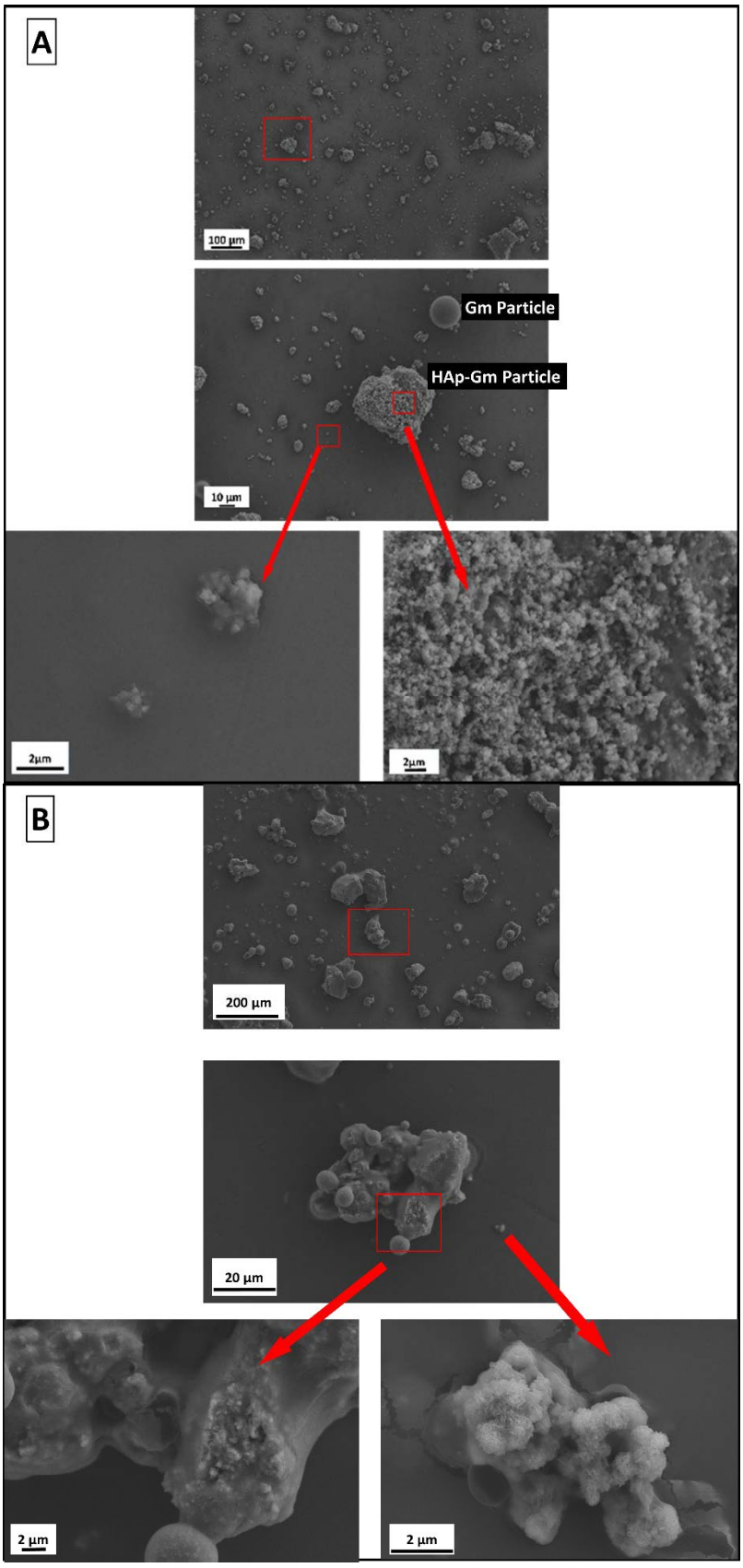

Figure 3.9 The observation of Gm and HAp-Gm agglomerated particles in and on PLA thin film coating at low and high magnifications at two different locations (A and B) on Ti6Al4V disc

Although the thickness of PLA thin film coated Ti6Al4V without the HAp particles was found to be approximately 400 nm, the thickness of PLA thin film with the Gm and HAp-Gm agglomerated particles increased according to the amounts and size of particles and the overall viscosity of the PLA solution.

It is postulated that according to the 3D optical microscope and SEM observations, PLA acts as glue holding the particles together and bonding to the substrate. The large clusters and smaller particles on the surface are also covered with PLA film, and they are strongly attached.

In certain areas, the thickness varies according to the agglomerate sizes. Therefore, the thickness is not uniform for this specific PLA biocomposite thin film coating, and the PLA film is thicker around the large particles to keep them stable on the surface.

According to SEM images in *Figures 3.5, 3.7, 3.8, and 3.9*, it was observed that there was a difference in color density and magnitude of the colored zones. This was seen in only the PLA thin film coating and around the large cluster coated PLA darker colored regions. This color changes due to reflection as a function of thickness.

3.3.4 Physicochemical analyses of PLA and PLA-Gm-(HAp-Gm) thin film coated Ti6Al4V disc surfaces

Figure 3.10 A to *C* shows the FT-IR spectra of HAp and PLA composites coated on Ti6Al4V discs at different Gm concentrations. In the FT-IR spectra, the PLA and HAp major peaks were clearly identified, and all minor Gm peaks were highlighted.

FT-IR spectra results shown in *Figure 3.10 A* for PLA thin film composites indicate the following peaks: –C=O (1746 cm^{-1}), –C-H (1451–1358 cm^{-1}), -C-O ester (1180–1043 cm^{-1}) and -C-O stretch (867–751 cm^{-1}). Additionally, the v4 PO_4 peaks (600–502 cm^{-1}) characteristic peaks of HAp were seen in *Figure 3.10 B* and *D*. Although the HAp characteristic peaks are major peaks for the PLA-HAp coated sample, they were minor peaks for the PLA-Gm-(HAp-Gm) coated samples. The FT-IR spectra of PLA and HAp correctly match with the literature values (Nikolic et al., 2010, Lasprilla et al., 2012, Farah et al., 2016). On the other hand, Gm characteristic peaks in *Figure 3.10 C* and *D* were obtained, as minor peaks, amide I-II groups which are N-H stretch (1619 and 1523 cm^{-1}). This is in agreement with the literature values (Sionkowska et al., 2016). These results clearly demonstrate that Gm and the HAp particles were within the PLA composite thin film as PLA-Gm, PLA-HAp, and PLA-Gm-(HAp-Gm) films coated on Ti6Al4V discs.

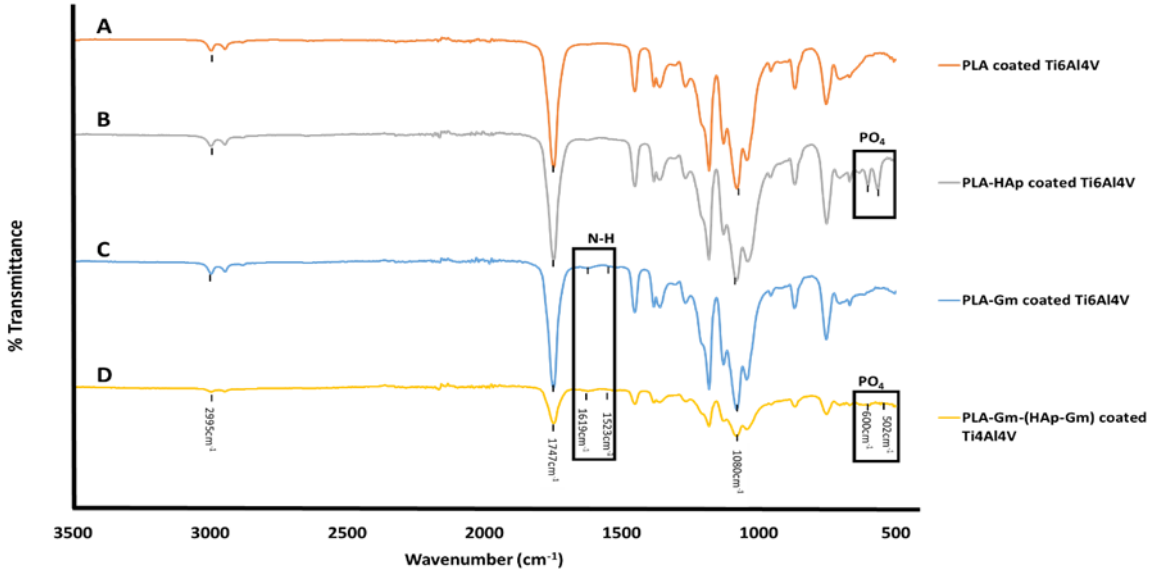

Figure 3.10 FT-IR results of all sets of PLA biocomposite coated Ti6Al4V discs. The characteristic peaks of Gm (1619 and 1523 cm^{-1}, which are amide group I-II) and HAp (600–502 cm^{-1} that are PO_4 group) were labeled on the spectrum separately

3.3.5 Application of PLA-Gm-(HAp-Gm) thin film coating system on different metallic bone implants

There are many advantages to combining the drug delivery coating systems with existing implant technologies. These include eliminating well-known clinical problems such as surgery-related infections and reducing time and cost for hospitalization and most importantly, reducing pain and suffering.

Therefore, the PLA-Gm-(HAp-Gm) thin film coating system was applied to the different metallic dental and orthopedic implants, which were Ti6Al4V alloy, and have a different surface texture. *Figure 3.11* shows uncoated versus PLA-Gm-(HAp-Gm) thin film coated in three different metallic bone implants that are commercially available. The implants are the screw-shaped dental implant (supplied by University of Birmingham Alabama, Birmingham, USA) (*Figure 3.11 A*), Huckstep

intramedullary implant (UNSW Orthopedic Surgery) (*Figure 3.11 B*), and hip – amputee implant (BresMed Pty Ltd Sydney, Australia) (*Figure 3.11 C*). The PLA biocomposite thin film coating system was successfully applied to the different bone implants with different surface texture.

All three Ti6Al4V alloy implants first were heat-treated at 500 °C for 16 hours then dip coated in the PLA-Gm-(HAp-Gm) solution with a method explained in the **Chapter 2**. All three were homogenously coated, and the polymeric thin film coating was strongly bonded to the substrate. No other treatment is required, but sterilization possibly with Gamma rays due to the HAp particles within the composite is recommended.

These three experiments demonstrated that the method can be used to upscale existing medical implants easily and in cost-effective ways. Further testing on these and the coated implants will be covered within the next few chapters.

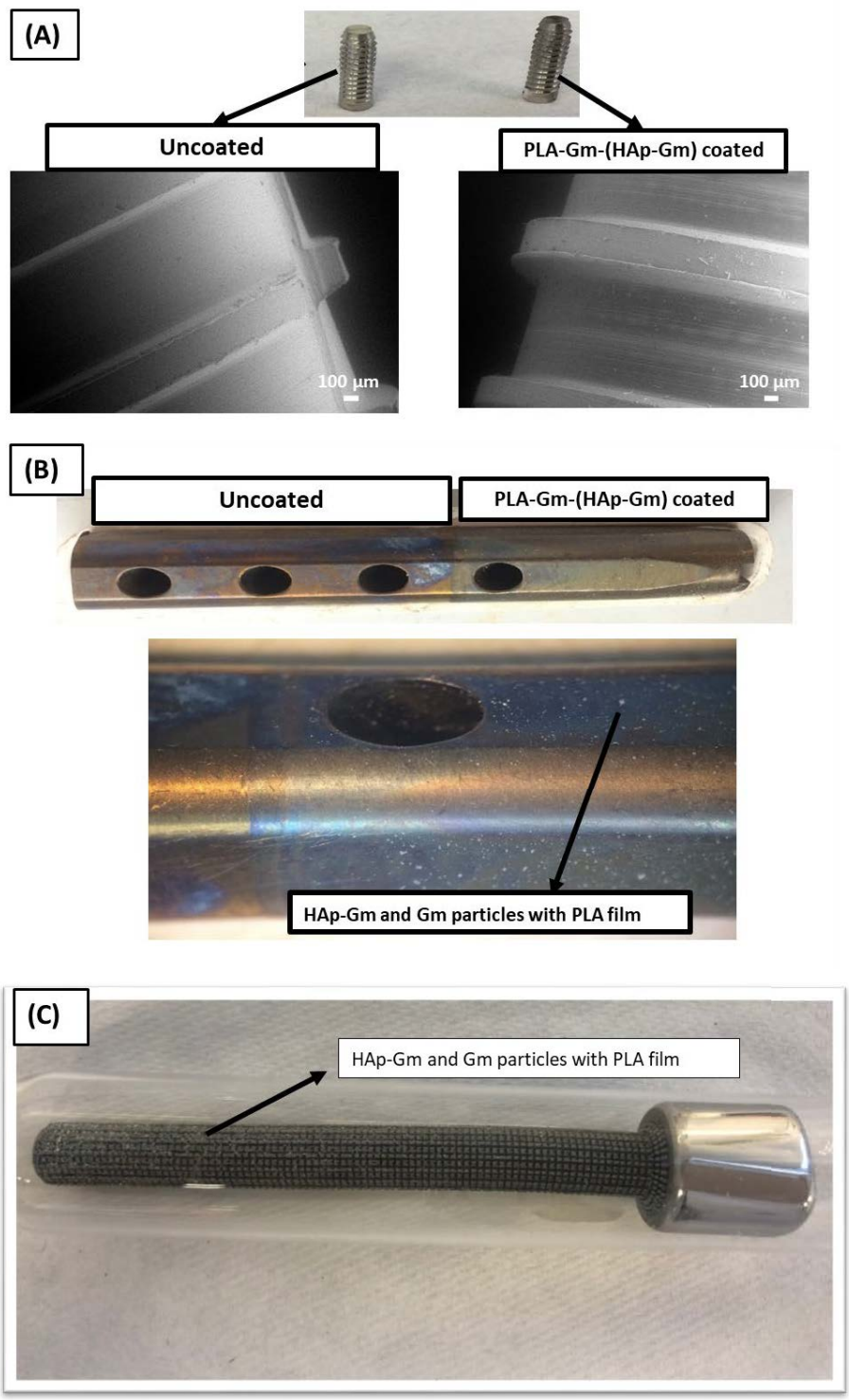

Figure 3.11 The Ti6Al4V metallic screw-shaped dental implant, Alabama, Birmingham (*A*), Huckstep intramedullary implant (*B*), and hip – amputee implant, BresMed Australia (*C*) with and without PLA-Gm-(HAp-Gm) thin film coating

3.4. Conclusion

PLA biodegradable polymeric thin films were coated on the Ti6Al4V discs and a few orthopedic and dental implants successfully without any surface or edge cracks. The Ti6Al4V discs were coated successfully with PLA-HAp, PLA-Gm, and PLA-Gm-(HAp-Gm) biocomposite thin films with the dip coating method. SEM results showed that the PLA-Gm-(HAp-Gm) coated Ti6Al4V samples at predetermined Gm concentrations (5%, 10%, 15%, 20%, and 30% w/w) have uniformly distributed Gm and the HAp-Gm particles were in various sizes ranging between 0.1 and 5 µm. They were distributed within the PLA matrix, and some agglomerated larger clusters were also observed. Surface clusters, although few, were around 10-30 µm size consisting of much smaller size particles of around 100 nm to 300 nm. In the FT-IR analysis, it was observed clearly that Gm and the HAp particles were combined with the PLA thin film matrix.

3.5 References

AHMED, J., VARSHNEY, S. K. & JANVIER, F. 2014. Rheological and thermal properties of stereocomplexed polylactide films. *Journal of Thermal Analysis and Calorimetry,* 115**,** 2053-2061.

CALHOUN, J. H., HENRY, S. L., ANGER, D. M., COBOS, J. A. & MADER, J. T. 1993. The treatment of infected nonunions with gentamicin-polymethylmethacrylate antibiotic beads. *Clin Orthop Relat Res***,** 23-7.

CHOI, A. H. & BEN-NISSAN, B. 2014. Sol-gel coatings on titanium. *In:* MATINLINNA, J. P. (ed.) *Handbook of Oral Biomaterials* Pan Stanford

CHOI, A. H., BEN-NISSAN, B. & BENDAVID, A. 2017. *Thin Films and Nanocoatings of Hydroxyapatite on Titanium Implants: Production Methods and Adhesion Testing*, LAP LAMBERT Academic Publishing.

CHOI, A. H., KARACAN, I. & BEN-NISSAN, B. 2018. Surface modifications of titanium alloy using nanobioceramic-based coatings to improve osseointegration: a review. *Materials Technology***,** 1-10.

DORATI, R., DETRIZIO, A., MODENA, T., CONTI, B., BENAZZO, F., GASTALDI, G. & GENTA, I. 2017. Biodegradable Scaffolds for Bone Regeneration Combined with Drug-Delivery Systems in Osteomyelitis Therapy. *Pharmaceuticals (Basel, Switzerland),* 10**,** 96.

FARAH, S., ANDERSON, D. G. & LANGER, R. 2016. Physical and mechanical properties of PLA, and their functions in widespread applications — A comprehensive review. *Advanced Drug Delivery Reviews,* 107**,** 367-392.

GAVASANE, A. & PAWAR, H. 2014. Synthetic Biodegradable Polymers Used in Controlled Drug Delivery System: An Overview. *Clinical Pharmacology & Biopharmaceutics,* 3**,** 121.

GOODMAN, S. B., YAO, Z., KEENEY, M. & YANG, F. 2013. The future of biologic coatings for orthopaedic implants. *Biomaterials,* 34**,** 3174-83.

INZANA, J. A., SCHWARZ, E. M., KATES, S. L. & AWAD, H. A. 2016. Biomaterials approaches to treating implant-associated osteomyelitis. *Biomaterials,* 81**,** 58-71.

KIMURA, H., OGURA, Y., MORITERA, T., HONDA, Y., WADA, R., HYON, S. H. & IKADA, Y. 1992. Injectable microspheres with controlled drug release for glaucoma filtering surgery. *Investigative Ophthalmology & Visual Science,* 33**,** 3436-3441.

LASPRILLA, A. J., MARTINEZ, G. A., LUNELLI, B. H., JARDINI, A. L. & FILHO, R. M. 2012. Poly-lactic acid synthesis for application in biomedical devices - a review. *Biotechnol Adv,* 30**,** 321-8.

LUCKE, M., SCHMIDMAIER, G., SADONI, S., WILDEMANN, B., SCHILLER, R., HAAS, N. P. & RASCHKE, M. 2003. Gentamicin coating of metallic implants reduces implant-related osteomyelitis in rats. *Bone,* 32**,** 521-31.

LYNDON, J. A., BOYD, B. J. & BIRBILIS, N. 2014. Metallic implant drug/device combinations for controlled drug release in orthopaedic applications. *Journal of Controlled Release,* 179**,** 63-75.

MACHA, I. J., BEN-NISSAN, B. & MILTHORPE, B. 2014. Improvement of Elongation in Nanosurface Modified Bioglass/PLA Thin Film Composites. *Current Nanoscience,* 10**,** 200-204.

MACHA, I. J., CAZALBOU, S., BEN-NISSAN, B., HARVEY, K. L. & MILTHORPE, B. 2015. Marine structure derived calcium phosphate-polymer biocomposites for local antibiotic delivery. *Mar Drugs,* 13**,** 666-80.

NANDI, S. K., BANDYOPADHYAY, S., DAS, P., SAMANTA, I., MUKHERJEE, P., ROY, S. & KUNDU, B. 2016. Understanding osteomyelitis and its treatment through local drug delivery system. *Biotechnology Advances,* 34**,** 1305-1317.

NIKOLIC, L., RISTIC, I., ADNADJEVIC, B., NIKOLIC, V., JOVANOVIC, J. & STANKOVIC, M. J. S. 2010. Novel microwave-assisted synthesis of poly (D, L-lactide): The influence of monomer/initiator molar ratio on the product properties. 10**,** 5063-5073.

PRIOR, S., GAMAZO, C., IRACHE, J. M., MERKLE, H. P. & GANDER, B. 2000. Gentamicin encapsulation in PLA/PLGA microspheres in view of treating Brucella infections. *Int J Pharm,* 196**,** 115-25.

SANTOS, A., SINN AW, M., BARIANA, M., KUMERIA, T., WANG, Y. & LOSIC, D. 2014. Drug-releasing implants: current progress, challenges and perspectives. *Journal of Materials Chemistry B,* 2**,** 6157-6182.

SIONKOWSKA, A., KACZMAREK, B. & GADZALA-KOPCIUCH, R. 2016. Gentamicin release from chitosan and collagen composites. *Journal of Drug Delivery Science and Technology,* 35**,** 353-359.

STROBEL, C., SCHMIDMAIER, G. & WILDEMANN, B. 2011. Changing the Release Kinetics of Gentamicin from Poly(D, L-Lactide) Implant Coatings Using Only One Polymer. 34**,** 304-316.

TOBIN, E. J. 2017. Recent coating developments for combination devices in orthopedic and dental applications: A literature review. *Advanced Drug Delivery Reviews,* 112**,** 88-100.

TRAJKOVSKI, B., PETERSEN, A., STRUBE, P., MEHTA, M. & DUDA, G. N. 2012. Intra-operatively customized implant coating strategies for local and controlled drug delivery to bone. *Advanced drug delivery reviews,* 64**,** 1142-1151.

WU, P. & GRAINGER, D. W. 2006. Drug/device combinations for local drug therapies and infection prophylaxis. *Biomaterials,* 27**,** 2450-67.

Chapter 4

Cumulative and Continuous Drug Release Studies on PLA Biocomposite Coated Implants

Chapter 4: Cumulative and Continuous Drug Release Studies on PLA Biocomposite Coated Implants

The properties and production methods of the PLA biocomposite were explained in **Chapter 3.** The system is a very suitable implant coating method for the design of controlled and long-term drug delivery systems because of its biodegradability, biocompatibility, and its relatively low and controllable degradation rate (Macha et al., 2017, Macha et al., 2019, Nair and Laurencin, 2007). The Gm antibiotic-loaded converted HAp drug carrier particle, converted from high purity coral, and the production method were explained in **Chapter 2.** It should be added that past reported work suggests that these biocomposite coatings can improve the control of the Gm release rate and extend the release time (Macha et al., 2015b).

In this current work, the HAp particles were produced from the high purity coral skeleton of the Porites genus via a hydrothermal conversion technique, based on the pioneering work of Roy and Linnehan (Roy and Linnehan, 1974, Ben-Nissan, 2003). The final converted coralline HAp is a chemically and structurally similar material to the human cancellous bone. It is biocompatible, bioactive and is a thermodynamically stable bioceramic (Ben-Nissan, 2003, Choi and Ben-Nissan, 2017, Choi et al., 2014, Macha et al., 2015a, Karacan et al., 2019). The following chapter covers the drug dissolution studies with two different methods using these composites.

In principle, this chapter provides the background for the combination of the PLA biocomposite drug delivery system and the determination of their drug release stages and patterns. Specifically, the main aim of this chapter is the determination of Gentamicin antibiotic (Gm) release patterns from two biocomposites, namely PLA-Gm and PLA-Gm-(HAp-Gm) thin film coated Ti6Al4V implant discs. We investigated two commonly used dissolution methods; the first is called the Continuous Dissolution Method and the other is the Cumulative Dissolution Method. A comparison between the Cumulative and Continuous Dissolution Methods was also carried out to obtain the Gm release patterns. In addition the effect of the different dissolution mediums such as PBS solution and ultra-pure water was carried out to determine the effects of the dissolution medium on the biocomposite degradation mechanisms.

4.1 Introduction

Next-generation multifunctional implantable systems, which include the function of the drug delivery systems, have been proposed in order to advance the osseointegration of bone implants and improve bioactivity and prevent toxic metallic ion dissociations (Chou et al., 2011, Chou et al., 2013a, Chou et al., 2013b, Choi et al., 2015).

Controlled drug delivery systems have very diverse applications for biomedical development. The systems can be modified with appropriate biomaterial selection, which can, in turn, be used as the matrix for incorporating different types of pharmaceuticals or minerals for various types of treatments. Based on the type of application, the implantable drug delivery systems are designed to enhance the effectiveness of the drug by controlling the long-term drug release rate while reducing or limiting the adverse side effects (Rajgor et al., 2011, Chou et al., 2013a).

Recent research in combination with drug delivery systems and metallic medical implants, including dental and orthopedic implants, shows that these natural and/or synthetic biodegradable polymers such as collagen or poly-lactic acid (PLA) can be used with other additives to deliver controlled dissolution rates.

It has been widely accepted that the most important challenges during any surgery or insertion of bone implants are implant-related postoperative infections, lack of osseointegration, and difficulty of bone regeneration (Ben-Nissan et al., 2016, Macha et al., 2016).

In general, when implant-related infections are observed, the worst scenario is to replace them with the new implant (revision surgery), which could be very painful, and sometimes surgically complicated. Another solution is to apply different conventional antibiotic therapies, which are not always successful treatments (Wu and Grainger, 2006, Aviv et al., 2007). Therefore, many researchers have been focusing on the use of new multifunctional bioactive coated implants for in situ drug delivery to prevent postoperative complications and/or treat certain bone diseases such as osteomyelitis. It has been reported that using specific drug release systems made of composites for implant coating is very effective in the prevention and treatment of these infectious diseases (Chou et al., 2011, Macha et al., 2014).

According to published work, the 10% Gm loaded poly (D, L-Lactideta) (PDLL) coated orthopedic devices have significantly reduced implant-related infections in the animal model (Lucke et al. 2003). It was also reported that approximately 80% of the Gm was released within 48 hours (Lucke et al., 2003). Dissolution rates depend on the chemistry of the matrix, the amount of the additives

and types, thickness of the films, surface area, and the micro and nanoporosity, which controls the dissolution rates and amounts. Additionally, Vester et al. (2010) have reported that the 10% Gm loaded PDLL film-coated metallic implants successfully reduced bacterial adhesion and prevented the biofilm formation for seven days' release observation and in vivo results. The designed specific system releases more than 60% Gm in one minute, and then the slow release was observed for 48 hours (Vester et al., 2010).

As stated above, dependent on several factors the biodegradable polymeric coatings have some limitations, especially uncontrollable drug release kinetics and in some polymeric composites the lack of chemical stability. It was suggested that these biodegradable polymeric drug delivery systems should be applied only in short term drug release conditions (Montanaro et al., 2011). However, this approach is controversial due to a number of material and surface factors that influence the dissolution of these coatings. In addition to factors mentioned earlier, the type of drug used, the dimensions and geometry of the drug delivery system, and the environmental conditions during drug release are some additional factors that influence the drug release behavior (Siepmann and Siepmann 2008).

Several other problems can be observed during the use of orally consumed antibiotics; high dosages can be released in a very short time period, which can cause adverse effects through over-dosing. The resultant release period (one to three months) might not be enough for the proper treatment of the early infection period and post-surgery (Montanaro et al., 2011).

In order to improve the control mechanisms of drug release kinetics for the biodegradable polymeric coating on the implants, bioactive particles such as bioceramics or bio-glasses are used as drug carriers both as coating or as monolithic solid loaded subcutaneous delivery systems (Chou et al., 2011, Simchi et al., 2011). Biodegradable polymer-bioceramic composites are an especially ideal approach as a drug delivery system included implant coating material. This is because of the bioactive nature of the ceramic materials that stimulate tissue growth (Chou et al., 2013). The bioceramics in the biodegradable polymers will improve the controlled drug release, bioactivity and biocompatibility (Macha et al., 2016).

Accelerating the applied research on biodegradable polymer-bioceramic composites has been proposed during the last decade. This can be designed as drug delivery coating systems for improving the control of the initial drug release and to obtain long-term steady-state drug release profiles for the inhibition of implant-related infections (Aviv et al., 2007, Ben-Nissan et al., 2016). It has been proposed that in biodegradable polymers, the degradation of the polymeric matrix occurs through the cleavage of covalent bonds by chemical reactions. Degradation can occur in the bulk of

the material and on its surfaces with various mechanisms. For the dissolution, the surrounding aqueous solvent of the biodegradable polymer must penetrate through to the polymer, and the water or the solution from the environment must interact with it via a charge interaction or diffusional processes. It has been reported that some of the biodegradable synthetic polymers such as polylactic acid, and poly(ε-caprolactone) depend on the hydrolytic cleavage of ester bonds (Park et al., 1993, Nair and Laurencin, 2007, Liechty et al., 2010). Some of the drug release studies published have reported that release behavior of active substances (such as antibiotics) from biodegradable materials might contain three common release stages (Rothstein et al., 2009, Stephens et al. 2000, Macha et al., 2019).

Stage I

Stage I is typically known as ‘‘the initial burst”. Stage I is the accelerated initial release of the drug particles or drug-loaded particles on or adjacent to the biodegradable matrix by dissolution so that it can be categorized as a surface release. The burst release depends on the surface characteristics of the biodegradable matrix, drug solubility, the environment, and the percentage of the drugs adjacent to the biodegradable matrix. The initial burst release is a first-line factor interfering with the zero-order rule (Chinna Reddy et al., 2011, Pokrowiecki, 2018, Macha et al., 2019)**.**

Stage II

The polymer chains from the polymeric matrix begin to degrade after the initial burst release occurs. Soluble oligomers are produced, and chain mobility effectively increases due to the rise in the number of pores in the polymer matrix. The formation of pores is due to the heterogeneous degradation of the polymer matrix and starts with an amorphous region of the polymeric matrix. The surface porosity creates a suitable environment for the fluid transport phenomena, and it is essential for the release of drugs from the polymeric matrix. Stage II refers to internal drug release. The drug release by diffusion can be controlled by the mass transfer process within the narrow pores (Fredenberg et al., 2011, Macha et al., 2019). Degradation and diffusion are the most dominant mechanisms at this stage.

Stage III

While the degradation of the polymer matrix progresses, the pores on the matrix get larger and start to coalesce. Therefore, the dissolution buffer solution penetrates into the polymer matrix, which hydrolyzes the polymer and increases the degradation rate. The penetration of the dissolution buffer into the polymer matrix provides the channels required for the drug particles to dissolve the matrix and transport them by a diffusion mechanism where the drug is transported to the surface of the polymeric matrix. The release of the drug continues until the complete degradation of the polymeric

matrix is achieved (Fredenberg et al., 2011, Macha et al., 2017, Macha et al., 2019). The above stages do not take into account the dissociation of the other additives within the matrix, such as hydroxyapatite particles used in our studies and the related influence in dissolution and drug release.

In our experimental work, it was first postulated and then observed that possibly during the second (and definitely during the third) stages, the coralline HAp particles release the drugs that incorporated in its nano and mesopores. After the initial dissolution of the drugs in these nano and mesopores, the structure of HAp or calcium phosphate degrades. More particles are generated and dissolved, which diffuses or migrates to the surface and dissolves within the surrounding environment. The incorporated drugs and dissociated calcium phosphate ions diffuse into the liquid environment, which will be migrating through the body and synovial fluids during the implantation.

Drug dissolution rate determination methods such as the Cumulative and Continuous methods and related kinetic calculations have been used to measure the drug release patterns of the drug-loaded biodegradable polymeric or natural material (such as foraminifera) matrix systems (Chou et al., 2014, Macha et al., 2017).

In this chapter, drug release studies of the Gm antibiotic from the PLA-Gm and PLA-Gm-(HAp-Gm) thin film coated Ti6Al4V discs were carried out. With this current approach, it is envisaged that this current research will supply a simulation of the dissolution of HAp drug carrier particles on the future bone implants in a simulated body environment. In addition, both the Cumulative and Continuous Dissolution Methods will be compared to identify the most appropriate method.

4.2 Experimental Methods

The dissolution study was conducted with two common methods, namely; the Continuous and Cumulative drug release methods for obtaining Gm release patterns from PLA-Gm, and PLA-Gm-(HAp-Gm) coated Ti6Al4V discs under SINK conditions, which were immersed in 0.1M phosphate buffered saline (PBS) solution.

PBS tablets (Astral Scientific; [0.14 M NaCl, 0.0027M KCl, 0.01M Phosphate buffer, pH 7.4]) were dissolved in ultrapure MilliQ water (1 PBS tablet in 100mL) at room temperature and the PBS solution was sterilized within an autoclave.

For the drug release experiment, PLA thin film coated Ti6Al4V discs were used as a control sample. PLA-Gm and PLA-Gm-(HAp-Gm) thin film coated Ti6Al4V discs at predetermined Gm concentrations

(5%, 10%, 15%, 20% and 30% w/w) were prepared to determine the Gm release with and without the HAp drug carrier particles. All prepared disc samples were sterilized under UV light, for 10 minutes each side. Each disc was placed into a tightly sealed plastic vial (to avoid any evaporation) with a 10ml sterile PBS solution. The prepared containers were then placed into a temperature-controlled water bath shaker (sw23 water bath, John Morris scientific, USA) mixing at a constant speed of 100 rpm at 37 ± 0.1 °C.

The diagram showing the steps from the dip coating process to the drug dissolution point is given in *Figure 4.1*. The experimental steps, shown in *Figure 4.1* are the same for both the Continuous and Cumulative methods. Only the number of vials and the sampling techniques are different.

4.2.1 Continuous Dissolution Method

In this method every sample was placed in a vial and after each predetermined time period an individual vial was removed to measure the amount of Gm.

The Gm concentrations of each vial was determined using a Cary 100 UV-Vis spectrophotometer (Agilent Technologies, Victoria, Australia, Cary Series UV-Vis Spectrophotometer) with a quartz cuvette at a maximum absorbance for the gentamicin-o-phthaldialdehyde complex, (λmax = 332 nm), via the procedures described in **Chapter 2**.

4.2.2 Cumulative Dissolution Method

The Cumulative Dissolution Method involves a single sample vial where the dissolution products containing liquid was removed as a function of time, and the same amount of new solution was added to the container (Chou et al., 2014, Nojehdehyan et al., 2016). After the removal of a specific amount of solution, the Gm concentration of the PLA-Gm and PLA-Gm-(HAp-Gm) coated Ti6Al4V samples were determined in a similar method, by using Agilent Technologies, Victoria, Australia, Cary Series UV-Vis Spectrophotometer with a quartz cuvette at a maximum absorbance limit of gentamicin-o-phthaldialdehyde complex, (λmax = 332 nm) using procedures described in **Chapter 2**.

The following processes used are the same for both Continuous and Cumulative methods: 2.5g of the O-phthaldialdehyde reagent was prepared by dissolving in 62.5ml methanol and by further adding 3ml of 2-hydroxyethylmercaptan to 560ml, and of 0.04M sodium borate in ultrapure MilliQ water. The reagent was stored in a brown bottle in darkness and settled for at least 24 hours prior to use (Aviv et al., 2007).

Further, to the above, 1ml of the sampling solution from the PLA biocomposite thin film coated Ti6Al4V discs embedded PBS solution (for each predetermined time point), 1ml O-phthaldialdehyde reagent and 1ml Isopropanol were mixed and incubated for 30 minutes at room temperature. In this environment, the O-phthaldialdehyde and gentamicin react with each other and a complex molecule is formed; easily detectable at a 332 nm wavelength.

In order to convert the absorbance values of Gm in the PBS solution to the vial concentration values, a standard curve was prepared with six different Gm-PBS solutions at known Gm concentrations (0.250, 0.125, 0.062, 0.031, 0.016 mg/ml). The absorbance values of six different Gm-PBS solutions were measured as described above, then the standard absorbance values versus the concentration graph was plotted to obtain unknown -measured -Gm concentrations. A calibration curve for gentamicin in PBS was plotted before each measurement.

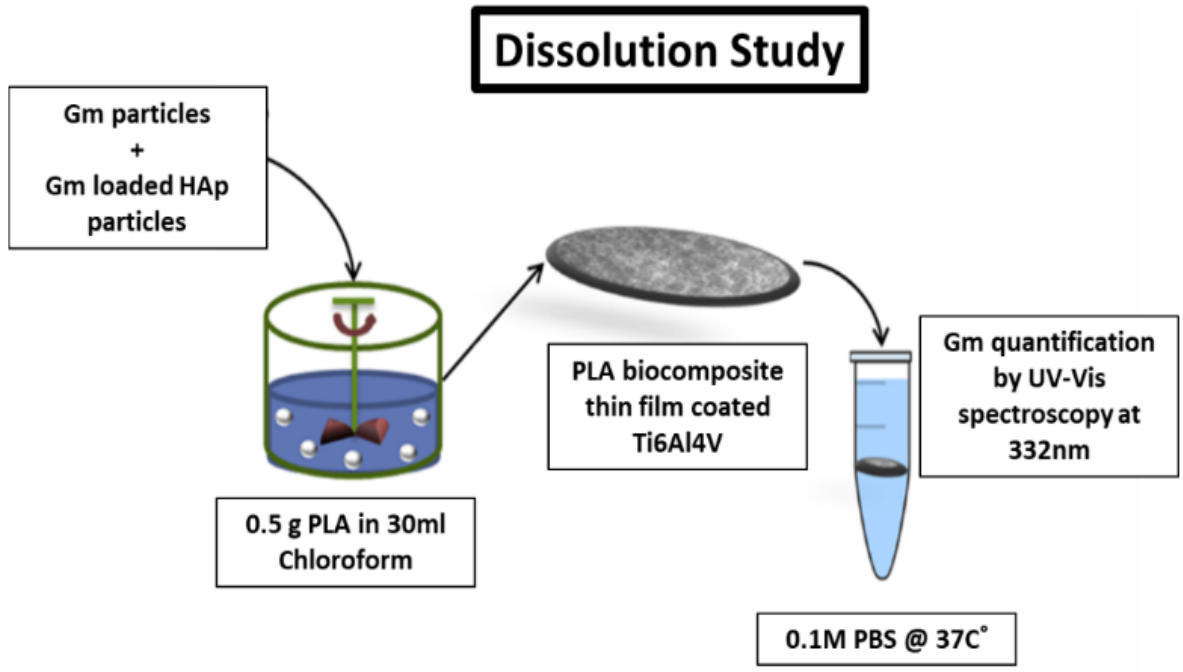

Figure 4.1 The diagram for the dissolution study to obtain Gm amount release from the PLA thin film biocomposite

4.2.3 Surface Morphology and Chemical Characterization Analyses

4.2.3.1 Scanning Electron Microscope (SEM) and Energy-Dispersive Spectroscopy (EDS)

The surface morphology and chemical composition of the PLA and PLA biocomposite thin film coated Ti6Al4V discs before and after the dissolution study were established by Scanning Electron

Microscopy (SEM) (ZEISS Supra SSVP, Zeiss, Germany) which was equipped with an EDS analyzer. The samples were sputter-coated with a 7nm thin layer of Au/Pd (Leica EM ACE600 Sputtering and Carbon Thread Coater, Germany) in order to reduce charging. The samples were kept under vacuum overnight to remove any moisture before the imaging process. Images were taken at various magnifications and at acceleration voltages of 5-15 kV.

4.2.3.2 Fourier-transform infrared spectroscopy (FT-IR)

The FT-IR spectra of the PLA biocomposite thin film coated samples were collected at Nicolet FT-IR (Nicolet, Magna-IR 6700 Spectrometer FT-IR, Thermo-Scientific, Madison, USA), using the ATR mode, from wave number 2000 to 200 cm^{-1} at a resolution of 4 cm^{-1}.

4.3 Results and Discussions

4.3.1 Gm release pattern from PLA thin film biocomposite coated Ti6Al4V discs with the Continuous in vitro dissolution method

The in vitro Continuous Dissolution Method was utilized on both the PLA-Gm and PLA-Gm-(HAp-Gm) thin film coated Ti6Al4V discs, which had predetermined Gm concentrations (5%, 10%, 15%, 20% and 30% w/w). The tests were carried out for 30 days. The experiment was designed to obtain the differences of the Gm release patterns for the PLA coated Ti6Al4V system with and without HAp bioceramic particles to indicate the release profiles of the composites.

The early stages, which were given in the introduction to this chapter, have been reported to depend on the particle size and amount and to their dissociation rates. It is thought that in our experimental condition where a number of different mixtures were experimented, including HAp particles, the order of dissolution progress mainly depends on the experimental environmental conditions.

It is postulated that if the composite has additional HAp particles, the stages might involve the following steps:

(i) Burst effect: the surface drug release from the PLA coated implant surfaces, dissolution of large loosely bound agglomerated clusters and smaller Gm particles shown in the following *Figure 4.2*,

(ii) PLA matrix dissolution due to the drug release from the surface, and the surface deterioration, pore formation, delamination of the matrix and the release and transport of the drug from within the matrix to the surface and into the solution,

(iii) Drug release from HAp particle surfaces and interconnected open pores, HAp particle deterioration and dissolution and further drug release,

(iv) Combination of all three above-mentioned stages at once due to the simultaneous breakdown of the matrix (PLA) and the HAp particles and further release.

As stated above, the drug release rates depend on the number of material and environmental factors, but it was also observed that the initial stage was faster for the PLA-Gm composite than the PLA-Gm-(HAp-Gm) composite. Knowing the inclusion of the HAp particles, which have lower dissolution rates, which in turn are dependent on the particle size and composition, it is not surprising that this can affect the dissolution rates. Following the dissolution results these anticipated stages and transport mechanisms are reinforced.

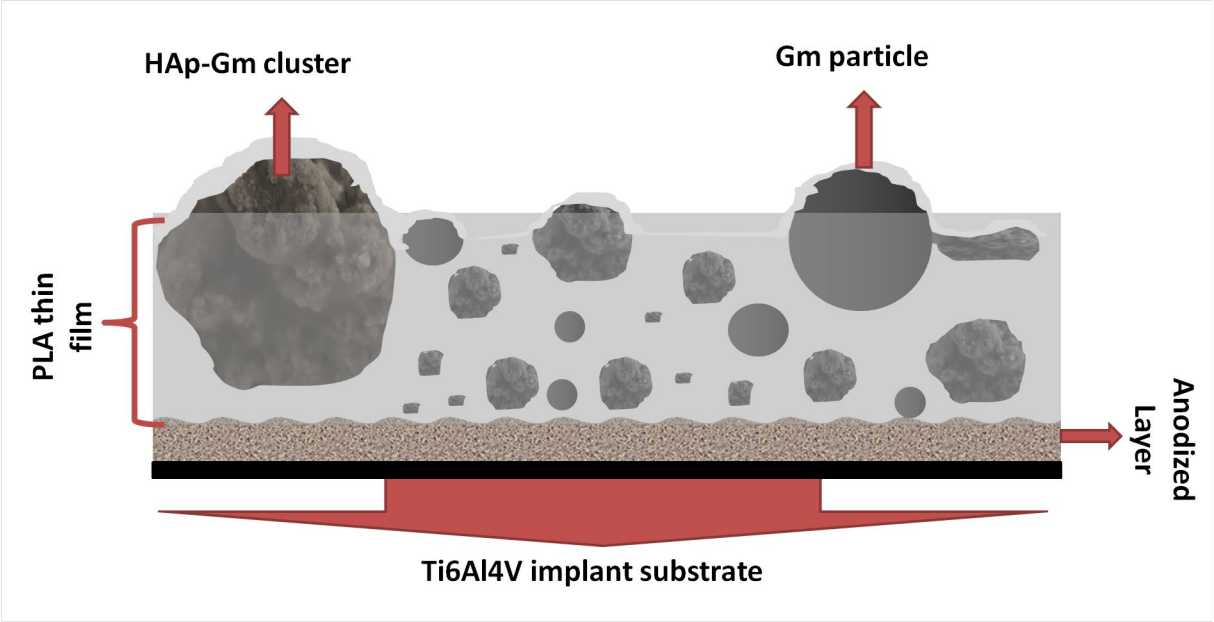

Figure 4.2 Schematic diagram of the proposed cross-sectional view of the biocomposite, showing possible particle size distribution and dissolution paths

The cross-section shows the Ti6Al4V substrate, the thermally anodized layer that will be explained in detail in **Chapter 5** and the PLA biocomposite matrix showing large clusters and small particles of Gm and the coralline HAp on both the surface of the composite and within the matrix.

The Gm release pattern of the composites in PBS during the 30 day tests are shown in *Figure 4.3* for both the PLA-Gm (*A*) and PLA-Gm-(HAp-Gm) (*B*) coated Ti6Al4V discs at Gm concentrations of 5%, 10%, 15%, 20% and 30%. The first and second stages were observed during 30 days of dissolution studies in both systems with and without HAp (drug carrier particles). There is no full PLA degradation in this 30-day period, although the surface PLA layer coating the clusters and the Gm particles might start at this stage dependent on their thickness. However, an immediate burst release was clearly observed. The release mechanisms can be postulated as a combination of the dissolution of the surface Gm and diffusion mechanisms. After the burst release of loose surface particles, degradation of the PLA and the later stage dissociation of HAp particles trigger the dissolution and hence influence the diffusion rates of the drug.

It is possible that the first stage consists of only the surface bound Gm release. It is a fast detachment from the surfaces by dissolution and diffusion that includes Gm from both PLA thin film and some HAp particle surfaces exposed to the environment. The first stage, the “initial burst effect” is observed from just few hours after the beginning of the experiment and up to the third day for our discs. It depends on the sample size and time (t = Day 0–3) and this stage is relatively faster than next stages.

After the initial burst effect, the second stage, “internal release” depends on the degradation of the PLA thin film matrix which contributes to slow drug delivery. The dissolution rate and path at this second stage includes a number of sub-stages dependent on the size of the delivery substrate, the drugs, particles used and the environment (t = Day 3-30). In this stage, the PLA thin film matrix starts to degrade and allows the liquid medium to penetrate into the PLA thin film for the release of Gm particles embedded in the PLA thin film for the PLA-Gm and PLA-Gm-(HAp-Gm) coated Ti6Al4V samples. The second stage Gm release for the PLA-Gm-(HAp-Gm) coated Ti6Al4V samples allows the PBS liquid to penetrate into the HAp particles where the HAp surface-bound drug attached to meso and nano pores starts to dissolve and diffuse out. The dissolution rate is slower due to the strong inorganic nature of HAp drug carrier particles. Therefore, the time required for the Gm to diffuse out from the HAp particles is much longer than the initial burst stage and hence the delay in release occurs for the required slow drug delivery. In *Figure 4.3* the plateau observed in this stage is representative of this mechanism and behavior.

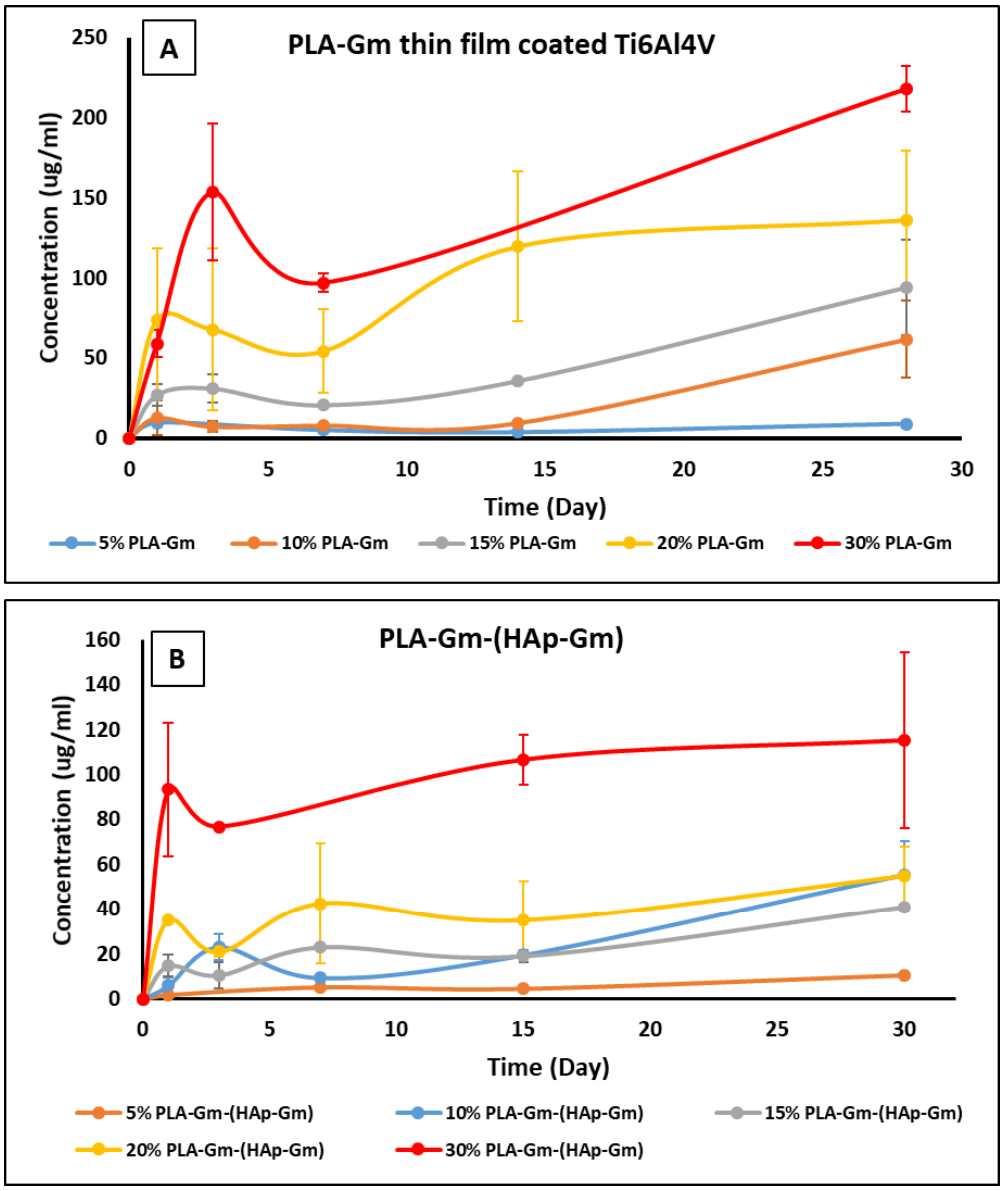

Figure 4.3 Gm release results of (A) PLA-Gm and (B) PLA-Gm-(HAp-Gm) coated Ti6Al4V discs at 5%, 10%, 15%, 20% and 30% Gm concentrations for 30 days dissolution experiment in 10ml PBS solution (Error bars refer to the mean values (SEM) of the data)

In *Figure 4.3,* in order to show the effects of the slow dissolution of the HAp drug particles, the PLA-Gm and PLA-Gm-(HAp-Gm) thin film coated Ti6Al4V discs containing the 5%, 10%, 15%, 20% and 30% Gm concentrations are compared.

In the PLA-Gm thin film coated sample; after Day 1, the recorded Gm drug release concentrations (see *Table 4.1*) were 9.56µg/ml for the 5% Gm containing discs; 12.65µg/ml for the 10%; 26.90µg/ml for the 15%; 105.25µg/ml for the 20% and 59.06µg/ml for the 30% Gm samples. However, after Day 7 the drug release (observed in *Table 4.1*) was 5.05µg/ml Gm for the 5%; 8.00µg/ml for the 10%;

20.63µg/ml for the 15%; 54.29µg/ml for the 20% and 96.97µg/ml for the 30% Gm samples. A good correlation between the differing amounts of Gm from 5% to 30% was observed in the PLA-Gm coated samples without additional particles.

In the PLA-Gm-(HAp-Gm) thin film coated samples; after Day 1 the drug release concentration (observed in *Table 4.1*) was 1.98µg/ml for the 5% mixture; 5.83µg/ml for the 10%; 14.58µg/ml for the 15%; 34.81µg/ml for the 20% and 93.35µg/ml for the 30%.

After Day 7 the drug release concentration (see *Table 4.1*) was 5.29µg/ml for the 5% mixture; 9.31µg/ml for the 10%; 22.88µg/ml for the 15%; 42.38µg/ml for the 20% and 121.48µg/ml for the 30% PLA-Gm-(HAp-Gm) thin film coated Ti6Al4V. The dissolution plots of the PLA-Gm-(HAp-Gm) coated Ti6Al4V samples show a good correlation between the differing amounts of Gm concentrations. It was observed that the initial burst release rate of Gm increases with an increased Gm concentration (from 5% to 30% Gm).

Table 4.1 The average Gm release concentrations after Day 1 and Day 7 for PLA-Gm and PLA-Gm-(HAp-Gm) thin film coated Ti6Al4V discs

	PLA-Gm/ Day 1	PLA-Gm/Day 7	PLA-Gm-(HAp-Gm) / Day 1	PLA-Gm-(HAp-Gm) / Day 7
5%	9.56 µg/ml	5.05 µg/ml	1.98 µg/ml	5.29 µg/ml
10%	12.65 µg/ml	8.00 µg/ml	5.83 µg/ml	9.31 µg/ml
15%	26.90 µg/ml	20.63 µg/ml	14.58 µg/ml	22.88 µg/ml
20%	105.25 µg/ml	54.29 µg/ml	34.81 µg/ml	42.38 µg/ml
30%	59.06 µg/ml	96.97 µg/ml	93.35 µg/ml	121.48 µg/ml

According to the data above, as expected the initial burst of Gm release is higher and faster for the PLA-Gm biocomposite than for the PLA-Gm-(HAp-Gm) coated Ti6Al4V samples. The Gm release was observed as a gradual increase from Day 1 to Day 30 for the PLA-Gm-(HAp-Gm) coated Ti6Al4V samples. However, instead of two large Gm release spikes like in the PLA-Gm coated samples, a gradual and relatively slow Gm release pattern was observed for the PLA-Gm-(HAp-Gm) coated samples.

The difference in the Gm release pattern between the PLA biocomposite thin film coated Ti6Al4V discs with and without HAp drug carrier microspheres might be explained by the existence of HAp particles that can prolong the Gm release time. This is due to a number of factors such as the diffuse path of Gm from the meso and nano pores of HAp particles, the PLA thin film surface area and hence

the HAp particle/PLA interfaces. In conclusion, the HAp particles affect the drug release rates and they are appropriate for the slow drug delivery system design.

Macha *et al.* (2017) in their thin film studies, reported on the Gentamicin and Bisphosphonate drug release patterns from PLA thin film with and without HAp microspheres, and their relations with the theoretical in vitro drug release stages (Macha et al., 2016, Macha et al., 2017). While their study was based only on the PLA biocomposite film without any substrate, both sides of the film were in contact with the dissolution medium. Curling of the thin films in the solution was observed and influenced the dissolution kinetics. However, in this current study, the PLA biocomposite thin film coated Ti6Al4V discs were utilized and one side of the PLA thin film was blocked by the Ti6Al4V substrate which influenced the dissolution rate and mechanisms. We also obtained similar patterns to the bisphosphate experiment for the stage I and stage II dissolution.

4.3.2 Surface morphology of PLA thin film biocomposite coated Ti6Al4V discs during the Gm release study (SEM and EDS)

The morphological changes of the PLA biocomposite thin film coated Ti6Al4V discs were carried out using SEM and EDS. There are a number of factors that can be controlled in order to obtain a slow and controlled drug release system: the degradation rate of the polymeric matrix (PLA), the type of pharmaceuticals used (the Gm antibiotic), and the properties of drug carrier particles (Coral derived HAp). Therefore, it can be postulated that the slower the degradation rate is, the longer the release time is.

The surface morphology of PLA thin film coated Ti6Al4V discs without Gm and HAp-Gm particles were analyzed by SEM and EDS after 7 and 30 days of dissolution studies (in PBS solution) in order to observe the degradation pattern of the PLA polymeric matrix.

The SEM results (*Figure 4.4*) show the surfaces of the PLA thin film coating on Day 7 (*Figure 4.4 B*) which is exactly the same as Day 0 (*Figure 4.4 A*). However, some precipitation was also observed on the PLA thin film surface on Day 30 (*Figure 4.4 C*). The chemical composition of the precipitate particles was analyzed by EDS. In the EDS mapping (*Figure 4.4 C and D*), the precipitate particles were identified as Na and Cl ions possibly NaCl precipitates due to the chemical composition of the PBS solution.

Once the biodegradable polymers contacted the biological media (PBS solution in our simulated experiment) it was reported that they started to break down via hydrolysis. PLA degrades into lactic

acid (LA) and to carbon dioxide and water with the hydrolytic cleavage of ester bonds (Gavasane et al., 2014, da Silva et al., 2018). The degradation rate of PLA depends on many factors such as pH, temperature, contacting body fluid type, and also bacterial infection which increases the degradation rate of the polymer due to enzyme secretion (da Silva et al., 2018). The diffusion of the PBS solution into the PLA matrix causes the degradation of the PLA microstructure, which occurs both on the surface and inside the polymer, through the formation of internal cavities (Agarwal et al., 1998). Additionally, da Silva et al. (2018) reported the effect of temperature on the degradation of PLA, and that the degradation rate increases 4 folds in a 37 °C solution, which is similar to body temperature (da Silva et al., 2018).

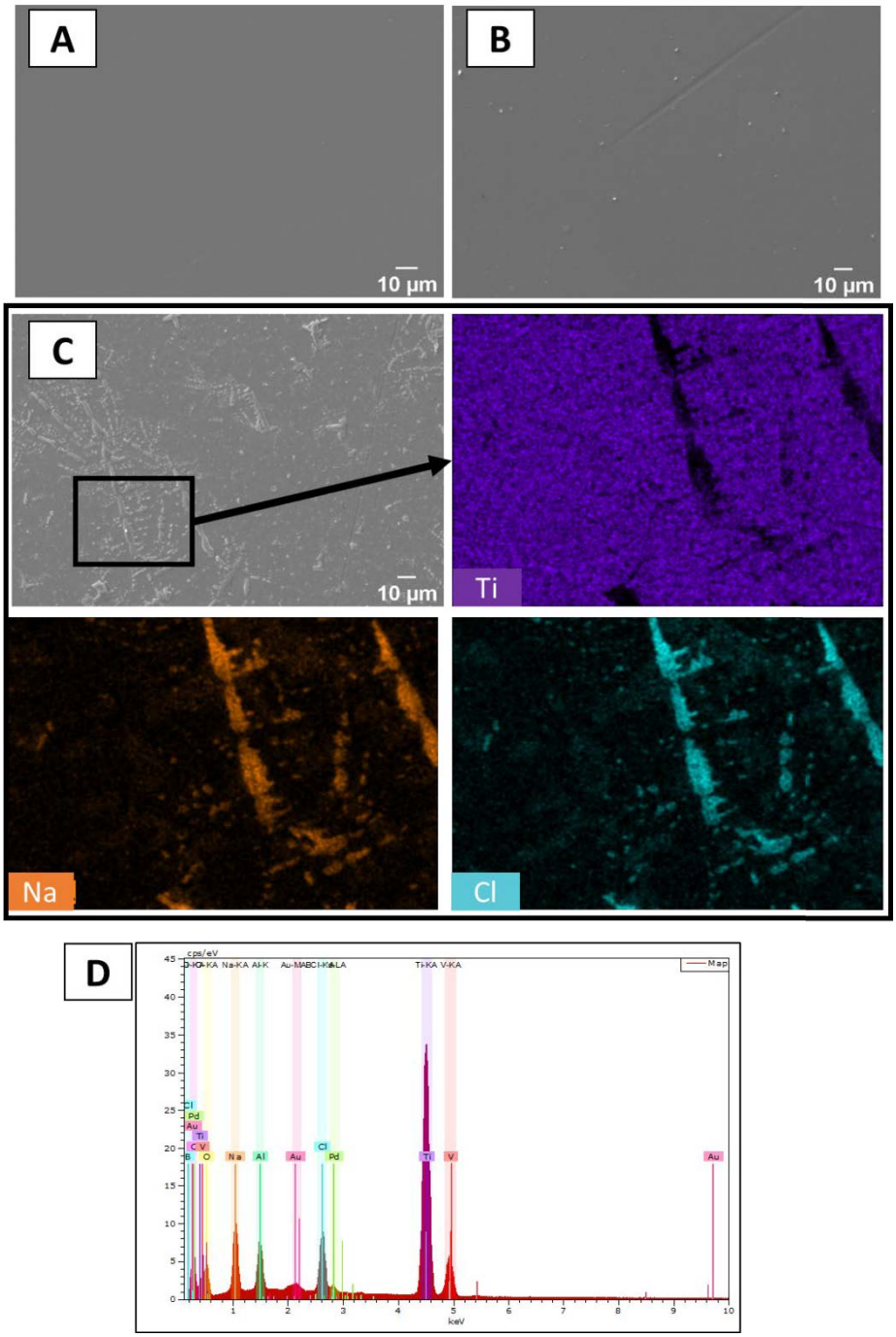

Figure 4.4 The surface observations of PLA coated Ti6Al4V discs for the drug release study at Day 0 (A), Day 7 (B), Day 30 (C) with EDS-surface mapping results with the EDS spectra (D)

Figure 4.5 represents the morphology comparison of the PLA-Gm thin film coated Ti6Al4V discs' surfaces at 5%, 10%, 15%, 20% and 30% Gm concentrations before (Day 0) and after (Day 30) the dissolution experiment. Day 0 shows the Gm particles and agglomerated clusters which are mostly on the surface and covered with a thin PLA film or partially embedded into the PLA matrix depending on their size. The average particle size of Gm particles in the PLA thin film is 1-10 µm, and Gm

particles or “clusters” as partially embedded or on the PLA thin film is around 10-50 µm as explained in detail in **Chapter 3** and shown schematically in *Figure 4.2*. Due to these different particle distribution patterns, it is assumed that thickness of the film changes in certain areas dependent on these clusters, however the number of these large particles and clusters is very small in comparison with the rest of the matrix.

After the dissolution on Day 30, empty holes were seen on the PLA-Gm thin film coated Ti6Al4V discs as shown in *Figure 4.5.* This figure shows that nearly all large and some of the small sized Gm particles were released or removed from the surface of the composite after 30 days of the dissolution experiment and hence it affects the burst rate. Although PLA film early stage degradation was only found on the PLA film area around the Gm particles, which are the weakest PLA film coating areas due to size of Gm particles, the rest of the PLA thin film surface areas without the Gm particles remained relatively without a major degradation as shown clearly in *Figure 4.4*. The figures given represent only selected areas while the morphology explained is very relevant to the full surface area of the coating.

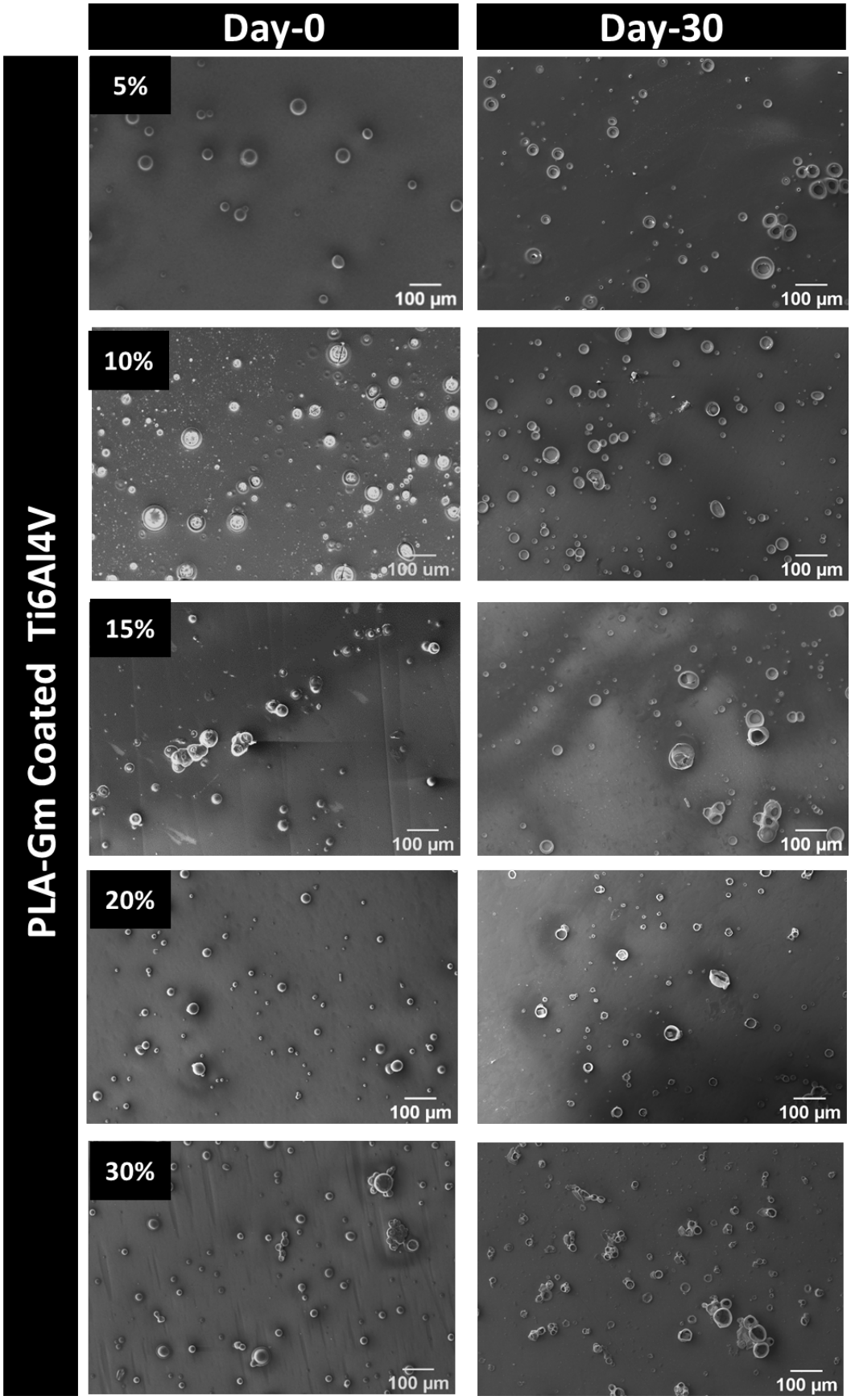

Figure 4.5 The surface observations for PLA-Gm coated Ti6Al4V discs at 5%-30% Gm concentrations before and after (Day 0 and Day 30) the drug release study

EDS mapping results on the PLA-Gm thin film coated Ti6Al4V surface after Day 30 of the dissolution experiment, showed spherical pore-like blisters (*Figure 4.6*). EDS mapping results proved that the spherical blisters observed are holes on the PLA thin film coating from the Gm release. There wasn't any white precipitation due to the NaCl, because EDS spectra gives only Ti, Al and V peaks.

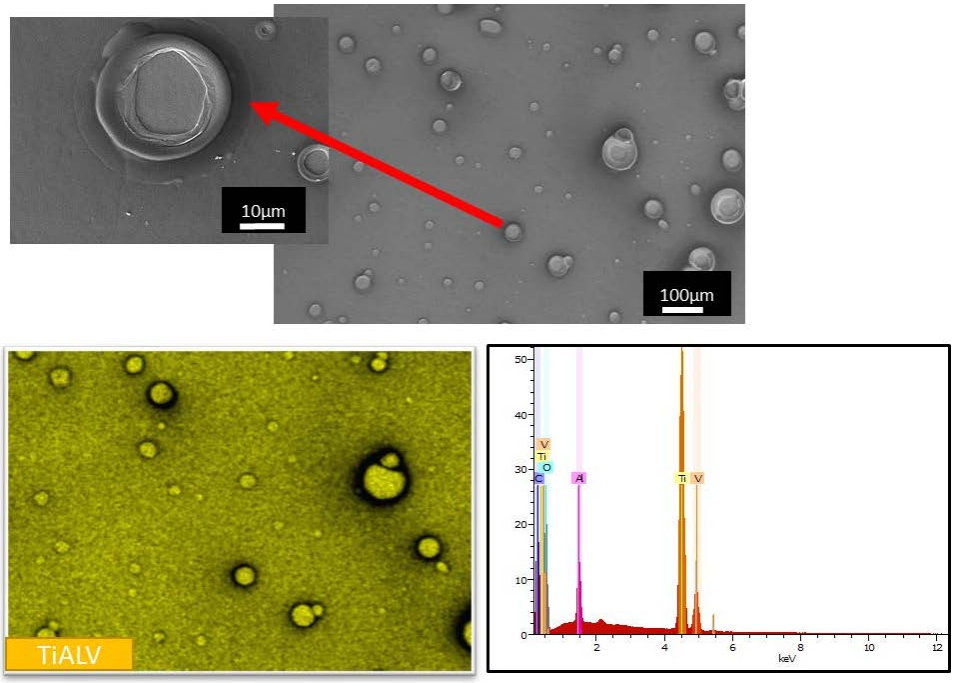

Figure 4.6 The surface observation and EDS-surface mapping results for PLA-Gm coated Ti6Al4V discs after the drug release study (Day 30)

In comparison to the above study (*Figure 4.5*), which only included Gm, *Figure 4.7* represents the morphology of the HAp containing PLA-Gm-(HAp-Gm) thin film coated Ti6Al4V discs at predetermined Gm concentrations (5% to 30% w/w) before (Day 0) and after (Day 30).

As explained in **Chapter 3**, the general structures of Gm and HAp-Gm particles on the PLA thin film matrix exists in agglomerated forms with different sizes on Day 0. The distribution of drug and HAp drug loaded particles within the PLA matrix coating on the Ti6Al4V discs is uniform. The particle size of HAp-Gm microspheres in the PLA thin film is varied; they are approximately 0.1-5 µm. The system contains agglomerated HAp-Gm particles which are around 10-30 µm in size and in addition to the matrix they can be observed on the surfaces of the films. The particle size and distribution analyses were covered in detail in **Chapter 3**.

After 30 days of the dissolution study, the PLA-Gm-(HAp-Gm) thin films still contained some of the HAp-Gm agglomerated particles.

Additionally, the SEM results for Day 30 show some holes on the surface from the release of Gm particles. These holes are similar to the Day 30 results for the PLA-Gm thin film coated Ti6Al4V surface shown in *Figure 4.5*.

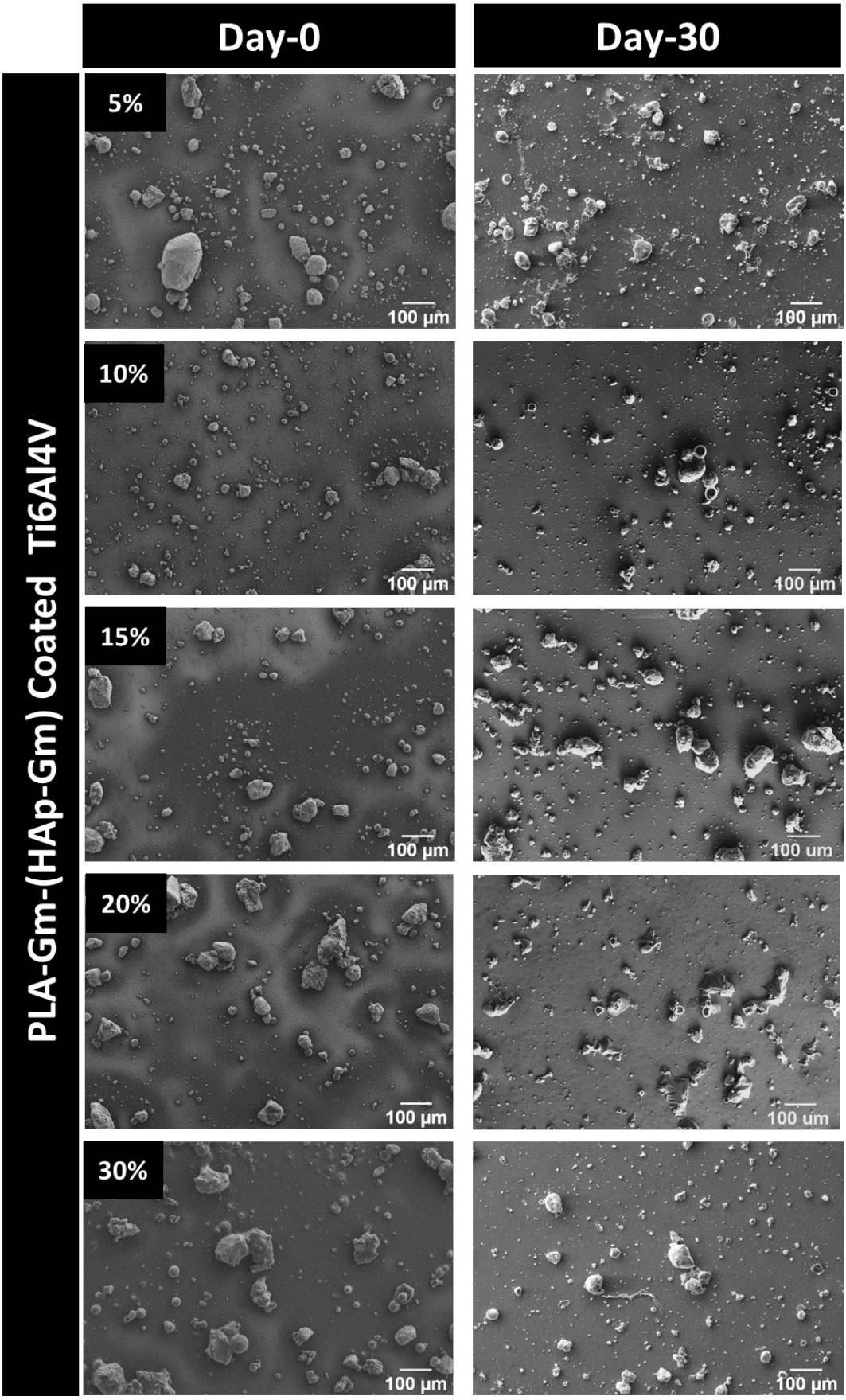

Figure 4.7 SEM surface observations of PLA-Gm-(HAp-Gm) coated Ti6Al4V discs at 5%-30% Gm concentrations before and after (Day 0 and Day 30) the drug release study

The particles observed on the surface of the PLA-Gm-(HAp-Gm) thin film coated Ti6Al4V disc on Day 30, were identified as HAp particles by EDS analysis as shown in *Figure 4.8*. According to the EDS mapping results, Ca and P elemental maps directly match with the particles on the surface in *Figure 4.8* confirming hydroxyapatite. Additionally, some NaCl precipitation was also observed on the surfaces. Although, the continuous Gm release was still observed during the dissolution study up to and beyond 30 days, some of the HAp particles remained on the surfaces of the discs. In addition to Gm delivery, they might help to improve bioactivity and osseointegration of future implant surfaces due to the properties of these HAp bioceramics particles.

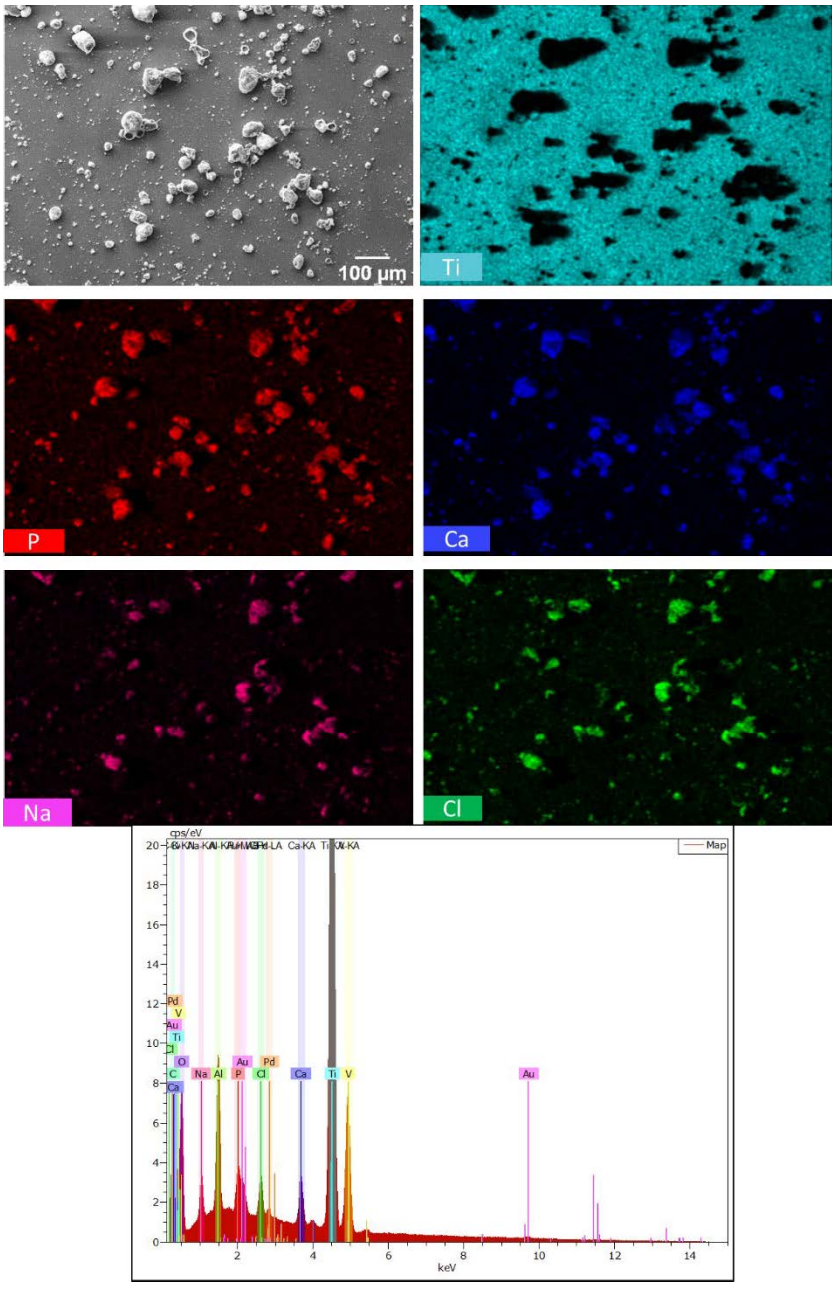

Figure 4.8 The surface observation and EDS-surface mapping results for PLA-Gm-(HAp-Gm) coated Ti6Al4V discs after the drug release study. It is showing Ti6Al4V substrate, Ca, P, Na, and Cl

4.3.3 Chemical characterization on the surface of PLA thin film biocomposite coated Ti6Al4V discs during the Gm release study (FT-IR)

Figure 4.9 shows the FT-IR analysis of the samples. FT-IR results also support the SEM and EDS results. There were not any apparent differences in the FT-IR spectra for the control PLA (*A*), and the two biocomposites. The FT-IR spectra for the PLA-Gm (*B*) and PLA-Gm-(HAp-Gm) (*C*) thin film coated Ti6Al4V discs on Day 0 and Day 30 were shown in *Figure 4.9*. PLA-Gm-(HAp-Gm) thin film coated Ti6Al4V discs at 5%, 10%, 15%, 20% and 30% GM concentrations were also given separately in *Figure 4.10* to compare the chemical structure of the samples on Day 0 and Day 30. Although it is difficult to detect the Gm peaks in the FT-IR studies (explained earlier in **Chapter 3**) HAp peaks were seen on both Day 0 and Day 30, proving that the particles in *Figure 4.7* and *Figure 4.8* are HAp particles.

As stated earlier, the degradation of PLA is complex but starts with the hydrolytic cleavage of ester bonds (Agarwal et al., 1998). In our studies, the ester bonds (–C-O) of PLA were detected after 30 days as shown in *Figure 4.8* and *Figure 4.10*. Therefore, it can be clearly stated that the degradation of PLA occurred in the PLA thin film around the Gm particles and clusters and some of the HAp-Gm particles.

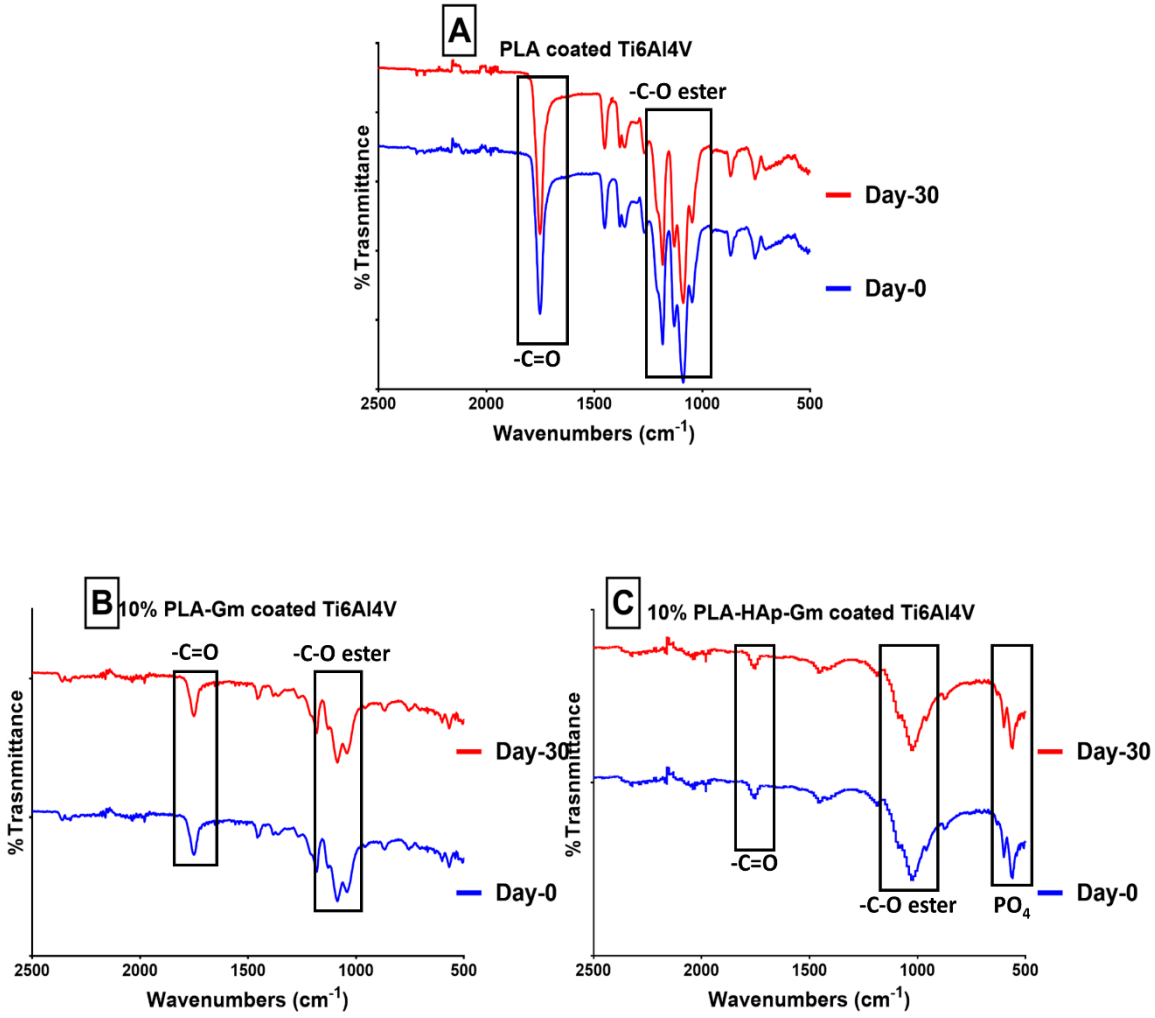

Figure 4.9 FT-IR spectra for PLA, PLA-Gm and PLA-Gm-(HAp-Gm) coated Ti6Al4V discs before and after the drug release study

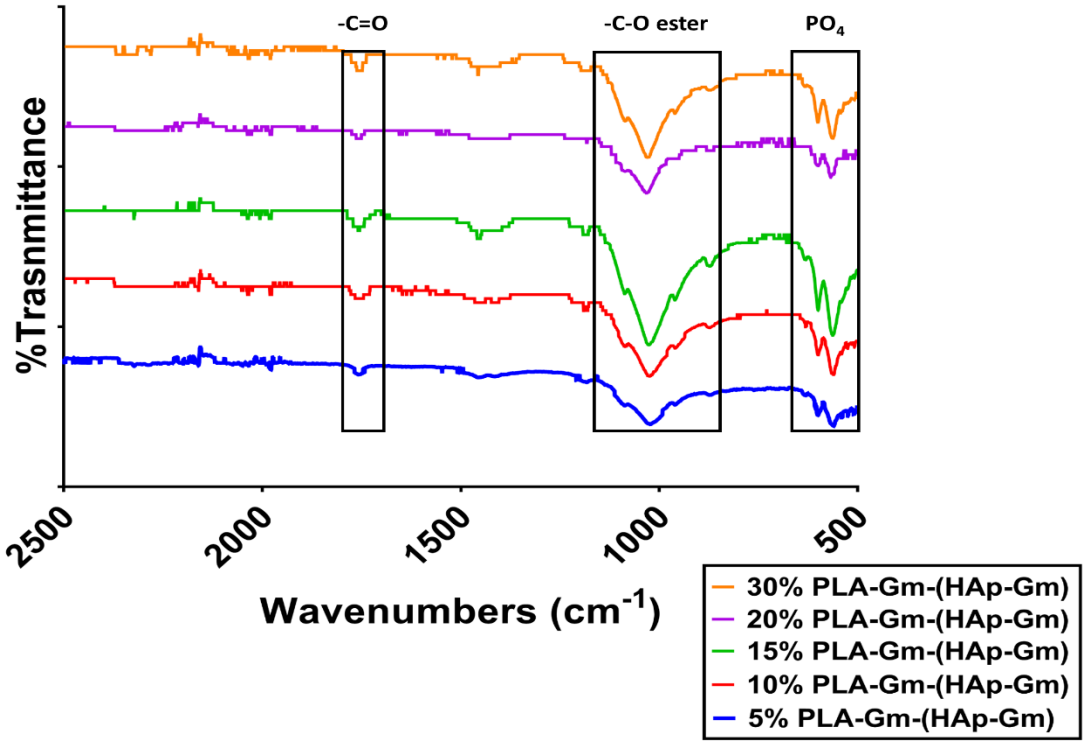

Figure 4.10 *Full* FT-IR spectra for PLA-Gm-(HAp-Gm) coated Ti6Al4V discs at 5%, 10%, 15%, 20% and 30% Gm concentrations after the drug release study (Day 30)

4.3.4 In vitro Continuous vs. Cumulative Dissolution Methods for Gm release from PLA thin film biocomposite coated Ti6Al4V discs

In *Figure 4.11*, the graph illustrates the cumulative release rate of Gm with and without HAp microspheres in the first week. The results show that the initial burst release of loosely attached Gm particles and clusters were faster than the initial burst release of HAp-Gm microspheres, indicating that HAp microspheres strongly affect the drug release rate.

The initial burst release profile (explained in the previous section) for the Continuous Dissolution Method testing shown, is nearly the same as the Cumulative method shown in *Figure 4.11*.

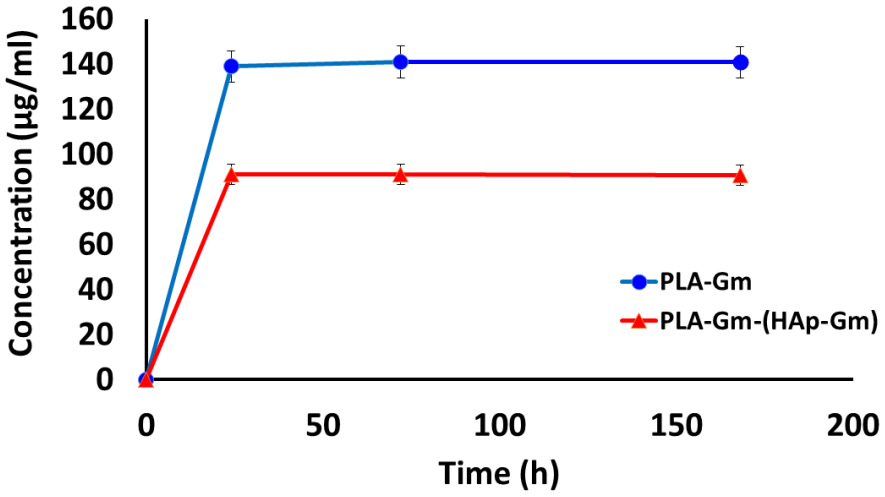

Figure 4.11 The dissolution experiment for PLA-Gm and PLA-Gm-(HAp-Gm) thin film coated Ti6Al4V discs with the Cumulative method for 7 days

The Cumulative and Continuous methods were compared in *Figure 4.12* for 30 days. These two methods were applied on PLA-Gm-(HAp-Gm) thin film coated Ti6Al4V discs at 15% Gm concentration only. Both methods showed the difference in drug release rate with and without HAp particles in the system. Additionally, they clearly demonstrated that HAp particles improve the control of the drug release and extend the release time. However, surprisingly the Cumulative method indicated (*Figure 4.11*) that there wasn't any release after the initial burst release. On the other hand, the drug release continued for 30 days at stage I and stage II and beyond for the Continuous method which brings serious questions on the accuracy of the Cumulative method.

Figure 4.12 shows that for the time period tested, the Continuous method gives a more accurate representation of the drug release patterns and stages, because the extra dilution was not required for the Continuous method.

The drug release pattern is crucial information, especially for implant related infections or osteomyelitis, because controlling the antibiotic drug release amount according to time is one of the key points in preventing infection during and after surgery and timely intervention prior to a possible serious infection.

In an ideal homogenous system where particles are the same size and the film thickness is the same and uniform, it is expected that two methods in the first reading should show same slope and inclination. However, in our system, the size of the coralline HAp particles and their locations in the

PLA thin film coating system differ, hence there will some differences in the dissolution rate and in the first day slope. That is the reason what observed in the Figure 4.12 shown.

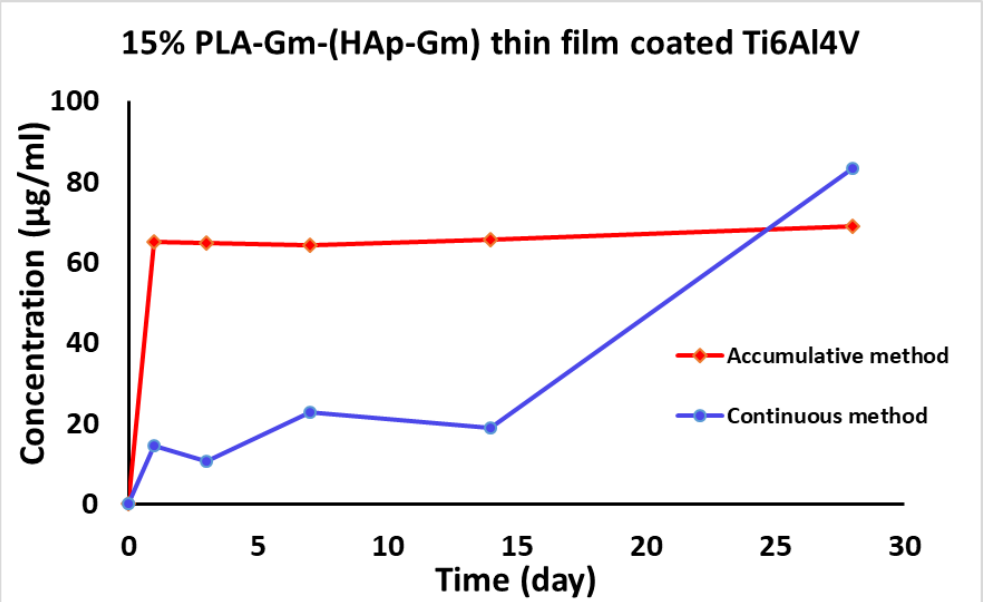

Figure 4.12 The comparison between the Cumulative method and Continuous method on 15% PLA-Gm-(HAp-Gm) thin film coated Ti6Al4V disc for 30 days dissolution experiment

4.3.5 Comparison of PBS solution and Ultra-pure water as a dissolution medium for the Continuous Dissolution Method for Gm release

The dissolution medium can be one of the most important variables for the testing of local drug release rate and pattern. There are various options for the dissolution medium to simulate the environment of the human body such as Trish-HCl, simulated body fluid, PBS or ultra-pure water. Therefore, based on previously published work the composite specifically developed, the 30% Gm containing PLA-Gm-(HAp-Gm) coated Ti6Al4V samples were tested in PBS solution and also in ultra-pure water as the two different dissolution mediums**.** The Continuous method was utilized for 6 weeks. In *Figure 4.13*, the difference of the Gm release pattern into PBS and ultra-pure water is shown. This difference observed is a higher dissolution in rate burst stage in the PBS, likely due to the influence of the PBS composition. The PBS solution contains the phosphate buffer which might have influenced the outcome by reacting with the Gm, the HAp or both.

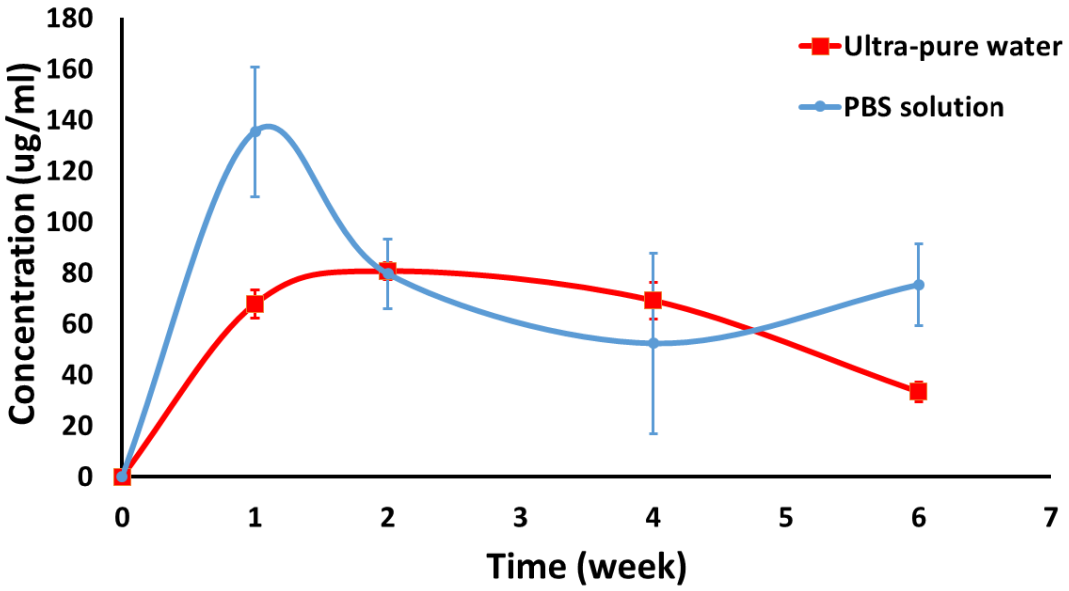

Figure 4.13 The comparison between the phosphate buffer PBS solution and ultra-pure water as dissolution mediums on the 30% PLA-Gm-(HAp-Gm) coated Ti6Al4V disc for 6weeks by using the Continuous Dissolution Method

4.4. Conclusion

The results of the Continuous dissolution study of 30 days show that the different Gm concentrations (5%, 10%, 15%, 20% and 30% w/w) in both the PLA-Gm and PLA-Gm-(HAp-Gm) coated Ti6Al4V samples are highly correlated specifically with the initial burst Gm release. The HAp particles as a drug carrier in the PLA matrix improved the controlled Gm release and prolonged the Gm release due to the calcium phosphate dissolution rate and hence reduction in the total drug release rate. It is well known that coral based HAp particles can also stimulate bioactivity and bone regeneration due to their Ca^{2+} and PO_4^{2-} supply and their unique interconnected porous structure.

The Continuous Dissolution Method was found to be the ideal method when it compared with the Cumulative Dissolution Method this is because using individual discs for each time intervals, we can avoid any additional external dilution factors that can influence the readings.

The effect of dissolution mediums such as PBS solution and ultra-pure water showed that the Gm release pattern changes according to the dissolution medium. To clarify a possible reaction between the Gm antibiotic and PBS solution, further studies on Gm dissolution in different PBS solutions are suggested. Specifically, different compositions of PBS are highly recommended. Additionally, in order to create a more realistic analysis, a dynamic testing method should be used, and a fully dynamic

micro-fluidity experiment should be conducted. Dynamic testing methods and a series of new PBS compositions of the dissolution medium are a good option for further studies.

The flexibility of the PLA biocomposite thin film coating system is due to its application area and the adjustable antibiotic dosages. This allows them to be used for any future clinical applications, specifically for orthopedic and maxillofacial implants of any shape and size. Depending on the degree of clinical dosage required, the PLA biocomposite antibacterial coating system could be designed to release the drug in both short and prolonged periods of time.

4.5 References

AGARWAL, M., KOELLING, K. W. & CHALMERS, J. J. 1998. Characterization of the degradation of polylactic acid polymer in a solid substrate environment. *Biotechnol Prog,* 14**,** 517-26.

AVIV, M., BERDICEVSKY, I. & ZILBERMAN, M. 2007. Gentamicin-loaded bioresorbable films for prevention of bacterial infections associated with orthopedic implants. *J Biomed Mater Res A,* 83**,** 10-9.

BEN-NISSAN, B. 2003. Natural bioceramics: from coral to bone and beyond. *Current Opinion in Solid State and Materials Science,* 7**,** 283-288.

BEN-NISSAN, B., MACHA, I., CAZALBOU, S. & CHOI, A. H. 2016. Calcium phosphate nanocoatings and nanocomposites, part 2: thin films for slow drug delivery and osteomyelitis. *Nanomedicine (Lond),* 11**,** 531-44.

CHINNA REDDY, P., CHAITANYA, K. S. & MADHUSUDAN RAO, Y. 2011. A review on bioadhesive buccal drug delivery systems: current status of formulation and evaluation methods. *Daru,* 19**,** 385-403.

CHOI, A. H. & BEN-NISSAN, B. 2017. Calcium Phosphate Nanocomposites for Biomedical and Dental Applications: Recent Developments. *In:* THAKUR, V. K., THAKUR, M. K. & KESSLER, M. R. (eds.) *Handbook of Composites from Renewable Materials.* Scrivener Publishing LLC.

CHOI, A. H., BEN-NISSAN, B., CONWAY, R. C. & MACHA, I. J. 2014. Advances in Calcium Phosphate Nanocoatings and Nanocomposites. *In:* BEN-NISSAN, B. (ed.) *Advances in Calcium Phosphate Biomaterials.* Berlin, Heidelberg: Springer Berlin Heidelberg.

CHOI, A. H., CAZALBOU, S. & BEN-NISSAN, B. 2015. Nanobiomaterial Coatings in Dentistry.', Frontiers of oral biology. *In:* DEB, S. (ed.) *Biomaterials for Oral and Craniomaxillofacial Applications.* London: Front Oral Biol. Basel, Karger.

CHOU, J., BEN-NISSAN, B., GREEN, D. W., VALENZUELA, S. M. & KOHAN, L. 2011. Targeting and Dissolution Characteristics of Bone Forming and Antibacterial Drugs by Harnessing the Structure of Microspherical Shells from Coral Beach Sand. *Advanced Engineering Materials,* 13**,** 93-99.

CHOU, J., HAO, J., BEN-NISSAN, B., MILTHORPE, B. & OTSUKA, M. 2013a. Coral exoskeletons as a precursor material for the development of a calcium phosphate drug delivery system for bone tissue engineering. *Biol Pharm Bull,* 36**,** 1662-5.

CHOU, J., ITO, T., BISHOP, D., OTSUKA, M., BEN-NISSAN, B. & MILTHORPE, B. 2013b. Controlled release of simvastatin from biomimetic beta-TCP drug delivery system. *PLoS One,* 8**,** e54676.

CHOU, J., VALENZUELA, S., GREEN, D. W., KOHAN, L., MILTHORPE, B., OTSUKA, M. & BEN-NISSAN, B. 2014. Antibiotic delivery potential of nano- and micro-porous marine structure-derived beta-tricalcium phosphate spheres for medical applications. *Nanomedicine (Lond),* 9**,** 1131-9.

DA SILVA, D., KADURI, M., POLEY, M., ADIR, O., KRINSKY, N., SHAINSKY-ROITMAN, J. & SCHROEDER, A. 2018. Biocompatibility, biodegradation and excretion of polylactic acid (PLA) in medical implants and theranostic systems. *Chem Eng J,* 340**,** 9-14.

FREDENBERG, S., WAHLGREN, M., RESLOW, M. & AXELSSON, A. 2011. The mechanisms of drug release in poly(lactic-co-glycolic acid)-based drug delivery systems--a review. *Int J Pharm,* 415**,** 34-52.

GAVASANE, A. & PAWAR, H. 2014. Synthetic Biodegradable Polymers Used in Controlled Drug Delivery System: An Overview. *Clinical Pharmacology & Biopharmaceutics,* 3**,** 121.

KARACAN, I., BEN-NISSAN, B. & SINUTOK, S. 2019. Marine-Based Calcium Phosphates from Hard Coral and Calcified Algae for Biomedical Applications. *In:* CHOI, A. H. & BEN-NISSAN, B. (eds.) *Marine-Derived Biomaterials for Tissue Engineering Applications.* Singapore: Springer.

LIECHTY, W. B., KRYSCIO, D. R., SLAUGHTER, B. V. & PEPPAS, N. A. 2010. Polymers for drug delivery systems. *Annu Rev Chem Biomol Eng,* 1**,** 149-73.

LUCKE, M., SCHMIDMAIER, G., SADONI, S., WILDEMANN, B., SCHILLER, R., HAAS, N. P. & RASCHKE, M. 2003. Gentamicin coating of metallic implants reduces implant-related osteomyelitis in rats. *Bone,* 32**,** 521-31.

MACHA, I., BOONYANG, U., CAZALBOU, S., BEN-NISSAN, B., CHARVILLAT, C., OKTAR, F. & GROSSIN, D. 2015a. Comparative study of Coral Conversion, Part 2: Microstructural evolution of calcium phosphate. *JOUrnal of the Australian Ceramic Society,* 51**,** 149-159.

MACHA, I. J., BEN-NISSAN, B. & MILTHORPE, B. 2014. Improvement of Elongation in Nanosurface Modified Bioglass/PLA Thin Film Composites. *Current Nanoscience,* 10**,** 200-204.

MACHA, I. J., BEN-NISSAN, B., SANTOS, J., CAZALBOU, S. & MILTHORPE, B. 2016. Hydroxyapatite/PLA Biocomposite Thin Films for Slow Drug Delivery of Antibiotics for the Treatment of Bone and Implant-Related Infections. *Key Engineering Materials,* 696**,** 271-276.

MACHA, I. J., BEN-NISSAN, B., VILCHEVSKAYA, E. N., MOROZOVA, A. S., ABALI, B. E., MULLER, W. H. & RICKERT, W. 2019. Drug Delivery From Polymer-Based Nanopharmaceuticals-An Experimental Study Complemented by Simulations of Selected Diffusion Processes. *Front Bioeng Biotechnol,* 7**,** 37.

MACHA, I. J., CAZALBOU, S., BEN-NISSAN, B., HARVEY, K. L. & MILTHORPE, B. 2015. Marine structure derived calcium phosphate-polymer biocomposites for local antibiotic delivery. *Mar Drugs,* 13**,** 666-80.

MACHA, I. J., CAZALBOU, S., SHIMMON, R., BEN-NISSAN, B. & MILTHORPE, B. 2017. Development and dissolution studies of bisphosphonate (clodronate)-containing hydroxyapatite-polylactic acid biocomposites for slow drug delivery. *J Tissue Eng Regen Med,* 11**,** 1723-1731.

MONTANARO, L., SPEZIALE, P., CAMPOCCIA, D., RAVAIOLI, S., CANGINI, I., PIETROCOLA, G., GIANNINI, S. & ARCIOLA, C. R. 2011. Scenery of Staphylococcus implant infections in orthopedics. *Future Microbiol,* 6**,** 1329-49.

NAIR, L. S. & LAURENCIN, C. T. 2007. Biodegradable polymers as biomaterials. *Progress in Polymer Science,* 32**,** 762-798.

NOJEHDEHYAN, H., EKRAMI, M., SHAHRIARI, M., KARIMI, R. & JABERIANSARI, Z. 2016. Loading of gentamicin onto poly lactic-co-glycolic acid and poly lactic-coglycolic acid/nano-hydroxyapatite composite microspheres. *Biomedical Research,* 27**,** 70-78.

PARK, H., PARK, K. & SHALABY, W. S. 1993. *Biodegradable hydrogels for drug delivery*, CRC Press.

POKROWIECKI, R. 2018. The paradigm shift for drug delivery systems for oral and maxillofacial implants. *Drug Deliv,* 25**,** 1504-1515.

RAJGOR, N., PATEL, M. & BHASKAR, V. 2011. Implantable Drug Delivery Systems: An Overview. *J Surgical Neurology International,* 2.

ROY, D. M. & LINNEHAN, S. K. 1974. Hydroxyapatite formed from coral skeletal carbonate by hydrothermal exchange. *Nature,* 247**,** 220-2.

SIMCHI, A., TAMJID, E., PISHBIN, F. & BOCCACCINI, A. R. 2011. Recent progress in inorganic and composite coatings with bactericidal capability for orthopaedic applications. *Nanomedicine,* 7**,** 22-39.

VESTER, H., WILDEMANN, B., SCHMIDMAIER, G., STOCKLE, U. & LUCKE, M. 2010. Gentamycin delivered from a PDLLA coating of metallic implants: In vivo and in vitro characterisation for local prophylaxis of implant-related osteomyelitis. *Injury,* 41**,** 1053-9.

WU, P. & GRAINGER, D. W. 2006. Drug/device combinations for local drug therapies and infection prophylaxis. *Biomaterials,* 27**,** 2450-67.

Chapter 5

Mechanical testing of antimicrobial biocomposite coating on metallic medical implants as a drug delivery system

Chapter 5: Mechanical testing of antimicrobial biocomposite coating on metallic medical implants as a drug delivery system

This chapter contains the background of the surface modifications carried out on the Ti6Al4V based bone implants and their mechanical properties. The effect of the thermal anodization technique on Ti6Al4V alloy discs and implants as surface modifications was investigated and the mechanical properties at nano and micro scale were determined.

5.1. Introduction

The understanding of the mechanical properties of mineralized tissues such as bone, enamel and dentin is essential for successfully designing long-lasting bone implants due to age-related deterioration and disease (Kruzic and Ritchie, 2008).

During the last three decades, Ti6Al4V alloy was found to be the most attractive type of Ti alloy for dental and orthopedic implant applications, because of its better mechanical properties (Cigada et al., 1992, Paital and Dahotre, 2009, Ataee et al., 2018). Most orthopedic and dental implants require sufficient strength and hardness. Ti6Al4V alloy has excellent fatigue and tensile strength, superior corrosion and wear resistance, relatively low modulus of elasticity, good hardness, and low density in comparison to other metals and alloys. Currently 20-30% of commercially available metal-based medical implants are made of Ti6Al4V alloy (Krząkała et al., 2013).

Ti6Al4V alloy has the closest Young's modulus of elasticity (E) (~110 GPa) to the human cortical bone (~25 GPa) when compared with other metallic alloys. However, the E value of Ti6Al4V is still higher than the E value of human bone, which might lead to complications in the long-term, such as bone resorption or stress shielding (Guillemot, 2005b, Ataee et al., 2018). While Ti6Al4V alloy has a high corrosion resistance and biocompatibility, it has certain limitations, such as the release of Al and V ions, which may cause allergic reactions in certain patients with metal sensitivity (Cigada et al., 1992, Paital and Dahotre, 2009, Rath et al., 2012). Therefore, creating a suitable microenvironment

between the implant surface and host with different surface modifications can prolong the lifetime of the implant as a result of improving its mechanical and biological properties. The surface modifications of the metallic implants can stimulate the cell proliferation, tissue, and bone growth around the implant surface, increase osseointegration and bioactivity, and avoid the implant failures (Kargupta et al., 2014, Lewallen et al., 2014, Lan et al., 2020).

The surface modifications are applied through a number of different techniques. These include: chemical, physical and biological such as chemical vapor deposition (CVD), physical vapor deposition (PVD), sol-gel, atomic layer deposition (ALD), acid etching (roughening), plasma coating, and thermal oxidation (TO), or anodization to deposit coatings on both micro and nano sizes (Roest, 2008, Choi et al., 2013, Ben-Nissan et al., 2014, Patel et al., 2014).

Thermal anodization treatment is an important surface modification for the Ti and Ti alloy implants, especially for Ti6Al4V implants. While a thin oxide layer naturally exists on Ti6Al4V surfaces because of their extraordinarily high reactivity, the thermal anodization technique increases the thickness and strength of oxide film. Anodization naturally or artificially initiates changes to the microstructure of the oxide layer (Ratner, 2001, Textor et al., 2001). While the naturally grown oxide layer on the Ti6Al4V alloy has an amorphous microstructure, the thermal anodization treatment causes a microcrystalline microstructure of the oxide layer on the Ti6Al4V alloy. An oxide film such as TiO_2 (a thermodynamically, and chemically very stable oxide form) is primarily present in the oxide layer of Ti6Al4V with a natural or anodic oxide film grown in air. It has been reported that the TiO_2 film on Ti6Al4V improves corrosion resistance and biocompatibility (Textor et al., 2001, Wong et al., 2019).

Nanocoatings and thin film coatings are most commonly used in implant surface modifications for improving the mechanical and biological properties of metallic implants. The surface coatings might include an oxidizing layer, a bioceramics-based matrix such as HAp, a biodegradable polymeric-based matrix, or a combination of different materials such as composites (Farah et al., 2016, Choi et al., 2018).

Scratch tests with different indenter shapes are commonly used and are highly effective methods in determining the adhesion properties of the polymeric, metallic, or ceramic thin film coatings, and highly effective methods. During scratch testing, a diamond or hard metal stylus is drawn across the coating's surface at continuously increasing loads and at a constant velocity (Cope et al., 2005, Bull and Berasetegui, 2006, Ben-Nissan et al., 2013, Dogar Cutean et al., 2015). While in nanoindentation, hard indenters are utilized in a mN range to penetrate the substrate in less than a few hundred nanometer depths. Young Modulus (E) and Hardness (H) for thin film coating materials at the micro-

or nano-scale are determined during a nanoindentation test. Additionally, the elastic-plastic response (for the combination of a coating material and a substrate when subjected to loading and unloading) is obtained by this technique (Piveteau, 2001, Cope et al., 2005, Ben-Nissan et al., 2013, Dogar Cutean et al., 2015).

The phenomenon of adhesion relates to chemical reactions and the physical effects between the substrate and the thin film applied to its surface. There are two types of forces, which are primary interatomic and secondary forces. Examples of interatomic forces include ionic and covalent bonds and secondary forces are hydrogen bonds. Additionally, secondary forces are weaker than interatomic forces.

The design, function, and properties of nano-, micro- and macro-coating materials are changed according to their application (i.e. dental or orthopedic implants), so various methods are required in order to measure mechanical properties of thin film coated biomedical devices accurately. Some of the important tests for the determination of mechanical and adhesion properties coating thin film implants are tensile pull-off and shear testing, scratch testing, pin-on-disc testing, nanoindentation, bending testing, micro-tensile testing and bulge-blister testing (Ben-Nissan et al., 2015, Ben-Nissan and Choi, 2017). Two of these, commonly used on thin films nanoindentation and scratch testing, will be explained further in the following sections.

5.1.1 Nanoindentation testing

The nanoindentation assesses the measurement of the implants' mechanical properties and coatings in the biomedical field. A basic explanation of this technique is the determination of Young's Modulus (E) and Hardness (H) for thin film coating materials at the micro or nanoscale levels. Additionally, the elastic–plastic response on the combination coating material and substrate (according to loading and unloading curves) is obtained by this technique (Swain and Menčík, 1994, Piveteau, 2001, Latella et al., 2012).

During the nanoindentation testing process, the indenter contacts the surface of the specimen, and the load, whose range is referred with mN, is applied by the indenter. The penetration depth is measured according to the load value, and it should be around 10% of the coating material thickness to obtain successful results. In order to get successful results during the nanoindentation technique, the other most important factors reported are (Piveteau, 2001, Ben-Nissan et al., 2013, Choi et al., 2016):

- ✔ Sample preparation
- ✔ Indenter tip shape

- ✔ Initial indenter penetration
- ✔ Calibration of the equipment
- ✔ Surface roughness
- ✔ Loading Rate

The Berkovic indenter (a sharp indenter) is commonly used for the E and H mechanical properties measurements of various coating materials. In some cases, different types of tips (such as spherical tips) are preferred for measuring the elastic-plastic response (Swain and Menčík, 1994). Additionally, this type of indenter tip increases penetration depth contact stress. A schema of the nanoindentation device and different types of indenters are shown in *Figure 5.1*.

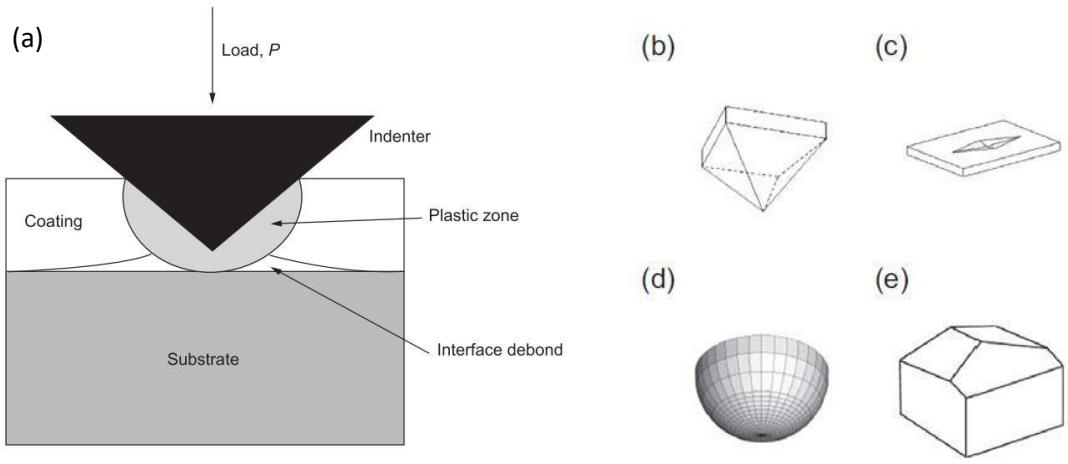

Figure 5.1 Schema of nanoindentation device (a) (Roest et al., 2011), various indenter tip shapes Vickers indenter (b), diamond-shaped indenter (c), spherical indenter (d), Berkovich indenter (e) (Choi et al., 2016)

5.1.2 Scratch testing

The substrate's coating adhesion strength is analyzed through the scratch testing technique. It is a very effective, useful, and fast method for determining the critical load range based on the adhesion properties of coating materials. During scratch testing, a diamond or hard metal stylus is used to draw across at continuously increasing loads, and at a constant velocity. The general schema for the scratch testing method is illustrated in *Figure 5.2* (Bull and Berasetegui, 2006, Ben-Nissan et al., 2013, Dogar Cutean et al., 2015).

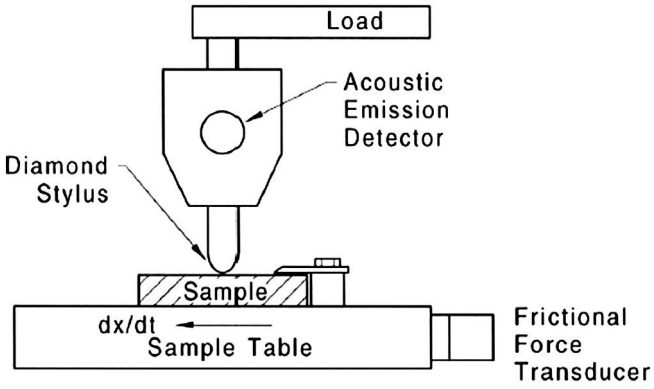

Figure 5.2 The schema for scratch testing devices (Ben-Nissan et al., 2013)

The results of the scratch test are provided at some critical loads, which are used for the measurement of adhesion strength. Other important factors for scratch testing are thickness, hardness, and roughness of coating surface, the shape of the tip, scratching speed, loading rate, environment and coating surface and substrate properties respectively (Choi et al., 2016).

In previous chapters, the surface morphology and structural characterization of PLA-Gm-(HAp-Gm) thin film coated Ti6Al4V discs were investigated. Therefore, in this chapter, the determination of the mechanical properties of PLA-Gm-(HAp-Gm) thin film coated thermally anodized and untreated Ti6Al4V discs were focused and compared to uncoated substrates. The effects of the anodization process on coating quality were observed and the mechanical properties were determined with the nanoindentation and scratch testing methods.

5.2 Experimental Methods

5.2.1 The Substrate Material Preparation

The Ti6Al4V discs (2 cm Dia and 3mm thick, Good Fellows UK) were highly polished. The polishing was first done with 320 grit, and then by using 1200PSA silicon carbide papers. Final polishing was done with 0.2 µm alumina particles, used in the third and fourth steps, in order to get a mirror surface. The Ti6Al4V discs were cleaned with 100% acetone by ultra-sonication for 10 minutes. They were dried under vacuum overnight within a desiccator.

Four sets of highly polished Ti6AL4V discs were prepared for this study:

1. Ti6Al4V discs as they were
2. Thermally treated anodized Ti6Al4V discs

3. PLA biocomposite thin film coated on untreated Ti6Al4V discs
4. PLA biocomposite thin film coated on anodized Ti6Al4V discs

The thermal anodization process was carried out at 500 °C for 16 hours in the air to obtain an oxidized layer on the surface of the discs.

5.2.2 Surface Characterization and Chemical Composition

5.2.2.1 Scanning Electron Microscope Analysis (SEM)

SEM (ZEISS Supra SSVP, Zeiss, Germany) was used to obtain the surface structure of untreated and anodized Ti6Al4V discs before the PLA biocomposite thin film coating.

The samples were placed on carbon stubs by a mutually conductive adhesive tape. They were coated with ultrathin 7nm layer of Au-Pd using the sputtering and carbon thread coater (EM ACE600, Leica microsystems, Germany). The samples were kept under vacuum overnight to get rid of any moisture before the imaging process. Images were taken at various magnifications at an acceleration voltage of 5-15 kV.

5.2.2.2 X-Ray mapping (XRM) and Energy Dispersive Spectroscopy (EDS)

The chemical composition of the Ti6Al4V surface before and after the anodization process was examined by Energy Dispersive Spectroscopy (EDS), (JEOL 7001 F FEGSEM Moran Scientific Microanalysis, Amptek SDD detector with C2 window) at 8kV. The determination of the specific element's locations and distributions on the surface was analyzed with X-Ray mapping (XRM) (JEOL 7001 F FEGSEM Moran Scientific Microanalysis and X-ray Mapping system, Amptek SDD detector with C1 Window (90nm Si3N4 window) Maps 1024x1024) for 50msec per point at15kV.

5.2.2.3 Secondary ion mass spectroscopy (SIMS)

All Secondary ion mass spectrometry (SIMS) measurements were performed using a Cameca IMS 5fE7 SIMS instrument (Cameca, France). A primary ion beam of Cs+ with an impact energy of 15.0 keV and beam current of 3 nA was employed to raster a 180 µm × 180 µm region of the surface. Negative secondary ions were accepted from a circular area limited to a diameter of 33 µm by ion optical aperture in order to avoid crater effects. The secondary ions included H-,12C-,14N-,16O-,19Fi-, 12C14N-,27Al ,48Ti-,51V-. For each crater, the total depth (measured by a KLA Tencor Alpha-Step IQ profilometer [KLA-Tencor, U.S.A.]), was used to calculate the average ion beam sputter rate necessary for converting the SIMS analysis time into depth profile.

5.2.2.4 Atomic Force Microscope (AFM)

The surface microstructure and topography of the untreated and anodized samples were characterized using a Multimode 5 atomic force microscope (AFM, Park Systems, South Korea) operating in tapping mode. All investigations were performed under ambient conditions. For each sample, the area of 5 × 5 µm was scanned. Commercial silicon cantilevers type NSC16AlBS (a nominal tip radius of approximately 8 nm), nominal cantilever force (26 N/m, and a nominal resonance frequency of 190 Hz were used.

5.2.3 Mechanical and Adhesion Testing

5.2.3.1 Nanoindentation

Nanoindentation of both treated (anodized) and untreated (un-anodized) Ti6Al4V substrates, and the coated samples were carried out using a Nano-Triboindenter (Hysitron Inc., USA), with a calibrated Berkovich indenter for determination of hardness and elastic modulus. A < 1µm radius 90 included angle conical indenter tip was used for the scratch tests. All tests were conducted in ambient conditions. Two different load ranges were used with the Berkovich indenter in order to determine the properties accurately due to the film thickness and the influence of the indenter penetration depth.

Firstly, a range of 50-70mN loads was applied on treated (anodized) and untreated Ti6Al4V discs for both coated and uncoated forms to compare the effects of the treatment and of PLA composite coating on the properties of the substrates. The loading rate ranged from 5 mN/s to 10 mN/s. Additionally, a maximum indentation depth of 1000 nm was used.

Secondly, a range of loads was applied (between 0.1 and 5 mN) on all samples to determine the mechanical properties of both coated and uncoated samples. The holding time at the maximum loads for all tests was 20 s to minimize the time-dependent plastic creep deformation on the estimation of hardness and elastic modulus.

5.2.3.2 Micro Scratch Test

For the adhesion properties, a scratch tester (Hysitron Inc., USA) was used with a <1 µm conical indenter tip radius, and 160 µN load was applied. The speed of the scratch application was 0.25µm/s, and the scratch length was 10 µm.

5.3 Results and Discussions

Anodized and untreated Ti6Al4V discs were successfully coated with PLA and PLA biocomposite containing HAp microspheres by the dip coating method. The results show a very uniform coating, covering the surfaces of the samples. *Figure 5.3 A and B* show highly polished anodized and untreated titanium samples before and after the PLA coating process respectively. A Zeiss 3D optical microscope was utilized.

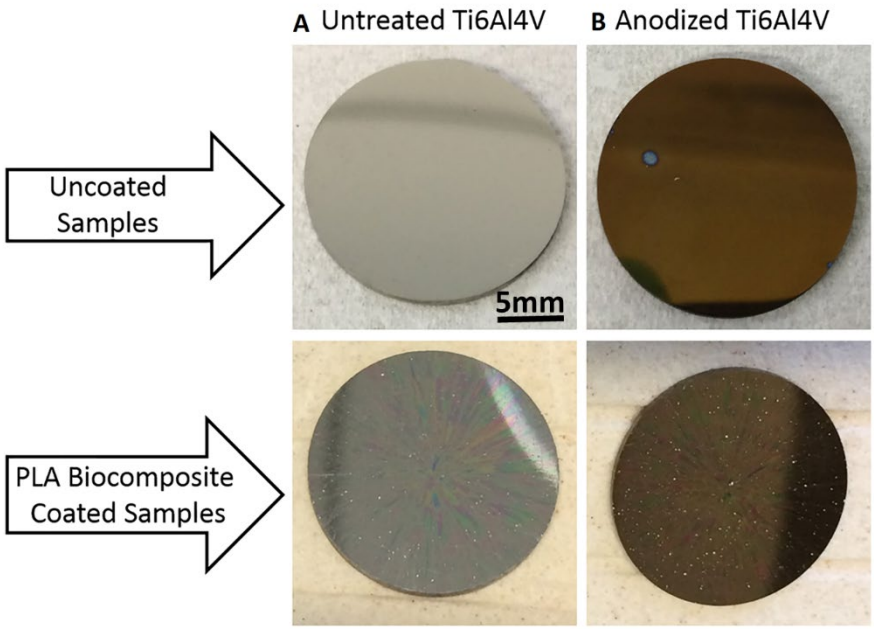

Figure 5.3 The anodized and untreated Ti6Al4V discs before (A) and after (B) PLA biocomposite coating

5.3.1 Surface Characterization and Chemical Composition analyses of untreated and anodized Ti6Al4V discs

The SEM observations of the surface morphology of both untreated and treated Ti6Al4V discs before coating are shown in *Figure 5.4*. While the untreated Ti6Al4V surface was observed to be smooth in *Figure 5.4-A*, the surface of the anodized Ti6Al4V sample shows a rough nano structure with very

fine grains associated with the fine oxide structure formed during the anodization process (*Figure 5.4 B*).

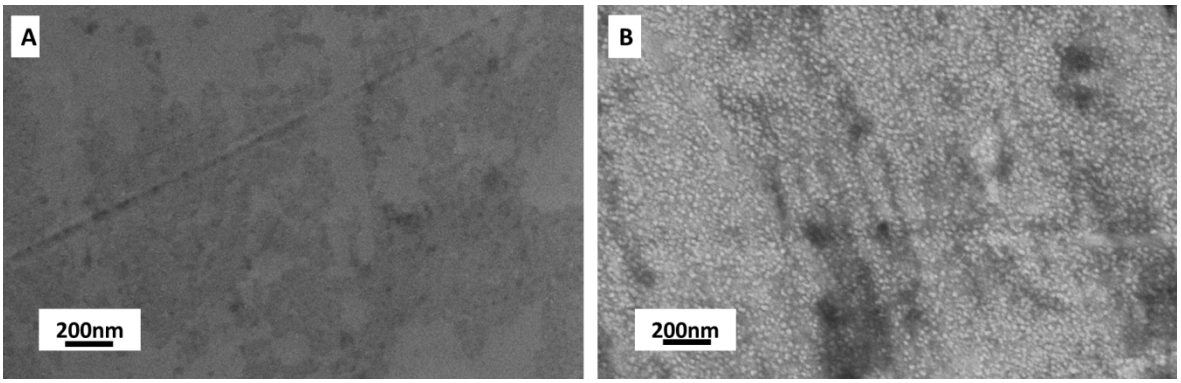

Figure 5.4 SEM results of both uncoated [A] untreated and [B] anodized Ti6Al4V disc showing the surface structure differences before and after the anodization process and the resultant grain structure on the treated Ti6Al4V disc

X-Ray mapping is used to track the distribution of the specific elements on the material surface. Three different locations (*Figure 5.5*) were chosen to determine the distribution of the specific elements such as Ti, Al, and V on the Ti6AL4V alloy surface. Location A covers a large area that shows Ti is around 88%, and Al (8.9%) weight ratio is higher than V weight (2.8%).

Energy Dispersive Spectroscopy (EDS) is a semi quantitative analysis method utilized during mapping, although segregation and distribution of the specific elements easily can be observed.

The two dimensional (2D) scatter diagrams refer to the pixel frequency of intensity values of one element to another (Wuhrer et al., 2006). The scatter diagrams for Ti vs. V and Al vs. V were given in *Figure 5.5* for XRM mapping area A. The intensity of points on the diagrams was colored with the thermal color scale. Thus, the intensity within the scatter diagram indicates the number of points in the image with similar concentration. In the scatter diagrams, the clusters were observed. The clusters reflect the Ti-V and Al-V ratios around 84.7 % of the Ti6Al4V surface.

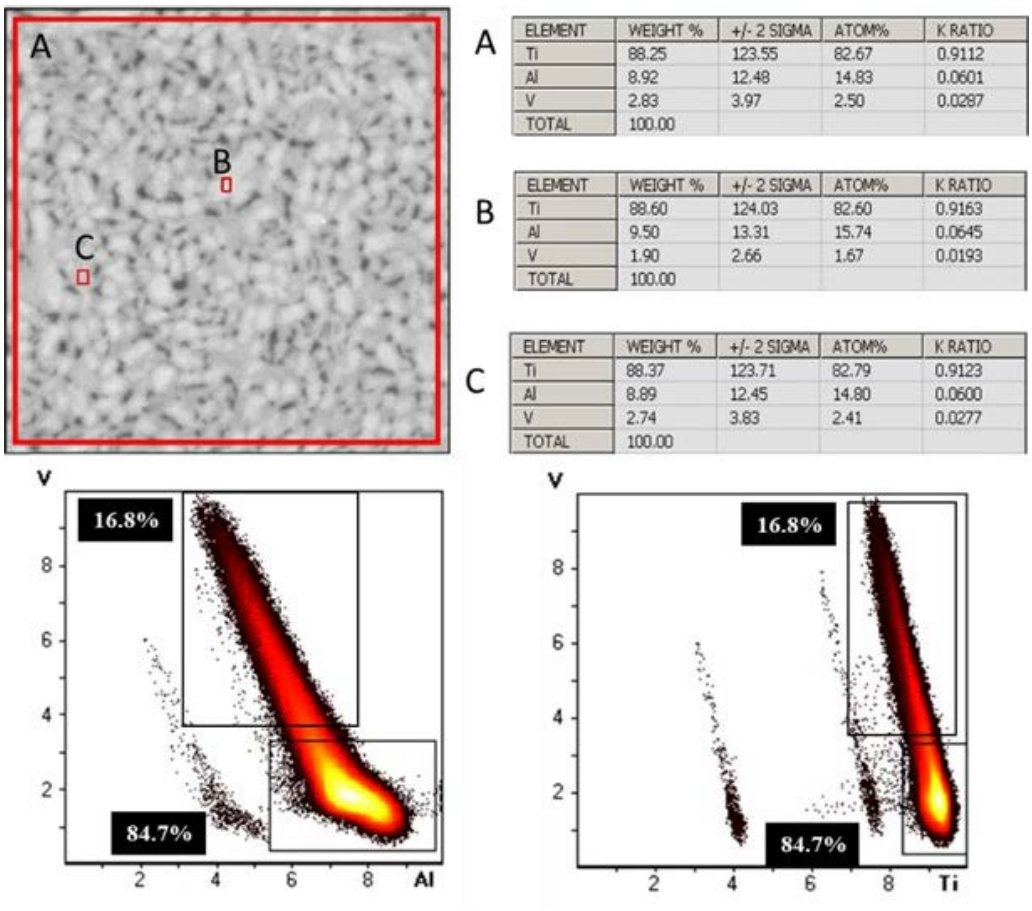

Figure 5.5 X-Ray mapping results of the three different locations (A, B, C) on Ti6Al4V discs with the their Ti, Al, and V ratios, and the 2D scatter diagrams for location A of Ti6Al4V surface

Figure 5.6 represents the EDS analyses and pseudo coloring of both untreated and anodized sample surfaces. In *Figure 5.6 A* and *B*, the surface pseudo coloring map is given for untreated and anodized samples. The color bar below each pseudo color image represents the color where two components were overlapping. The color changes gradually as the material changes from 100% of one component to another. The Ti is shown in red, the Al in green, and the V is in blue (*Figure 5.6 A)*. The Al is in red, V is in blue, and O is in green for *Figure 5.6 B*. The yellow color represents the overlapping of Ti and Al components, and the pink color is the overlapping of Ti and V components. According to *Figure 5.6 B*, the oxygen layer covers the surface of anodized Ti6Al4V samples is also observed by the pseudo coloring map.

As expected, EDS analysis shows mainly Ti, Al, and V element peaks and also a minor O peak for untreated samples in *Figure 5.6 C*. On the other hand, it shows a stronger O peak for the anodized Ti6Al4V sample than untreated one in *Figure 5.6 D*. Therefore, the EDS results support the pseudo color images. The thermal anodization process causes the formation of an extra oxide layer on top of

the remaining native oxide layer on the substrate, meaning that the thicker oxide layer is on the Ti6Al4V sample after the thermal anodization process.

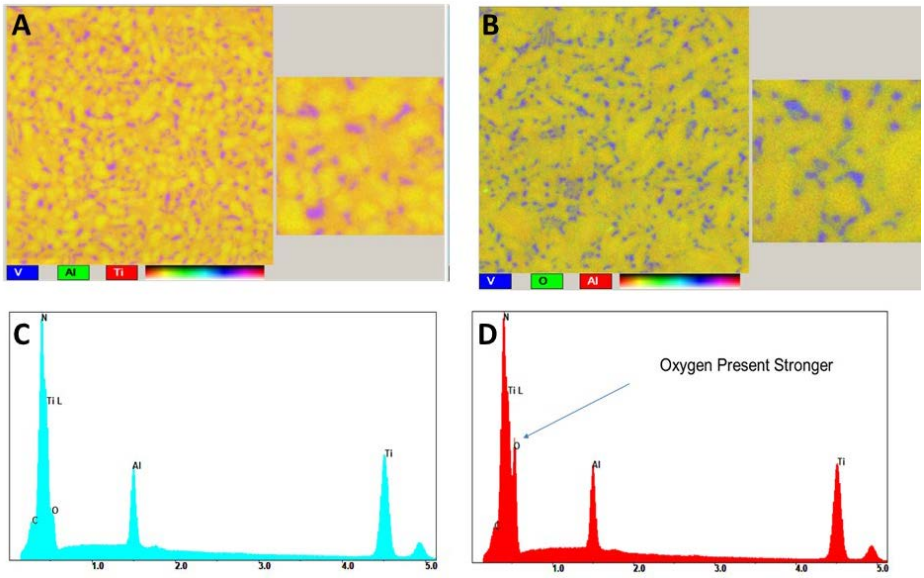

Figure 5.6 EDS (A, B) and pseudo coloring (C, D) map analyses of both untreated and anodized Ti6Al4V discs

According to XRM and EDAX results, the anodized layer was identified as TiO_2. The different TiO_2 phases, namely Rutile (JCPDS card no. 21-1276), Anatase (JCPDS card no. 21-1272), or their mixture, can be obtained according to the treatment (Roest, 2008, Scarpelli et al., 2018). Browne *et al.* (1994) reported the Rutile and Anatase TiO_2 phases on the Ti6Al4V surface after 0.75h thermal anodization treatment at 400 C˚ (Browne and Gregson, 1994). On the other hand, Roest *et al.* (2011) produced the TiO_2 layer on Ti6Al4V alloys via the electrolysis anodization technique for three different voltages (25, 50 and 75V). While the research group reported that only the rutile phase was obtained at 25V, both Rutile and Anatase phases were found at 50V and 75V. Several studies in the past showed different TiO_2 phases, including Rutile, Anatase, and their mixture. Additionally, the mixture of Rutile and Anatase gave better results for further sol gel oxide coatings (Roest, 2008, Roest et al., 2011).

SIMS depth profile (*Figure 5.7*) shows in the anodized Ti6Al4V sample. The composition of the oxide layer was identified as Oxy-Nitride. This result is not surprising considering that during thermal treatment both oxygen and nitrogen exist in the atmosphere. In addition, there is some minor carbon distribution (its origin is not clear).

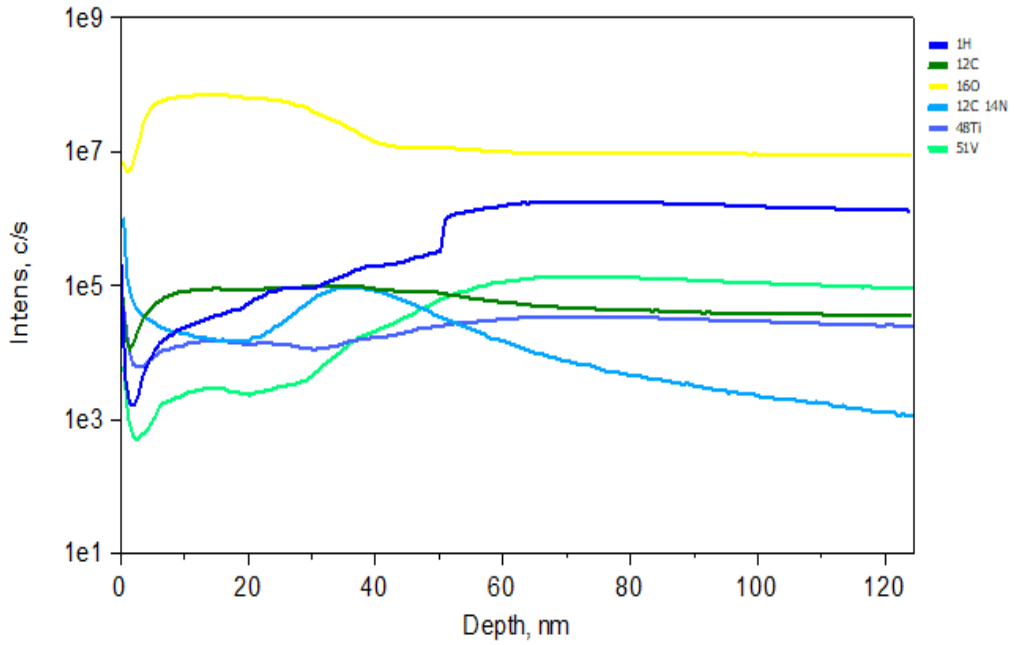

Figure 5.7 SIMS depth profile shows for the anodized Ti6Al4V sample

The roughness parameters of untreated and anodized Ti6Al4V discs surfaces were obtained via AFM topography analysis, and presented in *Figure 5.8* with 3D surface images of untreated (A) and anodized (B) Ti6Al4V surfaces. A clear difference of three main surface roughness parameters can be easily observed (The roughness average [Ra], average maximum height of the profile [Rz], and root mean square roughness [Rq]) between the untreated (*Figure 5.8 A*) and the anodized (*Figure 5.8 B*) surfaces. The average values of both parameters for the anodized sample are higher than the untreated sample. They are: Ra of 6.1 ± 0.5 nm and 2.6 ± 0.2 nm, Rz of 59.5 ± 16.7 nm and 19.6 ± 1.4 nm, Rq of 7.7 ± 0.7 nm and 3.2 ± 0.3 nm respectively; anodized samples show much rougher surfaces.

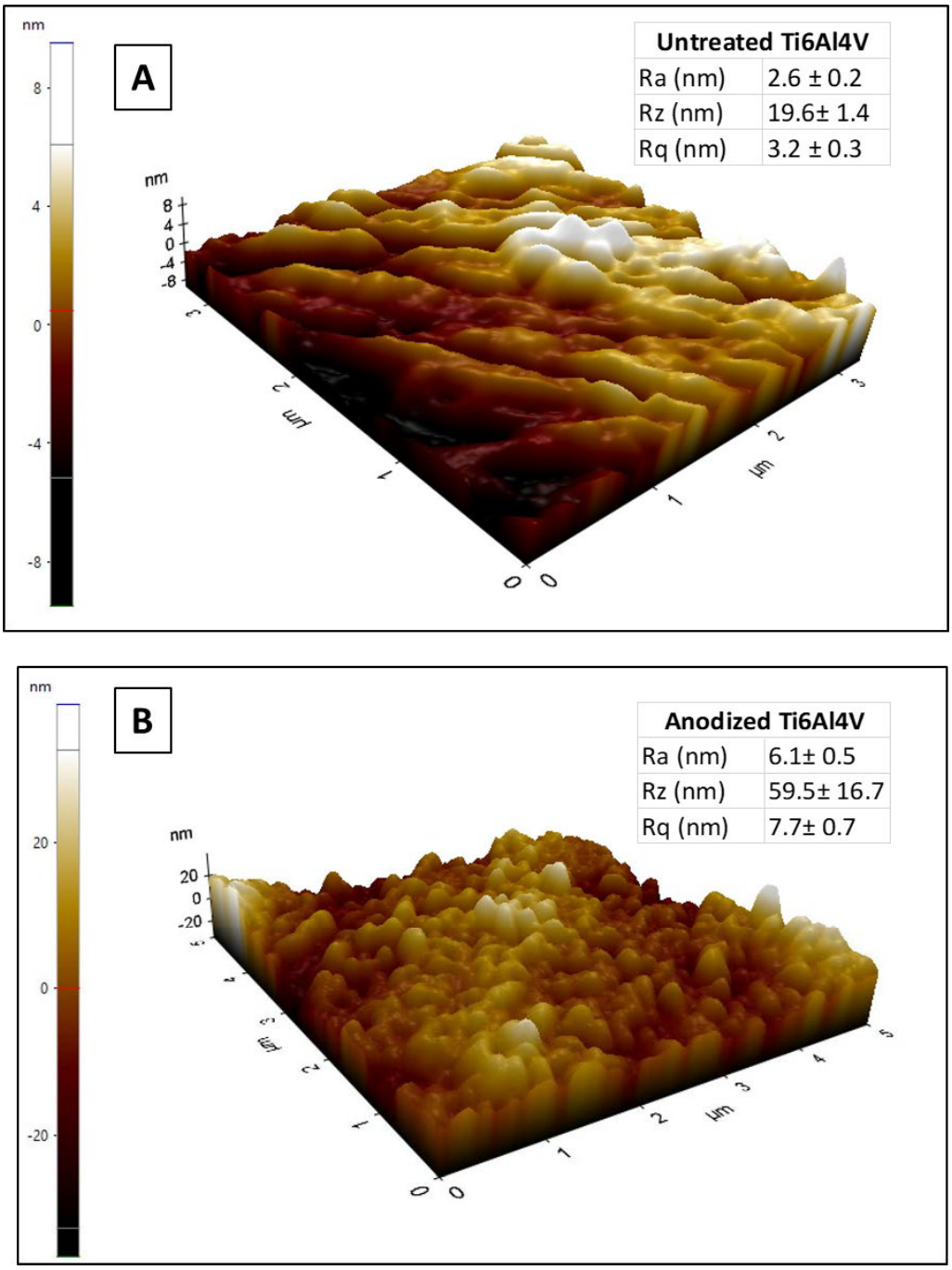

Figure 5.8 3D images from AFM analysis for untreated (A) and anodized (B) surfaces of Ti6Al4V discs with roughness parameters (Ra, Rz and Rq)

In the following section, the effect of thermal anodization on surface roughness and surface structure is further analyzed. Our study found that the surface roughness of Ti6Al4V was increased with the thermal anodization treatment. The surface structure and roughness are highly related to the osseointegration and bioactivity properties. It was reported that the effect of osseointegration can be improved by increasing surface roughness and, consequently, surface area (Milošev, 2010).

5.3.2 The Analyses of the Mechanical and Adhesion Properties

Nanoindentation and scratch tests were carried out on PLA films with and without HAp-Gm particles on the anodized and untreated Ti6Al4V discs to determine the mechanical and adhesion properties.

As shown in *Figure 5.9*, the hardness (H) and modulus of elasticity (E) values of uncoated, anodized, and untreated Ti6Al4V discs were obtained by nanoindentation analysis at high loads, namely 50-70 mN. The resultant indenter penetration depth ranged between 100 nm and 1000 nm in order to measure H and E values of both the surface oxidized layer and the Ti6Al4V substrate surface. It is important to note that the H and E values of the oxidized layer, which were labeled on the figures, were higher than the untreated Ti6Al4V substrate.

In Figure 5.9, the nanoindentation results of the anodized uncoated Ti6Al4V disc are shown at low loads. It can clearly be seen that the hardness values change from 3.6 to 6.5 GPa, while the E values at low loads are between 90 and 120 GPa. The increased radius of the indenter contact shows a marginal drop in H while elastic modulus shows a value closer to the Ti6Al4V due to higher penetration. On the other hand, *Figure 5.9* shows constant H and E values (both low and high contact radiuses) for highly polished Ti6Al4V (untreated and uncoated) discs.

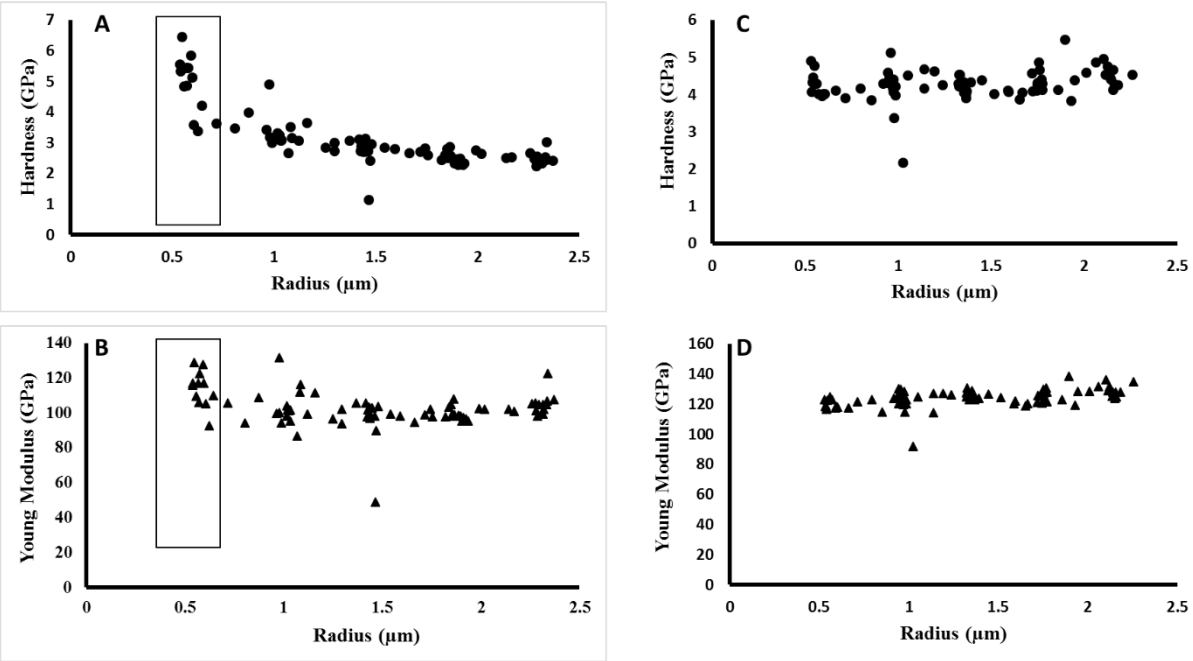

Figure 5.9 Nanoindentation results for H and E plotted versus radius of contact at maximum load. (A) H and (B) E of anodized uncoated Ti6Al4V disc respectively. (C) H and (D) E of untreated, uncoated Ti6Al4V disc respectively. The influence of the anodized layers is labeled in both A and B graphs

According to *Figures 5.9 A and B* and stated above, the H and E values of the anodized uncoated Ti6Al4V sample at low loads were higher than untreated, uncoated Ti6Al4V samples. Therefore, the nanoindentation analysis was conducted with low loads in order to compare anodized and untreated Ti6Al4V samples. The nanoindentation force-displacement curves in *Figure 5.10* show that the penetration depths for the anodized Ti6Al4V samples were less and resulted in higher hardness and E modulus. These curves also show a major change of slope at an approximately 40 to 50 nm penetration depth when the influence of the oxidized substrate occurs.

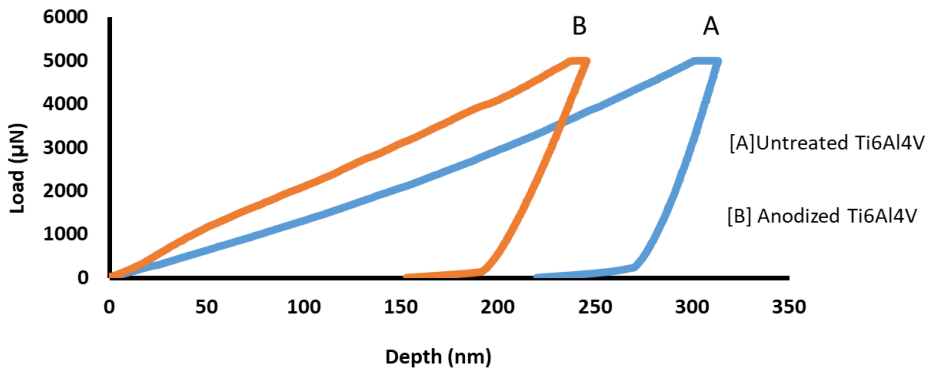

Figure 5.10 Comparison of Berkovich force-displacement indentation observations of both uncoated [A] untreated and [B] anodized Ti6Al4V discs at 5mN load. Note the steeper initial slope and inflection of the curve for the anodized sample

In our study, TiO_2 thin film on Ti6Al4V discs with high mechanical properties was observed by the thermal anodization process at 500 C˚. The influence of the anodization process on the highly polished Ti6Al4V surfaces were observed during the application of the nanoindentation test on the anodized and untreated Ti6Al4V samples at both high and low loads. The results show that the anodization process increases E and H values of the Ti6Al4V surface.

PLA and PLA biocomposite coated anodized and untreated Ti6Al4V samples were also analyzed with the nanoindentation test at high and low loads, in order to observe the effects of the anodization process on the PLA matrix biocomposite coating.

Nanoindentation analysis was done on untreated Ti6Al4V discs, PLA thin film and PLA-Gm-(HAp-Gm) thin film coated Ti6Al4V discs, to determine effect of PLA and PLA biocomposite thin film coating. The results (*Figure 5.11)* show clear differences between the hardness (H) and Young's modulus (E) values of the PLA biodegradable thin film coated and the uncoated, untreated Ti6Al4V discs according to the plastic depth (nm). The H and E values for the Ti6Al4V disc without the PLA thin film coating (Figure 5.11 A) were 4.3 GPa and 125.2 GPa respectively. As expected, the H and E values of PLA *(Figure 5.11 B)* and PLA biocomposite *(Figure 5.11 C)* thin films were much lower than the uncoated Ti6Al4V samples.

Under the same testing conditions, it was observed that the average H value (2.12 GPa) and the average E value (86.5 GPa) of PLA biocomposite coated samples were slightly higher than the average H value (1.58 GPa) and the E value (80.5 GPa) of the PLA only coated sample. The average H and E values of all samples are given at *Figure 5.11 D*. It can clearly be observed that both H and E values decreased after coating. It is thought that this can be an advantageous condition for an implant design, because the Young modulus values of coated samples are closer to the bone; the Young`s modulus value range is 10-25 GPa (Guillemot, 2005a).

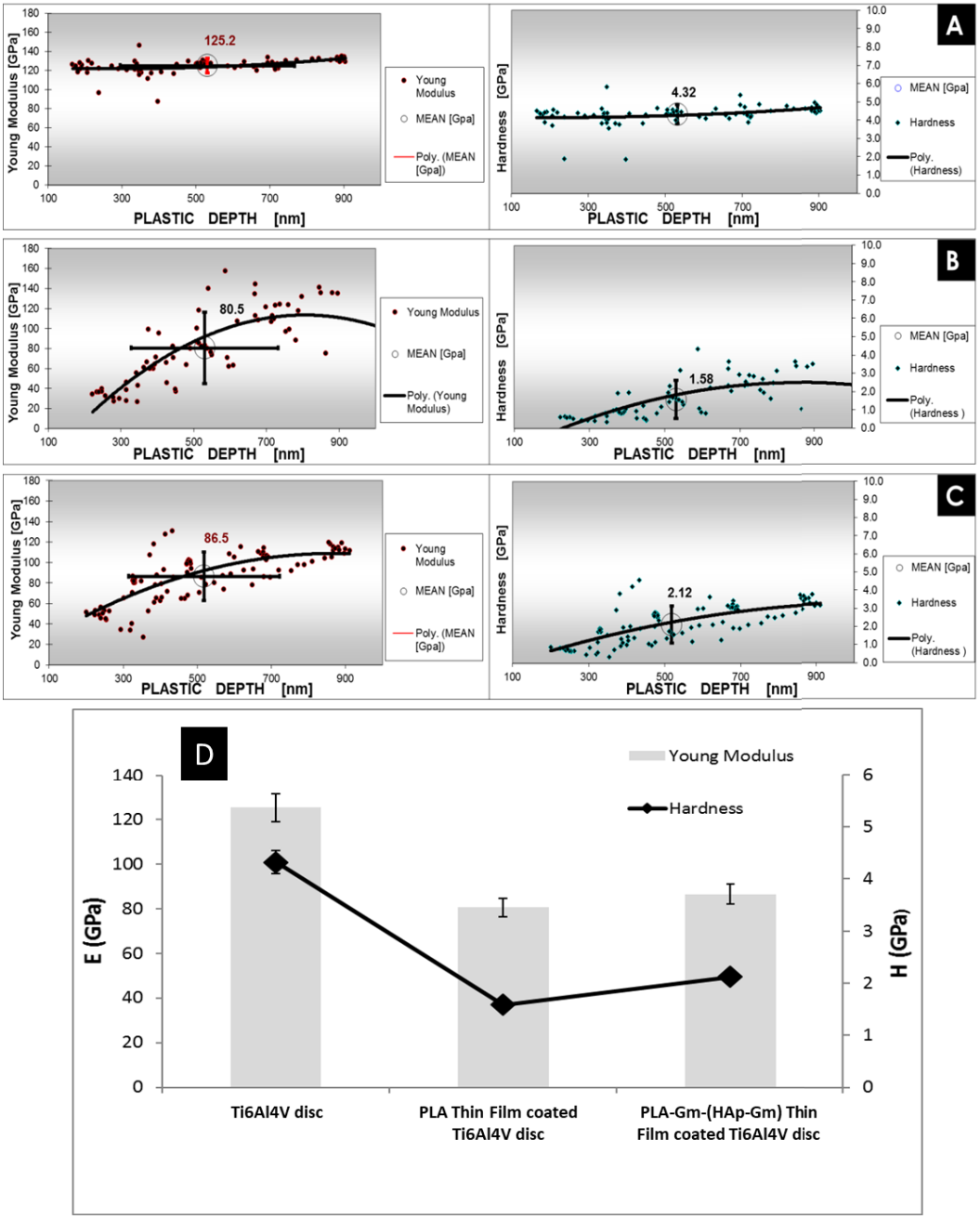

Figure 5.11 The nanoindentation Results for Uncoated (A), PLA coated (B) and PLA-biocomposite coated (C) untreated Ti6Al4V discs, and their hardness and Young's modulus values (D)

Figure 5.12 (below) shows the H and E values of anodized and untreated PLA-Gm-(HAp-Gm) coated Ti6Al4V discs versus contact radius.

During the nanoindentation tests, a wide load range was used, between 50 and 70 mN. It was applied in order to compare results for an extensive range of indentation depths. It was observed that the mechanical properties of PLA biocomposite films are influenced by the substrate hardness

(so-called substrate effect) at high loads. This is because of the difference in the wide penetration depth between the indenter and the film thickness.

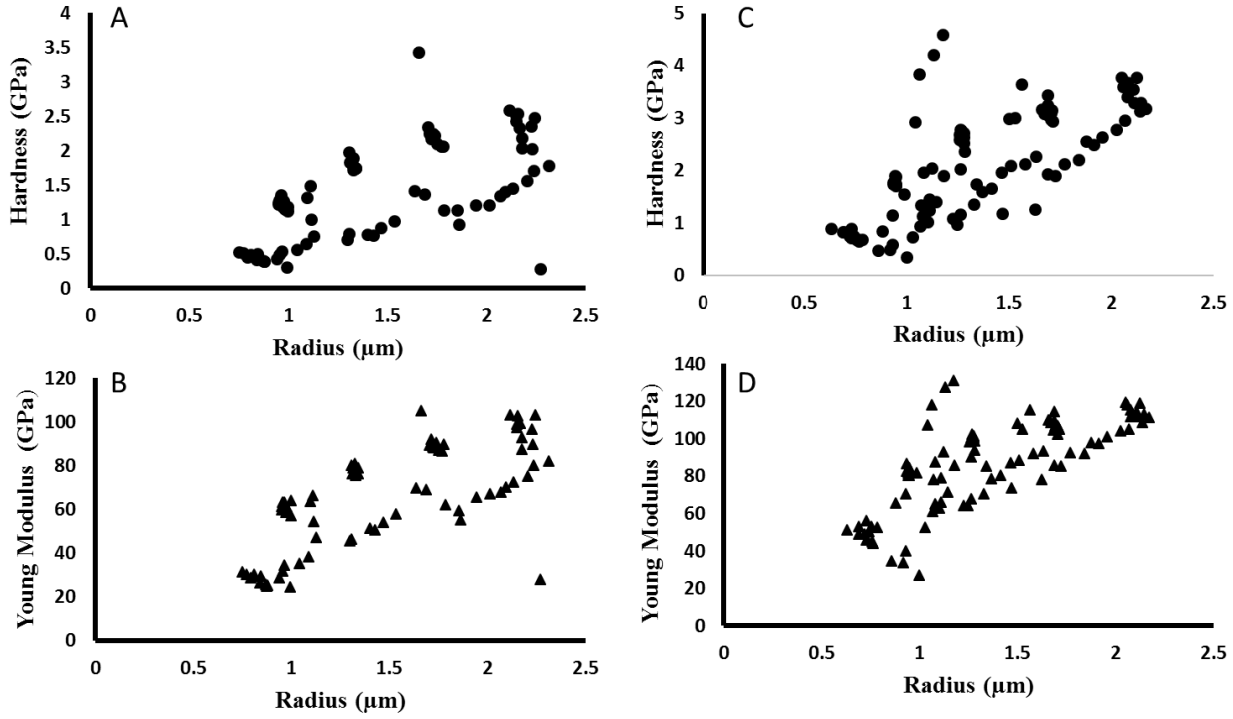

Figure 5.12 Nanoindentation results of anodized PLA-Gm-(HAp-Gm) coated Ti6Al4V disc: (A) H values against radius of contact, and (B) E values as a function of radius respectively; and nanoindentation results of untreated PLA-Gm-(HAp-Gm) coated Ti6Al4V disc: (C) H values versus contact radius, and (D) E values versus contact radius

The nanoindentation results of PLA-Gm-(HAp-Gm) coated anodized and untreated Ti6Al4V substrate surfaces are presented in *Figure 5.13* for a low load range between 0.1 and 5 mN. Applying a low load is important for determining the mechanical properties of the coating materials without the influence of the substrate material. According to *Figure 5.13*, the penetration depth of PLA-Gm-(HAp-Gm) coated anodized and untreated samples can be observed clearly. For example, when a 100µN load is applied on these two samples, the maximum penetration depth of an anodized PLA-Gm-(HAp-Gm) sample is around 60nm, and of an untreated sample is around 120nm. Hence, the coated anodized samples produced harder coatings.

Similarly, nanoindentation of uncoated samples applied at low loads showed that force-displacement curves the penetration depth for the anodized Ti6Al4V samples was less than the untreated ones and hence higher hardness for anodized uncoated samples (*Figure 5.10).*

For the nanoindentation tests, at maximum loads, the maximum penetration depth was approximately 500 nm, although the thickness of PLA film was measured at approximately 375nm.

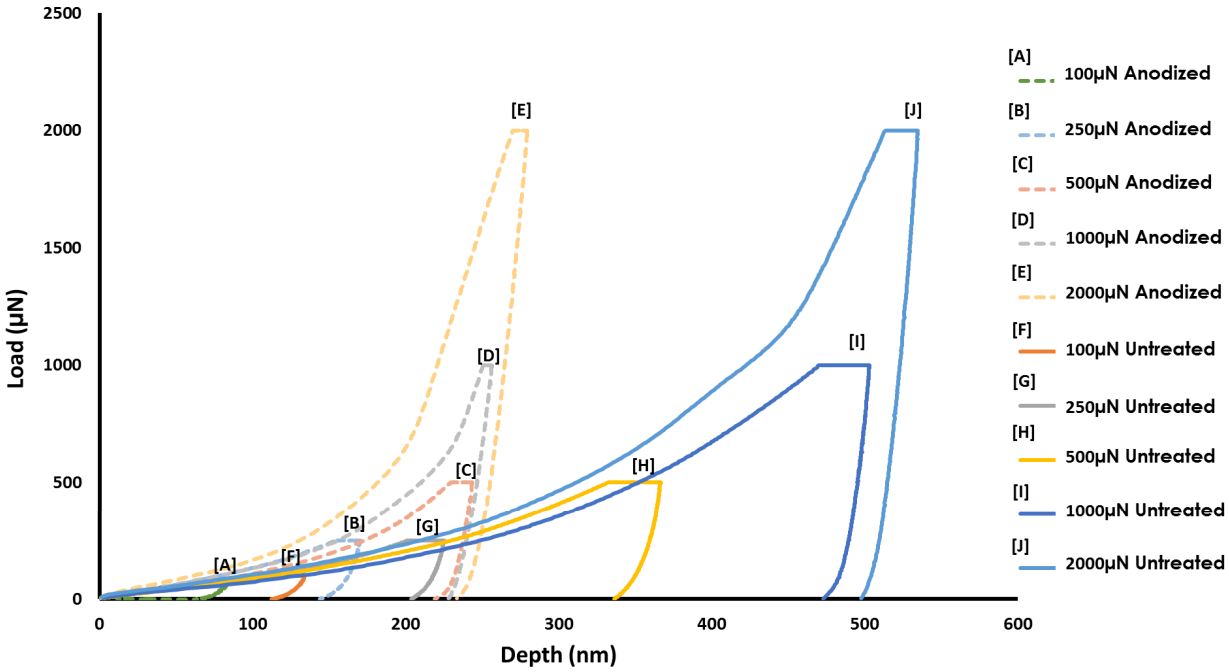

Figure 5.13 Nanoindentation force-displacement observations of PLA-HAp-Gm coated anodized and untreated samples according to various loading conditions

When the hardness and Young's modulus versus penetration depth profiles of PLA-Gm-(HAp-Gm) anodized and untreated coated samples are compared, the anodized substrates show higher hardness and Young's modulus (E) values than the untreated surfaces (*Figure 5.14)* for low load ranges (0.1-5mN).

Measured Young's modulus values for anodized PLA-Gm-(HAp-Gm) coated samples ranged between 20 and 70 GPa (dependent on applied loads). However, for the untreated PLA-Gm-(HAp-Gm) coated samples, it is between 20 and 50 GPa. It should be clarified that these are nanoindentation values of the coated samples and it is different to published bulk (monolithic) PLA values.

It was also observed that the hardness values of PLA biocomposite film coated anodized samples ranged from 0.45 to 1.9 GPa (dependent on the applied loads). Untreated coated samples ranged from 0.28 to 0.8 GPa, (*Figure 5.14)*. These results clearly show the substrate effect on the E and H values as a function of increased load.

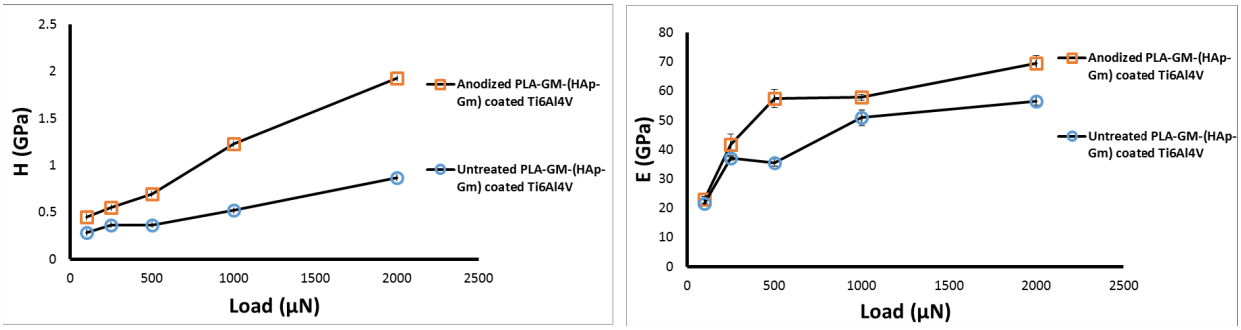

Figure 5.14 Nanoindentation test results of E and H values of PLA-Gm-(HAp-Gm) coated anodized and untreated Ti6AL4V discs as a function of load

Nanoindentation experiments (explained above) were conducted under low (0.1-5mN) and high (50-70mN) loads on the uncoated, PLA and PLA biocomposite coated untreated and anodized Ti6Al4V discs to observe H and E values. H and E values, shown in *Table 5.1* were changed according to nanoindentation loads for PLA biocomposite for coated untreated and anodized Ti6Al4V discs to investigate the effects of the biocomposite on mechanical properties. The results are shown in *Table 5.1*. As it can be seen from these figures at low loads, penetration on the indenter is low and lower H and E values are observed for the coated samples.

Table 5.1 The Hardness (H) and Young`s modulus (E) values of the samples are given according to low (0.1-5mN) and high (50-70 mN) applied nanoindentation loads

Samples	HARDNESS (GPa)	YOUNGs MODULUS (GPa)
Untreated Ti6Al4V	4-5	120 (50-70mN loads)
Anodized Ti6Al4V	3.6-6.5	90-120 (50-70mN loads)
PLA coated untreated Ti6Al4V	1.58	80.5 (50-70mN loads)
PLA-Gm-(HAp-Gm) coated untreated Ti6Al4V	2.12 0.28-0.8	86.5 (50-70 mN loads) 20-50GPa (0.1-5mN loads)
PLA-Gm-(HAp-Gm) coated anodized Ti6Al4V	0.45-1.9	20 to 70 GPa (0.1-5mN loads)

Scratch Tests

In this study, scratch tests using a <1 µm conical tip radius, 160 µN constant low load and approximately 200nm indentation depth (which is smaller than the thickness of the film) were utilized in order to determine the frictional response and adhesion of the films on the Ti6Al4V samples. Plastic deformation is observed in all PLA biocomposite coated samples, shown in the Scanning Probe Microscopy (SPM) results (in *Figure 5.15)*.

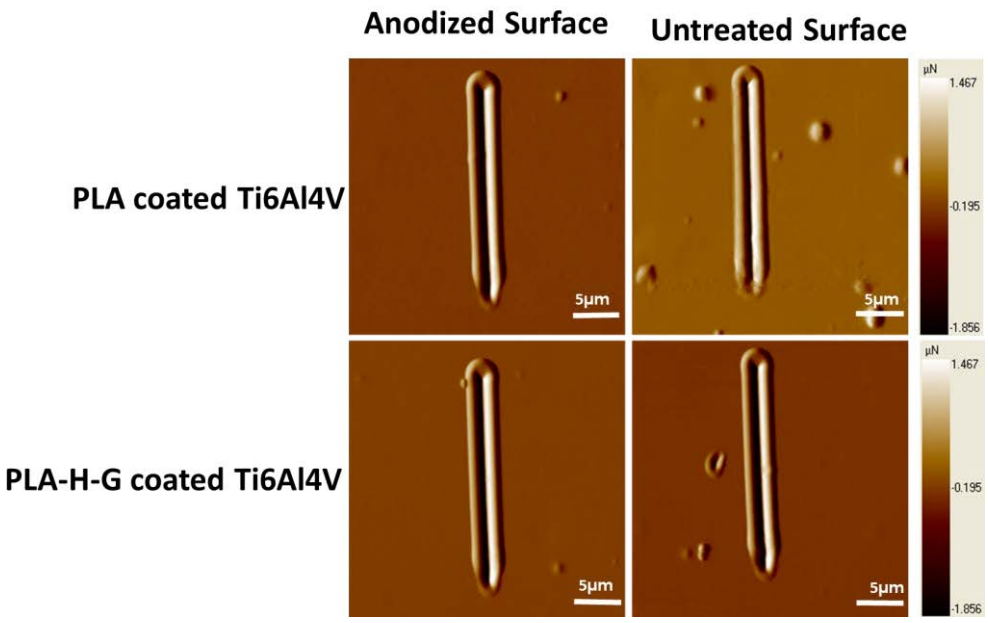

Figure 5.15 Micro-scratch test results for anodized and untreated PLA biocomposite coated Ti6Al4V samples. These observations were generated by the SPM scan facility of the triboindenter system

Plots of the coefficient of friction versus distance traveled are shown in *Figure 5.16* for all the samples. It was observed in *Figures 5.15* and *5.16* that when the PLA-Gm-(HAp-Gm) coating material is compared against the PLA film, there was no indication of a stick-slip like neither response nor evidence to suggest film delamination during scratching. There are also no statistically significant differences between their friction coefficient values. The presence of the pile-up of material either side of the scratch indicates that plastic deformation is observed on the PLA and PLA biocomposite coated surfaces with low loads, as shown in *Figure 5.12*. The limited difference in appearance between the SPM scans for the anodized and untreated coated surfaces suggests that most of the deformation and pile-up occurred in the PLA biocomposite coating itself rather than the metallic substrate. An estimate of the contact pressure from the diameter of the track suggests that it is only ~16 to 20 MPa, well below the yield stress for the deformation of the substrates.

For example, while an untreated Ti6Al4V disc with PLA coating and a untreated Ti6Al4V disc with PLA-Gm-(HAp-Gm) coating were compared, the friction coefficient value for the untreated PLA coated sample is 0.680 ± 0.013, while the untreated PLA-Gm-(HAp-Gm) biocomposite coated sample is 0.658 ± 0.014.

The friction coefficient versus lateral displacement graphs was prepared in order to compare the parameters which influence the PLA biocomposite deposited on anodized and untreated Ti6Al4V surfaces (*Figure 5.16*).

Friction coefficient parameters are known to have two major contributions, namely plowing and adhesion resistance forces (Cope et al., 2005, Ballarre et al., 2009). The observations suggest that while the plastic plowing contribution dominated the friction, the slight reduction in friction associated with the Gm containing films may be associated with a reduction in surface adhesion.

For both anodized and untreated substrates, PLA, and PLA-Gm-(HAp-Gm) coated samples, the resultant smooth tracks and the absence of stick-slip events during sliding indicate that both showed good adhesion to their respective substrates.

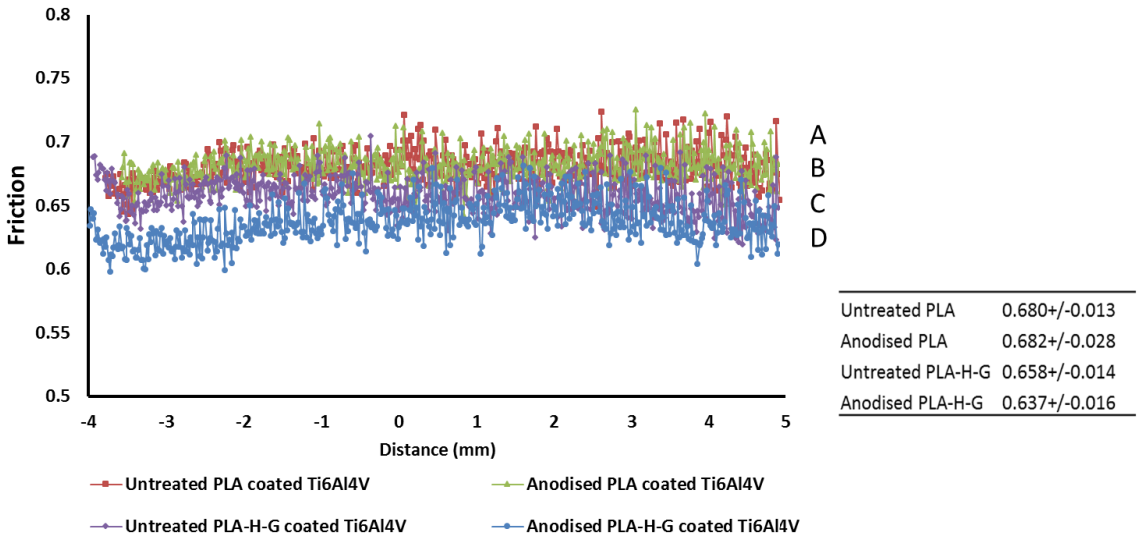

Figure 5.16 Friction coefficient vs. Lateral displacement graph for [A] PLA coated untreated, [B] PLA coated anodized, [C] PLA-Gm-(HAp-Gm) coated untreated, [D] PLA-Gm-(HAp-Gm) coated anodized Ti6Al4V discs

In summary, the mechanical testing results show that PLA biocomposite coating is much softer than the substrate, and the nanoindentation penetrates through this thickness. The substrate effect is clearly detectable from the results.

The degradation of the PLA-HAp composite and the adhesion between the implant and coating is very important in long term clinical applications. However, it is well known that most metallic

implants are inserted by force during surgery; they need to be bonded to the hard and soft tissues to stop micro-motion and hence the possibility of infection (Sotto-Maior et al., 2010).

The immediate strength and adhesion of our coating or, in general, any coating used on implants is reflected in their Young's modulus and hardness, which are easily obtainable for nano coated implants. This is also the case in our coatings. Without the appropriate strength or hardness, they cannot be inserted soundly or survive the surgical handling. The results obtained show that our PLA coatings can survive handling and insertion.

5.4 Conclusions

The nanoindentation results for uncoated but substrates for both treated and untreated Ti6Al4V discs at high and low loads showed that both H and E values of the treated Ti6Al4V are higher than the untreated Ti6Al4V samples. However, PLA-Gm-(HAp-Gm) thin film coated anodized Ti6Al4V samples showed E values of 20 to 70 GPa and H values of 0.45 to 1.9 GPa. For PLA-Gm-(HAp-Gm) thin film coated untreated Ti6Al4V samples, E values ranged from 20 to 50 GPa and H values from 0.28 to 0.8 GPa, showing the advantage of anodization of these substrates for clinical use due to their strong adhesion and properties.

When the E and H values of Ti6Al4V discs were compared before and after the PLA thin film biocomposite coating, the polymeric thin film matrix decreases the H values in a range from 3-4 GPa to 0.28-0.8 GPa and also decreases the E values from 120-140 GPa to 20-50 GPa for both treated (thermally anodized) and also untreated samples. This shows the effect of the polymeric coating. Nanoindentation studies clearly confirm that the increased E and H values observed at different applied loads are due to the substrate effect which is dependent on the indenter penetration depth, applied load value and the thickness of the films.

The scratch test results show that the incorporation of HAp and Gm particles into the PLA thin films does not influence the friction coefficient. The results of the nanoindentation clearly support those of the scratch tests at low loads, and they show that the PLA film coated treated samples are harder than the PLA untreated samples.

In polymeric based composite coatings, for realistic H and E results with both scratch and nanoindentation tests, low loads should be utilized with indenter penetration less than the film thickness.

5.5 References

ATAEE, A., LI, Y., FRASER, D., SONG, G. & WEN, C. 2018. Anisotropic Ti-6Al-4V gyroid scaffolds manufactured by electron beam melting (EBM) for bone implant applications. *Materials & Design,* 137**,** 345-354.

BALLARRE, J., JIMENEZ-PIQUE, E., ANGLADA, M., PELLICE, S. A. & CAVALIERI, A. L. 2009. Mechanical characterization of nano-reinforced silica based sol–gel hybrid coatings on AISI 316L stainless steel using nanoindentation techniques. *Surface and Coatings Technology,* 203**,** 3325-3331.

BEN-NISSAN, B., CHOI, A., ROEST, R., LATELLA, B. A. & BENDAVID, A. 2015. Adhesion of hydroxyapatite on titanium medical implants. *In:* MUCALO, M. (ed.) *Hydroxyapatite (HAp) for Biomedical Applications.* Woodhead Publishing.

BEN-NISSAN, B. & CHOI, A. H. 2017. Calcium Phosphate Nanocoatings: Production, Physical and Biological Properties, and Biomedical Applications. *In:* SAN, T. E., JIE, H. & MAMORU, A. (eds.) *Nanobioceramics for Healthcare Applications.* World Scientific.

BEN-NISSAN, B., CHOI, A. H. & BENDAVID, A. 2013. Mechanical properties of inorganic biomedical thin films and their corresponding testing methods. *Surface and Coatings Technology,* 233**,** 39-48.

BEN-NISSAN, B., CHOI, A. H., MACHA, I. J. & CAZALBOU, S. 2014. Sol-gel Nanocoatings of Bioceramics. *In:* ANTONIAC, I. V. (ed.) *Handbook of Bioceramics and Biocomposites.* Cham: Springer International Publishing.

BROWNE, M. & GREGSON, P. J. 1994. Surface modification of titanium alloy implants. *Biomaterials,* 15**,** 894-898.

BULL, S. J. & BERASETEGUI, E. G. 2006. Chapter 7 - An Overview Of The Potential Of Quantitative Coating Adhesion Measurement By Scratch Testing. *In:* SINHA, S. (ed.) *Tribology and Interface Engineering Series.* Elsevier.

CHOI, A. H., BEN-NISSAN, B., BENDAVID, A. & LATELLA, B. 2016. Mechanical behavior and properties of thin films for biomedical applications. *In:* GRIESSER, H. J. (ed.) *Thin Film Coatings for Biomaterials and Biomedical Applications.* Woodhead Publishing.

CHOI, A. H., BEN-NISSAN, B., MATINLINNA, J. P. & CONWAY, R. C. 2013. Current perspectives: calcium phosphate nanocoatings and nanocomposite coatings in dentistry. *Journal of dental research,* 92**,** 853-859.

CHOI, A. H., KARACAN, I. & BEN-NISSAN, B. 2018. Surface modifications of titanium alloy using nanobioceramic-based coatings to improve osseointegration: a review. *Materials Technology***,** 1-10.

CIGADA, A., CABRINI, M. & PEDEFERRI, P. 1992. Increasing of the corrosion resistance of the Ti6Al4V alloy by high thickness anodic oxidation. *Journal of Materials Science: Materials in Medicine,* 3**,** 408-412.

COPE, B. C., PACKHAM, D. E., LEGGETT, G., BEECH, J. C., LOWE, G. B., BRIGGS, D., BREWIS, D. M., CROCOMBE, A. D., DIXON, D. G., VAN OOIJ, W. J., PARBHOO, B., WARWICK, C. M., PRITCHARD, J., MILLINGTON, S., CHATFIELD, C., COMYN, J., DILLARD, D. A., KNEAFSEY, B., SHANAHAN, M. E. R. & POCIUS, A. V. 2005. Scratch Test. *In:* E., P. D. (ed.) *Handbook of Adhesion.* John Wiley & Sons, Ltd.

DOGAR CUTEAN, E. S., MITELEA, I., ŞERBAN, V. A. & CODREAN, C. 2015. Scratch Test and Adhesion Properties of Titanium Coatings Deposited by TIG Welding on Steels. *Advanced Materials Research,* 1111**,** 1-6.

FARAH, S., ANDERSON, D. G. & LANGER, R. 2016. Physical and mechanical properties of PLA, and their functions in widespread applications - A comprehensive review. *Adv Drug Deliv Rev,* 107**,** 367-392.

GUILLEMOT, F. 2005a. Recent advances in the design of titanium alloys for orthopedic applications. *Expert review of medical devices,* 2**,** 741-8.

GUILLEMOT, F. 2005b. Recent advances in the design of titanium alloys for orthopedic applications. *Expert Review of Medical Devices,* 2**,** 741-748.

KARGUPTA, R., BOK, S., DARR, C. M., CRIST, B. D., GANGOPADHYAY, K., GANGOPADHYAY, S. & SENGUPTA, S. 2014. Coatings and surface modifications imparting antimicrobial activity to orthopedic implants. 6**,** 475-495.

KRUZIC, J. J. & RITCHIE, R. O. 2008. Fatigue of mineralized tissues: cortical bone and dentin. *J Mech Behav Biomed Mater,* 1**,** 3-17.

KRZĄKAŁA, A., SŁUŻALSKA, K., DERCZ, G., MACIEJ, A., KAZEK, A., SZADE, J., WINIARSKI, A., DUDEK, M., MICHALSKA, J., TYLKO, G., OSYCZKA, A. M. & SIMKA, W. 2013. Characterisation of bioactive films on Ti–6Al–4V alloy. *Electrochimica Acta,* 104**,** 425-438.

LAN, W.-C., HUANG, T.-S., CHO, Y.-C., HUANG, Y.-T., WALINSKI, C. J., CHIANG, P.-C., RUSILIN, M., PAI, F.-T., HUANG, C.-C. & HUANG, M.-S. J. A. S. 2020. The Potential of a Nanostructured Titanium Oxide Layer with Self-Assembled Monolayers for Biomedical Applications: Surface Properties and Biomechanical Behaviors. 10**,** 590.

LATELLA, B., SWAIN, M. V. & IGNAT, M. 2012. Indentation and Fracture of Hybrid Sol-Gel Silica Films. *In:* NEMECEK, J. (ed.) *Nanoindentation in Materials Science.* IntechOpen.

LEWALLEN, E. A., RIESTER, S. M., BONIN, C. A., KREMERS, H. M., DUDAKOVIC, A., KAKAR, S., COHEN, R. C., WESTENDORF, J. J., LEWALLEN, D. G. & VAN WIJNEN, A. J. 2014. Biological Strategies for Improved Osseointegration and Osteoinduction of Porous Metal Orthopedic Implants. *Tissue Engineering Part B: Reviews,* 21**,** 218-230.

MILOŠEV, I. 2010. Metallic materials for biomedical applications: Laboratory and clinical studies. *Pure and Applied Chemistry,* 83**,** 309-324.

PAITAL, S. R., DAHOTRE, N. B. 2009. Calcium phosphate coatings for bio-implant applications: Materials, performance factors, and methodologies. *Materials Science and Engineering: R: Reports,* 66**,** 1-70.

PATEL, S. B., HAMLEKHAN, A., ROYHMAN, D., BUTT, A., YUAN, J., SHOKUHFAR, T., SUKOTJO, C., MATHEW, M. T., JURSICH, G. & TAKOUDIS, C. G. 2014. Enhancing surface characteristics of Ti–6Al–4V for bio-implants using integrated anodization and thermal oxidation. *Journal of Materials Chemistry B,* 2**,** 3597-3608.

PIVETEAU, L.-D. 2001. Sol-Gel Coatings on Titanium. *Titanium in Medicine: Material Science, Surface Science, Engineering, Biological Responses and Medical Applications.* Berlin, Heidelberg: Springer Berlin Heidelberg.

RATH, P. C., BESRA, L., SINGH, B. P. & BHATTACHARJEE, S. 2012. Titania/hydroxyapatite bi-layer coating on Ti metal by electrophoretic deposition: Characterization and corrosion studies. *Ceramics International,* 38**,** 3209-3216.

RATNER, B. D. 2001. A Perspective on Titanium Biocompatibility. *In:* BRUNETTE, D. M., TENGVALL, P., TEXTOR, M. & THOMSEN, P. (eds.) *Titanium in Medicine.* Berlin, Heidelberg: Springer.

ROEST, R. 2008. *INTERFACIAL CHARACTERISATION OF SOL- GEL DERIVED COATINGS OF HYDROXYAPATITE AND ZIRCONIA THIN FILMS WITH ANODISED TITANIUM SUBSTRATES.* PhD, UNIVERSITY OF TECHNOLOGY SYDNEY.

ROEST, R., LATELLA, B., HENESS, G. & BEN-NISSAN, B. 2011. Adhesion of Sol-Gel Derived Hydroxyapatite Nanocoatings on Anodised Pure Titanium and Titanium (Ti6Al4V) Alloy Substrates. *Surface & Coatings Technology - SURF COAT TECH,* 205**,** 3520-3529.

SCARPELLI, F., MASTROPIETRO, T. F., POERIO, T. & GODBERT, N. 2018. Mesoporous TiO2 Thin Films: State of the Art. *In:* YANG, D. (ed.) *Titanium Dioxide-Material for a Sustainable Environment.* IntechOpen.

SOTTO-MAIOR, B. S., ROCHA, E. P., ALMEIDA, E. O. D., FREITAS-JÚNIOR, A. C., ANCHIETA, R. B. & CURY, A. A. D. B. 2010. Influence of high insertion torque on implant placement: an anisotropic bone stress analysis %J Brazilian Dental Journal. 21**,** 508-514.

SWAIN, M. V. & MENČÍK, J. 1994. Mechanical property characterization of thin films using spherical tipped indenters. *Thin Solid Films,* 253**,** 204-211.

TEXTOR, M., SITTIG, C., FRAUCHIGER, V., TOSATTI, S. & BRUNETTE, D. M. 2001. Properties and Biological Significance of Natural Oxide Films on Titanium and Its Alloys. *Titanium in Medicine: Material Science, Surface Science, Engineering, Biological Responses and Medical Applications.* Berlin, Heidelberg: Springer Berlin Heidelberg

WUHRER, R., MORAN, K. & MORAN, L. 2006. Characterisation of materials through x-ray mapping. *Materials Forum,* 30.

Chapter 6

Antibacterial Studies for PLA Biocomposite Thin Film Coated Ti6Al4V Bone Implants

Chapter 6: Antibacterial Studies for PLA Biocomposite Thin Film Coated Ti6Al4V Bone Implants

This chapter investigates the antibacterial efficacy and cytotoxic effects of a Gentamicin (Gm 5%, 10%, 15%, 20% and 30% w/w) infused PLA-Gm-(HAp-Gm) thin film, coated over a Titanium-6-Aluminium-4-Vanadium (Ti6Al4V) implant. The two bacterial strains used for this study were *Staphylococcus aureus* and Staphylococcus *epidermidis*. This investigation was completed using a modified agar disc diffusion method, bacterial growth curves and assessment of biofilm formation.

6.1 Introduction

Bacterial infections following implant surgery are a major worldwide health burden, costing western nations between 1 and 3 billion USD per year (Darouiche, 2003, Wang et al., 2016, Ben-Nissan et al., 2016). Surgeries for correcting open bone fractures, joint replacements, or dental implants are all associated with a 10-50% risk of bacterial infection at the site of implant-bone integration, resulting in implant failure and in severe cases, requiring implant removal (Ribeiro et al., 2012, Inzana et al., 2016, Seebach and Kubatzky, 2019). Most importantly, implant composition, the raw material(s) used and the related surface properties (texture, porosity, or charge), play major roles in facilitating and supporting not only bacterial growth but also initiating bacterial biofilm formation (Campoccia et al., 2010, Ben-Nissan et al., 2016). In order to prevent bacterial growth and biofilm formation, the use of a combination of a polymeric-based drug delivery coating system, integrated within the biomedical metallic implant is an innovative concept that provides controllable and slow antibiotic release for the prevention of bacterial growth and biofilm formation (Santos et al., 2014, Macha et al., 2015, Nandi et al., 2016). It has been reported that a slow and progressive release of antibiotic(s) at the implant-tissue integration can effectively prevent post-implant bacterial infections (Manivasagam et al., 2010, Mantripragada et al., 2013).

The most common opportunistic pathogens that cause implant-related infections are *S. aureus and S. epidermidis* (Hetrick and Schoenfisch, 2006, Mishra et al., 2014). *S. aureus* is a gram-positive bacterial strain belonging to the coagulase-positive staphylococci (CoPS) group. It contributes to approximately 35% of all implant-related bacterial infections with infection severity attributed to

and corresponding to *S. aureus* biofilm formation (Montanaro et al., 2011, Loss et al., 2019). *S. epidermidis* is known as a coagulase-negative and gram-positive Staphylococcus (Namvar et al., 2014). It is usually considered a commensal bacterial colonizer of human (or other mammalian) skin. *S. epidermidis* are more likely to be found on human skin as potential pathogenic bacteria. However, *S. aureus* related infections are generally more deep and severe (Hetrick and Schoenfisch, 2006, Ben-Nissan et al., 2016). Therefore, they are two of the most common opportunistic pathogens causing medical device related infections, due to contamination during the insertion (Otto, 2009, Namvar et al., 2014).

Bacteria generally exist in a planktonic state, which refers to them existing as individual, free moving bacteria found in a solution. While a sessile population, are bacteria that are attached to any surface material or found within a biofilm (Garrett et al., 2008). Biofilms are characterized by a densely packed, sessile bacterial community attached to an inert surface. Members of these populations secrete an extracellular polysaccharide matrix to encapsulate the internal proliferating bacterial population. This extracellular polysaccharide matrix protects the encapsulated bacteria not only from the physicochemical and mechanical properties of the surrounding host environment, but also provides an impenetrable barrier to antibiotic treatments (Donlan, 2002, Renner and Weibel, 2011). Therefore, bacterial biofilms have a 10-1000 times greater resistance to antibacterial treatments than a single, planktonic bacterium (Garrett et al., 2008, Simchi et al., 2011, Fernandez-Yague et al., 2015). Thus, there arises the possibility to create implant composition material(s) and associated surface properties that include antibacterial surface coatings, designed to prevent or inhibit the initial bacterial attachment and subsequent biofilm formation on the implant surface (Wang et al., 2016).

The most common treatment for implant related bacterial infections worldwide is the oral, systemic delivery of the antibiotic, gentamicin (Gm), or Gm in combination with vancomycin. Gm belongs to the aminoglycoside antibiotic family and is a broad-spectrum antibiotic effective in killing both gram-negative and most gram-positive bacteria, including *S. aureus* and *S. epidermidis* (Varghese et al., 2017). However, high concentrations can ultimately result in both patient organ (Blunston et al., 2015) and system (Bhattacharya et al., 2015) damage. This is due to its high dosage related cytotoxic and nephrotoxic effects (Ben-Nissan et al., 2016). Long term, high-dose Gm therapy has been associated with bacterial antibiotic resistance (Ribeiro et al., 2012, Ben-Nissan and Green, 2013). Thus, to effectively treat challenging implant related infections like *S. aureus* biofilm formation, there is a need to develop a localized and controlled antibiotic delivery system that releases Gm at a constant rate in order to improve Gm efficacy and efficiency and reduce systemic related toxicity.

To decrease the risk of implant-tissue (specifically bone) related bacterial infections, a variety of implant designs have been developed. These include surface modifications with the aim of preventing the initial bacterial attachment, the incorporation of silver nano-particles (De Giglio et al., 2013, Pan et al., 2018), the attachment-resistant polymeric coatings (Kargupta et al., 2014), and drug delivery coating systems containing antibiotics (Macha et al., 2018). However, the long term, steady and controlled release of antibiotics from an implant still remains a challenge. Aviv *et al.* (Aviv et al., 2007) reported that two biodegradable polymeric based drug delivery coating systems were produced. They are Gm embedded within poly-lactic acid (PLA-Gm) and Gm embedded poly-(lactide-co-glycolide) (PLGA-Gm) films as an implant coating material at concentrations of 10% (w/w) and 30% (w/w). Although both PLA-Gm and PLGA-Gm systems were effective at inhibiting *S. aureus* and *S. epidermidis* growth, the initial burst Gm release of all PLA-Gm and PLGA-Gm films at 10%, 30% (w/w) were higher than the minimum inhibition concentration of the bacteria, and the initial Gm release from the majority of samples were over the toxic level of Gm. On the other hand, the results show that PLA-Gm films had a slower and more continuous Gm release due to the lower degradation rate of PLA polymer than PLGA-Gm, which released 80-90% Gm in six hours. Therefore, PLA biodegradable polymer has a more suitable degradation rate than PGLA for slow and controlled drug release coating systems, although its drug release rate was high. PLA is a suitable coating material for controlled long-term drug delivery because of its biodegradability, low degradation rate, and biocompatibility (Nair and Laurencin, 2007). These previous studies also reported fast dissolution rates.

In order to improve the control of the initial drug release and to obtain a long term continuous drug release, biodegradable PLA drug delivery coating systems can be combined with drug carrier particles such as ceramic based biomaterial particles (Macha et al., 2015, Karacan et al., 2017).

Thus, the main aim of this study was to develop, test and verify novel antibacterial biocomposite coating designs which include drug dissolution studies, characterization and *in vitro* studies. Therefore, this study focused on determining the efficacy of dose-dependent Gm release from PLA-Gm-(HAp-Gm) thin film coated Ti6Al4V implants to prevent not only localized *S. aureus* and *S. epidermidis* growth, but also *S. aureus* biofilm formation on the implant surfaces.

6.2 Experimental Methods

The production steps of PLA-Gm-(HAp-Gm) thin film coated Ti6Al4V discs at predetermined Gm concentrations (5%, 10%, 15%, 20%, and 30% w/w) were described in **Chapters 2** and **3** in detail. To sterilize the resulting PLA-Gm-(HAp-Gm) coated Ti6Al4V discs, each side was subjected to a 10 min incubation with ultraviolet light before bactericidal testing.

6.2.1 Determination of a Clear Zone for *S. aureus* and *S. epidermidis* using the Modified Agar Disc Diffusion Method

Staphylococcus *aureus* (S34) and Staphylococcus *epidermidis* (S29) were used with Mueller Hinton Clinical and Laboratory Standards Institute (CLSI) Agar Plates (Micro media). The direct colony suspension method was modified for the inoculum according to CLSI standards (CLSI, 2012). The inoculum was made from a suspension of isolated S34 colonies, which are selected from an eighteen-hour nonselective brain-heart infusion agar plate (Thermo Scientific). The suspension was prepared to match the 0.5 McFarland standard turbidity using distilled sterile water and a vortex mixer. The experimental setup was modified from the Agar disc diffusion method (Heatley, 1944, CLSI, 2012, Balouiri et al., 2016). The *S. aureus* colony (S34) was spread on a Muller Hilton Agar Plate. Each of the PLA biocomposite coated Ti6Al4V discs (Ø 13 mm), containing 5%, 10% or 20% (w/w) PLA-Gm-(HAp-Gm), were placed individually at the center of the inoculated Muller Hinton Agar Plate. The discs were pressed down to ensure complete contact with the agar surface. They were placed into a 37°C incubator overnight. After sixteen hours, the clear (disinfected) zone around the discs was measured and recorded. This experiment was designed to determine the effect of Gm in the PLA biocomposite coating on the *S. aureus* and also to compare the different Gm contents. The same testing steps were applied to *S. epidermidis* to observe the effect of the Gm release from PLA-Gm-(HAp-Gm) thin film coated Ti6Al4V discs at 5%, 10% or 20% w/w Gm concentrations.

6.2.2 *S. aureus* growth curve co-cultured with PLA-Gm-(HAp-Gm) coated Ti6Al4V discs

All bacterial experimental protocols followed the CLSI (2012) standard procedures. *S. aureus* was grown on brain-heart infusion agar plates (ThermoFisher Scientific, USA) and incubated overnight at 37 °C. For planktonic *S. aureus* growth, a single *S. aureus* colony was transferred to sterile Nutrient Broth Medium and incubated at 37 °C with orbital shaking at 100 rpm for sixteen hours. An Infinite

200Pro microplate reader (Tecan, Switzerland) was used to determine the absorbance values of *S. aureus* culture at OD_{600}. From the overnight culture, a starter culture was prepared and diluted to 0.01nm OD_{600}. To determine the growth curve of *S. aureus* biofilm formation was added to starter cultures and were incubated at 37 °C for twenty-four hours with OD_{600} values recorded at the beginning after thirty minutes to observe the log phase, then every hour for ten hours, and the final reading was at twenty-four hours. PLA-Gm-(HAp-Gm) coated Ti6Al4V discs at 5%, 10%, 15%, 20%, and 30% (w/w) Gm concentrations were introduced to the *S. aureus* culture during the exponential growth phase (determined to be 0.1nm OD_{600}). OD_{600} values were measured every hour for the first ten hours and a final reading was taken at twenty-four hours. The statistical analysis was performed using two-way ANOVA with Tukey's post-test. n=3. *S. aureus* cultures alone, *S. aureus* co-cultured with the Ti6Al4V disc alone (i.e. minus biocomposite coating) and PLA coated Ti6Al4V discs were used as controls.

6.2.3 *S. aureus* biofilm formation and cytoxicity on PLA-Gm-(HAp-Gm) coated Ti6Al4V discs

S. aureus overnight inoculum cultures were carried out as described above. To create the starter culture, it is incubated for sixteen hours. *S. aureus* cultures (1.12nm OD_{600}) were then diluted 1:100 using sterile Nutrient Broth Medium and incubated at 37 °C with orbital shaking for a further two hours to allow exponential growth (0.26nm OD_{600}). The starter culture was again diluted 1:100 and added to the UV-sterilized PLA-Gm-(HAp-Gm) coated Ti6Al4V discs with predetermined Gm concentrations (ranging from 5% to 30% (w/w) and controls. *S. aureus* was incubated with the PLA-Gm-(HAp-Gm) coated Ti6Al4V discs at 37 °C for twenty-four hours to allow bacteria to attach and a biofilm to form. After twenty-four hours, PLA-Gm-(HAp-Gm) coated Ti6Al4V discs were rinsed twice with saline solution (0.85% NaCl (w/v) to remove planktonic *S. aureus* cells and allows the immature biofilm to remain. To determine the viability of the immature *S. aureus* biofilm, a Live/Dead (Biotium, USA) staining protocol was conducted following the manufacturer instructions. The PLA-Gm-(HAp-Gm) coated Ti6Al4V discs containing the biofilm were rinsed twice with saline solution to remove the excess stain and fixed with a 4% paraformaldehyde/PBS (w/v) (PFA) solution for thirty minutes and rinsed twice with saline solution to remove residual PFA. The cytotoxicity profile of *S. aureus* following the Gm release from the PLA-Gm-(HAp-Gm) coated Ti6Al4V discs was visualized using the DeltaVision Elite microscopy. The Olympus 40x/1.35, UApo/1-UB768 magnification lenses were used with FITC filter that is for DMAO live stain (Ex/Em: 503/530 nm, green) and mCherry filter that is for EthD-III dead stain (Ex/Em: 530/620 nm, red). Fifteen fields of view from three individual

discs were taken per sample and analyzed via FIJI software, (Java-based Image Processing and Analysis Software by NIH Image) using an in-house script (developed by Dr. Evenhuis). The statistical analysis was performed using one-way ANOVA with Tukey's post-test. n=3.

6.3 Results and Discussions

Two critical points were investigated in order to observe the antibacterial effect of PLA biocomposite coating and also to compare different Gm concentrations within the composite on *S. aureus* (S34) and *S. epidermidis* (S29) bacteria. In *Figure 6.1*, the results provide the answers regarding these two points for *S. aureus*. Firstly, *Figure 6.1 A* shows that only Ti6Al4V discs without coating on the center of Muller Hinton Agar medium and no clear antibacterial reacted zone are observed. These results show that without gentamicin, the bacteria grow freely on bare titanium alloy surfaces. *Figure 6.1 B*, *C,* and *D* illustrate the outcome for the 5%, 10%, and 20% PLA-Gm-(HAp-Gm) coated Ti6Al4V discs respectively. The zones around the different Gm containing PLA biocomposite coated Ti6Al4V discs are clearly visible. The areal size of these clear zones was measured to determine the efficiency of the antibiotic at the different concentrations. The graph in *Figure 6.1 E* represents the clear zone comparison between Ti6Al4V disc without coating, and with 5%, 10%, and 20% PLA-Gm-(HAp-Gm) coated Ti6Al4V samples. While the clear zone for 5% PLA-Gm-(HAp-Gm) coated sample is 6cm^2, it is 7.6 cm^2 for the 10% PLA-Gm-(HAp-Gm) coated sample and 9.2cm^2 for the 20% PLA-Gm-(HAp-Gm) coated sample. The comparative difference clearly shows the effect of each percentage of Gm biocomposite on *S. aureus* after sixteen hours of incubation.

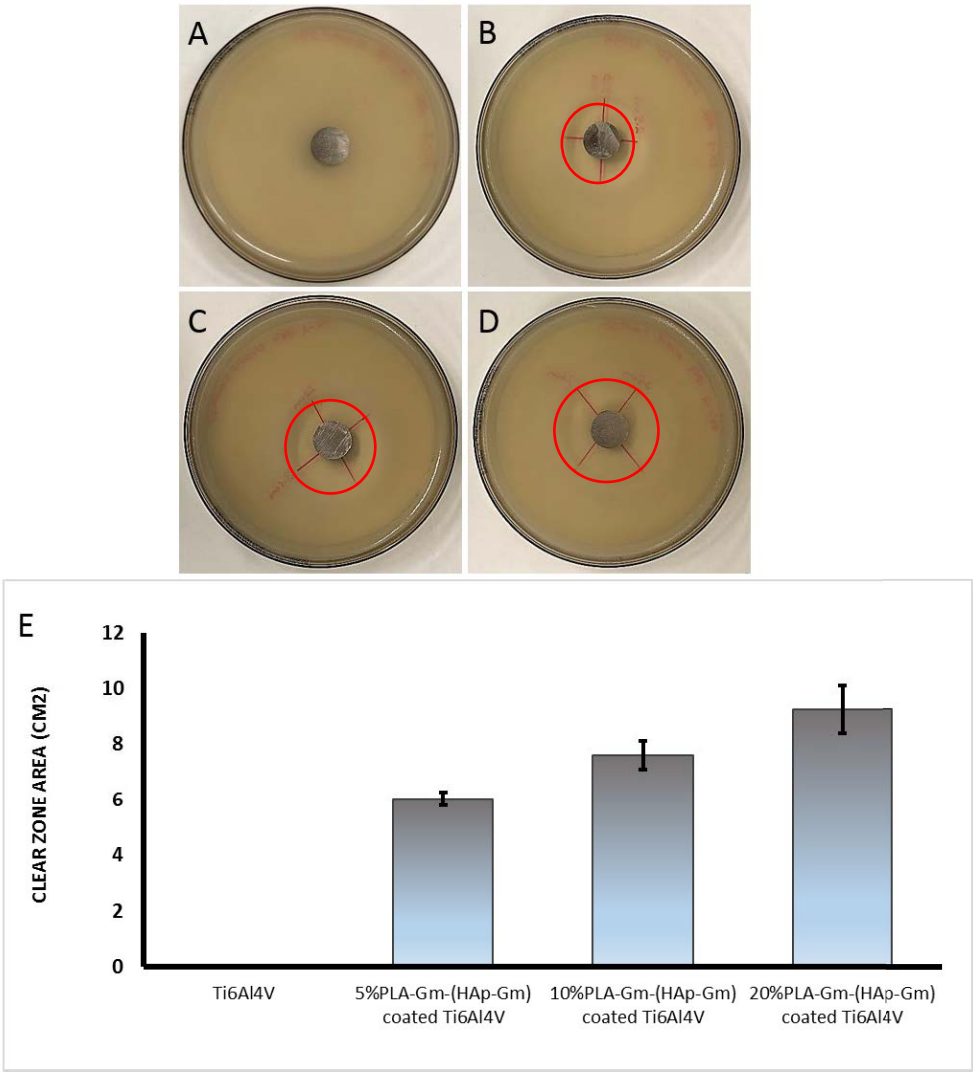

Figure 6.1 The Antibacterial test results for Ti6Al4V disc without PLA biocomposite coating (A) and 5% (B), 10% (C), or 20% (D) PLA biocomposite coating on the Ti6Al4V discs, using *S. aureus* S34 bacterial strain, following 16h incubation at 37˚C. (E) Bar graph with standard deviations, of the clear zone areas for each condition

In *Figure 6.2*, the results demonstrate the effects of PLA-Gm-(HAp-Gm) thin film coated Ti6Al4V samples at 5%, 10%, and 20% Gm concentrations on *S. epidermidis*. *Figure 6.2 A* shows that only the Ti6Al4V discs without coating placed at the center of a Muller Hinton Agar medium, showed no clear antibacterial reacted zone. These results match the results from the *S. aureus* tests in *Figure 6.1*. *Figures 6.2 B, C,* and *D* illustrate the outcome for 5%, 10% and 20% PLA-Gm-(HAp-Gm) coated Ti6Al4V discs respectively, and the clear zones around the different Gm containing the PLA biocomposite coated Ti6Al4V discs are clearly visible. The size of the clear zones around the 5%, 10%, and 20% Gm concentrations contained by the PLA-Gm-(HAp-Gm) thin film coated Ti6Al4V discs

were calculated using the formula of the area of an ellipse. *Figure 6.2 E* shows that the area of each of the three different concentrations of Gm was similar. Additionally, the size of the clear zones from the *S. epidermidis* experiment was found to be approximately two times larger than the *S. aureus* experiment.

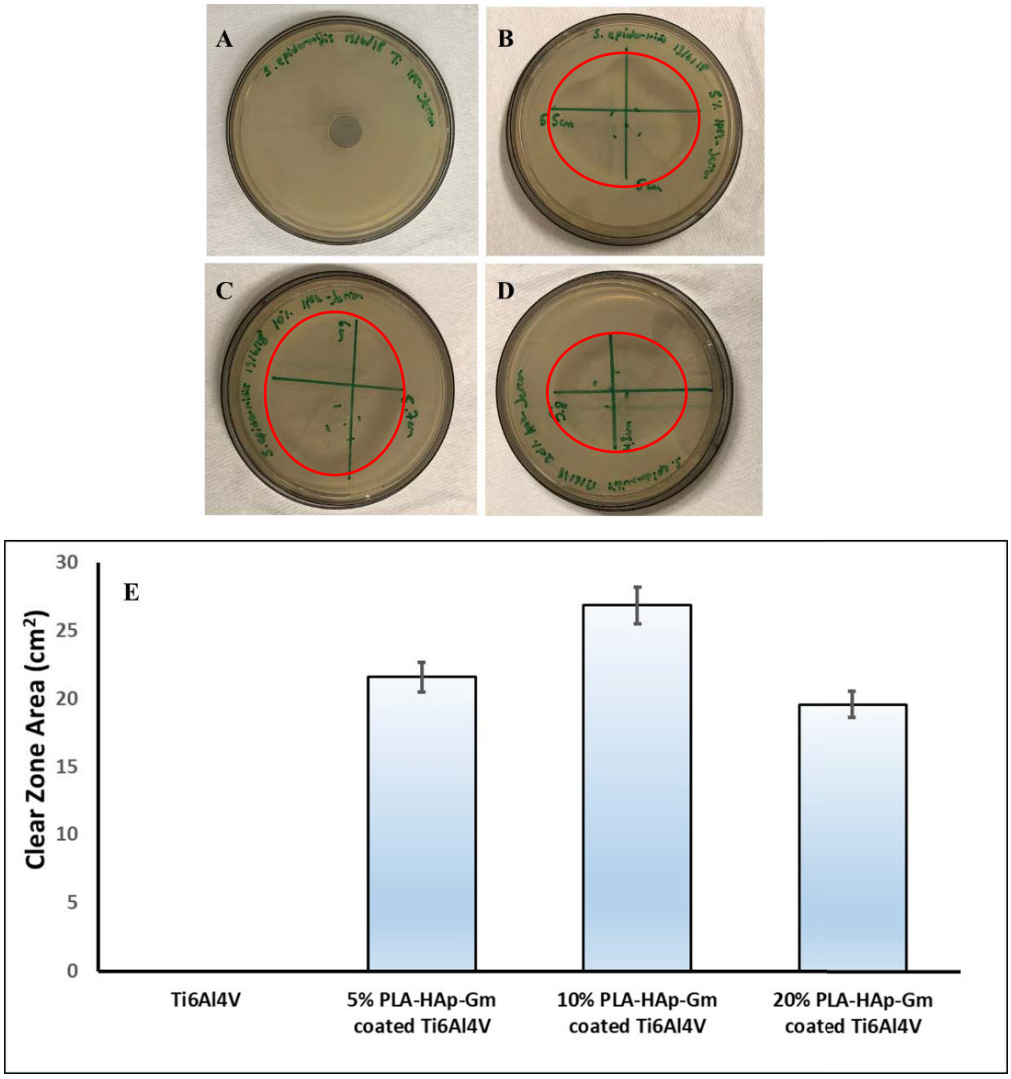

Figure 6.2 The Antibacterial test results for Ti6Al4V disc without PLA biocomposite coating (A) and 5% (B), 10% (C) and 20% (D) PLA biocomposite coating on the Ti6Al4V discs are given to use *S. epidermidis* (S29) bacterial strain after sixteen hours of incubation at 37˚C. Additionally, the clear zones of all samples are plotted as a bar diagram (E)

Although the Gm release from the PLA-Gm-(HAp-Gm) thin film coated Ti6Al4V discs, including the lowest Gm (5% sample) were effective at inhibiting the growth of both *S. aureus* and *S. epidermidis*, it was found that the Gm release from the PLA-Gm-(HAp-Gm) coated samples were more effective at inhibiting *S. epidermidis* growth compared to *S. aureus*. The results can be explained as the

difference of the minimum inhibitory concentration (MIC) between S. epidermids and S. aureus against the gentamicin.

Sabath *et al.* (1976) investigated that the susceptibilities of *S. aureus* and *S. epidermidis* were determined against each of 65 antibiotic agents. They reported that while the MIC range of *S. aureus* was found 0.2-1.6 µg/ml for gentamicin, the MIC range of *S. epidermidis* was 0.04-0.2 µg/ml. Although gentamicin is active antibiotic on both *S. aureus* and *S. epidermidis*, according to their susceptibility, it is more active antibiotic against S. epidermidis than S. aureus (Sabath et al., 1976). Additionally, *S. aureus* causes more severe and rapid implant-related infection than *S. epidermidis* (Hetrick and Schoenfisch, 2006, Ben-Nissan et al., 2016). Our results also match with literature. Due to the results from the modified agar disc diffusion experiment, the next antibacterial tests on PLA-Gm-(HAp-Gm) thin film coated Ti6Al4V discs at different Gm concentrations were conducted using only *S. aureus.*

6.3.1 PLA-Gm-(HAp-Gm) coated Ti6Al4V implants inhibited *S. aureus* exponential growth

To establish the log, exponential and stationary growth phases of the *Staphylococcus aureus* strain a twenty-four-hour growth curve was first conducted. It was found that the *S. aureus* culture reached the log phase within the first hour of growth and that the exponential growth phase was observed between hours one and seven (OD_{600}: 0.2±0.12 and 0.37±0.025, respectively; *Figure 6.3*). Finally, the *S. aureus* stationary phase was determined post seven hours of growth (*Figure 6.3*).

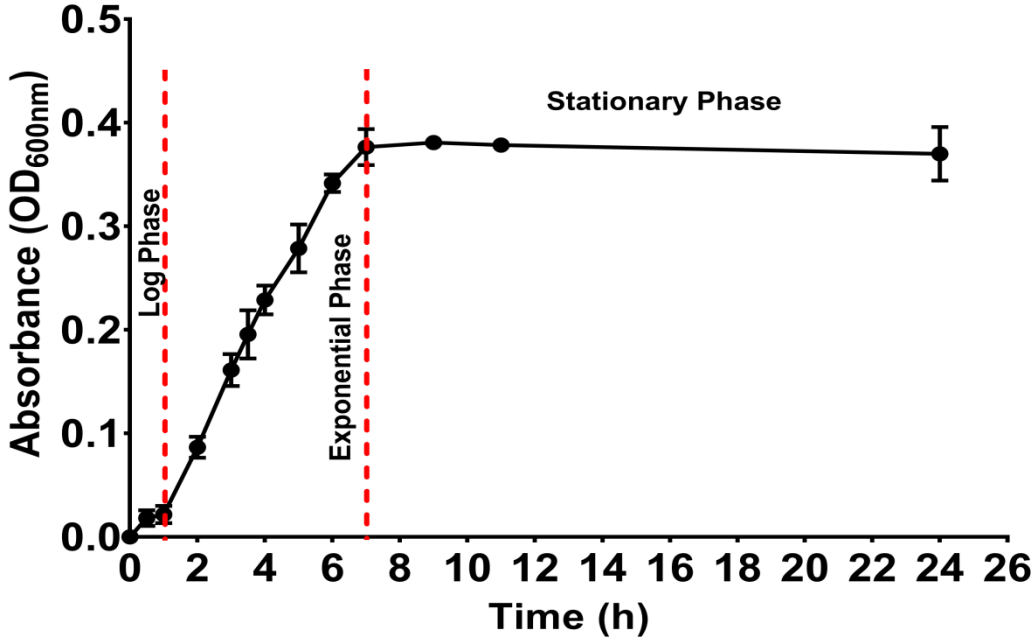

Figure 6.3 Graph represents the twenty-four hour growth curve of *S. aureus* biofilm formation. Optical density was measured at 600 nm (OD_{600})

To appropriately simulate an early *S. aureus* infection post implant surgery environment, PLA-Gm-(HAp-Gm) coated Ti6Al4V discs were introduced to *S. aureus* static cultures at 0.1 OD_{600} and the antibacterial effect of the Gm release from the PLA-Gm-(HAp-Gm) coated Ti6Al4V disc was determined (*Figure 6.4*). Furthermore, to ascertain if the antibacterial efficacy of the PLA-Gm-(HAp-Gm) coated Ti6Al4V discs was dependent on the Gm concentration, PLA-Gm-(HAp-Gm) coatings were loaded with a range of Gm concentrations (5%, 10%, 15%, 20%, 30% [w/w]). *S. aureus growth* curves co-cultured with one of the PLA-Gm-(HAp-Gm) coated Ti6Al4V discs or controls (*S. aureus alone*, Ti6Al4V disc, and PLA coated Ti6Al4V disc) were recorded over a course of twenty-four hours. Importantly, no significant difference in *S. aureus* growth was observed at any time point between the control conditions. *S. aureus* co-cultured with the PLA-Gm-(HAp-Gm) coated Ti6Al4V discs showed similar exponential growth profiles, irrespective of Gm concentration, throughout the first four hours when compared to controls (*S. aureus* alone, Ti6Al4V discs, and PLA coated Ti6Al4V discs). However, after four hours of co-culture, the growth of *S. aureus* co-cultured with the PLA-Gm-(HAp-Gm) coated Ti6Al4V discs plateaued, compared to controls (*Figure 6.4*), suggesting that active Gm had been released from the PLA biocomposite thin film coated Ti6Al4V, providing both bactericidal and bacteriostatic activity. All Gm concentrations (ranging from 5% to 30% w/w) contained the PLA-Gm-(HAp-Gm) coated Ti6Al4V discs showed significant inhibition of *S. aureus* growth when compared to control following seven hours of co-culture (*Figure 6.4*). The difference of *S. aureus*

growth between control samples and all PLA-Gm-(HAp-Gm) coated Ti6Al4V discs after seven hours co-culture was clearly observed, as seen in *Figure 6.4*. Interestingly, no significant difference in *S. aureus* growth was observed between the different Gm concentrations contained in the PLA-Gm-(HAp-Gm) coated Ti6Al4V discs, suggesting that 5% Gm (w/w) was sufficient to inhibit *S. aureus* growth over the twenty-four-hour time period continually.

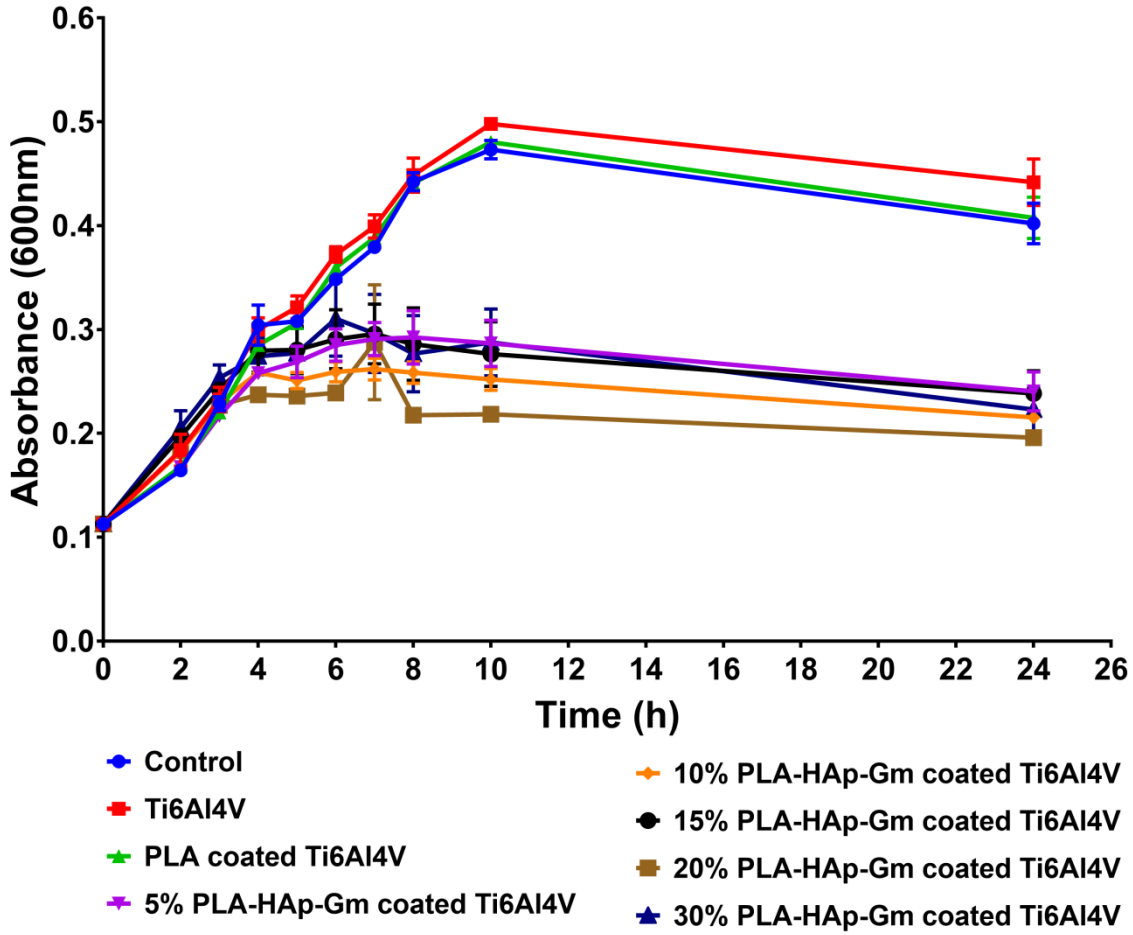

Figure 6.4 Graph depicts the *S. aureus* growth curves, and the addition of the PLA-Gm-(HAp-Gm) coated Ti6Al4V discs during the early exponential phase (two hours after bacterial growth was initiated). Absorbance was measured at 600 nm for twenty-four hours. Statistical analysis performed using two-way ANOVA with Tukey's post-test. n=3. Error bars denote SD. **p<0.01, ****p<0.0001

The inhibitory effect of the initial burst Gm release from the PLA-Gm-(HAp-Gm) coated Ti6Al4V samples at predetermined concentrations (5%-30% [w/w]) on the *S. aureus* growth at the planktonic stage of bacteria when the samples were placed into the exponentially grown *S. aureus* co-cultured medium, was observed after four hours of co-culture. Although the *S. aureus* growth decreased significantly following seven hours of co-culture when compared to the controls, the results showed

no significant changes in *S. aureus* growth between 5%-30% (w/w) range of PLA-Gm-(HAp-Gm) thin film coated Ti6Al4V samples. That might be the effect of HAp drug carrier particles on the systems that reduces the initial Gm release to avoid over-dose of the initial burst Gm release.

6.3.2 PLA-Gm-(HAp-Gm) coating inhibited *S. aureus* biofilm formation on the Ti6Al4V discs

To determine the appropriate and effective dosage of the initial Gm release required to inhibit bacterial adhesion and the subsequent biofilm formation on the implant surface, *S. aureus* was co-cultured with PLA-Gm-(HAp-Gm) coated Ti6Al4V discs for twenty-four hours under static conditions to allow biofilm(s) to form. Experimental controls were the same as mentioned previously. *S. aureus* adhesion (microcolonies) and growth to the PLA-Gm-(HAp-Gm) coated Ti6Al4V discs were visualized using deconvolution confocal microscopy following Live/Dead staining (*Figure 6.5*). Live *S. aureus* microcolonies were uniformly distributed over the control surfaces (*Figure 6.5*, green), corresponding with a live population of greater than 50% for each control surface (*Figure 6.6 A*). Interestingly, a significant decrease in the percentage of live *S. aureus* was determined for *S. aureus* co-cultured with the Ti6Al4V disc, compared to *S. aureus* alone (*Figure 6.6 A*). Live *S. aureus* microcolonies were observed on the PLA-Gm-(HAp-Gm) thin film coated Ti6Al4V discs (*Figure 6.5*). However, the percentage of live *S. aureus* was significantly lower for those discs preloaded with 15, 20 and 30% Gm (w/w) when compared to the control (PLA coated Ti6Al4V disc; *Figure 6.6 B*). No significant difference in live *S. aureus* was observed between the different Gm concentrations contained in the PLA-Gm-(HAp-Gm) thin film coated Ti6Al4V discs (*Figure 6.6 B*). Taken together, these results demonstrate that by PLA-Gm-(HAp-Gm) coated Ti6Al4V discs with concentrations of Gm above 15% (w/w), may serve to inhibit *S. aureus* biofilm formation on implants *in vivo*.

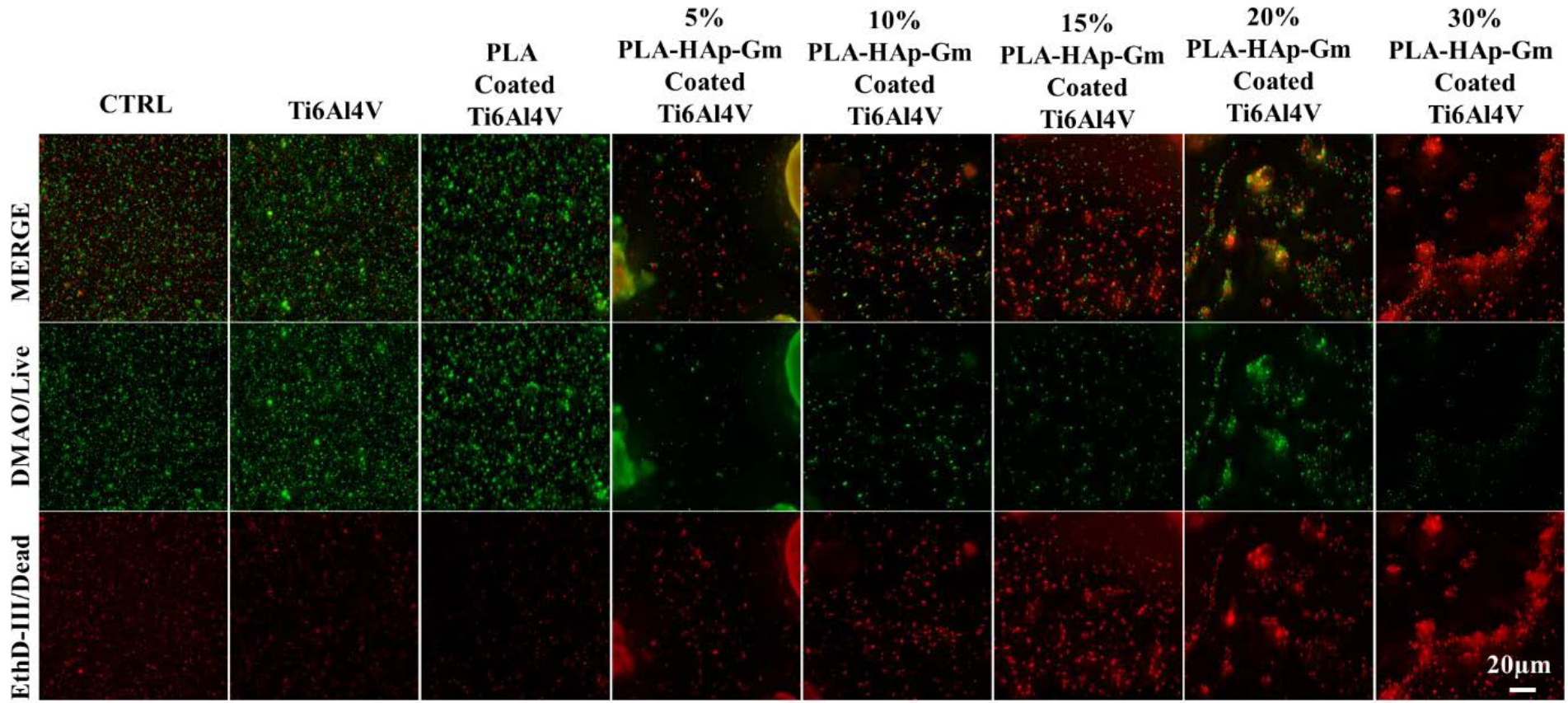

Figure 6.5 Representative fluorescent images *S. aureus* following twenty-four hours of co-culture with Ti6Al4V discs (as indicated). Samples were co-stained with DMAO (live; green) and EtD-III (dead; red), merged images are also shown. Scale bar represents 20 µm

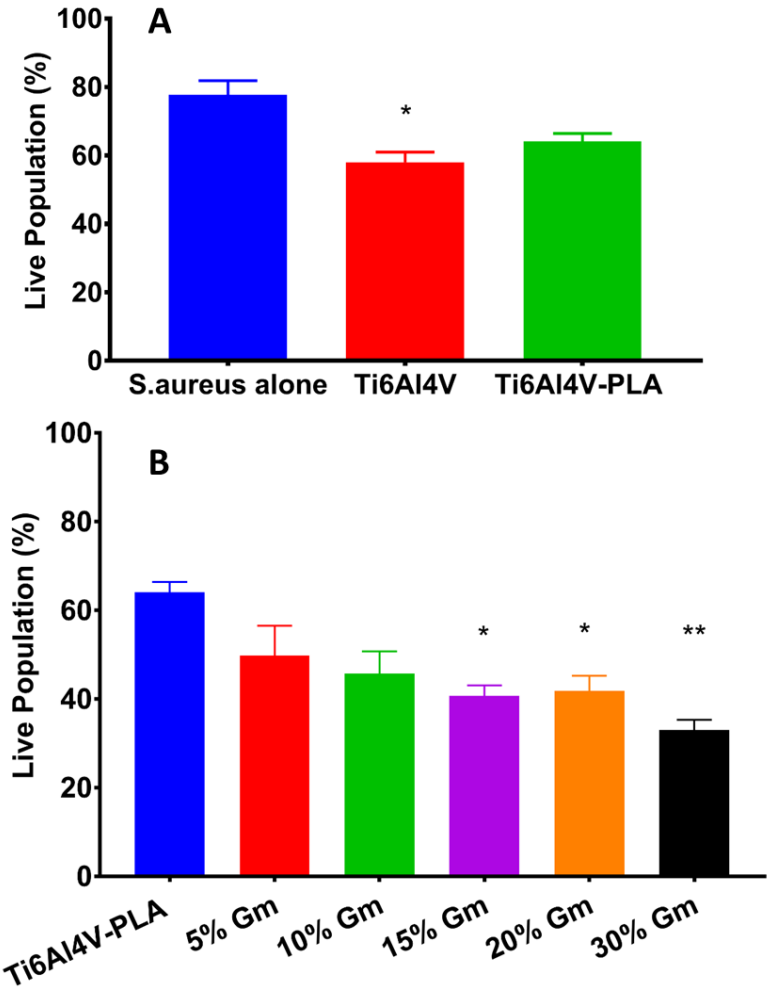

Figure 6.6 Graph represents the percentage of DMAO-positive (live) *S. aureus* following twenty-four hours of co-culture with the controls (A) (as indicated), and (B) PLA and PLA-Gm-(HAp-Gm) thin film coated Ti6Al4V discs (5% to 30% w/w Gm concentrations). The analysis was performed using ImageJ software. Statistical analysis performed using one-way ANOVA with Tukey's post-test. n=3 (15 images per sample). Error bars denote SEM. *p<0.05, **p<0.01

In these studies, the inhibition of the biofilm formation, bacterial attachment, and reduction of the live bacteria percentages on the PLA-Gm-(HAP-Gm) thin film coated Ti6Al4V implant surfaces at (5%-30%[w/w]) were successfully demonstrated. When the results of all Gm concentrations (5%-30% [w/w]) utilized for the PLA-Gm-(HAp-Gm) thin film coated Ti6Al4V discs were compared, it clearly shows that samples containing 15%, 20%, and 30% (w/w) Gm have significantly less bacterial

attachment and growth than the samples containing 5% and 10% Gm. Therefore, Gm and HAp-Gm particles within PLA thin film coating were able to change the surface properties of TI6Al4V metallic implants to reduce bacterial attachment and biofilm formation. PLA-Gm-(HAp-Gm) thin film coated Ti6Al4V implants at above 15% (w/w) Gm concentration might be effective to prevent *S. aureus* based implant-related infections. Based on these results, in *vitro* cell studies using samples containing > /= 15% (w/w) Gm concentration were undertaken using Human adipose-derived stem cells (ADSCs). This work is described in **Chapter 7**.

6.4 Conclusion

The biomimetic based bioceramic (HAp) containing the PLA biocomposite thin film coating system has been proven to be an effective controlled Gm release system capable of delivering drugs locally in the human body. It is predicted that use of these biocompatible and biomimetic coral skeleton-derived drug carrier particles for the prevention of *S. epidermidis* and *S. aureus* growth and *S. aureus* biofilm formation are very effective and can be investigated for clinical applications.

Our results demonstrate the importance of local and controlled drug delivery implant systems on the inhibition of bacterial infection and biofilm formation instead of using a high systemic dosage of antibiotics as a treatment.

The initial Gm release of PLA-Gm-(HAp-Gm) thin film coated Ti6Al4V discs at predetermined Gm concentrations (5%-30% w/w) were effective at reducing *S. aureus* growth in both a planktonic state and biofilm state. Gm contained in the PLA-Gm-(HAp-Gm) thin film coated Ti6Al4V samples (at concentrations from 5% to 30%) have shown the antibacterial effect on reducing bacterial attachment and biofilm formation on the surface. Gm contained in the PLA-Gm-(HAp-Gm) thin film coated Ti6Al4V samples (over 15% [w/w]) were more effective in decreasing biofilm formation on the surface. This proves that different ranges of Gm concentrations are applicable with PLA-Gm-(HAp-Gm) thin film coating design, which gives flexibility for adjusting antibiotic dosage according to the patient according to the type of treatment.

The significant reduction of bacterial attachment and percentage of dead microcolonies were observed for even the lowest Gm concentration (5% [w/w]) containing the PLA-Gm-(HAp-Gm) coated sample when compared with the control. It was confirmed that PLA-Gm-(HAp-Gm) thin film coating is promising as a biodegradable local and controlled drug delivery coating system for metallic bone implants in order to prevent bacterial growth and biofilm formation.

6.5 REFERENCES

AVIV, M., BERDICEVSKY, I. & ZILBERMAN, M. 2007. Gentamicin-loaded bioresorbable films for prevention of bacterial infections associated with orthopedic implants. *J Biomed Mater Res A,* 83**,** 10-9.

BALOUIRI, M., SADIKI, M. & IBNSOUDA, S. K. 2016. Methods for in vitro evaluating antimicrobial activity: A review. *Journal of Pharmaceutical Analysis,* 6**,** 71-79.

BEN-NISSAN, B. & GREEN, D. W. 2013. Marine materials in drug delivery and tissue engineering: from natural role models to bone regeneration and repair and slow delivery of therapeutic drugs, proteins, and genes. *In:* KIM, S. K. (ed.) *Marine biomaterials: Characterization, isolation and applications.* CRC Press.

BEN-NISSAN, B., MACHA, I., CAZALBOU, S. & CHOI, A. H. 2016. Calcium phosphate nanocoatings and nanocomposites, part 2: thin films for slow drug delivery and osteomyelitis. *Nanomedicine (Lond),* 11**,** 531-44.

BHATTACHARYA, M., WOZNIAK, D. J., STOODLEY, P. & HALL-STOODLEY, L. 2015. Prevention and treatment of Staphylococcus aureus biofilms. *Expert Review of Anti-infective Therapy,* 13**,** 1499-1516.

BLUNSTON, M. A., YONOVITZ, A., WOODAHL, E. L. & SMOLENSKY, M. H. 2015. Gentamicin-induced ototoxicity and nephrotoxicity vary with circadian time of treatment and entail separate mechanisms. *Chronobiol Int,* 32**,** 1223-32.

CAMPOCCIA, D., MONTANARO, L., SPEZIALE, P. & ARCIOLA, C. R. 2010. Antibiotic-loaded biomaterials and the risks for the spread of antibiotic resistance following their prophylactic and therapeutic clinical use. *Biomaterials,* 31**,** 6363-77.

CLSI 2012. Methods for Dilution Antimicrobial Susceptibility Tests for Bacteria that Grow Aerobically: Approved Standard. *Performance Standards for Antimicrobial Disk Susceptibility Tests.* Pennsylvania, USA: Clinical and Laboratory Standards Institute.

DAROUICHE, R. O. 2003. Antimicrobial approaches for preventing infections associated with surgical implants. *Clin Infect Dis,* 36**,** 1284-9.

DE GIGLIO, E., CAFAGNA, D., COMETA, S., ALLEGRETTA, A., PEDICO, A., GIANNOSSA, L. C., SABBATINI, L., MATTIOLI-BELMONTE, M. & IATTA, R. 2013. An innovative, easily fabricated, silver nanoparticle-based titanium implant coating: development and analytical characterization. *Analytical and Bioanalytical Chemistry,* 405**,** 805-816.

DONLAN, R. M. 2002. Biofilms: microbial life on surfaces. *Emerg Infect Dis,* 8**,** 881-90.

FERNANDEZ-YAGUE, M. A., ABBAH, S. A., MCNAMARA, L., ZEUGOLIS, D. I., PANDIT, A. & BIGGS, M. J. 2015. Biomimetic approaches in bone tissue engineering: Integrating biological and physicomechanical strategies. *Advanced Drug Delivery Reviews,* 84**,** 1-29.

GARRETT, T. R., BHAKOO, M. & ZHANG, Z. 2008. Bacterial adhesion and biofilms on surfaces. *Progress in Natural Science,* 18**,** 1049-1056.

HEATLEY, N. G. 1944. A method for the assay of penicillin. *Biochemical Journal,* 38**,** 61-65.

HETRICK, E. M. & SCHOENFISCH, M. H. 2006. Reducing implant-related infections: active release strategies. *Chemical Society Reviews,* 35**,** 780-789.

INZANA, J. A., SCHWARZ, E. M., KATES, S. L. & AWAD, H. A. 2016. Biomaterials approaches to treating implant-associated osteomyelitis. *Biomaterials,* 81**,** 58-71.

KARACAN, I., MACHA, I. J., CHOI, G., CAZALBOU, S. & BEN-NISSAN, B. 2017. Antibiotic Containing Poly Lactic Acid/Hydroxyapatite Biocomposite Coatings for Dental Implant Applications. *Key Engineering Materials,* 758**,** 120–125.

KARGUPTA, R., BOK, S., DARR, C. M., CRIST, B. D., GANGOPADHYAY, K., GANGOPADHYAY, S. & SENGUPTA, S. 2014. Coatings and surface modifications imparting antimicrobial activity to orthopedic implants. *Wiley Interdiscip Rev Nanomed Nanobiotechnol,* 6**,** 475-95.

LOSS, G., SIMÕES, P. M., VALOUR, F., CORTÊS, M. F., GONZAGA, L., BERGOT, M., TROUILLET-ASSANT, S., JOSSE, J., DIOT, A., RICCI, E., VASCONCELOS, A. T. & LAURENT, F. 2019. Staphylococcus aureus Small Colony Variants (SCVs): News From a Chronic Prosthetic Joint Infection. 9.

MACHA, I. J., CAZALBOU, S., BEN-NISSAN, B., HARVEY, K. L. & MILTHORPE, B. 2015. Marine structure derived calcium phosphate-polymer biocomposites for local antibiotic delivery. *Mar Drugs,* 13**,** 666-80.

MACHA, I. J., KARACAN, I., BEN-NISSAN, B., CAZALBOU, S. & MÜLLER, W. H. 2018. Development of antimicrobial composite coatings for drug release in dental, orthopaedic and neural prostheses applications. *SN Applied Sciences,* 1**,** 68.

MANIVASAGAM, G., DHINASEKARAN, D. & RAJAMANICKAM, A. 2010. Biomedical Implants: Corrosion and its Prevention - A Review. *Recent Patents on Corrosion Science,* 2**,** 40-54.

MANTRIPRAGADA, V. P., LECKA-CZERNIK, B., EBRAHEIM, N. A. & JAYASURIYA, A. C. 2013. An overview of recent advances in designing orthopedic and craniofacial implants. *J Biomed Mater Res A,* 101**,** 3349-64.

MISHRA, P. K., ASHOUB, A., SALHIYYAH, K., AKTUERK, D., OHRI, S., RAJA, S. G. & LUCKRAZ, H. 2014. Role of topical application of gentamicin containing collagen implants in cardiac surgery. *Journal of Cardiothoracic Surgery,* 9**,** 122.

MONTANARO, L., SPEZIALE, P., CAMPOCCIA, D., RAVAIOLI, S., CANGINI, I., PIETROCOLA, G., GIANNINI, S. & ARCIOLA, C. R. 2011. Scenery of Staphylococcus implant infections in orthopedics. *Future Microbiol,* 6**,** 1329-49.

NAIR, L. S. & LAURENCIN, C. T. 2007. Biodegradable polymers as biomaterials. *Progress in Polymer Science,* 32**,** 762-798.

NAMVAR, A. E., BASTARAHANG, S., ABBASI, N., GHEHI, G. S., FARHADBAKHTIARIAN, S., AREZI, P., HOSSEINI, M., BARAVATI, S. Z., JOKAR, Z. & CHERMAHIN, S. G. 2014. Clinical characteristics of Staphylococcus epidermidis: a systematic review. *GMS Hyg Infect Control,* 9**,** 23.

NANDI, S. K., BANDYOPADHYAY, S., DAS, P., SAMANTA, I., MUKHERJEE, P., ROY, S. & KUNDU, B. 2016. Understanding osteomyelitis and its treatment through local drug delivery system. *Biotechnology Advances,* 34**,** 1305-1317.

OTTO, M. 2009. Staphylococcus epidermidis--the 'accidental' pathogen. *Nature reviews. Microbiology,* 7**,** 555-567.

PAN, C., ZHOU, Z. & YU, X. 2018. Coatings as the useful drug delivery system for the prevention of implant-related infections. *J Orthop Surg Res,* 13**,** 220.

RENNER, L. D. & WEIBEL, D. B. 2011. Physicochemical regulation of biofilm formation. *MRS Bull,* 36**,** 347-355.

RIBEIRO, M., MONTEIRO, F. J. & FERRAZ, M. P. 2012. Infection of orthopedic implants with emphasis on bacterial adhesion process and techniques used in studying bacterial-material interactions. *Biomatter,* 2**,** 176-94.

SABATH, L. D., GARNER, C., WILCOX, C. & FINLAND, M. 1976. Susceptibility of Staphylococcus aureus and Staphylococcus epidermidis to 65 antibiotics. *Antimicrob Agents Chemother,* 9**,** 962-9.

SANTOS, A., SINN AW, M., BARIANA, M., KUMERIA, T., WANG, Y. & LOSIC, D. 2014. Drug-releasing implants: current progress, challenges and perspectives. *Journal of Materials Chemistry B,* 2**,** 6157-6182.

SEEBACH, E. & KUBATZKY, K. F. 2019. Chronic Implant-Related Bone Infections-Can Immune Modulation be a Therapeutic Strategy? *Front Immunol,* 10**,** 1724.

SIMCHI, A., TAMJID, E., PISHBIN, F. & BOCCACCINI, A. R. 2011. Recent progress in inorganic and composite coatings with bactericidal capability for orthopaedic applications. *Nanomedicine,* 7**,** 22-39.

VARGHESE, D. S., PARWEEN, S., ARDAH, M. T., EMERALD, B. S. & ANSARI, S. A. 2017. Effects of Aminoglycoside Antibiotics on Human Embryonic Stem Cell Viability during Differentiation In Vitro. *Stem Cells International,* 2017**,** 2451927.

WANG, Z., WANG, Y., ITO, Y., ZHANG, P. & CHEN, X. 2016. A comparative study on the in vivo degradation of poly(L-lactide) based composite implants for bone fracture fixation. *Scientific Reports,* 6**,** 20770.

Chapter7

Human Adipose Derived Stem Cell Studies on PLA Biocomposite Thin Film Coated Implants

Chapter7: Human Adipose Derived Stem Cell Studies on PLA Biocomposite Thin Film Coated Implants

This chapter covers the effect of PLA biocomposite thin film coatings on Ti6Al4V implants on human adipose-derived stem cells (ADSC) at five different predetermined Gm concentrations (5%-30% w/w). Additionally, two different substrate implant materials which are Ti6Al4V and thermally anodized Ti6Al4V were tested on ADSCs. The ADSCs exposed to the implant materials were subsequently analyzed by fluorescent microscopy, secretory cytokine assays, proteomic analysis with bioinformatics interrogation by systems biology.

7.1 Introduction

Stem cells are biological and functional living units that play an important role in the regeneration of tissues and organs, and in the development of whole organisms because of their self-renewal potential and ability to separate into different cell lineages. Although embryonic, there are different types of stem cells including fetal, embryonic and adult. Adult stem cells are proving to be the most suitable source for clinical applications such as bone regeneration (Frontini-lopez et al., 2018, Kargozar et al., 2019).

Mesenchymal or stromal stem cells (MSCs), which are adult stem cells, are often used in the tissue engineering field and in stem cell-based therapies such as repairing damaged tissues, because of their multi-potential differentiation ability. MSC reservoirs have been found within different types of tissues including bone-marrow, placenta, amniotic fluid, menstrual blood, dental pulp, and adipose tissue (Tsuji et al., 2014). Adipose tissue is a rich source of adult stem cells termed adipose-derived stem cells (ADSC). ADSCs have been expansively used in clinical research, regenerative medicine and tissue regeneration applications (Feisst et al., 2015).

The harvesting process of ADSCs is also relatively easier in large quantities with a minimally invasive technique, very low negative impact and discomfort for the patient, whereas the harvesting process of bone-marrow derived stem cells (BMSCs) is highly painful for the patient. ADSCs can be extracted by lipoaspiration from adipose tissue with more than 95% purity, high proliferative ability, and multi

differentiation potential. The yield of cells per gram of adipose tissue is higher than that of any other stem cell reservoir tissues (Argentati et al., 2018, Romagnoli et al., 2015).

Additionally, bone marrow-derived MSCs (BMSCs) and adipose-derived MSCs (ADSCs) have been commonly used for bone tissue engineering (Frontini-lopez et al., 2018, Haimi et al., 2009). Clinical trials conducted with MSCs indicate their potential use in a broad range of medical applications. Increasing numbers of stem cell-based clinical trials are using MSCs on soft and hard tissue for regeneration, immune disorders, cardiovascular diseases, osteoarthritis, liver disorders, respiratory disorders, spinal cord injury, kidney failure, muscular dystrophy, and ischemic injuries (Frese et al., 2016, Ullah et al., 2015).

Adult adipose-derived stem cells can be used to study drug delivery systems, drug discovery, and regenerative medicine in addition to the aforementioned clinical trial areas. The ability of ADSCs to differentiate into hard tissue cells such as bone, cartilage, and muscle, provides further potential for their application in regenerative medicine and tissue engineering (da Rocha et al., 2018). ADSCs can secrete an extensive selection of the cytokines, chemokines, and growth factors, such as VEGF, FGF basic, and PDGF in the targeted environment. Therefore, they are a high potential source for regenerative medicine, especially for controlled local drug delivery system applications (Frese et al., 2016, Storti et al., 2019).

Recently, many different studies shown that the response and behavior of ADSCs (seeded on different types of biomaterials), change according to their surrounding microenvironment. Understanding the molecular events and metabolic changes on the stem cells due to the interactions of the stem cell-biomaterial interface is highly essential for designing functional bio-hybrid implantable systems without failure (Argentati et al., 2018). Therefore, the selection of biomaterials plays a pivotal role in providing the substrate and improving cell adhesion, proliferation, differentiation of the cells, and protecting the cells during the transplantation (Green et al., 2012, Gao et al., 2017). The surface properties of biomaterial such as adhesion, chemical characterization, topological and mechanical properties, are strongly effective on the interaction between stem cells and their microenvironment. They also provide the regulation of stem cell fate due to the soluble stem cell niche signals such as cytokines or growth factors (Sun et al., 2012, da Rocha et al., 2018).

Notably, new biomaterial or scaffolds with stem cells have been investigated as an alternative therapeutic strategy to improve bone repair and to inhibit implant failures in the treatment of bone fractures and bone-related diseases (Iaquinta et al., 2019).

The most common material used for implants and prosthetics are metallic-based materials, particularly titanium and titanium alloys such as Ti6Al4V often used in orthopedic and dental implants. The key advantage of these materials is their bioinert property, meaning no chemical interactions or bonding with bone tissue. Therefore, in order to improve their longevity, the surface of bioinert metallic-based implants has been modified with the coating of new biodegradable, bioactive and biocompatible biomaterials. Surface improvements through an increase in bioactivity, osseointegration, and better implant-bone adaptability by surface macro- and micro-texturing have been the primary focus of research (Choi et al., 2018).

In our PLA biocomposite thin film coating system, PLA matrix and coral-derived HAp particles are the key materials, and they play crucial role for the drug delivery system. At the same time, the biodegradable PLA matrix, and HAp particles also cause the surface modification on the Ti6Al4V implants to improve the bioactivity of the implant surface and to obtain better implant-bone adaptability. The biocompatibility and bioactive properties of coral-derived HAp and PLA-HAp biocomposites have been investigated by others. For example, Singh *et al.* (2017) examined the effects of seeding rat adipose-derived stem cells (rADSCs) and human adipose-derived stem cells (hADSCs) onto biomimetic coralline scaffolds. Moreover, it was demonstrated that ADSCs could be successfully cultured onto the coralline scaffolds that provide a suitable microenvironment for ADSCs to proliferate (Singh, 2017).

Danoux *et al.* (2014) compared a PLA bone graft and a nano sized HAp containing a PLA biocomposite bone graft in vitro with human MSCs and in vivo with mature male mongrel dogs. The study showed that the proliferation of human MSCs were higher for the PLA-HAp biocomposite bone graft than the PLA bone graft. Additionally, the research group reported that heterotrophic bone formation was observed on the PLA-HAp biocomposite bone graft after implanted in the dog. The results show the bioactivity and osseoinductivity properties of the HAp bioceramic (Danoux et al., 2014).

The use of antibiotics is highly important in regenerative medicine and transplantation processes. Especially for transplantation, the stem cells must be cultured under optimal conditions; protective antibiotic therapy provides a successful and safe transplantation process (Skubis et al., 2017). Gentamicin is used as a systemic antibiotic therapy in orthopedics, for example, in osteomyelitis treatment, but gentamicin has been reported to be ototoxic and nephrotoxic at high concentrations. Therefore, the development of a local or targeted slow drug delivery system for simvastatin and gentamicin can be highly beneficial in preventing adverse side-effects or postoperative complications (Ben-Nissan et al., 2016, Chou et al., 2013, Chou et al., 2016).

Kagivata *et al.* (2008), reported the effects of different dosages of gentamicin (10, 20, 50, 100 and 200 µg/ml) on the proliferation and differentiation of MSCs, and found that 20ug/ml is the safe concentration for MSCs and is effective in inhibiting bacterial contamination. 20ug/ml gentamicin in the culture media provides safe and effective MSC growth for hard tissue regeneration (Kagiwada et al., 2008).

Macha *et al.* (2017) determined the effect of PLA biocomposite thin film containing coral derived HAp particles and Gm antibiotics on the surface attachment of human ADSCs. Strong cell attachment and proliferation of ADSCs on PLA biocomposites thin film surface were reported (Macha et al., 2017).

While there are many in vitro, in vivo, and clinical trials at various levels to explain stem cells-biomaterials interactions, the interactions of ADSCs with the microenvironment and effects of those interactions on ADSCs and their differentiation are still not clear. Thus, the aim of this study was to determine the interactions of PLA biocomposite coated Ti6Al4V implants at predetermined Gm antibiotic concentrations with human ADSCs. Therefore, the Gm antibiotic dosages, and Ti6Al4V implant surface modifications (PLA biocomposite thin film coating), and thermal anodization effects on human ADSCs were investigated. ADSCs were tested based on their attachment ability, growth, immunological response and the changes on their proteomes respectively in order to determine the interactions.

7.2 Experimental Methods

7.2.1 Cell Culture Method for Human Adipose-Derived Stem Cells (ADSCs)

The procedures of adult human ADSCs isolation and expansion were used from Santos *et al.* (2017), utilizing cells cryo-stored from UTS-HREC Santos-2013000437 (Santos et al., 2017). Adult Adipose-derived stem cells (ADSCs) were extracted from abdominal lipoaspirates. ADSCs were cultured in Dulbecco's modified eagle medium (DMEM) Glutmax/F12 (Gibco, Life Technologies, Carlsbad, CA, USA) with 10% fetal bovine serum (FBS), (Gibco, Life Technologies, Carlsbad, CA, USA) and incubated at 37°C at 5% CO_2. The medium was discharged with a fresh one every 84 hours, and replaced with the fresh DMEM-10% FBS medium. ADSCs were passaged 3-4 times before being utilized in the experiments. Therefore, only 4-9 passages (P4-9) of cells were used. All cell culture processing was performed in a laminar flow biosafety cabinet (Logic+ biosafety cabinet, Laboconco, Australia) under sterile conditions.

When the ADSCs were above 95% confluency, the medium was discharged, and the cells were washed with 0.1M phosphate-buffered saline (PBS, [Astral Scientific; 0.14 M NaCl, 0.0027M KCl, 0.01M Phosphate buffer, pH 7.4]). Then 2ml TrypLE Express (Gibco, Life Technologies, Carlsbad, CA, USA) was added for T75 flask and incubated at 15min, 37°C at 5% CO_2 to detach the cells. The cell mixture was collected in a 14ml falcon tube and centrifuged down at 1000 x g, 4-5 minutes. The cell pellet was gently suspended in a 1ml sterile PBS solution. In order to count the cell number, 10µl cell suspension was mixed with 10µl Trypan blue stain (ThermoFisher Scientific, Life Technologies, Carlsbad, CA, USA) and incubated for 30 seconds at room temperature. The cell number and live to dead ratio were determined using Trypan blue staining by the automated cell counter (Countess™ II Automated Cell Counter, ThermoFisher Scientific). Fresh DMEM-10%FBS medium was added to the cell PBS mixture to keep the concentration 20000 cell/ml.

Three main experimental setups were planned for this chapter. The samples for the first one are PLA, PLA-HAp, PLA-Gm (30% [w/w] Gm concentration) and PLA-Gm-(HAp-Gm) (30% [w/w] Gm concentration) thin film coated Ti6Al4V discs. The second experimental setup was designed to test the effects of PLA-Gm-(HAp-Gm) (30% [w/w] Gm concentration) thin film coated Ti6Al4V discs at predetermined Gm concentrations (5%, 10%, 15%, 20%, 30% [w/w]) on ADSCs. The samples for the final setup contained Ti6Al4V and thermally anodized Ti6Al4V and were designed to analyze the effect of the anodization process on ADSCs.

All samples of PLA biocomposite coated Ti6Al4V discs and controls were sterilized under UV light at 10 minutes each side. 20000 cells/well were seeded on the PLA biocomposite thin film coated TI6Al4V discs and on to the control samples into the 24 well plate (Nunc, ThermoScientific, Carlsbad, CA, USA), because the Ti6Al4V discs can fit in one well of 24well plate without any large gap between the disc and the well. And ADSCs were incubated 37°C at 5% CO_2 after they were seeded on the PLA biocomposite thin film coated Ti6Al4V disc samples. The DMEM-10% FBS medium from each sample was discharged with a fresh one every 84 hours, and the discharged medium for each time point (days 3, 7, 10, and 14) was collected and stored at -80°C for Bio-plex assay. At the end of the 14 days, microscopy imaging, and proteomics analyses were done on the ADSC cells.

7.2.2 Scanning Electron Microscope (SEM)

The dehydration process was applied to the ADSCs on the PLA biocomposite coated Ti6Al4V discs after the cells were fixed with 4% (w/v) PFA. The samples were stored under vacuum for the SEM imaging. After the cells were fixed, they were washed with ultrapure H_2O, five times to remove all PFA and salt. The cells were dehydrated in graded concentrations of ethanol; 20%, 30%, 50%, 70%, 80%, 90%, 96% for 10 minutes each. Finally, the cells were washed with 100% ethanol twice for 15-

30 minutes each, then left to dry in the vacuum desiccator overnight. Before SEM imaging, the samples were coated with a 7nm thin layer of Au-Pd using a sputter coater.

SEM (ZEISS Supra SSVP, Zeiss, Germany) was used in order to obtain the morphological structure of fixed ADSCs on the PLA biocomposites coated Ti6Al4V discs. All discs were kept stable by the mutual conductive carbon adhesive tape on the SEM stubs to place into the SEM. Images were taken at 100, 200, and 500x magnifications at an acceleration voltage of 5 kV, and with InLens signal.

7.2.3 Fluorescent Imaging with Fluorescence Deconvolution Microscope

The cells were rinsed on PLA biocomposite thin film coated Ti6Al4V discs in 24 well plates with the sterile PBS solution and fixed in 4% (w/v) paraformaldehyde/PBS (PFA) for 30mins at room temperature in the dark. After the cells were fixed, the cells were washed twice with PBS solution to remove all PFA. The nucleus of the cells was stained by DAPI staining, and the cytoskeleton of the cells was stained by phalloidin staining. For cytoskeleton staining, 1 ml 1:2000 dilutions of phalloidin staining in PBS solution were added on each sample and incubated for 30 minutes in the dark. The samples were washed three times with PBS solution. Then for the nucleus staining, 1ml 1:10000 dilutions of DAPI staining were added to the PBS solution on each sample and incubated for 20 minutes in the dark. The samples were washed three times with PBS solution. The samples were kept in the PBS solution and stored at +4 ˚C and covered with aluminum foil to keep away from the light during fluorescent imaging.

Fixed and stained ADSCs on the PLA biocomposite coated Ti6Al4V discs were visualized using the Inverted wide-field fluorescence deconvolution microscope (Delta Vision Elite) with a plate holder using the Olympus 20X/0.45/U-Plan FL LWD/1-UB768 magnification lenses with DAPI filter for nucleus stain (Ex: 381-412nm / Em: 420-456nm, blue) and TRITC filter for phalloidin cytoskeleton stain (Ex: 531-565nm / Em: 573-611nm, red). Ten fields of view from three individual discs were taken per sample to analyze the cell morphology and to calculate the total cell number on each disc via FIJI software, (Java-based Image Processing and Analysis Software by NIH Image). The statistical analyseis were performed using one-way ANOVA with Tukey's post-test. n=3 for PLA-Gm-(HAp-Gm) coated Ti6Al4V samples and *Student t-test, unpaired, two-tails, n=3 for Ti6Al4V and A-Ti6Al4V samples*.

7.2.4 Bio-plex Assay

An experiment of 14 days conducted with ADSCs on control (ADSCs only), Ti6Al4V, PLA coated Ti6Al4V, and PLA biocomposite coated Ti6Al4V discs. ADSCs conditioned mediums for each sample in 500µl aliquots were collected at days 3, 7, 10, and 14, and then stored at –80 ˚C for the Bio-Plex Pro

immunoassay kit (Bio-plex human 27-plex, M50-0KCAF0Y BioRad Laboratories). The Bio-Plex kit is a commercially available multiplex bead-based sandwich immunoassay kit. The concentrations of 27 cytokines (*Table 7.1*) which are FGF basic, Eotaxin, G-CSF, GM-CSF, IFN-γ, IL-1β, IL-1ra, IL-2, IL-4, IL-5, IL-6, IL-7, IL-8, IL-9, IL-10, IL-12 (p70), IL-13, IL-15, IL-17, IP-10, MCP-1 (MCAF), MIP-1α, MIP-1β, PDGF-BB, RANTES, TNF-α, and VEGF in the ADSCs conditioned medium at days 3, 7, 10 and 14 were determined by using the Bio-plex kit. Assays were performed according to the manufacturer's instructions. DanteR software (DanteR version 1.0.0.10. R version 2.12.0 The R Foundation for Statistical Computing, Auckland, New Zealand) was used to complete the data analysis (Taverner et al., 2012).

Table 7.1 All Cytokine names and their types in the Bio-plex assay

Name	Full name (systematic name)	Cytokine Type
IL-1β	Interleukin 1β	Pro-inflammatory cytokine (Lopez-Castejon and Brough, 2011)
IL-1ra	Interleukin 1 receptor antagonist	Anti-inflammatory cytokine (Borthwick, 2016)
IL-2	Interleukin 2	Pro-inflammatory cytokine (Shachar and Karin, 2013)
IL-4	Interleukin 4	Anti-inflammatory cytokine (Opal and DePalo, 2000)
IL-5	Interleukin 5	Anti-inflammatory cytokine (Zhang and An, 2007)
IL-6	Interleukin 6	Anti-inflammatory / Pro-inflammatory Cytokine (Zhang and An, 2007)
IL-7	Interleukin 7	Pro-inflammatory cytokine (Pripp and Stanišić, 2014)
IL-8	Interleukin 8	Pro-inflammatory cytokine (Srinivasan et al., 2017)
IL-9	Interleukin 9	Pro-inflammatory cytokine (Goswami and Kaplan, 2011)
IL-10	Interleukin 10	Anti-inflammatory cytokine (Opal and DePalo, 2000)
IL-12	IL-12 Interleukin 12A and 12B	Pro-inflammatory cytokine (Srinivasan et al., 2017)
IL-13	Interleukin 13	Anti-inflammatory cytokine (Opal and DePalo, 2000)
IL-15	Interleukin 15	Pro-inflammatory cytokine (Pripp and Stanišić, 2014)
IL-17	Interleukin 17	Pro-inflammatory cytokine (Pripp and Stanišić, 2014)
Eotaxin	Eotaxin 1	Chemokines (Kayaba and Chihara, 2001)
IFN-γ	Interferon γ	Pro-inflammatory cytokine (Srinivasan et al., 2017)
FGF	Fibroblast growth factor	Growth factor (Brogi et al., 1994)

basic

Gm-CSF	Granulocyte-macrophage CSF	Colony-stimulating factor
MCP-1	Monocyte chemoattractant protein 1 (CCL2)	Chemokines (Zhang and An, 2007)
MIP-1α	Macrophage inflammatory protein 1a (CCL3)	Chemokines (Zhang and An, 2007)
MIP-1β	Macrophage inflammatory protein 1b (CCL4)	Chemokines (Zhang and An, 2007)
IP-10	CXCL10 (interferon-γ-inducible protein 10)	Chemokines (Vazirinejad et al., 2014)
PDGF-BB	Platelet-derived growth factor polypeptide	Growth factor (Van Steensel et al., 2010)
RANTES	RNATES (CCL5)	Chemokines (Kayaba and Chihara, 2001)
TNF-α	Tumor necrosis factor a	Pro-inflammatory cytokine (Srinivasan et al., 2017)
G-CSF	Granulocyte colony stimulating factor	Colony-stimulating factor
VEGF	Vascular endothelial growth factor	Growth factor (Brogi et al., 1994)

7.2.5 Protein Extraction

ADSCs on the PLA biocomposite thin film coated Ti6Al4V discs were detached after 14 days by TrypLE Express (Gibco) then put into the Eppendorf tubes to centrifuge at 1000 x g for 4-5mins to obtain the cell pellets. After TrypLE was discharged, the cell pellet was washed with a sterile PBS solution and centrifuged again. The cell pellets were resuspended in 100 µL 8 M urea (Merck KGaA, Darmstadt, Germany) and 100 mM NH_4HCO_3 (Merck KGaA, Darmstadt, Germany), pH9. The samples were then heated to 95 °C on a heat block for 10 minutes, then centrifuged for 1 minute at 5000× g. Reduction and alkylation of the obtained proteins were performed in a single step by adding a final concentration of 10 mM tributylphosphine (TBP, Merck KGaA, Darmstadt, Germany) and 20 mM acrylamide monomers (Merck KGaA, Darmstadt, Germany). The samples were incubated for 90 minutes at room temperature then quenched with a final concentration of 50 mM dithiothreitol (DTT, Merck KGaA, Darmstadt, Germany). 1µl benzonase (Sigma Aldrich, Australia) was added to the samples to break down the DNA molecules and then incubated for 60minutes in the water bath sonication (Micro process controlled bench-top ultrasonic cleaner, Thermoline Scientific, Australia). The samples were vortexed and spun down on a mini-centrifuge at 2000× g for 2 seconds. The

samples were then diluted to 1M urea by adding 100 mM NH_4HCO_3, then adding 0.5 µg of trypsin (Promega, USA) to digest at 37 ˚C for 16 hours for the protein digestion to obtain peptides.

The peptides were then desalted and cleaned using the SDB-RPS Stage Tip column method, which is a modified protocol from Rappsilber et al. (2007). SDB-RPS disks were developed for the mixed-mode extraction of polar and non-polar analytes. SDB-RPS is dual-mode and works as both reversed-phase and strong cation exchange mechanisms. The SDB (styrenedivinylbenzene) material has Zip-tip C18-like reversed-phase characteristics from the benzene rings. The sulfonic acid group that it is derivatized with gives it a permanent negative charge on top of the RP characteristics (RPS = Reverse-phase sulphonic). Peptides are retained in high salt and low/no organic, or low/no salt and high organic + 1% TFA (Trifluoroacetic acid) to drive them to the sulfonic acid groups.

10% TFA was added to the samples to make a final concentration of 1% to stop the trypsin. It acidifies the solution for solid phase extraction. The samples were centrifuged at maximum speed for 5 minutes. They were then loaded into the stage tip column, which contains a SDB-RPS disk, then centrifuged at 5000rpm until all liquid was passed through and the peptides were captured by the column. 60ul Isopropanol/TFA 1% (v/v) was added and then centrifuged at 5000rpm until all liquid was passed through from the column. 60ul TFA 1% (v/v) was added and then centrifuged at 5000rpm until all liquid was passed through from the column. The previous two steps help to wash all contaminants and salts from the column and the bound peptides.

The peptides were eluted with 60µl elution solvent (1M NH_4OH, 70% Acetonitrile) into clean vials. The vials with the peptides were placed into the vacuum centrifuge (Savant DNA 120, SpeedVac Concentrator, ThermoScientific, Carlsbad, CA, USA) to evaporate all liquid. Finally, 5ul MS loading solvent (2% acetonitrile (ACN) + 0.2% TFA) was added per µg sample.

7.2.6 LC/MS/MS Analysis

Using an Acquity M-class nanoLC system (Waters, USA), 5 µL of the sample was loaded at 15mL/min for 3 minutes onto a nanoEase Symmetry C18 trapping column (180mm x 20mm) before being washed onto a PicoFrit column (75 mmID x 300 mm; New Objective, Woburn, MA) packed with Magic C18AQ resin (3mm, Michrom Bioresources, Auburn, CA). Peptides were eluted from the column and into the source of a Q Exactive Plus mass spectrometer (Thermo Scientific) using the following program: 5-30% MS buffer B (98% Acetonitrile + 0.2% Formic Acid) over 90 minutes, 30-80% MS buffer B over 3 minutes, 80% MS buffer B for 2 minutes, 80-5% for 3 minutes. The eluting peptides were ionized at 2400V. A Data Dependent MS/MS (dd-MS2) experiment was performed, with a survey scan of 350-1500 Da performed at 70,000 resolution for peptides of charge state 2+ or

higher with an AGC target of 3e6 and maximum Injection Time of 50ms. The Top 12 peptides were selected and fragmented in the HCD cell using an isolation window of 1.4 m/z, an AGC target of 1e5 and maximum injection time of 100ms. Fragments were scanned in the Orbitrap analyzer at 17,500 resolution and the product ion fragment masses measured over a mass range of 120-2000 Da. The mass of the precursor peptide was then excluded for 30 seconds.

7.2.7 Data Processing and Analysis

The MS/MS data files were searched using Peaks Studio X+ against the Human Proteome database and a database of common contaminants with the following parameter settings. There were no fixed modifications. Variable modifications: propionamide, oxidized methionine, deamidated asparagine, phosphorylation. Enzyme: semi-trypsin. Number of allowed missed cleavages: 3. Peptide mass tolerance: 10 ppm. MS/MS mass tolerance: 0.05 Da. The results of the search were then filtered to include peptides with a –log10P score that was determined by the False Discovery Rate (FDR) of <1%, the score being that where decoy database search matches were <1% of the total matches. For this analysis, proteins that were present in the test samples but were not present in the control were selected. These proteins were searched by unique accession number on UniprotKB (www.uniprot.org) and the corresponding biological processes were returned for each protein as an Excel spreadsheet.

7.3 Results and Discussions

7.3.1 In vitro bioactivity analyses with Human Adult Adipose-Derived Stem Cells

Human adult ADSCs were passaged 3-4 times, with passages maintained below P10, before starting the experiments on PLA biocomposite thin film coated Ti6Al4V discs. ADSCs were cultured as morphologically homogeneous culture and visualized by an Olympus CK40 inverted microscope at 100x (*Figure 7.1 A*). The live and dead cell ratio was determined by using Trypan blue staining, which is 93% live and 7% dead ADSCs in total $6.22x10^5$ /ml (*Figure 7.1 B*). The cell size distribution via cell number after detaching the cells was also obtained as a graph in *Figure 7.1 B* and most of the cell population is in a 10-40 μm size range.

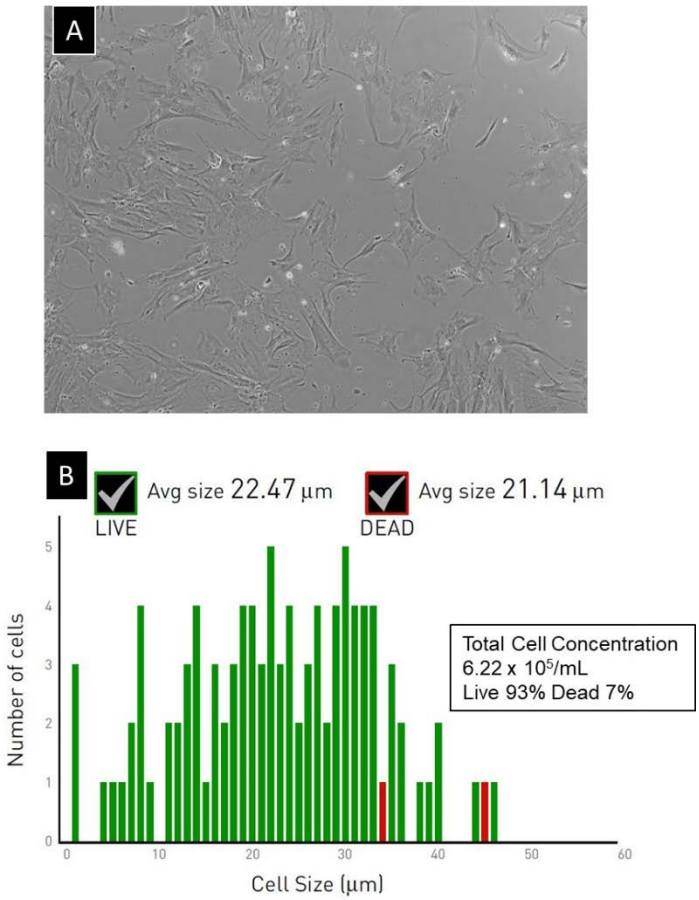

Figure 7.1 The live image of ADSCs in T75 flask (A) and the graph for the cell number and live/dead ratio for ADSCs with Trypan blue staining (B)

7.3.2 The effects of PLA, PLA-HAp, PLA-Gm, and PLA-Gm-(HAp-Gm) thin film coated Ti6Al4V metallic implants on ADSCs

Morphologically homogenous cultured ADSCs (P4-9) were detached, and 20000 cells/well for a 24 well plate was seeded on the five different samples (Ti6Al4V disc, PLA thin film coated Ti6Al4V disc, PLA-HAp thin film coated Ti6Al4V discs, PLA-Gm and PLA-Gm-[HAp-Gm]) thin film coated Ti6Al4V discs at 30% (w/w) Gm concentrations. ADSCs on the five different implant surfaces were cultured for 14 days to compare the effects of PLA biocomposite thin film coatings on ADSCs phenotypic and morphological features. The typical cell morphology of ADSCs can be identified as large-flat, fibroblast-like or spindle-shaped. According to SEM results in *Figure 7.2 A*, ADSCs growth was found on the Ti6Al4V disc without coating and covered the implant surface. The morphological appearance of ADSCs is a large and spread cytoplasm. Moreover, similar behavior of ADSCs was seen on PLA in (*Figure 7.2 B),* and PLA-HAp in (*Figure 7.2 C)* on the thin film coated Ti6Al4V disc surfaces. ADSCs growth was widespread on PLA and PLA-HAp thin film coated surfaces and covered all surfaces as a

coating. Therefore, the biocompatibility of PLA coating material is shown *in vitro* for 14 days of ADSCs growth. Additionally, the biocompatibility of the coral derived HAp bioceramic particles is also supported by 14 days ADSCs growth *in vitro*. Although ADSCs behave similarly on Ti6Al4V discs surface without coating and on PLA, PLA-HAp thin film coated Ti6Al4V disc surfaces, 30% (w/w) Gm contained PLA biocomposite coated Ti6Al4V samples, PLA-Gm (*Figure 7.2 D)* and PLA-Gm-(HAp-Gm) (*Figure 7.2 E)*, caused adverse effects on ADSCs growth. In *Figure 7.2 B*, the cell number on PLA-Gm and PLA-Gm-(HAp-Gm) thin film coated Ti6Al4V discs surface was lower than other samples, and the morphological appearance of the cells was observed to be a more elongated and stretched cytoplasm which can be the result of the cells under stress due to the high Gm concentration (30% w/w).

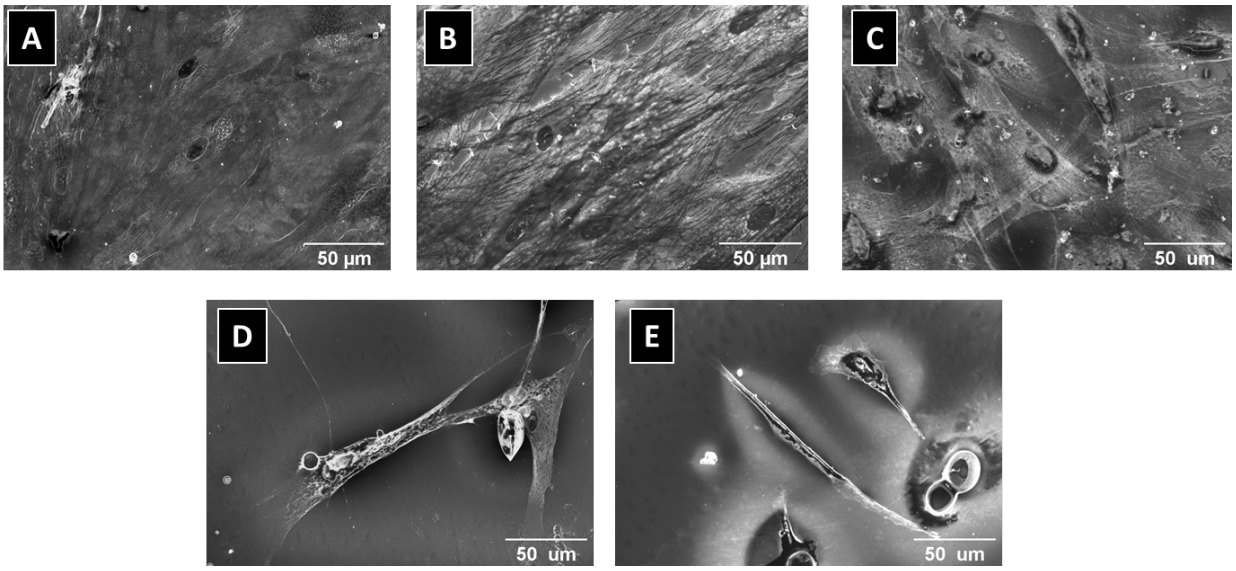

Figure 7.2 SEM images of ADSCs on the Ti6Al4V disc (A), PLA thin film (B), PLA-HAp thin film (C), PLA-Gm (30% w/w) thin film (D), and PLA-Gm-(HAp-Gm) (30% w/w) thin film coated Ti6Al4V discs after 14 days experiment

Cytokines play important and unique roles in metabolic and cellular processes, and they can be regulated in synchrony or regulate the expression of other cytokines in MSCs including ADSCs. The relative concentrations of the cytokines, individually and/or collectively, can be related to particular cellular events, such as stress responses or temporal differentiation (Santos et al., 2017).

The Bio-plex assay was conducted by the collected medium from five different samples at Day 7 and Day 14. The results were presented as a heat map with log $_{10}$ values of cytokines in *Figure 7.3*. The samples are the control (ADSCs only), Ti6Al4V disc, PLA thin film coated Ti6Al4V disc, PLA-HAp, PLA-

Gm at 30% (w/w) Gm concentration and PLA-Gm-(HAP-Gm) at 30% (w/w) Gm concentration thin film coated Ti6Al4V. Each sample displays similarities as well as differences in the cluster's dynamics with the heat map (*Figure 7.3*) which represents the cytokine concentration levels from high (red) to low (green).

Firstly, the expression patterns of the overall cytokine clusters for the control, Ti6Al4V, PLA coated and PLA-HAp coated Ti6Al4V samples were found to be similar to each other at Day 7. Most of the cytokine's concentrations were higher than Gm contained samples.

Although, the release pattern of the overall cytokine clusters for the PLA thin film coated Ti6Al4V sample was very similar when compared with the control and Ti6Al4V samples at Day 7. The pattern of the overall cytokine secretion clusters for the PLA thin film coated Ti6Al4V did not decrease at Day 14 as the control and Ti6Al4V samples did, so the cytokine secretion level stayed stable at Days 7 and 14 for PLA coated Ti6Al4V. Only the ADSCs on the PLA thin film coated Ti6Al4V sample have the active immunological response for 14 days.

While the overall secretion pattern of the cytokine clusters for PLA-HAp coated Ti6Al4V samples was closer to PLA coated Ti6Al4V sample at Day 7, the concentration of cytokines for PLA-HAp coated Ti6AL4V decreased after 14 days. The secretion pattern of the cytokine clusters reflects the drastic drop for PLA-Gm and PLA-Gm-(HAp-Gm) thin film coated samples at Day 14, according to Day 7.

The pattern for the PLA-HAp coated sample without Gm was very close to the PLA coated Ti6Al4V at Day 7 and Day 14 due to their cytokines activity, however the effect of HAp particles on the cytokine secretion pattern of the PLA-Gm-(HAp-Gm) thin film coated samples were not observed when compared to PLA-Gm thin film coated sample. Therefore, for the cytokine secretion level at Day 7 and Day 14, the dual effect of HAp and Gm particles can be seen.

When the heat map was analyzed in detail according to each cytokine secretion pattern according to sample and time, IFN-g, IP-10, MIP-1b, MIP-1a, PDGF-bb, TFN-a, IL-4, IL-1ra, IL-2, IL-1b, IL-9, IL-10, IL-12, IL-13, IL-15, IL-7 cytokine clusters have a similar pattern as overall secretion behavior of cytokines for each samples at Day 7 and Day 14 as explained above.

On the other hand, for IL8, FGF basic, G-CSF, Gm-CSF, IL-17A, although the cytokine secretion level was higher for PLA-Gm and PLA-Gm-(HAp-Gm) thin film coated samples, a decreasing pattern was observed on Day 7 to Day 14.The controls and PLA and PLA-HAp thin film coated samples were stable on Day 7 and Day 14.

Finally, the IL-5, Eotaxin, RANTES, VEGF, MCP-1, and IL-6 cytokines have a similar pattern as a group. The first important point is that the secretion level increased from Day 7 to Day 14 for the control, Ti6Al4V, and PLA thin film coated Ti6Al4V samples, and they have higher secretion levels than PLA-HAp, PLA-Gm, and PLA-Gm-(HAp-Gm) thin film coated samples. Although the secretion level was low for the PLA-HAp, PLA-Gm, and PLA-Gm-(HAp-Gm) thin film coated samples for Day 7 and Day 14, the decreasing pattern was observed for all cytokines in this group for PLA-HAp and PLA-Gm-(HAp-Gm) thin film coated samples.

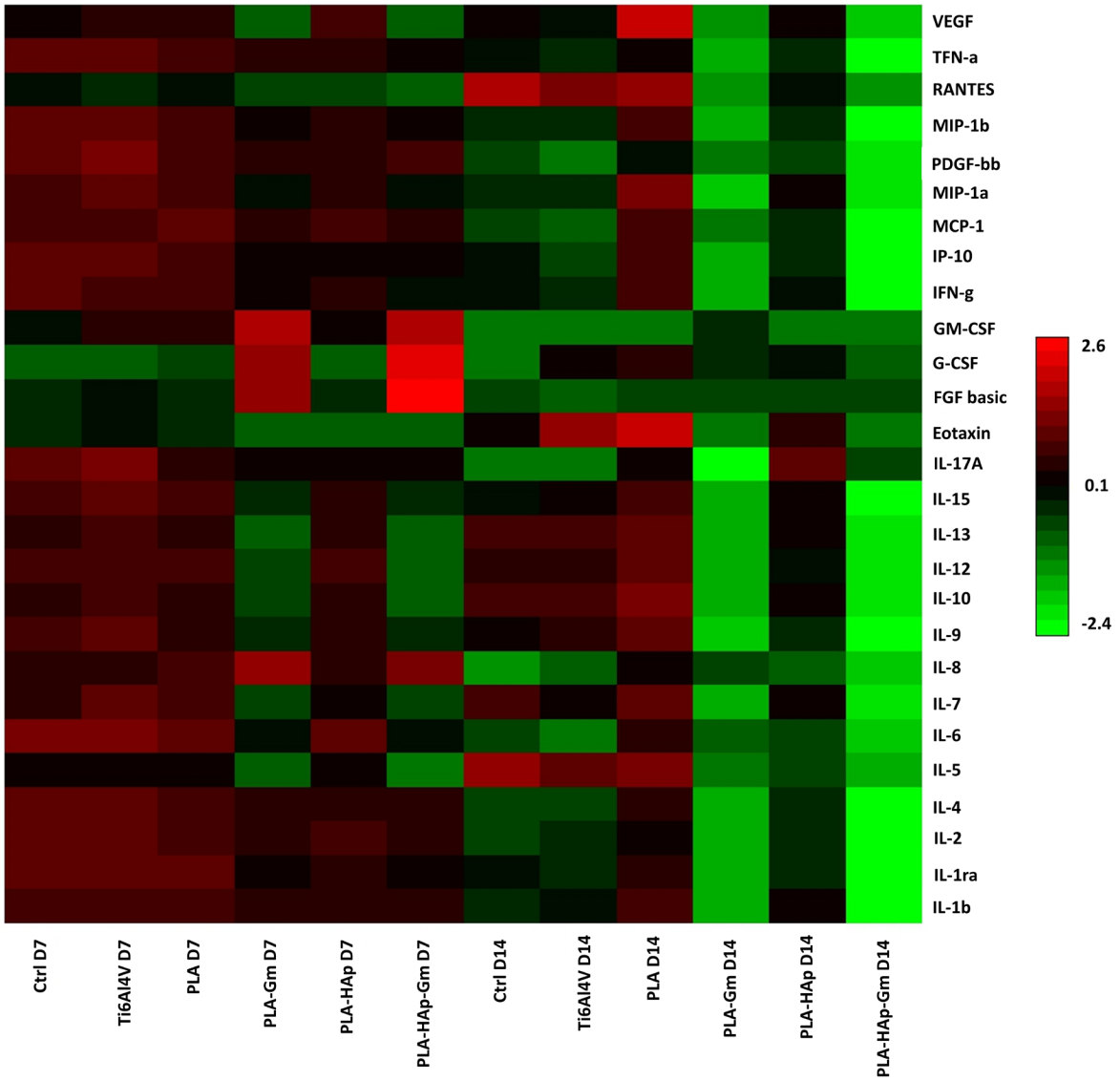

Figure 7.3 Bio-plex assay heat map data for ctrl, Ti6Al4V disc, PLA, PLA-HAp, PLA-Gm, and PLA-Gm-(HAp-Gm) thin film coated Ti6Al4V discs for Day 7 and Day 14. (The heat map scale is 2 fold increases in above red and 2 fold decreases in below green)

We obtained a similar immunological effect of PLA thin film coated samples on ADSCs with the control sample according to the expression patterns of the cytokine clusters at Day 7 and Day 14. Therefore, the Bio-plex results for Ti6Al4V and PLA thin film coating material matches with the SEM results in *Figure 7.2 B* due to the growth of ADSCs on those surfaces. The ADSCs covered the Ti6Al4V and PLA thin film coated Ti6Al4V surfaces after 14 days. The combination of Bio-plex and the microscopy results show the biocompatibility and bioactivity of PLA biodegradable coating material. Additionally, while the cytokine clusters secretion behavior for PLA-HAp was found similar as control samples, it shows that HAp particles do not have any immunological adverse effect on ADSCS.

30% Gm concentration caused adverse effects on the ADSCs. The secretion concentration of the cytokines was lower than the other samples at Day 7 and it decreased very drastically to nearly zero after 14 days. The adverse effect of 30% Gm concentration on ADSCs can be observed by the SEM images in *Figure 7.2* which match the Bio-plex assay. Therefore, five different Gm concentrations (5%, 10%, 15%, 20%, and 30%) contained PLA-Gm-(HAp-Gm) thin film coated Ti6Al4V samples were analyzed to obtain optimal Gm concentration without adverse effects for ADSCs.

7.3.3 The Gm dose effects of PLA-Gm-(HAp-Gm) thin film coated Ti6Al4V metallic implants at predetermined Gm concentration (5%, 10%, 15%, 20% and 30% w/w) on ADSCs

In this section, the Gm concentration effect on ADSCs was investigated. SEM images show the morphology features of ADSCs on the PLA-Gm-(HAp-Gm) thin film coated Ti6Al4V disc surfaces at predetermined 5% (*A*), 10% (*B*), 15% (*C*), 20% (*D*) and 30% Gm (*E*) concentrations in *Figure 7.4* as a top view of the surface. Although ADSCs spread and covered the PLA-Gm-(HAp-Gm) thin film coated Ti6Al4V disc surfaces at 5% and 10% Gm concentrations. The cell concentration started to decrease from the PLA-Gm-(HAp-Gm) thin film coated Ti6Al4V discs at 15%. At 20%, Gm containing the PLA-Gm-(HAp-Gm) thin film coated Ti6Al4V sample has relatively low ADSCs on the surface. On the other hand, the lowest cell number was observed at 30% Gm containing the PLA-Gm-(HAp-Gm) thin film coated Ti6Al4V sample, and the cell morphology changes due to the adverse effects of high antibiotic concentration.

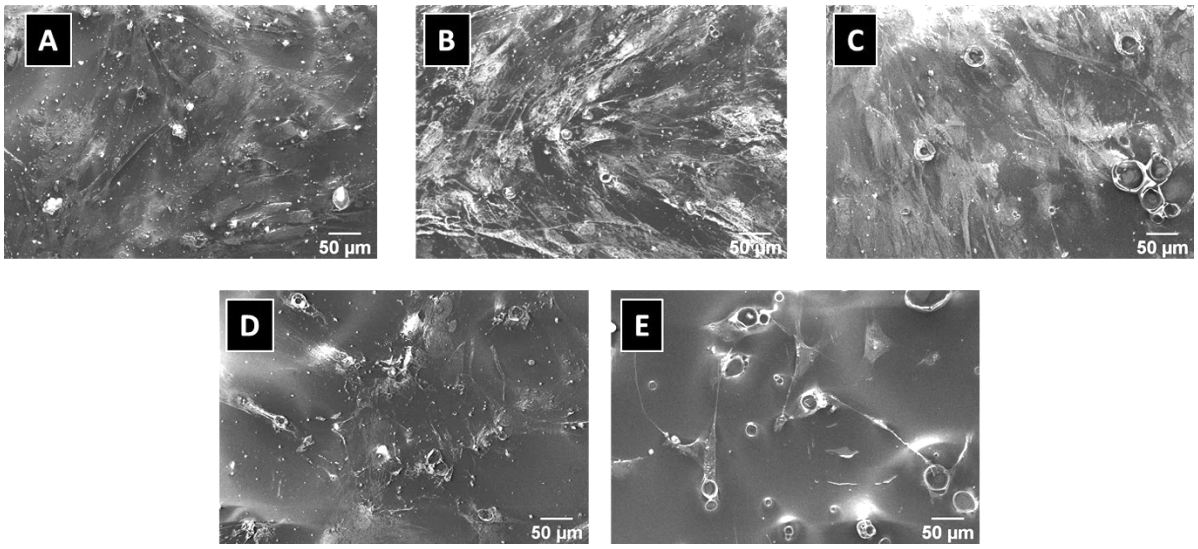

Figure 7.4 SEM images of ADSCs on PLA-Gm-(HAp-Gm) (30% w/w) thin film coated Ti6Al4V discs at the 5% (A), 10% (B), 15% (C), 20% (D), and 30% (E) (w/w) Gm concentrations after 14 days experiment

ADSCs were seeded on the PLA thin film coated Ti6Al4V disc and the PLA-Gm-(HAp-Gm) thin film coated Ti6Al4V discs at the predetermined Gm concentrations (5%-30%), and they were growth for 14days. After the staining of ADSCs *with Phalloidin (red, F-actin) and DAPI (blue, cell nuclei)*, they were observed by the fluorescence deconvolution microscope (Delta Vision Elite). The cell morphology (cell area, and circularity), and the cell number for all samples were investigated by using Image J software (Java-based Image Processing and Analysis Software by NIH Image). In this study, the cell morphology was analyzed to identify the effects of PLA biocomposite coating material and also the dose-dependent Gm release.

The cellular shape and morphological changes are important parameters for investigating the state of a cell, the effects of the different microenvironments, and biophysical factors such as biomaterial type, stiffness, and roughness on the cells. Therefore, the cellular response for the different microenvironments and biophysical factors is connected with the morphological changes of the cells. Image J is an open-source program for analyzing cell morphology according to the perimeter, area, length, and circularity of individual cells based on the microscopy images (Hart et al., 2018).

The shape of ADSCs was revealed by cytoskeleton Phalloidin actin staining (red) because the cytoskeleton keeps a balance between extracellular and intracellular forces, which affects the shape, and the nucleus of the ADSCs. This was observed with DAPI nucleus staining (blue) (*Figure 7.5*). The analyses of cell number (*A*), total cell area (*B*), single-cell area (*C*), and circularity (*D*) are shown in *Figure 7.6* according to the fluorescent images.

In *Figure 7.6 A*, the cell number on PLA thin film coated Ti6Al4V surface significantly increased according to the Ti6Al4V surface. For 5% and 10% PLA-Gm-(HAp-Gm) thin film coated Ti6Al4V samples; the cell number is similar to the Ti6Al4V surface, so there is no statistical difference. However, a very large cell number drop was observed for 15%, 20%, 30% PLA-Gm-(HAp-Gm) thin film coated Ti6Al4V samples, given in *Figure 7.5*. The total cell area analysis of the cells on the implant surface gives a very similar graph in *Figure 7.6 B*.

The fluorescent images (*Figure 7.5*) show that ADSCs on Ti6Al4V, PLA thin film coated Ti6Al4V, PLA-Gm-(HAp-Gm) thin film coated Ti6Al4V surfaces except for 30% Gm contained sample are stretching and forming projections. The circularity graph in *Figure 7.6 D* also proves that there are no statistical changes between the Ti6Al4V discs and PLA biocomposite thin film coated Ti6Al4V discs except the sample containing 30% Gm; the circularity values were approximately 0.4. Circularity is calculated by the normalizing ratio of area to the perimeter. While the circularity of a circle is 1, the circularity of a line is 0. ADSCs show significantly better spreading (smaller circularity) in the samples with smaller critical stress than the sample containing 30% Gm. The circularity of the ADSCs on the 30% PLA-Gm-(HAp-Gm) thin film coated Ti6Al4V disc is around 0.8.

The single-cell area was also measured by Image J, shown in *Figure 7.6 C*. The single-cell area of the cells on the PLA thin film Ti6Al4V disc was lower than the cells on the Ti6Al4V surface, although the PLA thin film coated Ti6Al4V has a significantly higher cell number. The 5% and 10% PLA-Gm-(HAp-Gm) thin film coated Ti6Al4V also have lower single cell areas than the Ti6Al4V, however, the total cell number and circularity did not change. It might be the effect of Gm release on the ADSCs' morphology. On the other hand, the single-cell area of the cells on the 15% and 20% PLA-Gm-(HAp-Gm) thin film coated Ti6Al4V, and the cells on the Ti6Al4V without coating don't have any significant difference. However, the 15% and 20% PLA-Gm-(HAp-Gm) thin film coated Ti6Al4V samples have a very low number of cells on their surface.

Due to the high Gm concentration, the cell number was very low on the 30% PLA-Gm-(HAp-Gm) thin film coated Ti6Al4V disc surface. Additionally, according to their significantly low single-cell area and high cell circularity, the cells on the surface were not healthy.

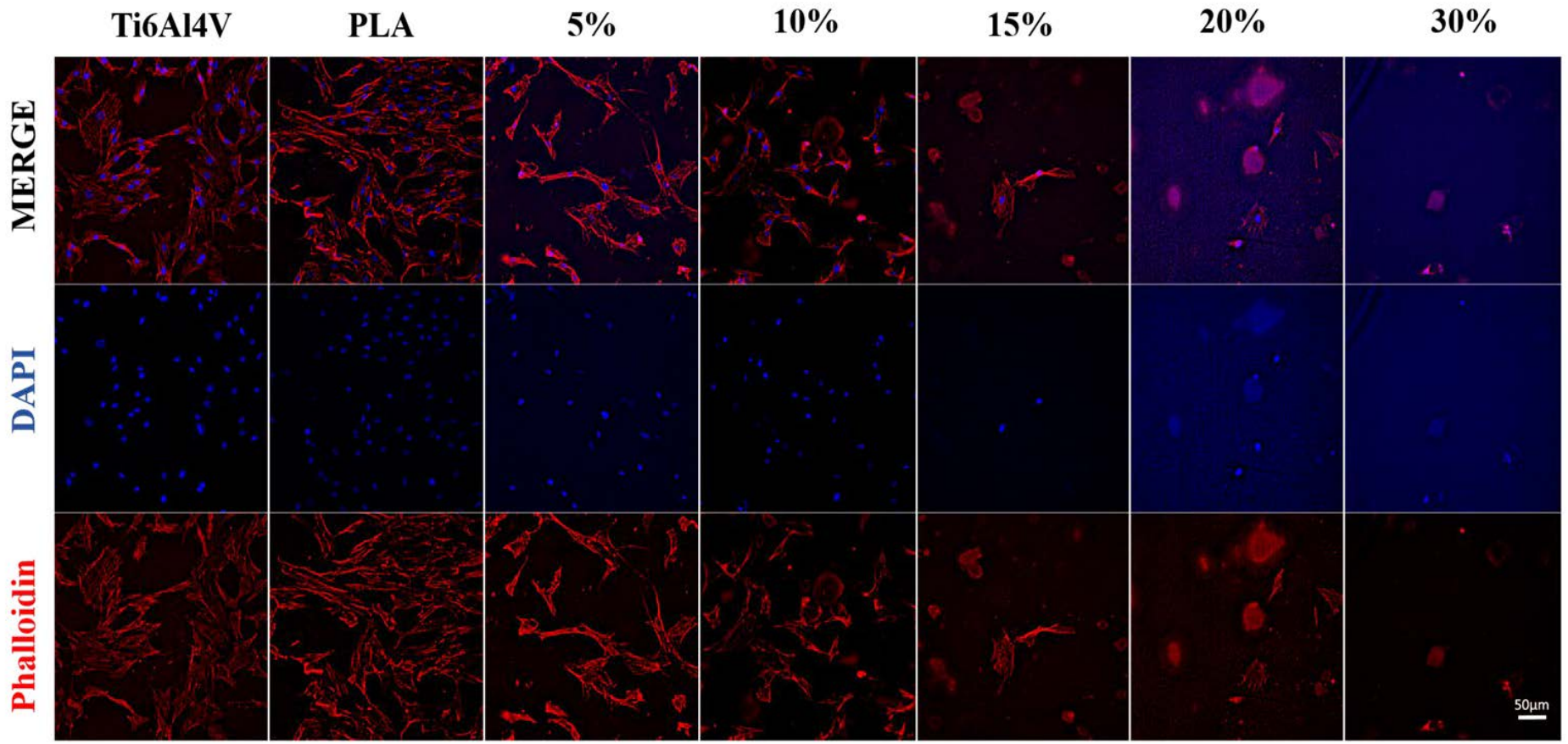

Figure 7.5 Fluorescence staining for Ti6Al4V, PLA coated Ti6Al4V and PLA-Gm-(HAp-Gm) coated Ti6Al4V at 5%, 10%, 15%, 20% and 30% Gm with Phalloidin (red, F-actin) and DAPI (blue, cell nuclei)

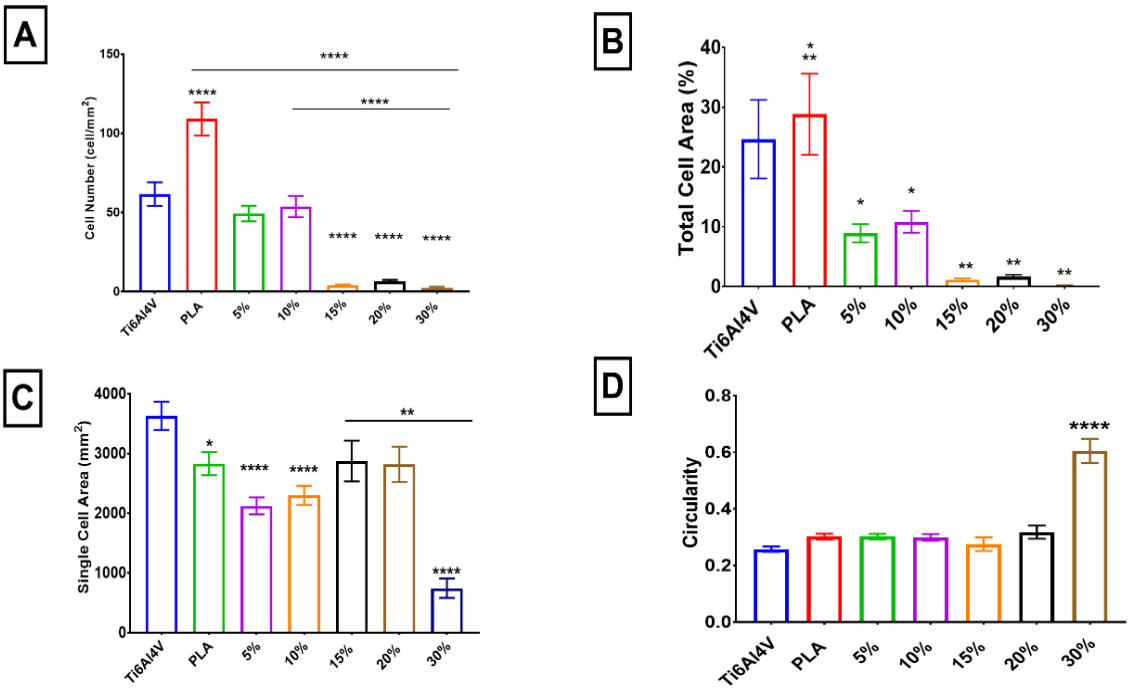

Figure 7.6 Graph represents the comparison of (A) the cell numbers, (B) total cell area %, (C) single cell area mm^2, and (D) circularity for PLA-Gm-(HAp-Gm) thin film coated Ti6Al4V discs (5% to 30% w/w Gm concentrations). The analysis was performed using ImageJ software. Statistical analysis performed using one-way ANOVA with Tukey's post-test. n=3. Error bars denote SEM. P values: *p<0.04, **p<0.008, **** p<0.0001

The fluorescent image (*Figure 7.7*) shows the ADSCs on the PLA thin film coated Ti6Al4V at 40x magnification in order to observe the cytoskeleton in detail. The cytoskeleton of ADSCs stretched and spread on the PLA film surface to interact with the surface and each other.

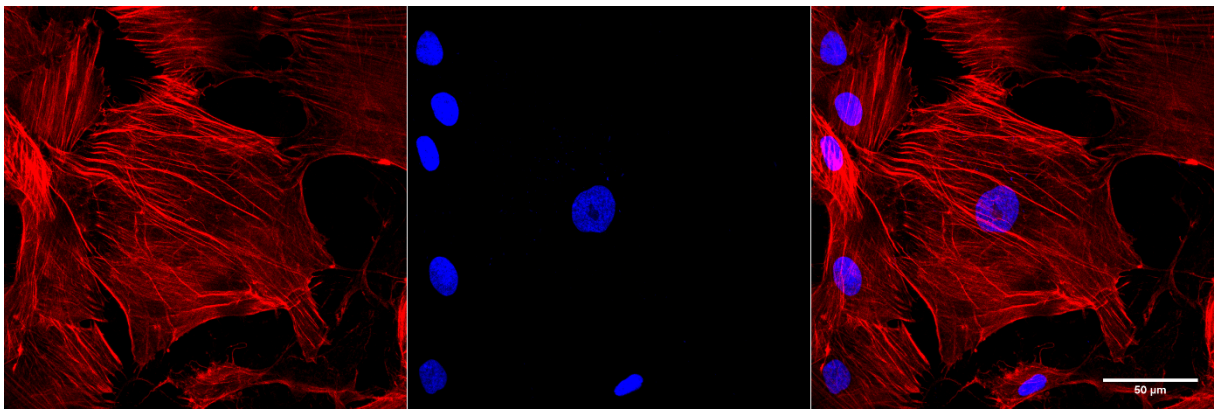

Figure 7.7 Fluorescence staining with Phalloidin (red, F-actin) and DAPI (blue, cell nuclei) for ADSCs on PLA thin film coated Ti6Al4V (x40)

The varied cytokine concentrations across the seven different samples over time were represented by the heat map in *Figure 7.8*. There are no defined cytokine groups that behave similar pattern as a cluster for all samples, the cytokines behave uniquely for each sample. The first observation is that IL-9, IL-15, IL-5, and G-CSF cytokines have very similar patterns in all samples. When the Ti6Al4V sample was investigated according to the heat map, it had higher cytokine expression levels at Day 3 than PLA coated Ti6Al4V sample, especially for MIP-a, IL-8, IL-10, Gm-CSF, MIP-1b. At Day 7, the concentrations of secreted cytokines were drastically decreased for both Ti6Al4V and PLA coated Ti6Al4V samples. The only exception is that RANTES for Ti6Al4V and IL-6 for PLA coated Ti6Al4V remained stable. For Day 10 and Day 14, the patterns of secreted cytokines are very similar and lower than Day 3 for both samples, except for the VEGF, IL-6 and Eotaxin cytokines. While the concentration level of secreted VEGF (growth factor) was higher only for the Ti6Al4V sample at Day 10, the secretion concentration of VEGF was increased only for Ti6Al4V and PLA coated Ti6Al4V at Day 14.

The majority of the cytokines from the 5% PLA-Gm-(HAp-Gm) coated Ti6Al4V sample were expressed at Day 3, and their pattern as a cluster was similar to the PLA coated Ti6Al4V sample. However, the concentration level of the MCP-1 chemokine, and the IFN-a pro-inflammatory cytokines were higher than the PLA coated Ti6Al4V. In addition to the IFN-a expression activity, IL-8 pro-inflammatory cytokine was gradually increased from Day 10 to Day 14. The reason for the high expression patterns of MCP-1 and IFN-a might be the immune response for the initial Gm release for the 5% PLA-Gm-(HAp-Gm) coated Ti6Al4V sample. The concentration of secreted cytokines for the 10% PLA-Gm-(HAp-Gm) coated Ti6Al4V sample was at the highest on Day 3 compared Days 7, 10 and 14 except for the PDGF-bb (platelet-derived growth factor) cytokine which behaved in the opposite way. PDGF-bb has a higher concentration for all Gm containing samples at Day 7.

PDGF-bb has multiple roles including tissue regeneration, repair, and especially the reconstruction of bone-related defects such as trauma, and infections (Zhang et al., 2018). The increasing of its expression level might be the recovery response for the ADSCs due to the initial Gm release because the cell medium was changed with the fresh medium, removing the initial released Gm from the samples at Day 7. Moreover, an initial immune response of the ADSCs according to the surface type was identified at Day 3. While the initial immune response for the Ti6Al4V sample was slightly high when compared to the PLA coated Ti6Al4V sample, the expression patterns of those two samples behaved similarly after Day 3.

VEGF is the vascular endothelial growth factor which expressed only in the samples without the Gm antibiotic. VEGF is multifunctional cytokine. It has a role as a potent angiogenic factor for the

vascular system, and it regulates the angiogenesis. VEGF also plays important roles in bone formation, extra cellular matrix remodelling and wound healing (Duffy et al., 2004, Mackie et al., 2011).

Gerber *et al,*. (1999), investigated the role of VEGF in endochondral bone formation with an in vivo experiment inactivating the growth factor on 24 day old mice. They reported that the inactivation of the growth factor caused the absence of blood vessel invasion, and it thickened the growth plate. Morphogenesis regulates and normalizes the blood vascular system related signals (Gerber et al., 1999). Therefore, VEGF plays a role in the resorption of cartilage with bone formation in order to normalize the growth plate architecture. In our results, the VEGF cytokines were expressed only for the Ti6Al4V and PLA coated Ti6Al4V samples. Therefore, the VEGF expression can evidence the stimulation of the osteogenic cell differentiation of ADSCs for the Ti6Al4V and PLA coated Ti6Al4V samples.

Finally, as an initial immune response, the 30% PLA-Gm-(HAp-Gm) coated Ti6Al4V sample had the highest response due to the high dosage of the initial Gm burst release. At Day 14, the expression patterns of cytokines for the 5% and 10% PLA-Gm-(HAp-Gm) coated Ti6Al4V samples were found to be similar to the Ti6Al4V and PLA coated Ti6Al4V samples, except for the expression level of VEGF. The expression levels of cytokines for the 15%, 20%, and 30% PLA-Gm-(HAp-Gm) coated Ti6Al4V samples were relatively low, and their expression patterns were similar to each other. It was found that the 15%, 20% and 30% Gm samples had very low amount of ADSCs on their surfaces. Therefore, the very low secretion level of overall cytokines from those samples might reflect the fluorescence deconvolution microscope results.

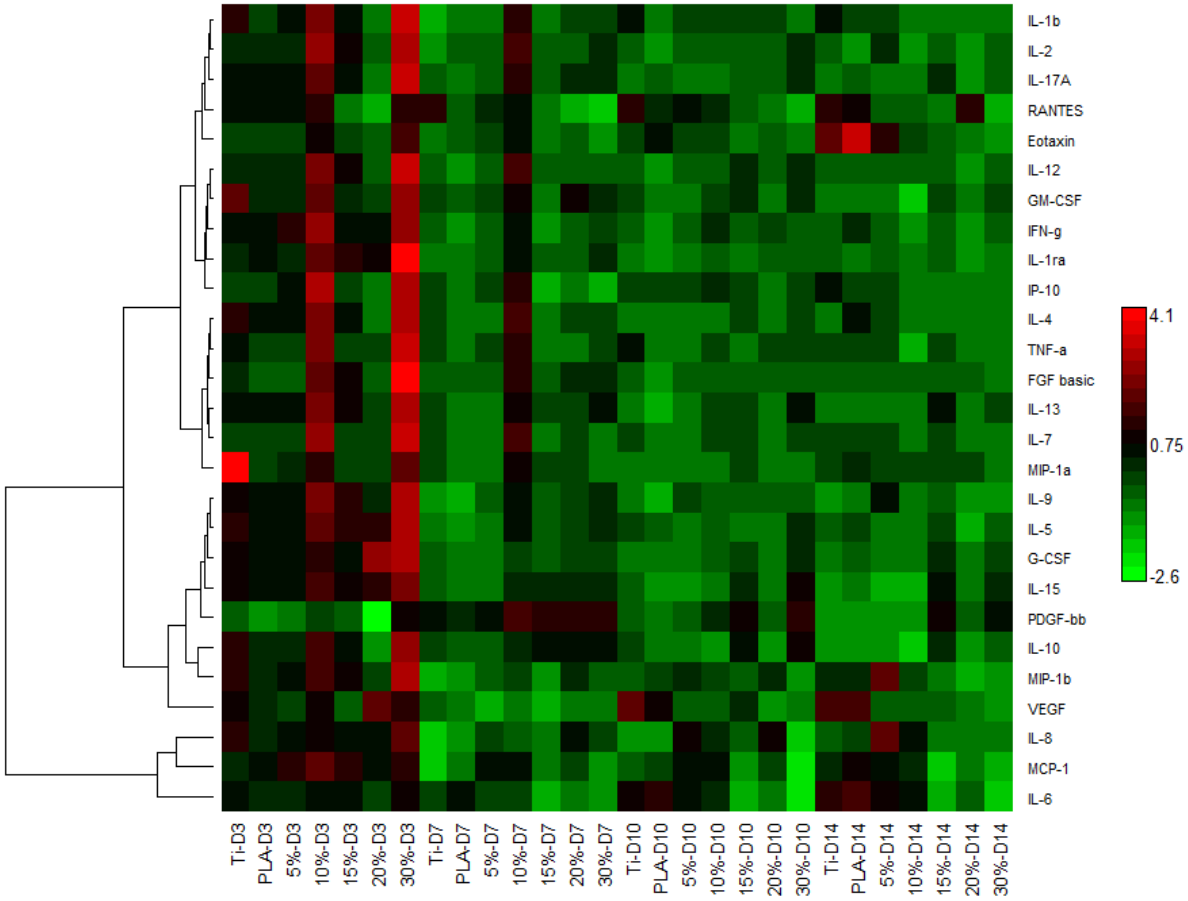

Figure 7.8 The heat map for the Bio-plex assay that includes 27 cytokines (y-axis) and 32 samples (x-axis), Ti6Al4V disc, PLA thin film coated Ti6Al4V disc, PLA-Gm-(HAp-Gm) thin film coated Ti6Al4V discs at predetermined Gm concentrations (5%, 10%, 15%, 20%, and 30%) for D3, 7, 10 and 14

The unique point of this experiment is to seed ADSCs on PLA biocomposite thin film coated Ti6Al4V discs instead of only on PLA biocomposite thin film. This is done to obtain both the material effect and surface effect. This is because the substrate effect from Ti6Al4V implants changes the E and H values of the PLA biocomposite thin film after the coating material which also changes the surface characterization of the implant.

7.3.4 The effects of Ti6Al4V metallic implants before and after the anodization process on ADSCs

The anodization process and its effects on the Ti6Al4V surface are given in **Chapter 5**. The thermal anodization technique was used to increase the TiO_2 layer (a naturally occurring thin layer) on the

Ti6Al4V surface which increases the surface roughness, young modulus and hardness values of the Ti6Al4V implant surface. The surface properties of the substrate (Ti6Al4V discs) affect the surface properties of PLA biocomposite thin film coating due to the substrate effect. Therefore, the changes in the PLA biocomposite's surface properties might affect cell behavior as well. The substrate surface properties are important for long term cell-surface interaction after the degradation of the PLA thin film. For the reasons above, the main focus of this section is the determination of effects of the anodized surface of the Ti6Al4V discs on the ADSCs' morphology and biological responses such as cytokine secretions. After the cytoskeleton Phalloidin actin staining (red) and DAPI nucleus staining (blue), the cell morphology was analyzed by the fluorescence deconvolution microscope (Delta Vision Elite), and the Image J program as per the previous section.

The cell morphological analyses in *Figure 7.9*, cell number *(A)*, total cell area *(B)*, single-cell area *(C),* and circularity *(D)* showed that the cells on both untreated and anodized Ti6Al4V (A-Ti6Al4V) disc surfaces spread and stretched nicely to cover the surface. It was found that the total cell area for the A-Ti6Al4V sample was significantly higher than the Ti6Al4V sample. The fluorescent images in *Figure 7.9 E* also prove that there is not any adverse effect of the A-Ti6Al4V surface on the ADSCs' morphology.

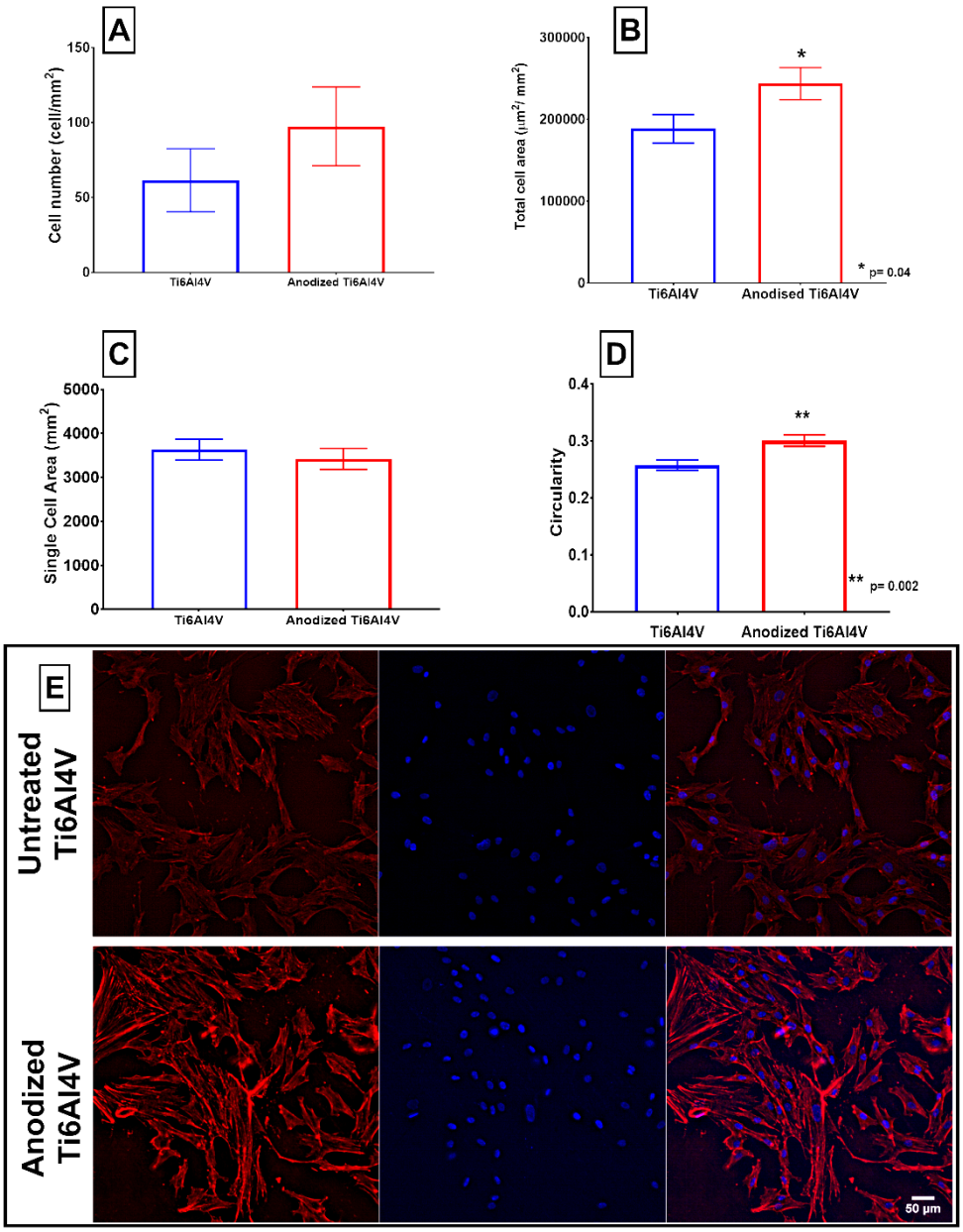

Figure 7.9 Graph represents the comparison of (A) the cell numbers, (B) total cell area %, (C) single cell area mm^2, and (D) circularity for Ti6Al4V and A-Ti6Al4V discs. The analysis was performed using ImageJ software. Statistical analysis performed using Student t-test, unpaired , two-tails, n=3, P values: * p=0.04, ** p= 0.002 (E) Fluorescence staining with Phalloidin (red, F-actin) and DAPI (blue, cell nuclei) for ADSCs on Ti6Al4V and A-Ti6Al4V discs

The Bio-plex data is represented in the heat map in order to observe the patterns of cytokine secretion levels for the ADSCs on the A-Ti6Al4V and Ti6Al4V samples in *Figure 7.10*. The results demonstrated that the overall release pattern of the cytokine clusters for the A-Ti6Al4V and Ti6Al4V samples were similar to each other at Days 3, 7 and 10. The concentration of the majority of the cytokines decreased at Day 7 and Day 10 for both samples. However, the concentration of the

cytokines as the overall clusters, increased significantly at Day 14 for the A-Ti6Al4V sample. When the secretion pattern for each cytokine according to the A-Ti6Al4V and Ti6Al4V samples were analyzed separately, they were divided into three different groups.

The first group has a large number of cytokines with similar secretion behavior: IL-5, IL-1ra, IL-6, IL-7, IL-12, IL-13, IL-15, IP-10, Gm-CSF, Eotoxin, IFN-g, FGF basic, TNF-a, PDGF-bb cytokines. Their activity was higher at Day 3, and then the activity was drastically decreased on Day 7 and Day 10 for both samples. On Day 14, while the cytokines' activity remained as low as Days 7 and 10 for the Ti6Al4V sample, the activity of all group-1 cytokines increased for the A-Ti6Al4V sample on Day 14.

The second group contains IL-2, VEGF, MIP-1a, IL-9 and IL-8 cytokines with similar behaviors. Those five cytokines show very little or no activity in the Ti6Al4V sample during the 14 day experiment. In the A-Ti6Al4V sample, their activity was very low (similar to the Ti6Al4V for Day 3 and Day 7), however, the cytokine secretion for the second group's cytokines increased gradually at Day 10 and Day 14.

The third group has five unique cytokines with unique patterns: IL-4, IL-10, Rantes, G-CSF, and MIP-1b cytokines. The IL-4 cytokine secreted only on Day 3 and Day 14 for the A-Ti6Al4V sample, and its activity was very low for the Ti6Al4V sample. The highest secretion period for IL-10 was on Day 3 for both samples; the secretion level of IL-10 decreased at Days 7 and 10. Finally, its secretion level slightly increased only in the Ti6Al4V sample at Day 14. The highest secretion period for MIP-1b was determined at Day 3 only in the Ti6Al4V, and then it drastically decreased. On the other hand, the MIP-1b cytokine was secreted at Day 14 for the A-Ti6Al4V sample. While the secretion of the Rantes cytokine had only one spike at Day 7 in the Ti6Al4V sample, it gradually increased from Day 10 to Day 14 in the A-Ti6Al4V sample.

Finally, the G-CSF cytokine was actively secreted only on Day 14 for both samples. Additionally, G-CSF cytokine had the highest activity for the Ti6Al4V sample at Day 14 according to the rest of the cytokines of the Ti6Al4V sample at Day 14.

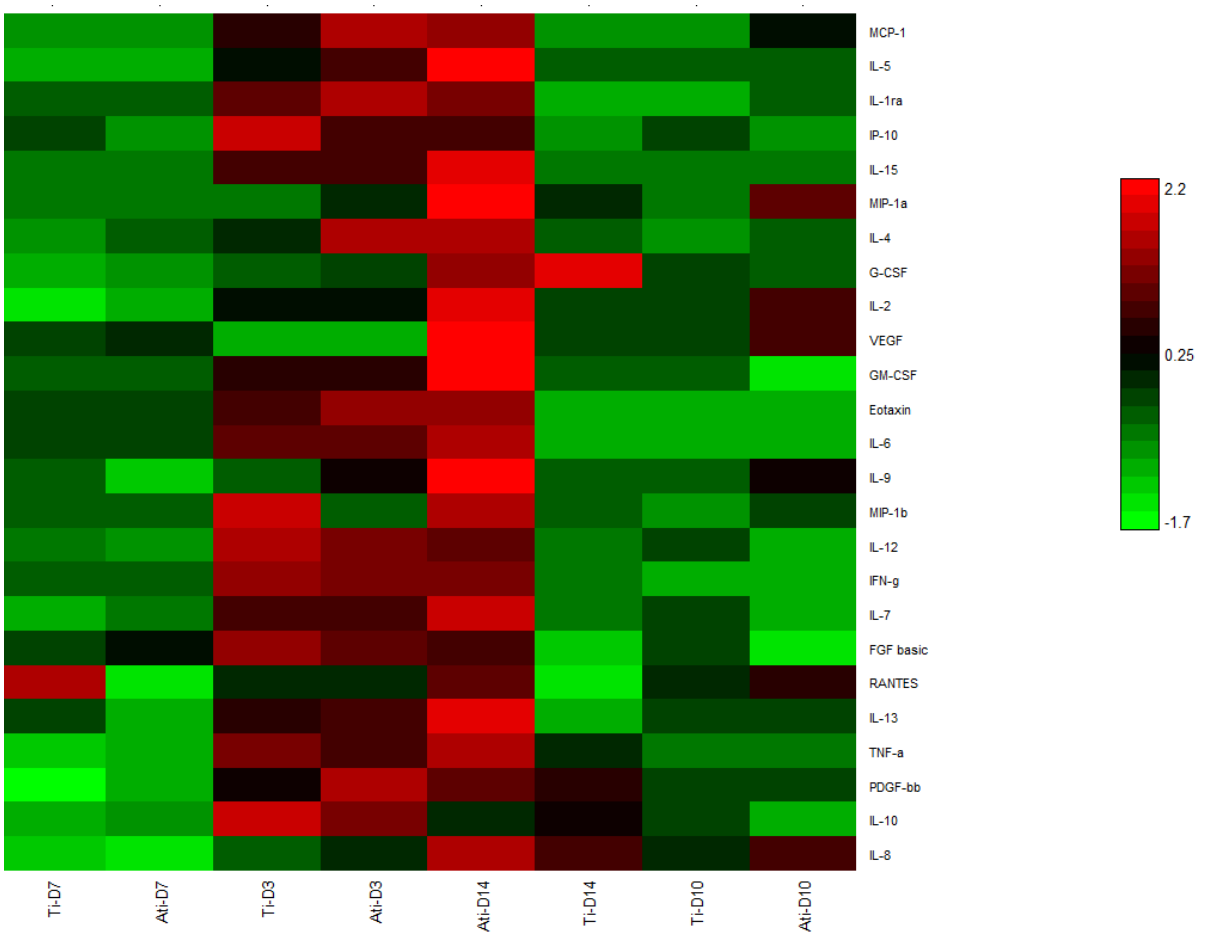

Figure 7.10 The heat map for the Bio-plex assay that includes 27 cytokines (y-axis) and 8 samples (x-axis), untreated Ti6Al4V disc, and anodized Ti6Al4V discs for Day3, 7, 10 and 14

7.3.5 Proteomics Analysis

The mass spectroscopy analysis and protein identification were conducted for seven different samples (n=3). Human ADSCs on the Ti6Al4V discs, the PLA coated Ti6Al4V discs, and the PLA-Gm-(HAp-Gm) coated Ti6Al4V discs at five Gm concentrations (5%-30%) were analyzed by the mass spectroscopy. The data, including identified proteins, were presented in three parts. The first part contains the comparison of ADSCs on the Ti6Al4V and PLA coated Ti6Al4V to observe the effect of the Ti6Al4V surface and the PLA thin film coating on the ADSCs. The second part has the identified protein data to compare the Ti6Al4V and PLA coated Ti6Al4V with the PLA-Gm-(HAp-Gm) coated Ti6Al4V discs at different Gm concentrations (5%, 10%, 15%, 20% and 30% w/w). The identified proteins acquired at the 95% confidence cut-off by the mass spectroscopy were analyzed through ClueGO (version 2.5.7), identifying the biological processes' ontology definitions. The number of total identified gene ontology (GO) biological processes for each sample is given in *Figure 7.11*. The

number of GO biological process was very close in the Ti6Al4V (799) and PLA coated Ti6Al4V (739). While the highest number of GO biological processes was identified in the 5% PLA-Gm-(HAp-Gm) coated Ti6Al4V, the lowest number was determined in the 30% PLA-Gm-(HAp-Gm) coated Ti6Al4V. In the third part, the Ti6Al4V disc surface was modified with the thermal anodization, and the same experiment procedure was followed as first and second parts to detect its effects on ADSCs.

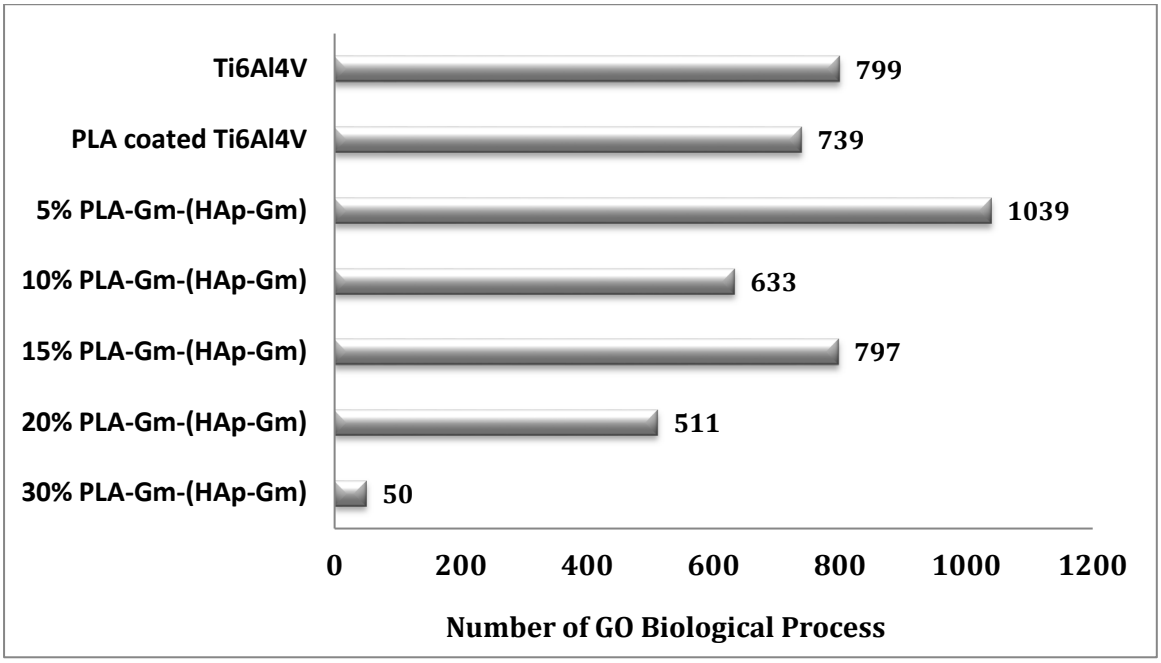

Figure 7.11 The graphs show the number of total identified gene ontologies biological processes for ADSCs which were seeded on Ti6Al4V discs, PLA coated Ti6Al4V discs and PLA-Gm-(HAp-Gm) coated Ti6Al4V discs at predetermined Gm concentrations (5%, 10%, 15%, 20% and 30% w/w)

7.3.5.1 Mass Spectroscopy Protein Data from ADSCs on Ti6Al4V and PLA coated Ti6Al4V discs

Figure 7.12 shows the two-way Venn diagram to illustrate the number of identified gene ontology biological processes for the Ti6Al4V and the PLA coated Ti6Al4V samples. The total number of GO biological processes for the Ti6Al4V sample was 799, and for the PLA coated Ti6Al4V sample was 739. According to the Venn diagram, the unique proteins in the Ti6Al4V were 194, and the unique proteins in the PLA coated Ti6Al4V were 134 while the shared processes for the PLA coated Ti6Al4V and the Ti6Al4V samples were 605.

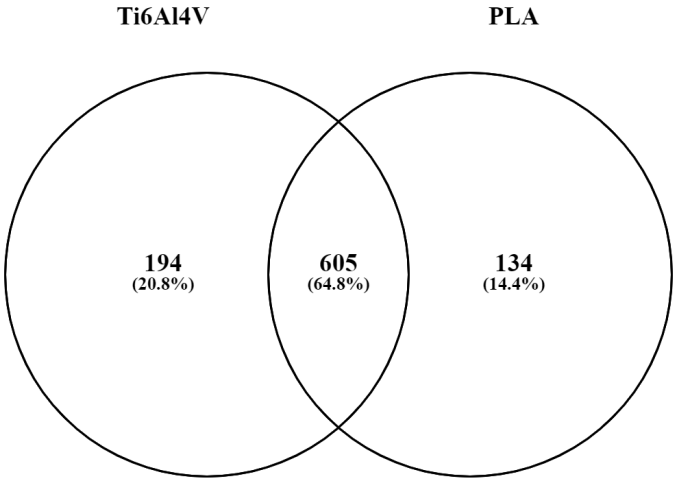

Figure 7.12 two-way Venn diagram illustrates the identified gene ontology biological processes for unique Ti6Al4V, unique PLA coated Ti6Al4V and shared proteins for Ti6Al4V and PLA coated Ti6Al4V

The unique GO biological processes from the two-way Venn diagram in *Figure 7.12* have screened at least four relevant search terms related to cellular changes, osteogenesis-related development, cell adhesion, and the regulation of the immune system. The list of relevant GO biological processes for the unique PLA coated Ti6Al4V, the unique Ti6Al4V samples, and their shared biological processes are given separately in *Table 7.2*. The GO biological processes in *Table 7.2*, *Table 7.3* (unique PLA coated Ti6Al4V), *Table 7.4* (unique Ti6Al4V), and *Table 7.5* (shared) were prepared to show the details of the identified protein numbers and the groups for the specific biological processes relevant to osteogenesis-related cellular development. The regulations of cell growth, cell adhesion, and positive regulation of immune response are some of the unique GO biological processes for the PLA coated Ti6Al4V in *Table 7.3*.

All the unique GO biological processes related to osteogenesis with the identified protein numbers and groups are given in *Table 7.4*. In addition to the activation of the immune response and the regulation of cell-matrix adhesion processes, the unique GO biological processes for Ti6Al4V include a biologically relevant pathway called the Wnt signaling pathway. The Wnt signaling pathway plays an important role to increase remodeling-based bone formation. There are two main Wnt signaling pathways: canonical (b-catenin dependent) and non-canonical (b-catenin independent) signaling pathways regulated by 19 secreted Wnt proteins. The canonical Wnt (cWnt) signaling pathway is related to the osteoblast maturation. The cWnt signaling pathway can activate bone formation. At the same time, it can decrease bone resorption. Therefore, this signaling pathway regulates the osteoclastogenesis to decrease osteoclast activity (Baron et al., 2018). The non-canonical Wnt signaling pathway and canonical Wnt signaling pathways can often influence each other. The non-

canonical Wnt signaling pathway can act with the Wnt\planar cell polarity signaling pathway (Wnt\PCP) and (Wnt\ Ca^{+2}) Ca^{+2}, which was observed as a specific GO biological process for the unique Ti6Al4V sample in *Table 7.4.*

Finally, both samples contain the GO biological processes, which are related to mainly three processes: the regulation of cell-matrix adhesion, the cell morphogenesis, and differentiation in *Table 7.5.* They also contain the muscle cell differentiation process, which might refer to early osteo-differentiation. The non-canonical Wnt signaling pathway-related GO biological process with the identified protein group was found for the shared biological processes of both samples in *Table 7.6.* Therefore, both the Ti6Al4V and PLA coated Ti6Al4V surfaces can positively regulate cell growth and proliferation, the surface adhesion of the cells. Additionally, they stimulate the Wnt signaling pathway to improve the cell differentiation feature of ADSCs. The key protein expression found within ADSCs cultured on the Ti6Al4V and PLA coated Ti6Al4V have been investigated with a critical role in cellular functionality and biological processes.

CTHRC1 (Collagen triple helix repeat-containing protein), CTNNB1 (Catenin beta-1), and ILK (Integrin-linked protein kinase) play a crucial role in the regulation of the Wnt signaling pathway due to stimulating cell differentiation, and bone formation. These essential proteins were identified in the Ti6Al4V, and PLA coated Ti6Al4V samples, within the different specific groups of GO biological processes. Additionally, ITGAV (Integrin alpha-V) is another key protein that exists in both the Ti6Al4V and PLA coated Ti6Al4V samples. It regulates the cell-substrate adhesion positively and improves cell proliferation.

CTHRC1, which is a 28-kD extracellular matrix glycoprotein, regulates the Wnt\PCP pathway by forming the CTHRC1-Wnt Ligand-Frizzled Receptor (Fzd) complex (Pyagay et al., 2005, Ma et al., 2014). It is a cofactor protein, which promotes activation of the Wnt\PCP pathway due to stabilizing ligand-receptor interaction. Therefore, CTHRC1 is a multifunctional protein. It plays a role in the regulation of bone remodeling, the stimulation of osteoblastic bone formation, cell proliferation, and cell migration (Yamamoto et al., 2009, Myngbay et al., 2019).

Kimura *et al.* (2008) investigated the role of CTHRC1 in bone tissue through an *in vivo* experimental design using two types of mice: CTHRC1 null mice and transgenic mice with over-expressed CTHRC1. Their micro-CT and histomorphometry results show that while the Cthrc1-null mice had low bone mass due to lack of osteoblastic bone formation, the transgenic mice displayed high bone mass because of an increase in osteoblastic bone formation. Thus, the study indicates that CTHRC1 has a role in the positive regulation of bone formation (Kimura et al., 2008).

Another key protein, CTNNB1, is also a multifunctional protein, and it plays critical roles in cell adhesion, cell differentiation, and survival. Additionally, it indicates the Wnt signaling pathway (Kato et al., 2011). It is the key coactivator protein for the canonical Wnt signaling pathway, also called the beta-catenin dependent Wnt pathway. The canonical Wnt signaling pathway functions with the regulating beta-catenin secretion, therefore its stability is controlled by Wnt proteins (MacDonald et al., 2009, van Schie et al., 2020).

Tanabe *et al.* (2016) analyzed the CTNNB1 gene expression and the pathways related to the CTNNB1 gene in mesenchymal stem cells. They were reported that *CTNNB1* stimulates the regulation of stem cell pluripotency and differentiation due to its role in the canonical Wnt signaling pathway.

ILK which is a multifunctional scaffold protein that localizes focal adhesions, and cell-matrix interactions. It is another important shared protein for the Ti6Al4V and PLA coated Ti6Al4V samples. It regulates various cellular processes, such as growth, differentiation, proliferation, and adhesion. Due to its role in the cell-extracellular matrix adhesion process, ILK protein is a key component of the regulations of cell shape, survival, proliferation, and differentiation (Wu et al., 2001, Yen et al., 2014).

Table 7.2 Unique GO Biological Process in table from two-way Venn diagram for the Ti6Al4V and PLA coated Ti6Al4V samples with most pertinent roles in cellular changes, osteo-related development, adhesion and immune system regulation

Unique PLA coated Ti6Al4V	Unique Ti6Al4V	Shared PLA and Ti6Al4V
• **Cell adhesion mediated by integrin**	• Wnt signaling pathway, planar cell polarity pathway	• Cell activation involved in immune response
• **Substrate-dependent cell migration**	• Regulation of cell growth	• Cell activation
• **Positive regulation of immune response**	• Wnt signaling pathway	• Immune response
• **Developmental cell growth**	• Regulation of cell morphogenesis involved in differentiation	• Interleukin-12-mediated signaling pathway
• **Regulation of immune system process**	• Positive regulation of cell development	• Cellular response to stress
• **Calcium-independent cell-matrix adhesion**	• Regulation of cell-matrix adhesion	• System development
• **Antimicrobial humoral immune response mediated by antimicrobial peptide**	• Positive regulation of cell morphogenesis involved in differentiation	• Regulation of substrate adhesion-dependent cell spreading
	• Antibacterial humoral response	• Regulation of cell morphogenesis
	• Positive regulation of cell growth	• Cell morphogenesis
	• Positive regulation of cell population proliferation	• Cell morphogenesis involved in differentiation
	• Wnt signaling pathway, calcium modulating pathway	• Cell differentiation
	• Activation of immune response	• Cell-matrix adhesion
	• Muscle tissue development	• Cell-substrate adhesion
		• Non-canonical Wnt signaling pathway
		• Regulation of cell differentiation
		• Positive regulation of cell differentiation
		• Substrate adhesion-dependent cell spreading
		• Regulation of cell adhesion
		• Muscle structure development
		• Muscle cell differentiation
		• Striated muscle cell differentiation
		• Striated muscle cell development
		• Muscle cell development

Table 7.3 The GO of proteins identified in biological processes with osteogenic associations with the identified protein groups across the unique PLA coated Ti6Al4V dataset

Unique PLA coated Ti6Al4V	Number of Identified proteins	False discovery rate	Proteins identified
Cell adhesion mediated by integrin	4	1.33E-02	FBN1,ITGA11,ITGAV,ITGB1
Substrate-dependent cell migration	4	3.56E-02	ATP5B,CTTN,ITGA11,MYH10
Positive regulation of immune response	26	4.21E-02	ACTB,ACTG1,ACTR3,ANXA1,ARPC2,ARPC4,ARPC5,HSP90AA1,HSP90AB1,HSP90B1,HSPA1A,HSPA1B,HSPD1,KRT1,MAPK3,MIF,MYO1C,NONO,PHB,RAC1,RAP1A,RBM14,RPS19,STXBP1,XRCC5,XRCC6
Developmental cell growth	7	4.73E-02	HSP90AA1,HSP90AB1,IQGAP1,ITGB1,MAP1B,PDLIM5,VCL
Antimicrobial humoral immune response mediated by antimicrobial peptide	8	4.76E-02	FAU,GAPDH,H2BFS,HIST1H2BC,HIST1H2BK,HIST2H2BE,HMGN2,RPS19
Regulation of immune system process	51	4.80E-02	ACTB,ACTG1,ACTR3,ANXA1,ARPC2,ARPC4,ARPC5,BST1,CALM1,CALM3,CALR,CD59,COL1A1,COL1A2,EZR,FBN1,GNAS,GPI,GSN,H3F3B,HIST1H3J,HIST1H4F,HIST2H3D,HSP90AA1,HSP90AB1,HSP90B1,HSPA1A,HSPA1B,HSPA9,HSPD1,ITGB1,KRT1,LGALS1,MAPK3,MIF,MSN,MYL9,MYO1C,NME1,NONO,PHB,PML,RAC1,RAP1A,RBM14,RPS19,SOD1,STXBP1,THBS1,XRCC5,XRCC6
Calcium-independent cell-matrix adhesion	2	4.86E-02	FN1,ITGB1

Table 7.4 The GO of proteins identified in biological processes with osteogenic associations with the identified protein groups across the unique Ti6Al4V dataset

Unique Ti6Al4V	Number of Identified proteins	False discovery rate	Proteins identified
Wnt signaling pathway, planar cell polarity pathway	10	1.70E-04	AP2A1,AP2A2,AP2S1,CDC42,CLTC,CTHRC1,PFN1,PTK7,RAC1,RHOA
Wnt signaling pathway, calcium modulating pathway	5	3.79E-02	CALM1,CALM3,CTNNB1,GNAO1,GNAT2
Wnt signaling pathway	15	0.0065	AP2A1,AP2A2,AP2S1,CALM1,CALM3,CDC42,CLTC,CTHRC1,CTNNB1,GNAO1, GNAT2,PFN1,PTK7,RAC1,RHOA
Positive regulation of cell morphogenesis involved in differentiation	13	4.70E-03	ACTR2,ARPC2,CALR,CDC42,DNM2,FLNA,FN1,GDI1,ILK,MAP1B,RAB11A,RAC 1,RHOA
Antibacterial humoral response	6	3.02E-02	FAU,H2BFS,HIST1H2BC,HIST1H2BJ,HIST1H2BK,HIST2H2BE
Positive regulation of cell population proliferation	41	3.76E-02	AKR1B1,ANXA1,ANXA2,BST1,CALR,CAPN1,CRIP2,CTHRC1,CTNNB1,CTSZ,DD X39B,EIF5A,EIF5A2,FLNA,FN1,GNAI2,GNAI3,HNRNPU,ILK,ITGAV,ITGB1,LAM C1,MIF,NME1,NME1-NME2,NME2,NPM1,PML,PPP1CC,PURA,RAB25,RPL23,RPS15A,RPS4X,S100 A13,S100A6,SHMT2,SLC25A5,SRSF6,TGM2,THBS1
Activation of immune response	22	3.91E-02	ACTB,ACTG1,ACTR2,ARPC2,ARPC4,CDC42,HSP90AA1,HSP90AB1,HSP90B1, HSPD1,KRT1,MAPK3,MYO1C,NONO,RAC1,RBM14,RPS27A,SFPQ,THY1,UBA 52,UBB,XRCC5

Table 7.5 The GO of proteins identified in biological processes with osteogenic associations with the identified protein groups across the shared Ti6Al4V and PLA coated Ti6Al4V datasets

Shared PLA and Ti6Al4V	Number of Identified proteins	False discovery rate	Proteins identified
Non-canonical Wnt signaling pathway	15	6.23E-06	AP2A1,AP2A2,AP2S1,CALM1,CALM3,CDC42,CLTC,CTHRC1,CTNNB1,GNAO1,GNAT2,PFN1,PTK7,RAC1,RHOA
Cellular response to stress	69	0.0118	ACAA2,AKR1B1,ANXA1,CALR,CRYAB,DBNL,DDX1,DDX39A,DNM2,EEF2,ERP44,GFPT1,GPX8,H2AFX,HIST1H4F,HIST3H2A,HIST3H3,HK2,HNRNPA1,HSP90B1,HSPA1A,HSPA1B,HSPA5,HSPA8,HYOU1,LARS,LMNA,LONP1,MAP2K3,MAPK3,MIF,MYLK,MYOF,NONO,NPM1,NQO1,P4HB,PDIA3,PDIA4,PDIA6,PGK1,PML,PPP1CA,PRDX1,PRDX5,PSMC2,PSMC4,PYCR1,PYCR2,RBM14,RHOA,RPL26,RPS27A,SCAP,SEC31A,SFPQ,STT3B,THBS1,TLN1,TPM1,TPP1,TRIM28,TXNDC5,TXNRD1,UBA1,UBA52,UBB,VCP,XRCC5
Cell morphogenesis involved in differentiation	36	7.11E-05	ACTN1,ATP8A2,CDC42,CNP,CRMP1,CTNNB1,DPYSL2,ENSG00000258947,ENSG00000258947,EZR,FLNA,FLNB,FN1,HSP90AA1,HSP90AB1,ILK,ITGAV,ITGB1,LAMC1,MAP1B,MAPK3,MYH10,MYH9,PALLD,PDLIM7,PLOD3,RAB10,RAB1A,RAB25,RAC1,S100A6,SPTAN1,STMN1,UCHL1,VCL,WDR1
Cell differentiation	20	0.00012	ACTA1,ACTC1,ACTG1,CALR,CAPN2,FHL2,FLNC,HNRNPU,ITGB1,KRT19,KRT8,LMNA,MYH10,MYH11,MYH9,MYOF,TMOD3,TPM1,UCHL1,WDR1
Positive regulation of cell differentiation	45	0.0116	ACTR2,ANXA1,AP2A1,ARPC2,ARSB,ATP8A2,BRINP1,CALR,CDC42,CLIC1,COL1A1,CTHRC1,CTNNB1,DDX39B,DNM2,DPYSL3,EHD2,ENG,FLNA,FN1,GDI1,GNAS,HNRNPU,HSP90AB1,HSPA1A,HSPA1B,HSPA5,IGFBP3,ILK,IQGAP1,LEPRE1,MAP1B,NME1,NME1-NME2,NME2,PA2G4,PDLIM7,PPP1CC,PTK7,RAB11A,RAC1,RAP1A,RHOA,SNX3,XRCC5
Substrate adhesion-dependent cell spreading	6	0.0139	FN1,ILK,ITGAV,LAMC1,RAB1A,RAC1
Cell-matrix adhesion	10	0.00016	BST1,CORO1C,ILK,IQGAP1,LIMCH1,RAC1,RHOA,THBS1,THY1,UTRN
	79	4.30E-23	ACLY,ACTR1B,ACTR2,ALDOA,ANPEP,ANXA2,AP2A2,APRT,ARSB,ATAD3B,BST1,CAP1,CAPN1,CCT2,CCT8,CD44,CD59,CKAP4,CNN2,COTL1,CTSB,CTSD,CTSZ,C

Cell activation involved in immune response	YB5R3,DBNL,DDOST,DYNC1H1,EEF1A1,EEF2,ERP44,GDI2,GNS,GPI,GSTP1,HSP90AA1,HSP90AB1,HSPA1A,HSPA1B,HSPA8,HSPD1,IQGAP1,ITGAV,KPNB1,KRT1,LGALS1,LRP1,MIF,MVP,NME1-NME2,NME2,PA2G4,PGAM1,PGM2,PKM,PPIA,PRDX6,PSMA5,PSMC2,PSMD1,PSMD6,PYGB,RAB10,RAC1,RAP1A,RAP1B,RHOA,RPS6,S100A11,S100A13,SIRPA,SIRPB1,SPTAN1,TUBB,TUBB4B,TXNDC5,VAT1,VCL,VCP,XRCC5

7.3.5.2 Mass Spectroscopy Protein Data to determine effect of Gm release from PLA-Gm-(HAp-Gm) coated Ti6Al4V discs on ADCSs at different Gm concentrations

After the determination of the unique proteins and GO biological processes of Ti6Al4V as an implant substrate and PLA as a matrix coated Ti6Al4V, PLA biocomposite thin film coated Ti6Al4V samples at five different Gm concentrations (5% to 30%) were analyzed. The PLA biocomposite thin film coating system contained HAp bioceramic drug carrier particles and Gm antibiotic particles. Although the amount of HAp particles were kept constant for each sample, the Gm ratio was changed for 5%, 10%, 15%, 20% and 30% w/w. Additionally, the aim was to identify the effect of Gm dosage on ADSCs. The identified unique proteins and the GO biological processes for the PLA-Gm-(HAp-Gm) coated Ti6Al4V samples at five different Gm concentrations (5%-30% w/w) were compared with the Ti6Al4V and PLA coated Ti6Al4V samples in this section. Each PLA-Gm-(HAp-Gm) coated Ti6Al4V sample was analyzed separately. In *Figure 3*, the three-way Venn diagrams for the total GO biological processes related to the identified protein numbers of Ti6Al4V, PLA coated, and PLA-Gm-(HAp-Gm) coated Ti6Al4V samples which are 5% (*A*), 10% (*B*), 15% (*C*), 20% (*D*), and 30% (*E*) w/w Gm ratio, respectively.

Figure 7.13 A shows that 260 unique GO biological processes were identified for the 5% Gm sample, and 573 biological processes were found for three of the samples. In *Figure 7.13 B*, 70 unique GO biological processes for the 10% Gm sample was determined, while the shared biological processes number is 485. For the 15% Gm sample, the unique GO biological processes are 163, and the shared processes are 482 in *Figure 7.13 C*. 98 unique and 352 shared GO biological processes were identified for the 20% Gm sample in *Figure 7.13 D*. Finally, 5 unique and 42 shared GO biological processes were identified for the 20% Gm contained sample in *Figure7.13 E*.

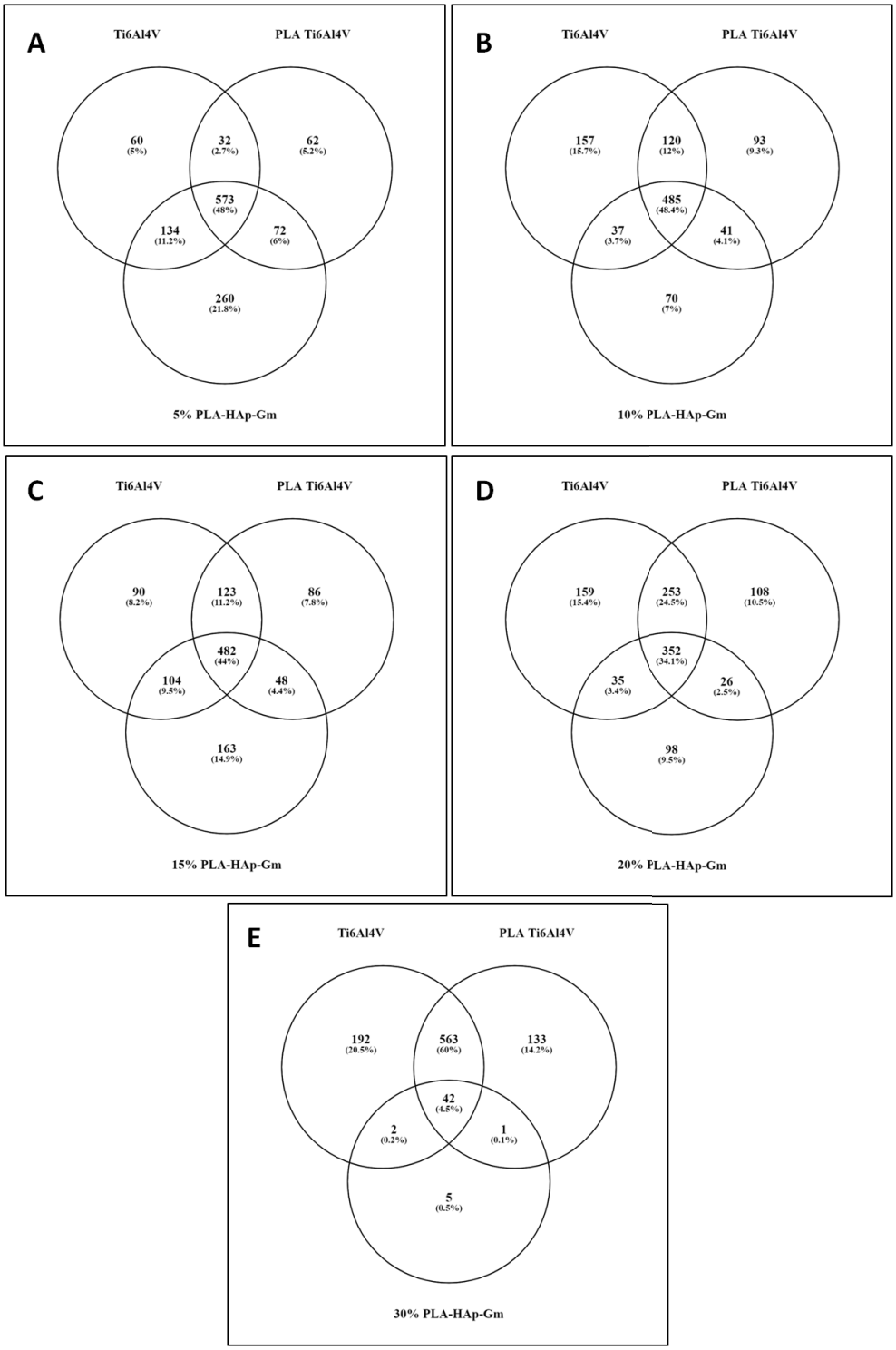

Figure 7.13 three-way Venn diagram illustrates the identified GO biological processes numbers for the comparison of Ti6Al4V, PLA coated Ti6Al4V with 5% (A), 10% (B), 15% (C), 20% (D), and 30% (E) PLA-Gm-(HAp-Gm) coated Ti6Al4V samples, separately

The unique GO biological processes for each PLA-Gm-(HAp-Gm) coated sample from the three-way Venn diagram in *Figure 3* were screened for at least three subjects. The subjects are cellular stress response, cellular growth, development, and differentiation. Finally, immune system regulations were used to determine the effects of Gm dosages on ADSCs. Therefore, the list of unique, relevant GO biological processes for all PLA-Gm-(HAp-Gm) coated samples (5-30% w/w) is given, separately in *Table 7.6***.**

In *Table 7.7*, some unique GO biological processes for the 5% PLA-Gm-(HAp-Gm) coated sample were illustrated with the number and group details of the identified proteins. In this sample, two antibiotic-related biological processes were identified, and they are antibiotic catabolic process, negative regulation of entry of bacterium into host cell. Additionally, the regulation of immune system processes can be seen in *Table 7.8*. Finally, the positive cell growth related GO biological process is an important point for the cell growth on this sample without the adverse effect of the Gm antibiotic due to its low concentration.

Table 7.8 shows the unique GO biological processes of the 10% PLA-Gm-(HAp-Gm) coated sample, including the number and group details of identified proteins. Although the 10% Gm sample has less identified proteins and GO biological processes, the antibiotic related one GO biological process, which is negative regulation of entry of bacterium into the host cell and the immune system response, was the same as the 5% Gm sample.

Many unique and osteogenesis-related GO biological processes with the specifically identified protein groups were determined from the 15% PLA-Gm-(HAp-Gm) coated sample (*Table 7.9*). Some of the biological processes are relevant to the regulation of osteoblast differentiation, cell proliferation, growth, and the positive regulation of immune system process and cell adhesion. The osteoblast differentiation, cell development, and bone development related GO biological processes were identified, and the stress related, biological process, negative regulation of binding, and bone resorption were found. In this case, they might be the Gm-dosage related adverse effects.

Table 7.9 represents the unique GO biological processes with the number and specific groups of the identified proteins for the 20% PLA-Gm-(HAp-Gm) coated sample. The 20% Gm contained sample has a relatively low number of GO biological processes according to the 5%, 10%, and 15% Gm samples. 20% PLA-Gm-(HAp-Gm) coated sample has bone development and cell population proliferation processes similar to the 15% Gm sample. Additionally, the skeletal system and skeletal muscle system related processes were also identified. The muscle system related processes might

refer to the early stage of osteogenesis activity. Therefore, the increased Gm dosage might cause a delay in the cell system as an adverse effect.

Finally, only one unique GO biological process was given for the 30% PLA-Gm-(HAp-Gm) coated sample in *Table 7.11*, which is related to cell death. The 30% Gm ratio has the highest antibiotic related adverse effect compared to other Gm ratios.

Table 7.6 Unique GO Biological Process in table from three-way Venn diagram for the unique PLA-Gm-(HAp-Gm) coated Ti6Al4V samples at predetermined Gm concentrations (5%-30% w\w) compared the Ti6Al4V and PLA coated Ti6Al4V samples with most pertinent roles in cellular changes, osteo-related development, adhesion and immune system regulation

5% PLA-Gm-(HAp-Gm)	10% PLA-Gm-(HAp-Gm)	15% PLA-Gm-(HAp-Gm)	20% PLA-Gm-(HAp-Gm)	30% PLA-Gm-(HAp-Gm)
• **Cell growth** • **Antibiotic catabolic process** • **Positive regulation of growth** • **Regulation of stress fiber assembly** • **Positive regulation of stress fiber assembly** • **Regulation of immune response** • **Regulation of growth** • **immune response-activating cell surface receptor signaling pathway** • **Skeletal muscle satellite cell migration** • **Negative regulation of entry of bacterium into host cell**	• Humoral immune response • Negative regulation of entry of bacterium into host cell • Skeletal muscle thin filament assembly	• Bone development • Regulation of stress fiber assembly • Cell population proliferation • Regulation of growth • Positive regulation of osteoblast differentiation • Cellular response to antibiotic • Bone remodeling • Positive regulation of cell adhesion • Positive regulation of immune system process • Negative regulation of binding • Regulation of osteoblast proliferation • Bone resorption	• Bone development • Striated muscle contraction • Skeletal muscle thin filament assembly • Cell population proliferation • Skeletal system development	• Programmed cell death

Table 7.7 The GO of proteins identified in biological processes with osteogenic associations with the identified protein groups across the unique 5% PLA-Gm-(HAp-Gm) coated Ti6Al4V dataset

Unique 5% PLA-Gm-(HAp-Gm)	Number of Identified proteins	False discovery rate	Proteins identified
Cell growth	13	2.30E-03	ALCAM,CTNNB1,CYFIP1,CYFIP2,DDX5,HSP90AA1,HSP90AB1,IQGAP1,ITGB1,MAP1B,PDLIM5,SLC3A2,VCL
Antibiotic catabolic process	7	1.52E-02	AKR1C3,ESD,HBA2,PRDX1,PRDX2,PRDX5,PRDX6
Positive regulation of growth	20	2.05E-02	BASP1,CDC42,CYFIP1,DDX39B,DDX3X,EIF4G1,EZR,FGF2,FN1,H3F3B,HIST1H1B,ILK,MACF1,MAP1B,PPIB,RAB11A,RHOA,RTN4,SFN,YBX3
Regulation of stress fiber assembly	7	3.05E-02	CDC42,CTGF,PFN2,RAC1,RHOA,RHOC,TPM1
Positive regulation of stress fiber assembly	9	3.05E-02	CDC42,CTGF,PFN1,PFN2,RAC1,RHOA,RHOC,STMN1,TPM1
Regulation of immune response	50	3.16E-02	A2M,ACTB,ACTG1,ACTR2,ACTR3,ANXA1,ARPC1B,ARPC2,ARPC3,ARPC4,ARPC5,B2M,BAX,CALM1,CALM3,CD59,CDC42,COL1A1,COL1A2,COL3A1,CYFIP1,CYFIP2,DHX9,EZR,FKBP1A,HMGB1,HSP90AA1,HSP90AB1,HSP90B1,HSPA1A,HSPA1B,HSPD1,ITGB1,KRT1,LTF,MATR3,MIF,MYO1C,NONO,PHB,RAC1,RAP1A,RBM14,RPS19,RPS3,SFPQ,STAT1,THY1,XRCC5,XRCC6
Regulation of growth	18	3.74E-02	ACTB,ACTG1,ACTR2,ACTR3,ARPC1B,ARPC2,ARPC3,ARPC4,ARPC5,BAX,CDC42,CYFIP1,CYFIP2,HSP90AA1,HSP90AB1,MYO1C,RAC1,THY1
Immune response-activating cell surface receptor signaling pathway	2	4.25E-02	RHOA,RHOC
Skeletal muscle satellite cell migration	20	3.22E-02	ACTB,ACTG1,ACTR2,ACTR3,ARPC1B,ARPC2,ARPC3,ARPC4,ARPC5,BAX,CALM1,CALM3,CDC42,CYFIP1,CYFIP2,HSP90AA1,HSP90AB1,MYO1C,RAC1,THY1
Negative regulation of entry of bacterium into host cell	2	4.25E-02	ITGAV,KRT6A

Table 7.8 The GO of proteins identified in biological processes with osteogenic associations with the identified protein groups across the unique 10% PLA-Gm-(HAp-Gm) coated Ti6Al4V dataset

Unique 10% PLA-Gm-(HAp-Gm)	Number of Identified proteins	False discovery rate	Proteins identified
Negative regulation of entry of bacterium into host cell	2	1.38E-02	ITGAV,KRT6A
Humoral immune response	11	4.12E-02	BST1,FAU,GAPDH,H2BFS,HIST1H2BC,HIST1H2BK,HIST2H2BE,HMGN2,KRT1,KRT6A,RPS19
Skeletal muscle thin filament assembly	2	4.51E-02	ACTA1,ACTC1

Table 7.9 The GO of proteins identified in biological processes with osteogenic associations with the identified protein groups across the unique 15% PLA-Gm-(HAp-Gm) coated Ti6Al4V dataset

Unique 15% PLA-Gm-(HAp-Gm)	Number of Identified proteins	False discovery rate	Proteins identified
Cell population proliferation	23	1.86E-02	CDV3,CTNNB1,EEF2,FGF2,FSCN1,GNAI2,GNAT1,H3F3A,H3F3B,IGFBP3,ILK,LRP1,MIF,MYH10,PA2G4,PCNA,PRDX1,RAB10,RAC1,RAP1B,SBDS,UCHL1,XRCC5
Regulation of stress fiber assembly	6	2.24E-02	CDC42,PFN1,RAC1,RHOA,STMN1,TPM1
Bone development	9	2.33E-02	AKAP13,AMER1,ANXA2,ENG,GNAS,LTF,PPIB,RHOA,SBDS
Regulation of growth	22	2.72E-02	CDC42,CRYAB,ENO1,ENPP1,FGF2,FN1,GNAS,GNB2L1,H3F3A,H3F3B,IGFBP3,ILK,MAP1B,PHB,PML,PPIB,PRAME,RAB11A,RHOA,SOD1,TKT,WISP3
Positive regulation of osteoblast differentiation	5	2.89E-02	CTHRC1,CTNNB1,GNAS,ILK,LTF
Cellular response to antibiotic	7	2.90E-02	ANXA1,GNAI1,HNRNPA1,HSPA5,NQO1,PCNA,RPL23
Bone remodelling	4	3.85E-02	CTHRC1,CTNNB1,RAC1,TPP1
Positive regulation of cell adhesion	14	4.38E-02	ANXA1,ARPC2,CALR,CCL21,CD44,CDC42,FLNA,FN1,ILK,RAC1,RAC3,RHOA,TGM2,TPM1
Positive regulation of immune	26	4.58E-02	ACTB,ACTG1,ANXA1,ARPC2,ARPC4,B2M,CALR,CCL21,CDC42,GNAS,GPI,KRT1,L

system process			TF,MIF,MSH2,MYO1C,NONO,PGLYRP2,PHB,RAC1,RAP1A,RBM14,RHOA,SFPQ,THBS1,XRCC5
Negative regulation of binding	8	4.83E-02	ACTB,B2M,CRMP1,HSPA5,PPP1CA,RALB,SRI,STMN1
Regulation of osteoblast Proliferation	3	4.99E-02	CTHRC1,LTF,RHOA
Bone resorption	3	4.99E-02	CTNNB1,RAC1,TPP1

Table 7.10 The GO of proteins identified in biological processes with osteogenic associations with the identified protein groups across the unique 20% PLA-Gm-(HAp-Gm) coated Ti6Al4V dataset

Unique 20% PLA-Gm-(HAp-Gm)	Number of Identified proteins	False discovery rate	Proteins identified
Cell population proliferation	15	3.17E-02	EEF2,FSCN1,GNAI2,GNAT1,H3F3A,H3F3B,IGFBP3,MIF,PRDX1,RAB10,RAC1,RPS6,SBDS,TGFBI,UCHL1
Bone development	8	4.80E-03	AKAP13,AMER1,ANXA2,ENG,GNAS,PPIB,SBDS,SERPINH1
Skeletal system development	11	4.87E-02	AKAP13,AMER1,ANXA2,CD44,ENG,GNAS,PPIB,PRDX1,SBDS,SERPINH1,TGFBI
Striated muscle contraction	6	1.12E-02	ACTC1,ALDOA,EEF2,PKP2,TNNC2,TPM1
Skeletal muscle thin filament assembly	2	2.03E-02	ACTA1,ACTC1

Table 7.11 The GO of proteins identified in biological processes with osteogenic associations with the identified protein groups across the unique 30% PLA-Gm-(HAp-Gm) coated Ti6Al4V dataset

Unique 30% PLA-Gm-(HAp-Gm)	Number of Identified proteins	False discovery rate	Proteins identified
Programmed cell death	7	2.72E-02	KRT18,KRT36,KRT37,KRT38,PKM,SCN2A,SLC25A4

The five-way Venn diagram in *Figure 7.14* shows the unique proteins of the PLA-Gm-HAp-Gm coated Ti6Al4V samples at the predetemined Gm concentrations (5%-30% w/w) after taking out the shared proteins of the Ti6Al4V and PLA coated Ti6Al4V samples. When the shared proteins of the Ti6Al4V and PLA coated Ti6Al4V with the PLA-Gm-(HAp-Gm) coated Ti6Al4V samples were separated, the unique identifed proteins were obtained easily; 433 proteins for the 5% PLA-Gm-(HAp-Gm), 34 proteins for the 10% PLA-Gm-(HAp-Gm), 80 proteins for the 15% PLA-Gm-(HAp-Gm), 46 proteins for the 20% PLA-Gm-(HAp-Gm), and 13 proteins for the 30% PLA-Gm-(HAp-Gm) coated Ti6Al4V sample.

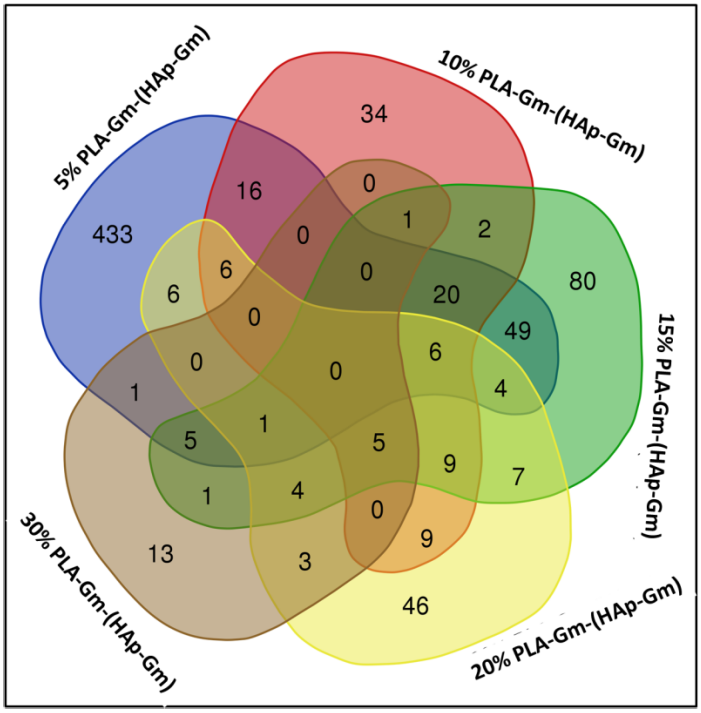

Figure 7.14 five-way Venn diagram illustrates the only unique identified protein numbers for 5% (A), 10% (B), 15% (C), 20% (D), and 30% (E) PLA-Gm-(HAp-Gm) coated Ti6Al4V samples, separately

According to identified unique proteins of the Venn diagram in *Figure 7.14*, the protein interaction networks for the 10%, 15%, 20%, and 30% PLA-Gm-(HAp-Gm) coated Ti6Al4V samples were given on the 5% PLA-Gm-(HAp-Gm) coated Ti6Al4V sample in *Figure 7.15*. The interaction network analysis (*Figure 7.15*) uses the Cytoscape overlays, and post color-coding for unique and shared proteins of the PLA-Gm-(HAp-Gm) coated Ti6Al4V samples. The network was completed in order to locate the interaction hubs between each sample and to visualize the protein pathways with different colors. In the interaction network, the nodes are Blue – unique 5%, Red – unique 10%, Green – unique 15%, Purple – unique 20%, Orange – unique 30% PLA-Gm-(HAp-Gm) coated Ti6Al4V samples, Yellow – shared Ti6Al4V and PLA coated Ti6Al4V, Grey – shared proteins for all.

The individual unique proteins were searched and showed as an interaction network (*Figure 7.15*) for the PLA-Gm-(HAp-Gm) coated Ti6Al4V (5% to 30%),and the shared Ti6Al4V-PLA coated Ti6Al4V samples. The unique proteins are relevant to osteogenesis development, cell adhesion and immune responses for PLA-Gm-(HAp-Gm) coated Ti6Al4V (5% to 30%) were given in separate tables for each sample with their descriptions, which were collected from UniProt (https://www.uniprot.org/) database. The unique proteins for the 5% Gm contained sample were represented in *Table 7.12.*

Fibroblast growth factor 2 (FGF2) is one of the unique proteins that were identified in the 5% Gm sample. The differentiation of stem cells occurred due to extracellular factors by stimulation of the outside signals, rather than genetic manipulation. One of the best growth factors for maintaining differentiation and self-renewal of the stem cells is FGF (Fibroblast growth factor) (Nusse, 2008). FGF2, which is one of the most common FGF ligands used in regenerative medicine, plays a critical role in bone development, organ regeneration, fracture and wound healing (Coffin et al., 2018, Ma et al., 2019). Additionally, it promotes the proliferation, survival, and osteogenic differentiation of adipose-derived stem cells. FGF2 secretion regulation is another key point for controlling spontaneous differentiation (Charoenlarp et al., 2017).

FGF has interaction with the intracellular signaling pathways, including RAS-MAPK, and it modulates the Wnt signaling pathway. The activation of FGF receptor phosphorylates the adaptor proteins for some major intracellular signaling pathways such as RAS-MAPK and signal transducer and activator of transcription (STAT). FGF2 promotes bone formation and osteoblast differentiation via the modulation of the Wnt signaling pathway (Fei et al., 2011, Ornitz et al., 2015).

One of the unique proteins is called Lactotransferrin (LTF), which is a multifunctional protein. LTF has several functions, such as the protection against microbial infections, the systemic immune response, positive regulation of bone maturation and osteoblast differentiation, and finally, regulation of iron absorption in intestines (Conneely, 2013, Ying et al., 2012). LTF is one of the key components of the immune system. Additionally, due to its ability to bind with iron, the LTF protein shows the antimicrobial activity. Jahani et al. (2015) conducted an experiment with gram-positive (*Staphylococcus epidermidis*, *Bacillus cereus*) and gram-negative (*Campylobacter jejuni*, *Salmonella species*) bacteria with pure LTF protein to determine its antibacterial activity. They reported that LFT decreased bacterial growth, and noticeable antibacterial activity of LFT was observed.

The 26S proteasome non-ATPase regulatory subunit 2 (PSMD2) is the main component of the ubiquitin-proteasome system (UPS). UPS is responsible for the degradation of cellular proteins to regulate cell protein quality, development, differentiation, proliferation, cell cycling, apoptosis, gene

transcription, signal transduction, senescence, antigen presentation, inflammation, and stress response. It has a crucial role in removing oxidative or cellular stressed cells that can cause accumulation of the toxic proteins. The expression of the PSMD2 protein is an essential multifunctional regulatory protein (Naujokat et al., 2007, Lee et al., 2014).

The unique proteins for the 10% Gm sample were represented in *Table 7.13*. 26S proteasome non-ATPase regulatory subunit 2 (PSMD2) was observed in ADSCs, which were seeded on the 10% Gm samples. It was identified in the 5% Gm sample as well. It is a crucial protein for preventing the accumulation of toxic or damaged proteins in the cell metabolism. Another important protein in this sample is the 14-3-3 protein/Tyrosine 3-Monooxygenase/Tryptophan 5-Monooxygenase Activation Protein Epsilon (YWHAE). It regulates many pathways related to cellular functions such as cell cycle, cell motility, and apoptosis. YWHAE also has a role in interacting with the stress adaptive signaling pathway. The YWHAE protein interacts with the insuline/glucose signaling pathway, responsible for the cell growth, anabolic metabolism, and inhibition of apoptosis. This pathway causes the interaction between YWEHAE and Ca2+/Calmodulindependent kinase-II (CAMKII) to inhibit apoptotic signals. In this sample, both proteins YWEHAE and CALML3 (Calmodulin-like protein 3) were identified (Fu et al., 2000, Pennington et al., 2018).

The unique proteins in the 15% Gm sample were represented in *Table 7.14*. Like ADSCs seeded on the 5% Gm sample, FGF2, and LTF proteins were identified in the 15% Gm sample. FGF2 plays a key role in bone development, osteogenic differentiation, and cell proliferation due to Wnt signaling pathway modulation. Additionally, the LFT protein has antimicrobial activity, which can be related to the Gm antibiotic in the system. It also promotes osteogenic differentiation.

The Thymosin beta-4 TMSB4X protein was also identified. It plays a role in regulating the immune response. It promotes cell migration, differentiation of stem cells, and tissue regeneration (Goldstein et al., 2012).

The unique proteins for the 20% Gm sample were represented in *Table 7.15*. The Troponin C, skeletal muscle (TNNC2) gene is expressed in fast skeletal troponin C (type II) for the skeletal muscle development. It has high calcium-binding affinity; therefore, intracellular Ca+2 concentrations are effective on the TNNC2 functional activities. Its function is to regulate the Ca+2 dependent striated muscle contraction (Li et al., 2015). The skeletal muscle development-related proteins were identified in the 20% Gm samples, which is different from the identified bone development related proteins in the 5%, 10%, and 15% Gm samples.

C-C motif chemokine 21 (CCL21) belongs to the CCL chemokines group. They act as mediators of leukocyte migration during the immune response. CCL21 plays an important role in the regulation of chemotaxis, which is cell migration in response to a chemical stimulus for the stem cells (Yao et al., 2004, Hocking, 2015).

The unique proteins for the 30% Gm sample were represented in *Table 7.16*. The TNNC2 skeletal muscle protein and CCL21 chemokine were identified in the 30% Gm sample. Those proteins were also found in the 20% Gm sample. The skeletal muscle system-related proteins were other similarities that were found for the 20%, and 30% Gm samples.

Lactotransferrin LTF was identified in the 30% Gm sample, showing antimicrobial activity. This may be related to a high Gm antibiotic concentration in the system. Additionally, it promotes osteogenic differentiation.

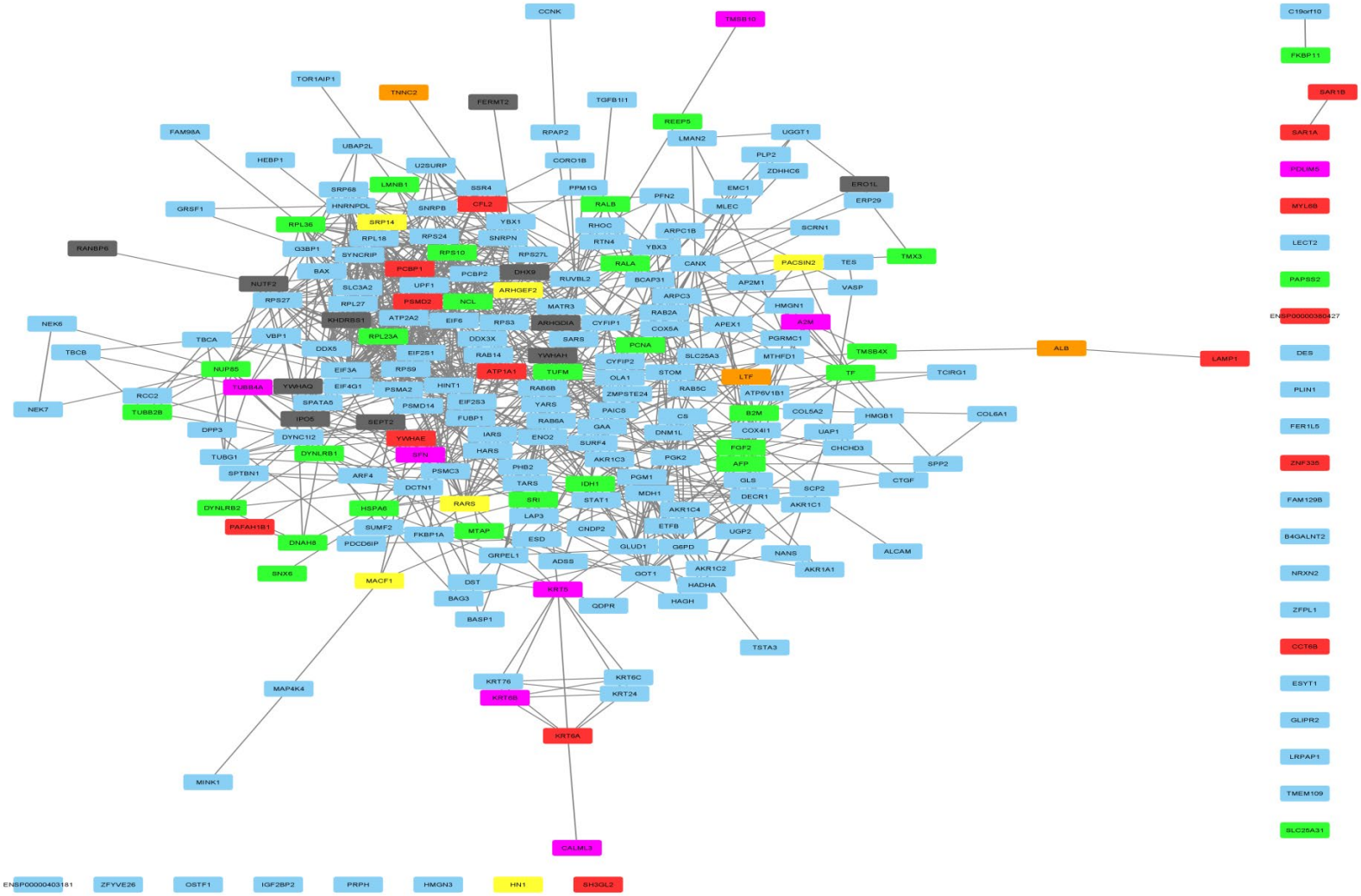

Figure 7.15 Cytoscape protein interaction network graph of proteins identified by mass spectrometry. Blue – unique 5%, Red – unique 10%, Green – unique 15%, Purple – unique 20% , Orange – unique 30% PLA-Gm-(HAp-Gm) coated Ti6Al4V samples, Yellow – shared Ti6Al4V and PLA coated Ti6Al4V, Grey – shared proteins for all

Table 7.12 The highest number of associated biological process and strongest relevance to osteogenic differentiation and development for unique 5% PLA-Gm-(HAp-Gm) coated Ti6Al4V samples

Name	Accession Number	Gene	GO Biological Process
Fibroblast growth factor 2	P09038	FGF2	Activation of MAPK activity, positive regulation of cell population proliferation
Lactotransferrin	P02788	LTF	Positive regulation of bone mineralization involved in bone maturation, positive regulation of osteoblast differentiation, positive regulation of osteoblast, antibacterial humoral response, antimicrobial humoral immune response mediated by antimicrobial peptide, bone morphogenesis proliferation
14-3-3 protein sigma	P31947	SFN	Positive regulation of cell growth, regulation of cyclin-dependent protein serine/threonine kinase activity, signal transduction
Signal transducer and activator of transcription 1-alpha/beta	P42224	STAT-1	cytokine-mediated signaling pathway, positive regulation of mesenchymal cell proliferation, positive regulation of smooth muscle cell proliferation, regulation of cell population proliferation
26S proteasome non-ATPase regulatory subunit 2	Q13200	PSMD2	MAPK cascade, positive regulation of canonical Wnt signaling pathway, Wnt signaling pathway, planar cell polarity pathway, regulation of hematopoietic stem cell differentiation
Microtubule-actin cross-linking factor 1, isoforms 1/2/3/5	Q9UPN3	MACF1	positive regulation of Wnt signaling pathway, regulation of cell migration, regulation of focal adhesion assembly, wound healing
PDZ and LIM domain protein 7	Q9NR12	PDLIM7	muscle structure development, ossification, positive regulation of osteoblast differentiation

Table 7.13 The highest number of associated biological process and strongest relevance to osteogenic differentiation and development for unique 10% PLA-Gm-(HAp-Gm) coated Ti6Al4V samples

Name	Accession Number	Gene	GO Biological Process
Calmodulin-like protein 3	P27482	CALML3	Calcium-mediated signaling, microtubule cytoskeleton organization
Keratin, type II cytoskeletal 6A	P02538	KRT6A	Antimicrobial humoral immune response mediated by antimicrobial peptide, cell differentiation, cornification, defense response to Gram-positive bacterium, positive regulation of cell population proliferation
14-3-3 protein epsilon	P62258	YWHAE	Intracellular signal transduction, MAPK cascade, membrane organization

Troponin C, skeletal muscle	P02585	TNNC2	Muscle filament sliding, regulation of muscle contraction, skeletal muscle contraction
26S proteasome non-ATPase regulatory subunit 2	Q13200	PSMD2	Wnt signaling pathway, planar cell polarity pathway, positive regulation of canonical Wnt signaling pathway, MAPK cascade
14-3-3 protein sigma	P31947	SFN	Positive regulation of cell growth, regulation of cyclin-dependent protein serine/threonine kinase activity, signal transduction

Table 7.14 The highest number of associated biological process and strongest relevance to osteogenic differentiation and development for unique 15% PLA-Gm-(HAp-Gm) coated Ti6Al4V samples

Name	Accession Number	Gene	GO Biological Process
116 kDa U5 small nuclear ribonucleoprotein component	Q15029	EFTUD2	Cellular response to drug
Lamin-B1	P20700	LMNB1	Interleukin-12-mediated signaling pathway
Lactotransferrin	P02788	LTF	Positive regulation of bone mineralization involved in bone maturation, positive regulation of osteoblast differentiation, positive regulation of osteoblast, antibacterial humoral response, antimicrobial humoral immune response mediated by antimicrobial peptide, bone morphogenesis proliferation
C-C motif chemokine 21	O00585	CCL21	Antimicrobial humoral immune response mediated by antimicrobial peptide, cell-cell signaling, cell maturation, cellular response to chemokine, positive regulation of cell-matrix adhesion
Beta-2-microglobulin	P61769	B2M	Antibacterial humoral response, defense response to Gram-negative bacterium, defense response to Gram-positive bacterium Source, innate immune response
Thymosin beta-4	P62328	TMSB4X	Negative regulation of interleukin-8 secretion, regulation of cell migration, regulation of inflammatory response
Fibroblast growth factor 2	P09038	FGF2	Activation of MAPK activity, positive regulation of cell population proliferation
14-3-3 protein sigma	P31947	SFN	Positive regulation of cell growth, regulation of cyclin-dependent protein serine/threonine kinase activity, signal transduction

Table 7.15 The highest number of associated biological process and strongest relevance to osteogenic differentiation and development for unique 20% PLA-Gm-(HAp-Gm) coated Ti6Al4V samples

Name	Accession Number	Gene	GO Biological Process
14-3-3 protein sigma	P31947	SFN	Positive regulation of cell growth, regulation of cyclin-dependent protein serine/threonine kinase activity, signal transduction
Troponin C, skeletal muscle	P02585	TNNC2	Muscle filament sliding, regulation of muscle contraction, skeletal muscle contraction
C-C motif chemokine 21	O00585	CCL21	Antimicrobial humoral immune response mediated by antimicrobial peptide, cell-cell signaling, cell maturation, cellular response to chemokine, positive regulation of cell-matrix adhesion
Calmodulin-like protein 3	P27482	CALML3	Calcium-mediated signaling, microtubule cytoskeleton organization
PDZ and LIM domain protein 5	Q96HC4	PDLIM5	Muscle structure development, actin cytoskeleton organization

Table 7.16 The highest number of associated biological process and strongest relevance to osteogenic differentiation and development for unique 30% PLA-Gm-(HAp-Gm) coated Ti6Al4V samples

Name	Accession Number	Gene	GO Biological Process
Troponin C, skeletal muscle	P02585	TNNC2	Muscle filament sliding, regulation of muscle contraction, skeletal muscle contraction
Actin, aortic smooth muscle	P62736	ACTA2	Muscle contraction, vascular smooth muscle contraction
Actin, gamma-enteric smooth muscle	P63267	ACTG2	Muscle contraction, positive regulation of gene expression
C-C motif chemokine 21	O00585	CCL21	Antimicrobial humoral immune response mediated by antimicrobial peptide, cell-cell signaling, cell maturation, cellular response to chemokine, positive regulation of cell-matrix adhesion
Lactotransferrin	P02788	LTF	Positive regulation of bone mineralization involved in bone maturation, positive regulation of osteoblast differentiation, positive regulation of osteoblast, antibacterial humoral response, antimicrobial humoral immune response mediated by antimicrobial peptide, bone morphogenesis proliferation

7.3.5.3 Mass Spectroscopy Protein Data from ADSCs on the untreated and thermally anodized Ti6Al4V discs

The effects of the thermal anodization process of the Ti6Al4V implant discs on the whole proteome of ADSCs were analyzed by mass spectroscopy with three biological triplicates of anodized and untreated Ti6Al4V discs. The mass spectrometry data was acquired, at the 95% confidence cut-off, a total of 893 proteins for ADSCs on the A-Ti6Al4V sample and a total of 783 proteins for ADSCs on the Ti6Al4V sample were found. The total identified protein numbers for the A-Ti6Al4V and Ti6Al4V samples are given in a Venn diagram (*Figure 7.16*). According to the Venn diagram, the unique A-Ti6Al4V protein numbers are 225, and the unique Ti6Al4V protein numbers are 115, while the shared proteins for the A-Ti6Al4V and Ti6Al4V samples were found to be 668.

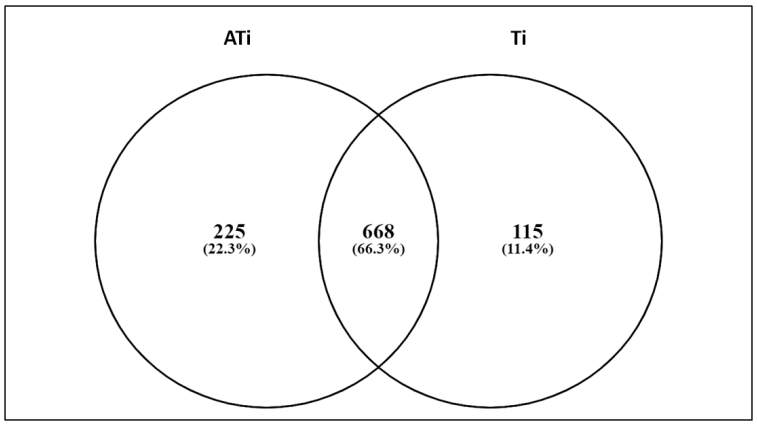

Figure 7.16 two-way Venn diagram illustrates the protein numbers for unique Anodized Ti6Al4V (A-Ti6Al4V), unique untreated Ti6AlV and shared proteins for A-Ti6Al4V and Ti6Al4V

The ten unique biological processes were categorized from the unique A-Ti6Al4V identified proteins. The obtained parental biological categories for the A-Ti6Al4V sample were directly related to bone and skeletal system development, the regulations of osteoblast development, and proliferation, and finally the antimicrobial response by antimicrobial peptides with immunological response (shown in *Figure 7.17*) with the observed protein numbers.

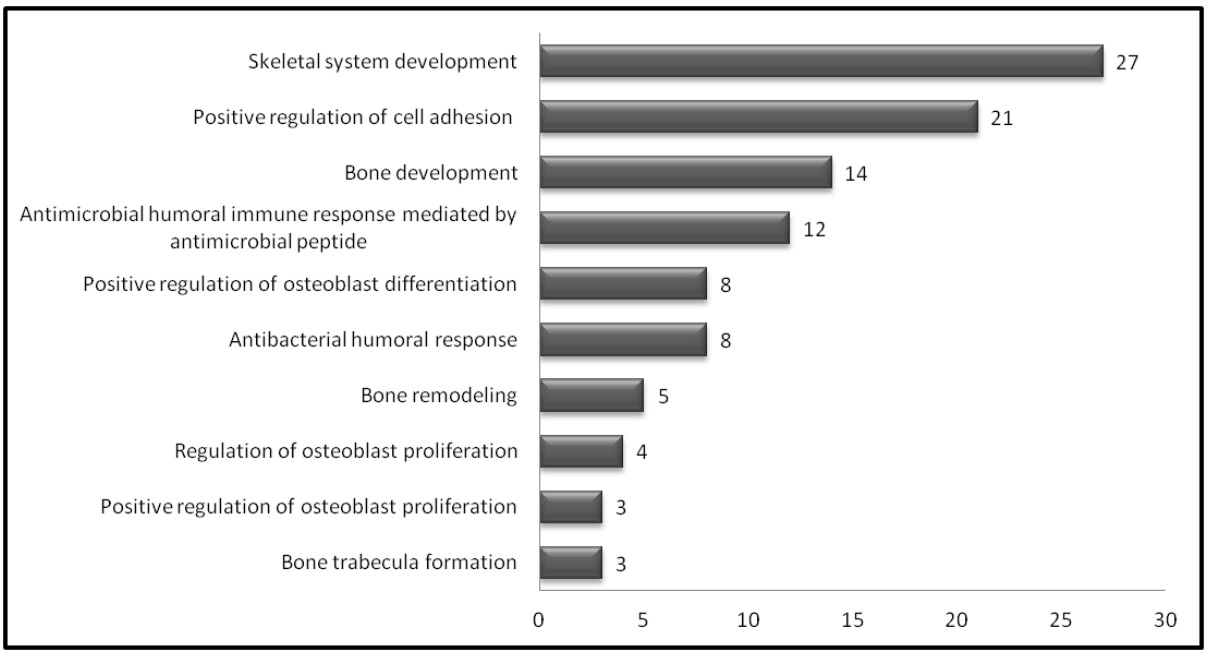

Figure 7.17 The graphs show the refined number ontologies of proteins identified with direct roles in a osteogenic biological process for unique A-Ti6Al4V sample and (B) the shared of Anodized and untreated Ti6Al4V samples

The unique GO biological processes for the A-Ti6Al4V sample from the two-way Venn diagram in *Figure 7.16* have screened at least four subjects: osteogenesis related systems, cell development, immunological response, and antimicrobial activities and differentiation to determine the effects of the thermally anodized Ti6Al4V disc surface on ADSCs. The Wnt signaling pathway-related GO biological processes especially non-canonical Wnt signaling pathway regulations and positive regulation of cell differentiation processes were identified in the ADSCs harvested from the Ti6Al4V surface without any treatment. The positive differentiation effect of the Ti6Al4V alloy was found on human ADSCs. However, this section of our research focuses on the effect of the thermally anodized layer on Ti6Al4V, which was analyzed based on its mechanical properties in **Chapter 5**.

In *Table 7.17*, the unique GO biological processes for A-Ti6Al4V were listed with the number and specific groups of identified proteins. In this sample, the unique GO biological processes can be separated into two main groups: osteogenic differentiation and antimicrobial response. The positive regulation of the osteoblast differentiation process with the canonical Wnt signaling pathway (directly related to osteoblast maturation and bone formation) were found.

While the individual unique proteins were searched, the unique A-Ti6Al4V proteins (given in *Table 7.18*) with their descriptions were collected from the UniProt (https://www.uniprot.org/) database.

All unique proteins from *Table 7.18* were used to create the network map in *Figure 7.18*, which shows the interactions between the unique A-Ti6Al4V proteins.

FGF2 was identified uniquely as a crucial growth factor in the A-Ti6Al4V dataset. Its functions are bone development, organ regeneration, and fracture/wound healing. It controls the stem cell differentiation to inhibit spontaneous cell differentiation due to its modulation function for the Wnt signaling pathway. Uncontrolled stem differentiation might cause tumor development.

One of the unique proteins is LFT, which is a multifunctional protein. Some functions of the LFT protein are the protection against microbial infections, its antimicrobial response, the systemic immune response, positive regulation of bone maturation and osteoblast differentiation, and finally, regulation of iron absorption in intestines (Conneely et al., 2013, Ying et al., 2012).

Fibrillin-1 is a large calcium binding glycoprotein that is located in the extracellular matrix. It supplies the structural signals and provides the positional information to the surrounding cells. A significant functional relationship exists between fibrillin-1 and TGFβ activity (Handford, 2000, Ramirez et al., 2004).

According to identified unique and special proteins for A-Ti6Al4V in *Table 7.18*, the Cytoscape protein interaction network (*Figure 7.18*) was prepared. The key proteins that interact with the Wnt signaling pathway, osteoblast differentiation, cell proliferation, bone development, antimicrobial and antibacterial responses, were highlighted on the interaction network. Finally, the important bone differentiation-related proteins are given in *Table 7.19* for the shared proteins relevant to cell proliferation, morphogenesis, and differentiation. *Figure 7.19* shows the Cytoscape protein interaction network for unique A-Ti6Al4V (orange), unique Ti6Al4V (blue), and shared proteins (green). In the interaction network, one big and a few small protein clusters were obtained. The middle protein for the big cluster is the CTNNB1 shared protein. It is a key component of the canonical Wnt signaling pathway as a coactivator. It regulates cell proliferation, differentiation, and cell morphogenesis. CTNNB1 protein was found for the Ti6Al4V, A-Ti6Al4V, and PLA coated Ti6Al4V samples.

Table 7.17 The GO of proteins identified in biological processes with osteogenic associations with the identified protein groups across the unique A-Ti6Al4V

Term description	Number of Identified proteins	Background gene count	False discovery rate	Proteins identified
Positive regulation of osteoblast differentiation	8	58	0.0041	CLIC1,CTHRC1,CTNNB1,FBN2,GNAS,ILK,LTF,PDLIM7
Skeletal system development	27	457	0.0043	ACP2,AKAP13,ANXA2,CD44,COL12A1,COL1A1,COL1A2,CTNNB1,ENG,FBN1,FBN2,FGF2,GNAS,LEPRE1,LTF,LUM,MAPK3,PAPSS2,PLS3,PPIB,PRDX1,RHOA,SBDS,SERPINH1,SPP2,TGFBI,THBS3
Bone trabecula formation	3	8	0.0198	COL1A1,FBN2,THBS3
Regulation of osteoblast proliferation	4	23	0.0353	CTHRC1,ITGAV,LTF,RHOA
Positive regulation of osteoblast proliferation	3	11	0.0353	CTHRC1,ITGAV,LTF
Bone remodeling	5	40	0.0418	CTHRC1,CTNNB1,RAC1,SPP2,TPP1
Antimicrobial humoral immune response mediated by antimicrobial peptide	12	107	0.0012	B2M,FAU,GAPDH,H2BFS,HIST1H2BC,HIST1H2BJ,HIST1H2BK,HIST2H2BE,HMGN2,LTF,RPL30,RPS19
Antibacterial humoral response	8	47	0.0013	B2M,FAU,H2BFS,HIST1H2BC,HIST1H2BJ,HIST1H2BK,HIST2H2BE,LTF
Bone development	14	166	0.0045	AKAP13,ANXA2,COL1A1,ENG,GNAS,LEPRE1,LTF,PAPSS2,PLS3,PPIB,RHOA,SBDS,SERPINH1,THBS3
Positive regulation of cell adhesion	21	375	0.0229	ANXA1,ARPC2,CALR,CCDC80,CD44,CDC42,DNM2,FLNA,FN1,HSPD1,ILK,IQGAP1,ITGAV,LGALS1,RAC1,RAC3,RHOA,RPS3,TGM2,THY1,TPM1

Table 7.18 The highest number of associated biological process and strongest relevance to osteogenic differentiation and development for the unique A-Ti6Al4V proteins (individual identified proteins)

Name	Accession Number	Gene	GO Biological Process
Lactotransferrin	P02788	LTF	Positive regulation of bone mineralization involved in bone maturation, positive regulation of osteoblast differentiation, positive regulation of osteoblast, antibacterial humoral response, antimicrobial humoral immune response mediated by antimicrobial peptide, bone morphogenesis proliferation
Fibroblast growth factor 2	P09038	FGF2	Positive regulation of cell population proliferation, stem cell proliferation, activation of MAPK activity
Fibrillin-1	P35555	FBN1	Skeletal system development, negative regulation of osteoclast differentiation,
Fibrillin-2	P35556	FBN2	Bone trabecula formation, positive regulation of bone mineralization, positive regulation of osteoblast differentiation, extracellular matrix organization
Mitogen-activated protein kinase 3	P27361	MAPK3	BMP signaling pathway, interleukin-1-mediated signaling pathway, positive regulation of cytokine secretion involved in immune response, regulation of ossification
Bifunctional 3'-phosphoadenosine 5'-phosphosulfate synthase 2	O95340	PAPSS2	Bone development, skeletal system development
Ras-related C3 botulinum toxin substrate 3	P60763	RAC3	Wnt signaling pathway, positive regulation of cell adhesion mediated by integrin, positive regulation of substrate adhesion-dependent cell spreading, regulation of cell shape, actin cytoskeleton organization, Rho protein signal transduction
Thrombospondin-3	P49746	THBS3	bone trabecula formation, cell-matrix adhesion, ossification involved in bone maturation
Beta-2-microglobulin	P61769	B2M	Antibacterial humoral response, antimicrobial humoral immune response mediated by antimicrobial peptide, defense response to Gram-negative bacterium, defense response to Gram-positive bacterium, regulation of immune response
Semenogelin-1	P04279	SEMG1	Antibacterial humoral response, antimicrobial humoral immune response mediated by antimicrobial peptide, antimicrobial humoral response
60S ribosomal protein L30	P62888	RPL30	Antimicrobial humoral immune response mediated by antimicrobial peptide,
Calcium/calmodulin-dependent protein kinase type II subunit delta	Q13557	CAMK2D	Cellular response to calcium ion, regulation of cell growth, regulation of cellular localization

A-kinase anchor protein 13	Q12802	AKAP13	Bone development
ATP-dependent RNA helicase DDX3X	O00571	DDX3X	Cell differentiation, positive regulation of canonical Wnt signaling pathway, positive regulation of cell growth, Wnt signaling pathway
Chloride intracellular channel protein 4	Q9Y696	CLIC4	Cell differentiation, cellular response to calcium ion, regulation of cytoskeleton organization, regulation of ion transmembrane transport
Integrin beta-5	P18084	ITGB5	Cell adhesion mediated by integrin, cell-matrix adhesion, transforming growth factor beta receptor signaling pathway

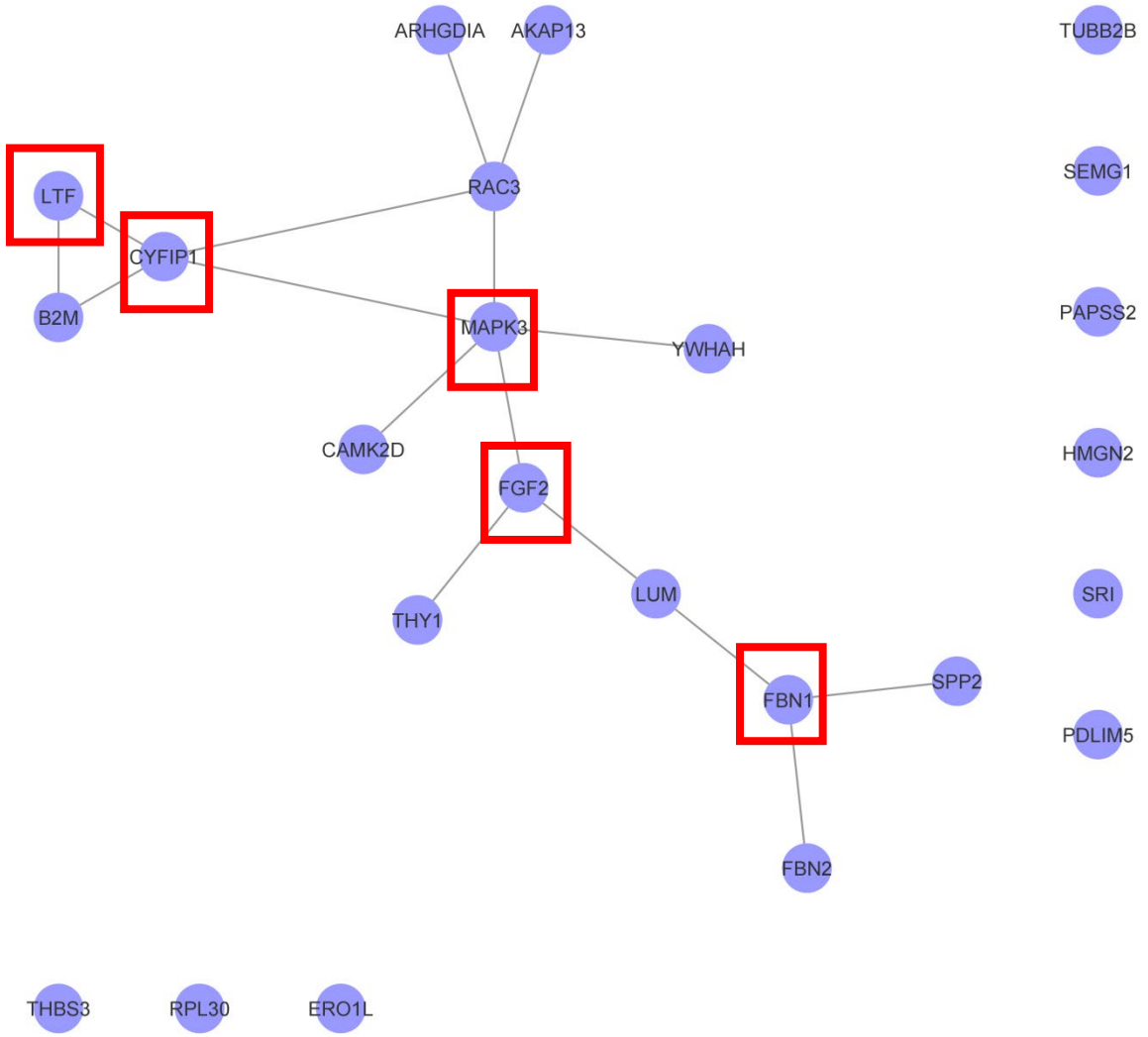

Figure 7.18 Cytoscape protein interaction network graph of the unique A-Ti6Al4V proteins relevant to osteogenesis development and antimicrobial activities were identified by mass spectrometry

Table 7.19 The highest number of associated biological process and strongest relevance to osteogenic differentiation and development for shared A-Ti6Al4V and Ti6Al4V proteins (individual identified proteins)

Name	Accession Number	Gene	GO Biological Process
Chloride intracellular channel protein 1	O00299	CLIC1	Chloride transport, positive regulation of osteoblast differentiation, regulation of cell cycle, regulation of ion transmembrane transport
Collagen triple helix repeat-containing protein 1	Q96CG8	CTHRC1	Ossification involved in bone remodeling, positive regulation of osteoblast differentiation, positive regulation of osteoblast proliferation, positive regulation of protein binding Source, Wnt signaling pathway, planar cell polarity pathway
Catenin beta-1	P35222	CTNNB1	Bone resorption, Wnt signaling pathway, regulation of canonical Wnt signaling pathway, cell morphogenesis involved in differentiation, positive regulation of osteoblast differentiation, positive regulation of skeletal muscle tissue development, stem cell population maintenance,
Integrin-linked protein kinase	Q13418	ILK	Positive regulation of BMP signaling pathway, positive regulation of canonical Wnt signaling pathway, positive regulation of cell-matrix adhesion, positive regulation of osteoblast differentiation
Integrin alpha-V	P06756	ITGAV	Positive regulation of cell adhesion, positive regulation of cell population proliferation, positive regulation of cytosolic calcium ion concentration, positive regulation of osteoblast proliferation, substrate adhesion-dependent cell spreading
Transforming protein RhoA	P61586	RHOA	Cell-matrix adhesion, positive regulation of cell growth, regulation of osteoblast proliferation, Wnt signaling pathway, planar cell polarity pathway
Ras-related C3 botulinum toxin substrate 1	P63000	RAC1	Positive regulation of substrate adhesion-dependent cell spreading, Wnt signaling pathway, planar cell polarity pathway, bone resorption, cell adhesion, cell-matrix adhesion
Collagen alpha-1(I) chain	P02452	COL1A1	Bone trabecula formation, osteoblast differentiation, positive regulation of canonical Wnt signaling pathway,
Annexin A2	P07355	ANXA2	interleukin-12-mediated signaling pathway,
CD44 antigen	P16070	CD44	Cell adhesion, cell-cell adhesion, cell-matrix adhesion, inflammatory response, wound healing, spreading of cells
Collagen alpha-2(I) chain	P08123	COL1A2	Bone mineralization, skeletal system development, regulation of immune response
Endoglin	P17813	ENG	Positive regulation of BMP signaling pathway, bone development, cell adhesion, regulation of cell adhesion, regulation of cell population proliferation

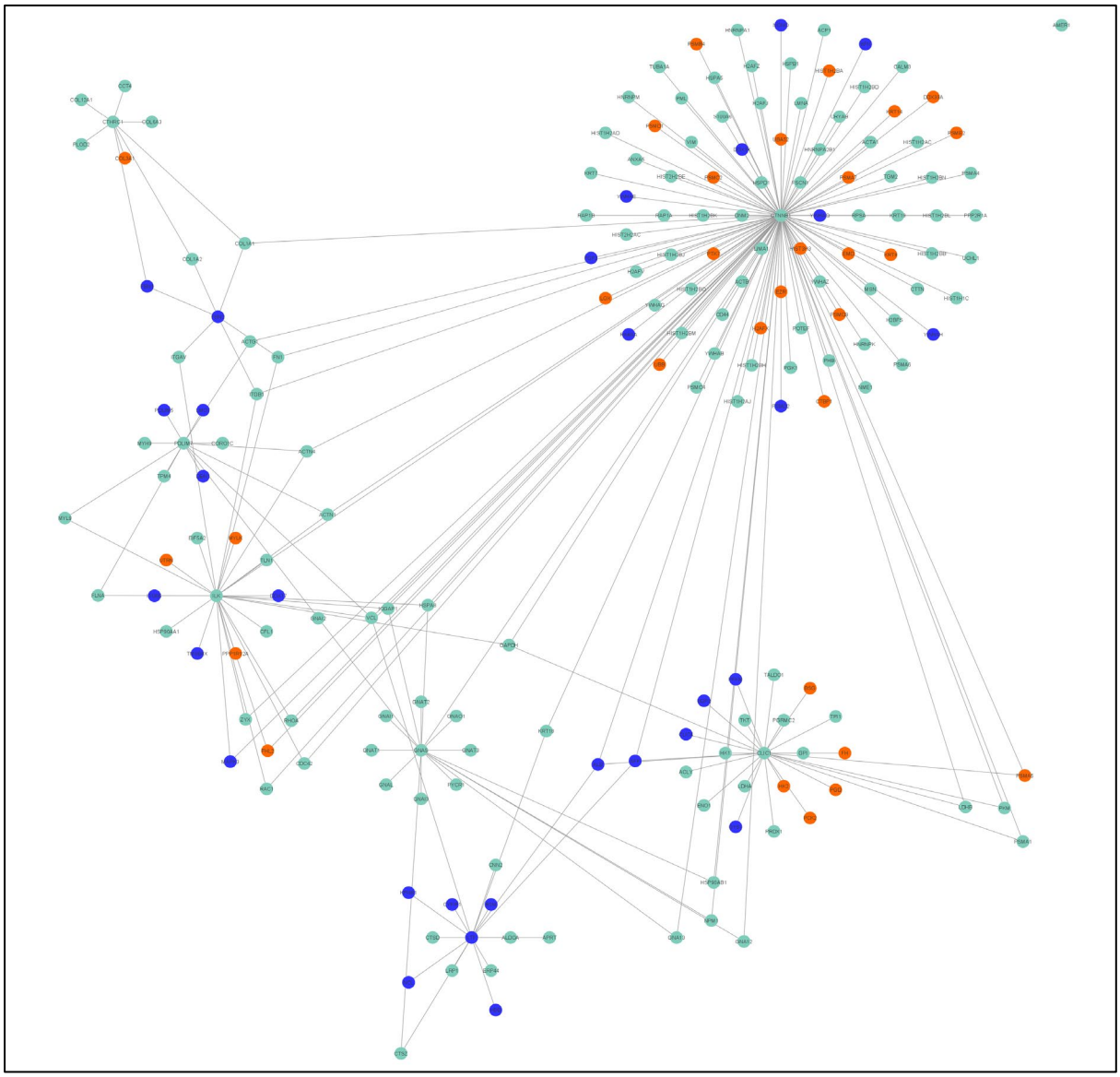

Figure 7.19 Cytoscape protein interaction network graph of proteins identified by mass spectrometry. Blue - unique proteins for A-Ti6Al4V, Orange – unique Ti6Al4V (orange), and Green - shared proteins for both A-Ti6Al4V and Ti6Al4V

The Ti6Al4V and PLA coated Ti6Al4V samples were determined as the positive regulation of cell morphogenesis, cell adhesion, muscle cell differentiation, and system development. Therefore, both Ti6Al4V as a substrate material and biodegradable PLA film as a coating matrix support the cell growth and proliferation of ADSCs. Mass spectroscopy results for these samples can be combined with the cell morphology analysis and secretory cytokine assays. While the ADSCs growth and cell attachment were found to be higher than the PLA biocomposite coated Ti6Al4V samples, the highest cell number was found on the PLA coated Ti6Al4V sample. Moreover, the unique GO biological

processes for the PLA coated Ti6Al4V are mostly cell-matrix adhesion and substrate-dependent cell migration.

Most of the unique proteins and biological processes for the Ti6Al4V samples play a key role in activating the Wnt signaling pathway, regulating bone development and osteoblast differentiation. We observed that while the PLA coating promotes the early phase of differentiation for ADSCs via cell morphogenesis and system development, the Ti6Al4V surface stimulates the late differentiation of ADSCs due to the Wnt signaling pathway. According to the results, the combination of two materials, (the Ti6Al4V implant as a substrate and the PLA thin film as a biodegradable temporary coating material) may be suitable for the ADSCs growth and also for our drug delivery system combined bone implant design.

The second stage involved analyzing the PLA-Gm-(HAp-Gm) coated Ti6Al4V. Therefore, the design has the Gm antibiotic at five different concentrations and bioactive HAp drug carrier particles. The samples contained the same amount of HAp particles with different Gm concentrations and were analyzed in order to obtain the Gm dosage effect on ADSCs. Gentamicin is an aminoglycoside antibiotic, and it has been used as a treatment mostly for bone and joint infections. Although the cytotoxicity effect of gentamicin has been reported for various animal and human models, the effect of dose-dependent gentamicin on the human adipose stem cells is not clear (Varghese et al., 2017).

It was reported that 100µg/ml and higher gentamicin concentration causes the osteogenic inhibitory effects. Additionally, if the gentamicin concentration was higher than 500µg/ml, the osteogenic differentiation was suppressed completely (Li et al., 2019). Therefore, the determination of the suitable and safe gentamicin dosage for human ADSCs is crucial in designing an applicable PLA-Gm-(HAp-Gm) thin film local controlled drug delivery bone-implant system.

The highest number of unique proteins was identified in the 5% PLA-Gm-(HAp-Gm) coated Ti6Al4V sample compared to other PLA-Gm-(HAp-Gm) coated Ti6Al4V samples. A possible reason may be due to the HAp particles. The identified unique proteins of the 5% PLA-Gm-(HAp-Gm) coated Ti6Al4V sample play a key role in positively regulating MAPK cascade and the Wnt signaling pathway, in order to improve osteoblast differentiation and cell proliferation. No noticeable adverse effects from the Gm were observed.

For the 10% PLA-Gm-(HAp-Gm) coated Ti6Al4V sample, the regulation of the Wnt signaling pathway, the positive regulation of cell growth, and the antimicrobial immune response-related GO biological processes were identified which is similar to the 5% PLA-Gm-(HAp-Gm) coated Ti6Al4V sample according to the proteomics data. The unique YWHAE protein was also found in the 10% PLA-Gm-

(HAp-Gm) coated Ti6Al4V sample. YWHAE is a regulatory protein for cellular functions such as cell cycle, cell motility, and apoptosis. It also interacts with the stress adaptive signaling pathway so that it might be the response of ADSCs for the 10% Gm initial release.

ADSCs responded for two main processes in the 15% Gm contained sample. The first one is osteogenic differentiation due to the FGF2 and LTF proteins with antimicrobial activity. The second one is an immune response due to the TMSB4X and LMNB1 proteins. The two GO biological functions can be separated by the effect of HAp particles and the effect of high Gm dosage.

The 20% PLA-Gm-(HAp-Gm) coated Ti6Al4V sample has muscle system development and muscle contraction processes related to unique proteins, which are different from the 5%, 10%, and 15% PLA-Gm-(HAp-Gm) coated samples. The CCL21 chemokine and also was identified for regulating chemotaxis. It could explain the cellular response to the high Gm dosage. The 30% PLA-Gm-(HAp-Gm) coated Ti6Al4V sample also has the CCL21 chemokine and the same muscle system development-related proteins as the 20% PLA-Gm-(HAp-Gm) coated Ti6Al4V sample. The expression of the muscle proteins instead of the bone proteins might also be due to the higher amount of Gm, slowing down the osteogenic potential. The muscle differentiation pathway is very close to the osteogenic differentiation pathway. The negative regulation of osteogenic differentiation potential (as a result of the Gm dosage) might cause the expression of muscle proteins as an alternative. The programmed cell death and the regulation of the apoptosis pathway were identified as the GO biological process in the 30% Gm samples. Additionally, it had the lowest protein number when compared with the other samples.

In summary, while the majority of the Gm related adverse effects were determined for the ADSCs seeded on the 30% PLA-Gm-(HAp-Gm) coated Ti6Al4V disc, there were negligible or very low adverse effects for ADSCs seeded on the 5% and 10% PLA-Gm-(HAp-Gm) coated Ti6Al4V discs. The cellular stress and immune responses were identified for ADSCs seeded on the 15% and 20% PLA-Gm-(HAp-Gm) coated Ti6Al4V discs. However, the regulation of the Wnt signaling pathway, the positive regulation of cell differentiation, and cell proliferation were identified for all PLA-Gm-(HAp-Gm) coated Ti6Al4V samples. HAp drug carrier particles may be why we obtained the positive regulation of bone development, cell proliferation, and osteogenic differentiation processes. HAp particles (due to their osteointegration and bioactive features on the surface) stimulated osteogenic differentiation and bone development for the ADSCs.

Singh *et al.* (2018) investigated the proteomic analyses of ADSCs seeded on a Porites coral derived porous HAp scaffold. According to the study, the cell adhesion, attachment, proliferation, and

osteoclast regulation related proteins were reported for the ADSCs seeded on Porites coral derived HAp bioceramic. Therefore, the dual responses of HAp drug carriers and Gm antibiotics were determined separately for the PLA-Gm-(HAp-Gm) samples.

Finally, the ADSCs seeded on the thermally anodized Ti6Al4V surface were analyzed by the proteomics analyses. While both of the samples have cell differentiation and cell morphogenesis related to the GO biological process (which refers to the early stage of differentiation) the unique A-Ti6Al4V sample regulates the osteoblast differentiation and maturation positively, meaning the osteogenic differentiation. We also found the FGF protein in the A-Ti6Al4V sample. According to the Bio-plex results, the secretion of FGF basic was increased in the A-Ti6Al4V sample at Day 14, while the secretion level was very low for the Ti6Al4V sample after Day 3. FGF-basic or bFGF is a growth factor and member of the fibroblast growth factor family. Generally, it regulates differentiation, migration, and cell growth and survival during regeneration and development. Due to the response delay for the differentiation between the samples, it is evident that the thermally anodized oxide layer on the Ti6Al4V stimulates osteogenic differentiation. Scarano *et al.*, (2018) investigated the influence of a thermally treated Ti6Al4V dental implant with in vivo experiments for eight weeks. A rabbit model was used to implant a thermally treated Ti6Al4V implant. They reported that the statistically significant difference of the bone-implant contact percentages was determined between the thermally treated and control groups histologically. The outcome of the study was that the thermally treated Ti6Al4V surface improves tissue healing around the implant and increases bioactivity. The results match our findings as well.

The LTF protein, which has the antibacterial response for gram-negative and gram-positive bacteria, was identified in the A-Ti6Al4V sample uniquely. Anodized Ti6Al4V material has good potential for bone implant applications due to its positive regulation for the osteogenic differentiation and possible antibacterial surface feature. A-Ti6Al4V is going to be ideal implant substrate material combined with our biodegradable, antibacterial PLA biocomposite thin film coating system to obtain long-lasting implantable design.

7.4. Summary and Conclusions

In this study, PLA biocomposite thin film coatings on Ti6Al4V implants were tested on human ADSCs at five different Gm concentrations (from 5% to 30% w/w) and two different substrate implant materials (Ti6Al4V and thermally anodized Ti6Al4V). The resultant cells were examined by fluorescent microscopy, secretory cytokine assays, proteomic analysis with bioinformatics interrogation by systems biology. The enormity of the work completed in this chapter, and its findings are best summarized in three main parts.

7.4.1. Ti6Al4V, PLA and PLA-HAp thin film coated Ti6Al4V samples:

ADSCs seeded on Ti6Al4V, PLA, and PLA-HAp thin film coated Ti6Al4V surfaces were widespread and covered the overall surfaces after 14 days. The Bio-plex results revealed, ADSCs on Ti6Al4V implant had higher cytokine expression levels at Day 3 than PLA coated Ti6Al4V sample, especially for MIP-a, IL-8, IL-10, Gm-CSF, MIP-1b. Thus an initial immune response of the ADSCs according to the surface type was identified on Day 3. The initial immune response for the Ti6Al4V sample was slightly higher compared to the PLA coated Ti6Al4V sample.

According to the protein mass spectroscopy findings, ADSCs on Ti6Al4V and PLA coated Ti6Al4V samples were determined as the positive regulation of cell morphogenesis, cell adhesion, muscle cell differentiation, and system development. Therefore, both Ti6Al4V as a substrate material and biodegradable PLA film as a coating have very high potential to use for bone implant applications.

A gene ontology analysis found that most of the unique proteins and biological processes for the Ti6Al4V samples play a key role in activating the Wnt signaling pathway, which regulates bone development and osteoblast differentiation. Additionally, it was observed that while the PLA coating promotes the early phase of differentiation for ADSCs via cell morphogenesis and system development, the Ti6Al4V surface stimulates the late differentiation of ADSCs due to the Wnt signaling pathway, matrix support the cell growth and proliferation of ADSCs.

The combination of Bio-plex and the microscopy results for 14 days of ADSCs growth in vitro show the biocompatibility and bioactivity of PLA biodegradable coating material. Additionally, while the cytokine clusters secretion behavior for PLA-HAp was found similar to control samples, it shows that HAp particles do not have any adverse immunological effect on ADSCS.

7.4.2 PLA-Gm-(HAp-Gm) thin film coated Ti6Al4V samples at five different Gm concentrations:

In this section, it was found that ADSCs growth and cell attachment on Ti6Al4V and PLA coated Ti6Al4V surfaces were higher than the PLA biocomposite coated Ti6Al4V samples. Furthermore, the 5% and 10% PLA-Gm-(HAp-Gm) thin film coated Ti6Al4V had lower single cell areas than the Ti6Al4V. However, the total cell number and circularity did not change.

According to the Bio-plex results, on Day 14, the expression patterns of cytokines for the 5% and 10% PLA-Gm-(HAp-Gm) coated Ti6Al4V samples were found to be similar to the Ti6Al4V, and PLA coated Ti6Al4V samples, except for the expression level of VEGF. VEGF is known to play important roles in bone formation, extracellular matrix remodeling, and wound healing; this could be afforded to HAp particles in the PLA biocomposite coating.

A further finding that may be due to the HAp particles was found in the mass spectroscopy results, where the highest number of unique proteins was identified in the 5% PLA-Gm-(HAp-Gm) coated Ti6Al4V sample compared to other PLA-Gm-(HAp-Gm) coated Ti6Al4V samples. The identified unique proteins of the 5% PLA-Gm-(HAp-Gm) coated Ti6Al4V sample was found to play a key role in positively regulating MAPK cascade and the Wnt signaling pathway, in order to improve osteoblast differentiation and cell proliferation. No noticeable adverse effects from the Gm were observed.

The single-cell area of ADSCs on PLA-Gm-(HAp-Gm) thin film coated Ti6Al4V samples, and the Ti6Al4V without coating do not have a significant difference. However, the 15%, 20%, and 30% PLA-Gm-(HAp-Gm) thin film coated Ti6Al4V samples had a very low number of cells on their surface. The Bioplex cytokines levels for the 15%, 20%, and 30% PLA-Gm-(HAp-Gm) coated Ti6Al4V samples were relatively low with similar expression patterns. The protein analysis showed the ADSCs responded with two main processes in the 15% Gm contained sample. First was osteogenic differentiation due to the FGF2 and LTF proteins with antimicrobial activity. The second was an immune response due to the TMSB4X and LMNB1 proteins. The two GO biological functions can be separated by the effect of HAp particles and the effect of high Gm dosage.

An interesting finding in the 20% Gm sample was the expression of the muscle proteins, which is thought to be a direct effect of the higher Gm content, slowing down the osteogenic potential. The muscle differentiation pathway is very close to the osteogenic differentiation pathway. The negative regulation of osteogenic differentiation potential (as a result of the Gm dosage) might cause muscle protein expression as an alternative.

In the final sample, 30% (w/w) Gm contained PLA biocomposite coated Ti6Al4V with and without HAp drug carrier particles caused adverse effects on ADSCs growth, which has the lowest cell number. The morphological appearance of the ADSCs was observed to be a more elongated and stretched cytoplasm, which can be the result of the unhealthy cells under stress due to the high Gm concentration (30% w/w).

The Bio-plex results confirm the adverse effects with a lower concentration of cytokines compared to other samples on Day 7 and subsequently decreasing very drastically to nearly zero after 14 days. Pro-inflammatory cytokine levels are higher for Gm contained samples, and anti-inflammatory cytokine levels are lower. The adverse effect of 30% Gm concentration on ADSCs can be observed by the SEM images, which match the Bio-plex assay. Conversely, there were negligible or very low adverse effects for ADSCs seeded on the 5% and 10% PLA-Gm-(HAp-Gm) coated Ti6Al4V discs.

7.4.3 Ti6Al4V and Thermally anodized Ti6Al4V samples:

The fluorescent images showed that the total cell area for the A-Ti6Al4V sample was significantly higher than the Ti6Al4V sample. While the Bio-plex results show a significant increase in the concentration of all cytokine clusters on Day 14 for the A-Ti6Al4V sample. Generally, pro-inflammatory cytokines levels were very low for Ti6Al4V and A-Ti6Al4V on Day 3 and 7. However, the cytokines levels were increased gradually at Day 10 and 14 for A-Ti6Al4V. Whereas anti-inflammatory cytokines, IL-4 was active only in the beginning (Day 3), and at the end (Day 14), IL-10 was active on Day 3 for both samples. It slightly increased for Ti6Al4V at D14.

The complementary proteomic analysis found both samples had proteins related to cell differentiation and cell morphogenesis through GO biological process (which refers to the early stage of differentiation) the unique A-Ti6Al4V sample regulates the osteoblast differentiation and maturation positively, meaning the osteogenic differentiation. Further findings and identification of the LTF protein, which has the antibacterial response for gram-negative and gram-positive bacteria, were identified in the A-Ti6Al4V sample uniquely. It shows the possible antimicrobial surface property of the thermally anodized Ti6Al4V implant.

The parallel identification of FGF-basic protein in mass spectrometry and Bio-plex analysis was expressed in the A-Ti6Al4V samples. FGF-basic is known to regulate differentiation, migration, and cell growth and survival during regeneration and development. Due to the response delay for the differentiation between the samples, it is evident that the thermally anodized oxide layer on the Ti6Al4V stimulates osteogenic differentiation.

In conclusion, while only PLA thin film coating has the highest cell number, 5% and 10% PLA-Gm-(HAp-Gm) coated Ti6Al4V samples did not have noticeable Gm related adverse effects as assessed by morphological, immunological and proteomics analyses. Besides, the positive regulation of osteogenic differentiation and Wnt signaling pathway regulations-related GO biological processes were identified, which could be the stimulation effect of HAp particles on ADSCs.

On the other hand, the adverse effects of dose-dependent Gm observed on 15%, 20%, and 30% PLA-Gm-(HAp-Gm) coated Ti6Al4V samples were identified with immune response-related GO biological processes. Additionally, the lowest cell and protein numbers were determined for 30% PLA-Gm-(HAp-Gm) coated Ti6Al4V sample compared with other samples.

When two substrates (Ti6Al4V and A-Ti6Al4V) were compared, the A-Ti6Al4V sample stimulates the osteogenic differentiation. It is possible that the antibacterial feature is due to its surface structure and chemistry.

The final conclusion from this study is that use of a <10% PLA-Gm-(HAp-Gm) coated A-Ti6Al4V implant design has a very high potential for medical bone implant applications as a long-lasting, antibacterial, biocompatible implant design. To determine the Gm effect on human ADSCs, proteomics analyses should be done further in 2D versus 3D culture comparative study conditions to closer simulate in vivo conditions.

7.5 References

ARGENTATI, C., MORENA, F., MONTANUCCI, P., RALLINI, M., BASTA, G., CALABRESE, N., CALAFIORE, R., CORDELLINI, M., EMILIANI, C., ARMENTANO, I. & MARTINO, S. 2018. Surface Hydrophilicity of Poly(l-Lactide) Acid Polymer Film Changes the Human Adult Adipose Stem Cell Architecture. *Polymers (Basel),* 10**,** 140.

BARON, R. & GORI, F. 2018. Targeting WNT signaling in the treatment of osteoporosis. *Curr Opin Pharmacol,* 40**,** 134-141.

BEN-NISSAN, B., MACHA, I., CAZALBOU, S. & CHOI, A. H. 2016. Calcium phosphate nanocoatings and nanocomposites, part 2: thin films for slow drug delivery and osteomyelitis. *Nanomedicine,* 11**,** 531-531–544.

BORTHWICK, L. A. 2016. The IL-1 cytokine family and its role in inflammation and fibrosis in the lung. *Seminars in immunopathology,* 38**,** 517-534.

BROGI, E., WU, T., NAMIKI, A. & ISNER, J. M. 1994. Indirect angiogenic cytokines upregulate VEGF and bFGF gene expression in vascular smooth muscle cells, whereas hypoxia upregulates VEGF expression only. *Circulation,* 90**,** 649-52.

CHAROENLARP, P., RAJENDRAN, A. K. & ISEKI, S. 2017. Role of fibroblast growth factors in bone regeneration. *Inflamm Regen,* 37**,** 10.

CHOI, A. H., KARACAN, I. & BEN-NISSAN, B. 2018. Surface modifications of titanium alloy using nanobioceramic-based coatings to improve osseointegration: a review. *Materials Technology***,** 1-10.

CHOU, J., ITO, T., OTSUKA, M., BEN-NISSAN, B. & MILTHORPE, B. 2013. Simvastatin-loaded beta-TCP drug delivery system induces bone formation and prevents rhabdomyolysis in OVX mice. *Adv Healthc Mater,* 2**,** 678-81.

CHOU, J., ITO, T., OTSUKA, M., BEN-NISSAN, B. & MILTHORPE, B. 2016. The effectiveness of the controlled release of simvastatin from beta-TCP macrosphere in the treatment of OVX mice. *J Tissue Eng Regen Med,* 10**,** E195-203.

COFFIN, J. D., HOMER-BOUTHIETTE, C. & HURLEY, M. M. 2018. Fibroblast Growth Factor 2 and Its Receptors in Bone Biology and Disease. *J Endocr Soc,* 2**,** 657-671.

CONNEELY, O. M. 2001. Antiinflammatory activities of lactoferrin. *J Am Coll Nutr,* 20**,** 389S-395S; discussion 396S-397S.

DA ROCHA, D. N., SANTANA BLAZUTTI MARCAL, R. L., MAZA BARBOSA, R., RICARDO MUNIZ FERREIRA, J. & PRADO DA SILVA, M. H. 2018. Mesenchymal Stem Cells Associated with Bioceramics for Bone Tissue Regeneration. *Biomaterials and Medical Applications,* 01.

DANOUX, C. B., BARBIERI, D., YUAN, H., DE BRUIJN, J. D., VAN BLITTERSWIJK, C. A. & HABIBOVIC, P. 2014. In vitro and in vivo bioactivity assessment of a polylactic acid/hydroxyapatite composite for bone regeneration. *Biomatter,* 4**,** e27664.

DUFFY, A. M., BOUCHIER-HAYES, D. J. & HARMEY, J. H. 2004. Vascular Endothelial Growth Factor (VEGF) and Its Role in Non-Endothelial Cells: Autocrine Signalling by VEGF. *In:* J., H. H. (ed.) *VEGF and Cancer.* Springer.

FEI, Y., XIAO, L., DOETSCHMAN, T., COFFIN, D. J. & HURLEY, M. M. 2011. Fibroblast growth factor 2 stimulation of osteoblast differentiation and bone formation is mediated by modulation of the Wnt signaling pathway. *J Biol Chem,* 286**,** 40575-83.

FEISST, V., MEIDINGER, S. & LOCKE, M. B. 2015. From bench to bedside: use of human adipose-derived stem cells. *Stem Cells Cloning,* 8**,** 149-62.

FRESE, L., DIJKMAN, P. E. & HOERSTRUP, S. P. 2016. Adipose Tissue-Derived Stem Cells in Regenerative Medicine. *Transfus Med Hemother,* 43**,** 268-274.

FRONTINI-LÓPEZ, Y.-R., GOJANOVICH, A.-D., MASONE, D., BUSTOS, D.-M. & UHART, M. 2018. Adipose-derived mesenchymal stem/stromal cells: from the lab bench to the basic concepts for clinical translation. *Biocell,* 42**,** 67-78.

FU, H., SUBRAMANIAN, R. R. & MASTERS, S. C. 2000. 14-3-3 proteins: structure, function, and regulation. *Annu Rev Pharmacol Toxicol,* 40**,** 617-47.

GAO, C., PENG, S., FENG, P. & SHUAI, C. 2017. Bone biomaterials and interactions with stem cells. *Bone Res,* 5**,** 17059.

GERBER, H. P., VU, T. H., RYAN, A. M., KOWALSKI, J., WERB, Z. & FERRARA, N. 1999. VEGF couples hypertrophic cartilage remodeling, ossification and angiogenesis during endochondral bone formation. *Nat Med,* 5**,** 623-8.

GOLDSTEIN, A. L., HANNAPPEL, E., SOSNE, G. & KLEINMAN, H. K. 2012. Thymosin beta4: a multi-functional regenerative peptide. Basic properties and clinical applications. *Expert Opin Biol Ther,* 12**,** 37-51.

GOSWAMI, R. & KAPLAN, M. H. 2011. A brief history of IL-9. *J Immunol,* 186**,** 3283-8.

GREEN, D. W., LI, G., MILTHORPE, B. & BEN-NISSAN, B. 2012. Adult stem cell coatings for regenerative medicine. *Materials Today,* 15**,** 60-66.

HAIMI, S., SUURINIEMI, N., HAAPARANTA, A. M., ELLA, V., LINDROOS, B., HUHTALA, H., RATY, S., KUOKKANEN, H., SANDOR, G. K., KELLOMAKI, M., MIETTINEN, S. & SUURONEN, R. 2009. Growth and osteogenic differentiation of adipose stem cells on PLA/bioactive glass and PLA/beta-TCP scaffolds. *Tissue Eng Part A,* 15**,** 1473-80.

HANDFORD, P. A. 2000. Fibrillin-1, a calcium binding protein of extracellular matrix. *Biochim Biophys Acta,* 1498**,** 84-90.

HART, M., LAUER, J., SELIG, M., HANAK, M., WALTERS, B. & ROLAUFFS, B. 2017. Shaping the Cell and the Future: Recent Advancements in Biophysical Aspects Relevant to Regenerative Medicine. *Journal of Functional Morphology and Kinesiology,* 3**,** 2.

HOCKING, A. M. 2015. The Role of Chemokines in Mesenchymal Stem Cell Homing to Wounds. *Adv Wound Care (New Rochelle),* 4**,** 623-630.

IAQUINTA, M. R., MAZZONI, E., BONONI, I., ROTONDO, J. C., MAZZIOTTA, C., MONTESI, M., SPRIO, S., TAMPIERI, A., TOGNON, M. & MARTINI, F. 2019. Adult Stem Cells for Bone Regeneration and Repair. *Front Cell Dev Biol,* 7**,** 268.

JAHANI, S., SHAKIBA, A. & JAHANI, L. 2015. The Antimicrobial Effect of Lactoferrin on Gram-Negative and Gram-Positive Bacteria. *International Journal of Infection,* 2**,** e27954.

KAGIWADA, H., FUKUCHI, T., MACHIDA, H., YAMASHITA, K. & OHGUSHI, H. 2008. Effect of Gentamicin on Growth and Differentiation of Human Mesenchymal Stem Cells. *Journal of Toxicologic Pathology,* 21**,** 61-67.

KARGOZAR, S., MOZAFARI, M., HAMZEHLOU, S., BROUKI MILAN, P., KIM, H.-W. & BAINO, F. 2019. Bone Tissue Engineering Using Human Cells: A Comprehensive Review on Recent Trends, Current Prospects, and Recommendations. 9**,** 174.

KATO, H., GRUENWALD, A., SUH, J. H., MINER, J. H., BARISONI-THOMAS, L., TAKETO, M. M., FAUL, C., MILLAR, S. E., HOLZMAN, L. B. & SUSZTAK, K. 2011. Wnt/beta-catenin pathway in podocytes integrates cell adhesion, differentiation, and survival. *J Biol Chem,* 286**,** 26003-15.

KAYABA, H. & CHIHARA, J. 2001. Eosinophils and related chemokines. *Rinsho Byori,* 49**,** 370-5.

KIMURA, H., KWAN, K. M., ZHANG, Z., DENG, J. M., DARNAY, B. G., BEHRINGER, R. R., NAKAMURA, T., DE CROMBRUGGHE, B. & AKIYAMA, H. 2008. Cthrc1 is a positive regulator of osteoblastic bone formation. *PLoS One,* 3**,** e3174.

LEE, H., CHOI, A. J., KANG, G. Y., PARK, H. S., KIM, H. C., LIM, H. J. & CHUNG, H. 2014. Increased 26S proteasome non-ATPase regulatory subunit 1 in the aqueous humor of patients with age-related macular degeneration. *BMB Rep,* 47**,** 292-7.

LI, M. X. & HWANG, P. M. 2015. Structure and function of cardiac troponin C (TNNC1): Implications for heart failure, cardiomyopathies, and troponin modulating drugs. *Gene,* 571**,** 153-66.

LI, H. & YUE, B. 2019. Effects of various antimicrobial agents on multi-directional differentiation potential of bone marrow-derived mesenchymal stem cells. *World J Stem Cells,* 11**,** 322-336.

LOPEZ-CASTEJON, G. & BROUGH, D. 2011. Understanding the mechanism of IL-1β secretion. *Cytokine & growth factor reviews,* 22**,** 189-195.

MA, M. Z., ZHUANG, C., YANG, X. M., ZHANG, Z. Z., MA, H., ZHANG, W. M., YOU, H., QIN, W., GU, J., YANG, S., CAO, H. & ZHANG, Z. G. 2014. CTHRC1 acts as a prognostic factor and promotes invasiveness of gastrointestinal stromal tumors by activating Wnt/PCP-Rho signaling. *Neoplasia,* 16**,** 265-78, 278 e1-13.

MA, Y., KAKUDO, N., MORIMOTO, N., LAI, F., TAKETANI, S. & KUSUMOTO, K. 2019. Fibroblast growth factor-2 stimulates proliferation of human adipose-derived stem cells via Src activation. *Stem Cell Res Ther,* 10**,** 350.

MACDONALD, B. T., TAMAI, K. & HE, X. 2009. Wnt/beta-catenin signaling: components, mechanisms, and diseases. *Dev Cell,* 17**,** 9-26.

MACHA, I. J., BEN-NISSAN, B., SANTOS, J., CAZALBOU, S., STAMBOULIS, A., GROSSIN, D. & GIORDANO, G. 2017. Biocompatibility of a new biodegradable polymer-hydroxyapatite composite for biomedical applications. *Journal of Drug Delivery Science and Technology,* 38**,** 72-77.

MACKIE, E. J., TATARCZUCH, L. & MIRAMS, M. 2011. The skeleton: a multi-functional complex organ: the growth plate chondrocyte and endochondral ossification. *J Endocrinol,* 211**,** 109-21.

MYNGBAY, A., BEXEITOV, Y., ADILBAYEVA, A., ASSYLBEKOV, Z., YEVSTRATENKO, B. P., AITZHANOVA, R. M., MATKARIMOV, B., ADARICHEV, V. A. & KUNZ, J. 2019. CTHRC1: A New Candidate Biomarker for Improved Rheumatoid Arthritis Diagnosis. *Front Immunol,* 10**,** 1353.

NAUJOKAT, C. & SARIC, T. 2007. Concise review: role and function of the ubiquitin-proteasome system in mammalian stem and progenitor cells. *Stem Cells,* 25**,** 2408-18.

NUSSE, R. 2008. Wnt signaling and stem cell control. *Cell Res,* 18**,** 523-7.

OPAL, S. M. & DEPALO, V. A. 2000. Anti-inflammatory cytokines. *Chest,* 117**,** 1162-72.

ORNITZ, D. M. & ITOH, N. 2015. The Fibroblast Growth Factor signaling pathway. *Wiley Interdiscip Rev Dev Biol,* 4**,** 215-66.

PENNINGTON, K. L., CHAN, T. Y., TORRES, M. P. & ANDERSEN, J. L. 2018. The dynamic and stress-adaptive signaling hub of 14-3-3: emerging mechanisms of regulation and context-dependent protein-protein interactions. *Oncogene,* 37**,** 5587-5604.

PRIPP, A. H. & STANIŠIĆ, M. 2014. The Correlation between Pro- and Anti-Inflammatory Cytokines in Chronic Subdural Hematoma Patients Assessed with Factor Analysis. *PLOS ONE,* 9**,** e90149.

PYAGAY, P., HEROULT, M., WANG, Q., LEHNERT, W., BELDEN, J., LIAW, L., FRIESEL, R. E. & LINDNER, V. 2005. Collagen triple helix repeat containing 1, a novel secreted protein in injured and diseased arteries, inhibits collagen expression and promotes cell migration. *Circ Res,* 96**,** 261-8.

RAMIREZ, F., SAKAI, L. Y., DIETZ, H. C. & RIFKIN, D. B. 2004. Fibrillin microfibrils: multipurpose extracellular networks in organismal physiology. *Physiol Genomics,* 19**,** 151-4.

RAPPSILBER, J., MANN, M. & ISHIHAMA, Y. 2007. Protocol for micro-purification, enrichment, pre-fractionation and storage of peptides for proteomics using StageTips. *Nature protocols,* 2**,** 1896-906.

ROMAGNOLI, C., ZONEFRATI, R., GALLI, G., PUPPI, D., PIROSA, A., CHIELLINI, F., MARTELLI, F. S., TANINI, A. & BRANDI, M. L. 2015. In Vitro Behavior of Human Adipose Tissue-Derived Stem Cells on Poly(ε-caprolactone) Film for Bone Tissue Engineering Applications. *BioMed Research International,* 2015**,** 323571.

SANTOS, J., MILTHORPE, B. K., HERBERT, B. R. & PADULA, M. P. 2017. Proteomic Analysis of Human Adipose Derived Stem Cells during Small Molecule Chemical Stimulated Pre-neuronal Differentiation. *Int J Stem Cells,* 10**,** 193-217.

SCARANO, A., CROCETTA, E., QUARANTA, A. & LORUSSO, F. 2018. Influence of the Thermal Treatment to Address a Better Osseointegration of Ti6Al4V Dental Implants: Histological and Histomorphometrical Study in a Rabbit Model. *Biomed Res Int,* 2018**,** 2349698.

SHACHAR, I. & KARIN, N. 2013. The dual roles of inflammatory cytokines and chemokines in the regulation of autoimmune diseases and their clinical implications. *J Leukoc Biol,* 93**,** 51-61.

SINGH, K. 2018. *The chracterisation of adipose derived stem cells on coralline scaffolds for bone tissue engineering.* Ph.D., University of Technology Sydney.

SKUBIS, A., GOLA, J., SIKORA, B., HYBIAK, J., PAUL-SAMOJEDNY, M., MAZUREK, U. & ŁOS, M. J. 2017. Impact of Antibiotics on the Proliferation and Differentiation of Human Adipose-Derived Mesenchymal Stem Cells. *Int J Mol Sci,* 18**,**2522.

SRINIVASAN, L., HARRIS, M. C. & KILPATRICK, L. E. 2017. 128 - Cytokines and Inflammatory Response in the Fetus and Neonate. *In:* POLIN, R. A., ABMAN, S. H., ROWITCH, D. H., BENITZ, W. E. & FOX, W. W. (eds.) *Fetal and Neonatal Physiology (Fifth Edition).* Elsevier.

STORTI, G., SCIOLI, M. G., KIM, B. S., ORLANDI, A. & CERVELLI, V. 2019. Adipose-Derived Stem Cells in Bone Tissue Engineering: Useful Tools with New Applications. *Stem Cells Int,* 2019**,** 3673857.

SUN, Y., CHEN, C. S. & FU, J. 2012. Forcing stem cells to behave: a biophysical perspective of the cellular microenvironment. *Annu Rev Biophys,* 41**,** 519-42.

TANABE, S., KAWABATA, T., AOYAGI, K., YOKOZAKI, H. & SASAKI, H. 2016. Gene expression and pathway analysis of CTNNB1 in cancer and stem cells. *World J Stem Cells,* 8**,** 384-395.

TAVERNER, T., KARPIEVITCH, Y. V., POLPITIYA, A. D., BROWN, J. N., DABNEY, A. R., ANDERSON, G. A. & SMITH, R. D. 2012. DanteR: an extensible R-based tool for quantitative analysis of -omics data. *Bioinformatics,* 28**,** 2404-6.

TSUJI, W., RUBIN, J. P. & MARRA, K. G. 2014. Adipose-derived stem cells: Implications in tissue regeneration. *World J Stem Cells,* 6**,** 312-21.

ULLAH, I., SUBBARAO, RAGHAVENDRA B. & RHO, GYU J. 2015. Human mesenchymal stem cells - current trends and future prospective. *Bioscience Reports,* 35.

VAN SCHIE, E. H. & VAN AMERONGEN, R. 2020. Aberrant WNT/CTNNB1 Signaling as a Therapeutic Target in Human Breast Cancer: Weighing the Evidence. *Front Cell Dev Biol,* 8**,** 25.

VARGHESE, D. S., PARWEEN, S., ARDAH, M. T., EMERALD, B. S. & ANSARI, S. A. 2017. Effects of Aminoglycoside Antibiotics on Human Embryonic Stem Cell Viability during Differentiation In Vitro. *Stem Cells Int,* 2017**,** 2451927.

VAN STEENSEL, L., PARIDAENS, D., DINGJAN, G. M., VAN DAELE, P. L. A., VAN HAGEN, P. M., KUIJPERS, R. W. A. M., VAN DEN BOSCH, W. A., DREXHAGE, H. A., HOOIJKAAS, H. & DIK, W. A. 2010. Platelet-Derived Growth Factor-BB: A Stimulus for Cytokine Production by Orbital Fibroblasts in Graves' Ophthalmopathy. *Investigative Ophthalmology & Visual Science,* 51**,** 1002-1007.

VAZIRINEJAD, R., AHMADI, Z., KAZEMI ARABABADI, M., HASSANSHAHI, G. & KENNEDY, D. 2014. The Biological Functions, Structure and Sources of CXCL10 and Its Outstanding Part in the Pathophysiology of Multiple Sclerosis. *Neuroimmunomodulation,* 21**,** 322-330.

WU, C. & DEDHAR, S. 2001. Integrin-linked kinase (ILK) and its interactors: a new paradigm for the coupling of extracellular matrix to actin cytoskeleton and signaling complexes. *J Cell Biol,* 155**,** 505-10.

YAMAMOTO, S., NISHIMURA, O., MISAKI, K., NISHITA, M., MINAMI, Y., YONEMURA, S., TARUI, H. & SASAKI, H. 2008. Cthrc1 selectively activates the planar cell polarity pathway of Wnt signaling by stabilizing the Wnt-receptor complex. *Dev Cell,* 15**,** 23-36.

YAO, L., HERLEA-PANA, O., HEUSER-BAKER, J., CHEN, Y. & BARLIC-DICEN, J. 2014. Roles of the chemokine system in development of obesity, insulin resistance, and cardiovascular disease. *J Immunol Res,* 2014**,** 181450.

YEN, C.-F., WANG, H.-S., LEE, C.-L. & LIAO, S.-K. 2014. Roles of integrin-linked kinase in cell signaling and its perspectives as a therapeutic target. *Gynecology and Minimally Invasive Therapy,* 3**,** 67-72.

YING, X., CHENG, S., WANG, W., LIN, Z., CHEN, Q., ZHANG, W., KOU, D., SHEN, Y., CHENG, X., PENG, L., ZI XU, H. & ZHU LU, C. 2012. Effect of lactoferrin on osteogenic differentiation of human adipose stem cells. *Int Orthop,* 36**,** 647-53.

ZHANG, J.-M. & AN, J. 2007. Cytokines, inflammation, and pain. *International anesthesiology clinics,* 45**,** 27-37.

ZHANG, M., YU, W., NIIBE, K., ZHANG, W., EGUSA, H., TANG, T. & JIANG, X. 2018. The Effects of Platelet-Derived Growth Factor-BB on Bone Marrow Stromal Cell-Mediated Vascularized Bone Regeneration. *Stem Cells Int,* 2018**,** 3272098.

Major Findings

- PLA based polymeric matrix, which includes an antibiotic (Gm) and coralline HAp microspheres that also incorporates Gm [which is designated as [PLA-Gm-(HAp-Gm)], can be coated on Ti6Al4V, and/or thermally anodized Ti6Al4V metallic bone implants is a very functional and adequate coating system.

- Coralline HAp microspheres has a high potential as drug delivery systems because of its unique chemistry, and its meso, and nanoporous structure, and natural minerals, such as Mg and Sr that improve bone regeneration due to their bioactivity and osseointegration properties. The reason behind the osteogenic differentiation-related positive responses, which was observed in vitro studies, can be due to the stimulation effect of HAp particles.

- It was found that the PLA biocomposite coatings have good adhesion with adequate mechanical properties and it is predicted that they can survive both the surgical handling and insertion.

- The thermally anodized Ti6Al4V in comparison to the untreated Ti6Al4V substrate showed superior nanoindentation and scratch test results. The results showed that the anodization process on Ti6Al4V has an advantage for clinical use due to their strong adhesion to the substrates and their physical and biological properties. The ADSCs seeded anodized Ti6Al4V sample regulates the osteogenic differentiation-related GO biological processes positively compared to the untreated Ti6Al4V sample.

- During the drug release studies, the continuous dissolution method was found to be a more appropriate, accurate, and adequate method than the cumulative dissolution method.

- Coralline HAp particles as a drug carrier in the PLA matrix improved the controlled and prolonged Gm release due to calcium phosphate dissolution and reduced total drug release rate.

- It was observed that the initial burst drug release is controlled by the PLA surface area, which contains both individual and clusters of Gm antibiotic particles. In the long-term, slow release is controlled by the deterioration and dissolution of the HAp particles within the matrix, loaded with the Gm antibiotic.

- In the antimicrobial applications, the Gm release from the PLA-Gm-(HAp-Gm) thin film coated Ti6Al4V discs, including the lowest Gm (5% Gm contained sample), were effectively inhibiting the growth of both *S. aureus* and *S. epidermidis*.

- 5% and 10% PLA-Gm-(HAp-Gm) coated Ti6Al4V samples did not have any noticeable Gm related adverse effects due to morphological, immunological, and proteomics analyses.

- The lowest cell number and protein number were determined for 30%PLA-Gm-(HAp-Gm) coated Ti6Al4V sample compared to other samples. This result strongly shows the adverse effect of using high percentages of antibiotic on human ADSC.

- It is suggested that 10% PLA-Gm-(HAp-Gm) coated thermally treated anodized Ti6Al4V implant design has a very high potential to be used for the clinical applications as long-lasting, antibacterial and bioactive implant design for the inhibition of implant-related bacterial infection and biofilm formation instead of using traditional systemic antibiotic treatments.

CHAPTER 8

Final Discussions and Conclusions

CHAPTER 8

Final Discussion and Conclusions

This chapter covers a summary of the work completed, results obtained, and the conclusion. A small section is also included at the end of this chapter covering future work for further research.

A new bioactive composite was developed and tested based on our hypothesis `A PLA biodegradable polymer biocomposite in combination with a controlled, slow-release drug delivery system can be easily applied as a functional coating material for metallic bone implants to enhance their biocompatibility and longevity and reducing surgery-related bacterial infections'.

In this research, a Poly-lactic acid matrix (PLA) based thin film multifunctional coating system was developed for applications in metallic orthopedic, dental and maxillofacial implantation. A new and unique local and controlled antibiotic and drug delivery system based on an implant coating was designed and the production method was optimized. The products were tested for their chemical, morphological, mechanical, and biological properties to improve longevity, bioactivity, curtain biofilm formation and implant-related bacterial infections.

These PLA biocomposites are biodegradable and have an antibacterial coating that includes the biomimetic approach of marine structures such as the coral skeleton derived HAp particles as the antibiotic carrier. Therefore, in this design, there were two control points; PLA biodegradable thin film matrix and HAp drug carrier particles, to obtain slow and controlled antibiotic (gentamicin [Gm]) release, in order to inhibit implant-related surgery site infections and serious clinical problems such as osteomyelitis.

The research specifically focused on the development and applications of Great Barrier based Porites coralline hydroxyapatite particles (HAp) containing the gentamicin antibiotic (Gm) and then embedded in a biodegradable polylactic acid thin film coating on medical implants. The final composition was based on the polymeric matrix, which included both Gm and HAp particles, developed as Gm in the PLA matrix and Hap microspheres that incorporated Gm (PLA-Gm-[HAp-Gm]), and coated on specific Ti6Al4V metallic bone implants.

These PLA-Gm-(HAp-Gm) coated Ti6Al4V samples were characterized in terms of their chemical, physical and biological properties. Extensive in vitro and antibacterial studies were conducted to evaluate bioactivity, biocompatibility, and antibacterial properties of the coating design.

The production of PLA biocomposite thin film matrix

HAp particles were produced from high purity coral skeleton of the Porites genus ($CaCO_3$) via the hydrothermal conversion technique, in the presence of an ammonium phosphate solution at 220 ˚C and 4 MPa pressure. The coralline HAp is chemically and structurally similar to the human cancellous bone. Therefore, it has high potential in drug delivery systems because of the unique chemistry, its meso- and nano-porous structure, which can be used to improve bone regeneration of the tissue around implants due to its bioactivity and osseointegration properties.

The coralline HAp particles were loaded with Gm antibiotics at different ratios: 5%, 10%, 15%, 20%, and 30% (w/w). During SEM studies, it was observed that a solution of Gm, if prepared with water, easily penetrates and coats the coralline HAp particles homogeneously. It fills both the nano and mesopores of the coralline HAp particles efficiently.
However, their addition or incorporation into the PLA matrix generated a different problem due to the lack of inadequate mixing and some agglomerations of the Gm containing HAp particles were observed as clusters of large particles. Clusters of these particles – although few in number – were mainly on the surface, and some were within the PLA matrix. These HAp-Gm particles are possibly one of the most important components in a multifunctional coating system for controlling local and slow-release of a range of drugs, minerals, proteins, and peptides, or even cells to the human body, for preventing or treating implant-related infections.

PLA biocomposite thin film coated Ti6Al4V disc-shaped implants were successfully produced, and morphological and structural analyses were carried out using FT-IR, SEM, XRD, EDS, and AFM. The imaging of the samples was carried out on SEM and AFM, which showed smooth PLA thin film with Gm and HAp-Gm particles on the Ti6Al4V disc surfaces. Some clusters were also observed, coated with PLA and adhered strongly. Profilometry measurements show that the PLA thin film dip-coated samples have ~ 400 nm film thicknesses when produced without Hap particles. However, the thickness of the PLA-Gm-(HAp-Gm) thin film on the Ti6Al4V disc increased due to the amounts and size of particles and the overall viscosity of the PLA solution.

Crystallographic analysis of the converted coral using FT-IR and XRD showed only the HAp phase. The agglomerated HAp particle average size range was around 200 to 400 nm in both SEM and BET

analysis, however some clusters were above a few micron sizes. While the BET surface area of the Porites coral particle was measured at 0.78 m^2/g, it was 18.93 m^2/g for HAp particles. On the other hand, after the drug loading process, the surface area of 5% HAp-Gm particles, was found to be 8.79m^2/g, which was less than the surface area of the unloaded HAp particles, but higher than the natural Porites coral's surface area. Therefore, it is postulated that the meso and nanopores of HAp particles were only partially filled with Gm due to the drug loading process.

Mechanical Characterization

The nanoindentation and scratch tests were conducted on several different samples; Ti6Al4V substrates, thermally anodized Ti6Al4V substrates, and PLA biocomposite thin film coated Ti6Al4V to determine the mechanical properties of these thin film coatings. The results show that the PLA biocomposite coatings have good adhesion with adequate mechanical properties and can survive surgical handling and insertion.

The thermally anodized samples showed excellent nanoindentation results. Young's modulus of elasticity E and the hardness H values of the PLA-Gm-(HAp-Gm) thin film coated anodized Ti6Al4V were for E from 20 to 70 GPa and for H from 0.45 to 1.9 GPa, respectively. On the other hand, the E and H values of PLA-Gm-(HAp-Gm) thin film coated untreated Ti6Al4V values ranged from 20 to 50 GPa for E and from 0.28 to 0.8 GPa for H.

The results showed the advantages of the anodization process on these substrates for clinical use due to their strong adhesion and their properties. It is thought that the TiO_2 anodized layer helps on both bonding and in osseointegration as covered in **Chapter 7**.

Drug Release Studies

Two different dissolution methods were used to compare the dissolution rates and profiles. When the Continuous Dissolution Method was compared with the Cumulative Dissolution Method, the Continuous Dissolution Method was found to be ideal. The main reason for that is that any additional solution added to replace the removed solution for the spectroscopic analysis in the Cumulative Method can influence the readings due to further dilution and should be avoided. However, using the individual discs for each time interval, such as in the Continuous Method, will give more accurate results.

The further trials with the various constituents of the PBS solution and its pH are strongly suggested for future works.

Another important finding is that the different Gm concentrations (5% - to 30% w/w) in both PLA-Gm and PLA-Gm-(HAp-Gm) coated Ti6Al4V samples are highly correlated with the initial burst of Gm release.

The coralline HAp particles as a drug carrier in the PLA matrix improved the controlled and prolonged Gm release due to the calcium phosphate dissolution rate and reduced the total drug release rate.

It was observed that the "burst" or the initial drug release was controlled by the PLA surface area, which contains Gm antibiotic particles both as individual particles and as clusters. However, the long-term slow release is controlled by the dissolution of the HAp particles, which are loaded with the Gm antibiotic as well.

These two steps, the burst, and the steady-state dissolution stages and their adequate control can allow us to adjust antibiotic concentration and release rates according to patients' needs and condition.

Antibacterial Behavior against *S. Aureus* and *S. Epidermidis* and Biofilm formation

It was observed from the results of the modified agar disc diffusion method that the Gm release from the PLA-Gm-(HAp-Gm) thin film coated Ti6Al4V discs, including the lowest Gm (5%), were effectively inhibiting the growth of both *S. aureus* and *S. epidermidis*.

For *S. aureus*, the size of the bacterial growth free/clear zones around the PLA-Gm-(HAp-Gm) thin film coated Ti6Al4V disc increased gradually due to the percentages of Gm in the samples. Additionally, it was found that the Gm release from the PLA-Gm-(HAp-Gm) coated samples were more effective at inhibiting *S. epidermidis* growth when compared to *S. aureus*.

The results can be explained as the difference of the minimum inhibitory concentration (MIC) between *S. epidermidis* and *S. aureus* against the gentamicin. MIC of *S. epidermidis* against the Gm is lower than the MIC of *S. aureus*.

A significant reduction of bacterial growth was found after 4 hours of the co-culture for the PLA-Gm-(HAp-Gm) thin film coated Ti6Al4V discs at all predetermined Gm concentrations (5% to 30%) when compared with the control samples which were the S. *aureus* culture, the Ti6Al4V discs without the PLA biocomposite coating and the PLA thin film coated Ti6Al4V discs without the antibiotic at the planktonic stage of S. *aureus*.

At the biofilm formation stage of S. *aureus*, significant reduction of bacterial attachment and an increase of dead microcolonies were observed for even the lowest 5% (w/w) Gm containing PLA-Gm-(HAp-Gm) coated samples. Additionally, the PLA-Gm-(HAp-Gm) thin film coated Ti6Al4V samples containing Gm (over 15% [w/w]) were more effective in decreasing biofilm formation on the surface.

Biocompatibility and bioactivity in vitro studies

The ADSCs morphology and cell number on the Ti6Al4V and thermally anodized Ti6Al4V samples were similar to the control according to fluorescent imaging results. At the same time, the PLA coated Ti6Al4V had the highest cell number compared to the rest of the data set. On the other hand, noticeable differences were observed on the morphology, and the cell number between ADSCs seeded on the 5%-10% PLA-Gm-(HAp-Gm) samples to the ADSCs seeded on the 15%-20%-30% PLA-Gm-(HAp-Gm) samples. Moreover, the 5% and 10% PLA-Gm-(HAp-Gm) coated Ti6Al4V samples did not have noticeable Gm related adverse effects due to morphological, immunological, and proteomics analyses. Additionally, the positive regulation of osteogenic differentiation and the regulations on the canonical and non-canonical Wnt signaling pathway-related GO biological processes were identified.

The reason behind the osteogenic differentiation-related positive responses can be the stimulation effect of HAp particles on ADSCs because HAp is a bioactive and osteoconductive material. Additionally, it increases osseointegration.

ADSCs seeded on the 15%, 20%, and 30% PLA-Gm-(HAp-Gm) coated Ti6Al4V samples showed the adverse effects of dose-dependent Gm. The adverse effects were identified with the immune response-related GO biological processes. Additionally, the lowest cell number and protein number were determined for the 30% PLA-Gm-(HAp-Gm) coated TI6Al4V sample compared to the other samples.

When the ADSCs seeded on the Ti6Al4V and the anodized Ti6Al4V were compared, the anodized Ti6Al4V sample stimulated more osteogenic differentiation-related proteins and GO biological processes. It is possible that it has the antibacterial feature due to its surface morphology, structure, and chemistry, because antibacterial response-related GO biological processes were expressed in the anodized Ti6Al4V samples. The Ti6Al4V sample expresses the cell morphogenesis and cell differentiation-related GO biological processes that can represent the early differentiation phase related processes for ADSCs.

The results suggests that the PLA-Gm-(HAp-Gm) thin film coated thermally anodized Ti6Al4V implants were the most appropriate design for implant longevity, improving bioactivity between the implant and surrounding tissue, and inhibiting bacterial infections due to implants or surgery.

The different ranges of Gm concentrations are applicable with the PLA-Gm-(HAp-Gm) thin film coating design, which gives flexibility for adjusting the antibiotic dosage according to the type of treatment for the specific patient.

We can conclude that all concentrations up to the 10% Gm containing PLA-Gm-(HAp-Gm) coated thermally treated anodized Ti6Al4V implant design have high potential for clinical applications as a long-lasting, antibacterial and bioactive implant design for the inhibition of implant-related bacterial infections and biofilm formation instead of using traditional systemic antibiotic treatments.

Future Research Suggestions

One of the future directions for this research is further antibiotic dissolution study using a fully dynamic micro-fluidity experiment with biological body fluids to observe the long-term release. It will evaluate the understanding of Gm release due to the PLA film degradation.

Another suggestion as a future study can be extended using in vivo experiments on the PLA biocomposite antibacterial implant coating design. Conducting the follow up in vivo experiments will help to determine two main approaches for this research. The first approach is the antibiotic dosage adjustment according to the antibiotic release rate and its bone healing capacity, as well as according to time. Secondly, to determine the Gm effect on human ADSCs, proteomics analyses should be done further in 2D versus 3D culture conditions in a comparative study to simulate in vivo conditions.

Finally, the results demonstrate that the PLA biocomposite antibacterial implant coating design can be investigated for its clinical feasibility in avoiding possible implant-related or surgery site infections and stimulating and improving the bioactivity of implantable devices. We suggest that the adaptation of the PLA biocomposite antibacterial implant coating design should be the direction of future investigations.

Appendix A

ICP calibration curves

24Mg (KED)

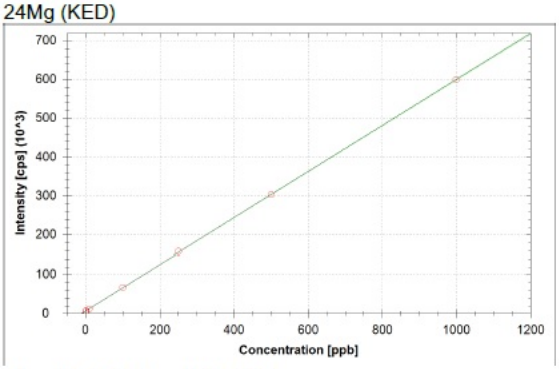

f(x) = 593.0051*x + 6749.4833
R^2 = 1.0000
BEC = 11.382 ppb
LoD = N/A

31P (KED)

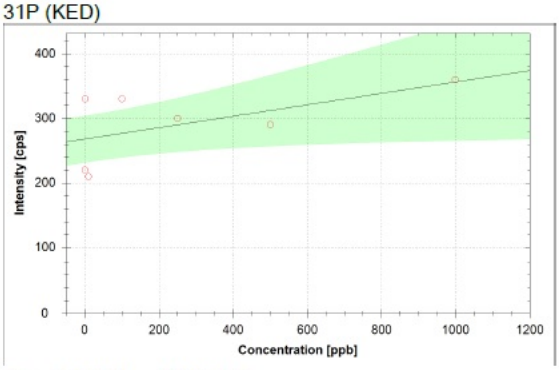

f(x) = 0.0883*x + 267.9627
R^2 = 0.3311
BEC = 3035.300 ppb
LoD = N/A

44Ca (KED)

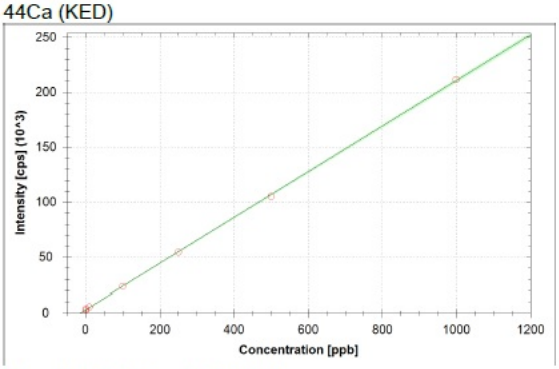

f(x) = 207.6709*x + 3031.2466
R^2 = 0.9999
BEC = 14.596 ppb
LoD = N/A

88Sr (KED)

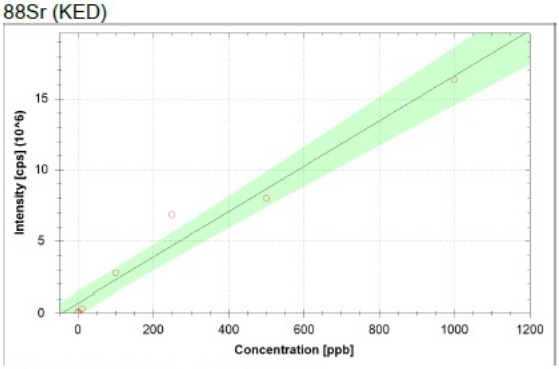

f(x) = 15932.1542*x + 680915.0118
R^2 = 0.9699
BEC = 42.738 ppb
LoD = N/A